UNIVERSITY OF CAPE TOWN

Department of Mechanical Engineering
Centre for Materials Engineering

Influence of Oxidation Treatment on the Corrosion Behaviour of Ti-6Al-4V alloy

By
Aloshan Shaun Chetty
CHTALO001
March 2011

Influence of the Oxidation Treatment on the Corrosion Behaviour of Ti-6Al-4V alloy

A thesis submitted to the Faculty of Engineering and Built Environment,
University of Cape Town, in fulfilment of the requirements
for the degree of Master of Science of Engineering

By
Aloshan Shaun Chetty
Centre for Materials Engineering
2011

ABSTRACT

Titanium-6Al-4V is a greatly desired alloy due to its attractive properties and exceptional corrosion resistance. Surface modifications such as thermal oxidation (TO) and oxygen boost diffusion hardening (OBDH) improve the tribological properties and wear resistance of Ti-6Al-4V. However, surface modification influences the corrosion behaviour of the metal. Therefore, the aim of this research project is to characterize how surface modifications influence the electrochemical behaviour of Ti-6Al-4V.

Electrochemical analysis was carried out on Ti-6Al-4V, in an untreated, TO and OBDH treated condition. Open circuit potential (OCP) tests were performed to determine the effect of time on the free corrosion potential of untreated and treated specimens. The potentiodynamic polarization technique was employed to determine the corrosion characteristics of the untreated and treated metal. Electrochemical impedance spectroscopy (EIS) was utilized to establish differences between the oxide layer present on untreated and surface treated Ti-6Al-4V specimens. The equivalent circuit for the alloy is determined and the impedance results are compared to the results obtained from potentiodynamic testing.

The OCP tests displayed an increase in potential over time, stabilizing at higher potentials for untreated and surface treated conditions. Potentiodynamic polarization results indicated that the TO specimens were very porous, allowing for the penetration of chloride ions from the electrolyte (3.5wt.% NaCl) and thereby contacting the substrate at the oxide/substrate interface. The untreated and OBDH specimens tended to produce similar electrochemical behaviour in both potentiodynamic and impedance results. However, the OBDH specimens resulted in a more stable passive layer, which remained protective even after breakdown at high potentials. The theoretical model proposed for Ti-6Al-4V displayed an excellent fit to the experimental data. Impedance data confirmed the porous oxide layer on TO specimens, as well as the similar behaviour between untreated and OBDH specimens.

All electrochemical tests confirmed that Ti-6Al-4V is highly protective against 3.5wt.% NaCl, due to the low current densities and passivating ability of the metal. The untreated metal displayed similar corrosion resistance to the OBDH treated specimens, whereas the TO specimen provided the least corrosion resistance due to its highly porous thermally oxidised layer. Ultimately, potentiodynamic and EIS testing concluded that the OBDH specimen provided the most compact passive layer (due to the high oxygen reservoir beneath the surface) and therefore the highest corrosion resistance.

ACKNOWLEDGEMENTS

I wish to express my appreciation to all those who have assisted me in the completion of this research project possible, in particular:

- Advanced Manufacturing Technology Strategy (AMTS) for providing the financial support required and the means to make this research possible.
- Professor R. D. Knutsen, for his continuous supervision, advice and constant guidance throughout this research project.
- Professor Candice Lang for being helpful and always offering a friendly word of advice
- Beverly Glass for welcoming me with a friendly smile and chat.
- Mr Glen Newins and the rest of the workshop staff for making any idea possible.
- Miranda Waldron, for her SEM expertise.
- Penny Park Ross for making sure all lab equipment was always at hand.
- I offer my regards and blessings to all the staff and students at the Centre for Materials Engineering who supported me in any respect during the completion of the project.
- I would like to extend a special thank you to all my close friends at the Centre for Materials Engineering, for making my lengthy days/nights of work on campus enjoyable and full of laughter, even during stressful times.

I would like to convey my utmost gratitude to my parents, without whom this research project would not be possible. Thank you for believing in me, supporting me and never questioning my decisions, but giving me guidance throughout. To a special person in my life, Jodilee, I owe you my everlasting gratefulness for your endless patience and encouraging words of support.

Above all I would like to thank God for giving me the intellect, strength and motivation to complete this research. Thank you for guiding me through all obstacles in my way to reach this point in my life.

Amen.

DECLARATION

I, Aloshan Shaun Chetty, know the meaning of plagiarism and declare that all the work in this document, save for that which is properly acknowledged, is my own.

Signature: Date:

TABLE OF CONTENTS

Page

1 INTRODUCTION 14

1.1 Motivation 14

1.2 Research Objectives 15

2 LITERATURE REVIEW: TITANIUM 16

2.1 Titanium 16

2.2 Allotropy of Titanium 16

2.3 Titanium alloys 17

2.3.1 Phase Stabilization 18

2.3.2 Property changes through phase stabilization 19

2.4 Ti-6Al-4V alloy 20

3 LITERATURE REVIEW: SURFACE ENGINEERING OF TITANIUM ALLOYS 22

3.1 Effect of Thermal Oxidation on Ti-6Al-4V 22

3.2 Oxygen Boost Diffusion Hardening 23

3.2.1 Step (i): Thermal Oxidation 24

3.2.2 Step (ii): Oxygen Boost Diffusion 26

3.2.3 Diffusion Phase Morphology 28

4 LITERATURE REVIEW: CORROSION RESISTANCE 30

4.1 Electrochemical Nature of Aqueous Corrosion 30

4.2 The Potentiodynamic Polarization Scan 31

4.3 Corrosion Rates 33

4.3.1 Polarization Resistance 33

4.3.2 Tafel Plots 34

4.4 Corrosion Resistance of Ti-6Al-4V 36

4.4.1 Characterization of Ti-6Al-4V oxide layer 37

4.4.2 Corrosion resistance of Thermally Oxidised Ti-6Al-4V 38

4.5 Electrochemical Polarization of Ti-6Al-4V 39

4.5.1 Composition of oxide layer at varying potentials 40

5 LITERATURE REVIEW: DIFFERENCES IN DC AND AC CURRENT 42

5.1 Faradaic Current and Corrosion 42

5.2 The Electric Double Layer 42
5.3 Direct Current (DC) and the Electric Double Layer 42
5.4 Alternating Current (AC) and the Electric Double Layer 43

6 LITERATURE REVIEW: ELECTROCHEMICAL IMPEDANCE SPECTROSCOPY (EIS) 44

6.1 THEORY 44
6.2 Vector Analysis 46
6.3 Equivalent Circuit Diagrams 48

6.3.1 Circuit Behaviour 50

6.4 Impedance Plots and Interpretation 51

6.4.1 The Nquist Plot 51
6.4.2 The Bode Plot 53

6.5 Electrochemical Impedance Evaluation of Ti-6Al-4V 54

7 EXPERIMENTAL PROCEDURE 59

7.1 Materials used 59
7.2 Specimen Preparation 59
7.3 Heat treatments 60
7.4 Hardness Testing 60
7.5 Electrochemical Testing 60

7.5.1 Specimen preparation for corrosion testing 60
7.5.2 Preparation of Electrolyte 61
7.5.3 Potentiostat 62
7.5.4 Reference Electrode 62
7.5.5 The Corrosion Cell 62
7.5.6 Standard Test 63
7.5.7 Open Circuit Potential (OCP) versus Time Tests 64
7.5.8 DC tests: Potentiodynamic scans 64
7.5.9 DC tests: Tafel plots 65
7.5.10 AC tests 65

7.6 Microscopy 65
7.7 Scanning Electron Microscopy (SEM) 65

8 RESULTS 66

8.1 Microstructure 66

8.1.1 Untreated Ti-6Al-4V 66
8.1.2 Thermally Oxidised Ti-6Al-4V 67
8.1.3 Oxygen Boost Diffusion Hardened (OBDH) Ti-6Al-4V 68

8.2 Hardness Profile 71

9 RESULTS: DC ANALYSIS 72

9.1 Long Term Immersion OCP (Open Circuit Potential)Tests 72

9.1.1 Comparison of OCP tests 72

9.2 Potentiodynamic Analysis 74

9.2.1 Untreated Ti-6Al-4V 74
9.2.2 Thermally Oxidised Ti-6Al-4V 77
9.2.3 Oxygen Boost Diffusion Hardened (OBDH) Ti-6Al-4V 80
9.2.4 Comparison of Treated with Untreated Ti-6Al-4V 84

9.3 Corrosion Micrographs 87

9.3.1 Untreated Ti-6Al-4V 87
9.3.2 OBDH Ti-6Al-4V 88

9.4 Corrosion Rates 89

10 RESULTS: AC ANALYSIS (EIS) 90

10.1 Equivalent Circuit Model 91
10.2 Untreated Ti-6Al-4V 92

10.2.1 OCP impedance plots 92
10.2.2 Overlays of Potential Variation Impedance Plots 93

10.3 Thermally Oxidised Ti-6Al-4V 95

10.3.1 OCP impedance plots 95
10.3.2 Overlays of Potential Variation Impedance Plots 96

10.4 Oxygen Boost Diffusion Hardened (OBDH) Ti-6Al-4V 98

10.4.1 OCP impedance plots 98
10.4.2 Overlays of Potential Variation Impedance Plots 99

10.5 Evaluation of Impedance Data 100
10.6 E.I.S Trends with Potential Variation 102

10.6.1 Untreated Ti-6Al-4V 102
10.6.2 Thermally Oxidised (TO) Ti-6Al-4V 106
10.6.3 Oxygen Boost Diffusion Hardened (OBDH) Ti-6Al-4V 110

11 DISCUSSION 114

11.1 Microstructure analysis 114

11.1.1 Untreated Ti-6Al-4V 114
11.1.2 Thermally Oxidized (TO) Ti-6Al-4V 114
11.1.3 Oxygen Boost Diffusion Hardened (OBDH) Ti-6Al-4V 114

11.2 Hardness Profile 115

12 DISCUSSION: ELECTROCHEMICAL ANALYSIS 116

12.1 Long Term Immersion OCP (Open Circuit Potential) Tests 116
12.2 Potentiodynamic Analysis 117

12.2.1 Untreated Ti-6Al-4V 117
12.2.2 Thermally Oxidized (TO) Ti-6Al-4V 118
12.2.3 Oxygen Boost Diffusion Hardened (OBDH) Ti-6Al-4V 119
12.2.4 Comparison of treated with untreated Ti-6Al-4V 121

12.3 Corrosion Micrographs 122
12.4 Corrosion Rates 123

13 DISCUSSION: AC ANALYSIS (EIS) 124

13.1 Overlays of Untreated and Treated Ti-6Al-4V 124
13.2 EIS analysis of untreated Ti-6Al-4V 125

13.2.1 Nquist Plot Analysis 125
13.2.2 Bode Phase Plot Analysis 126
13.2.3 Untreated Ti-6Al-4V EIS Trends 127

13.3 EIS analysis of OBDH Ti-6Al-4V 129

13.3.1 Nquist Plot Analysis 129
13.3.2 Bode Phase Plot Analysis 129
13.3.3 OBDH Ti-6Al-4V EIS Trends 130

13.4 EIS Analysis of TO Ti-6Al-4V 131

13.4.1 TO Ti-6Al-4V EIS Trends 132

13.5 Evaluation of EIS data integrity 134

14 CONCLUSIONS 135

14.1 Surface treated Ti-6Al-4V 135
14.2 Potentiodynamic (DC) Analysis 135
14.3 Electrochemical Impedance Spectroscopy (AC) Analysis 136

15 REFERENCES 137
16 APPENDIX 144

16.1 Untreated Ti-6Al-4V Potential Variation Impedance Plots 145
16.2 TOTi-6Al-4V Potential Variation Impedance Plots 153
16.3 OBDH Ti-6Al-4V Potential Variation Impedance Plots 161

LIST OF FIGURES

Figure 1: Flow chart of titanium and its allotropes..... 17
Figure 2: Phase diagrams of titanium alloys (Qazi et al. 2002). 18
Figure 3: Ti-6Al-4V pseudo-binary phase diagram (Lutjering & Williams 2007). 20
Figure 4: Cross section microstructure of the Ti-6Al-4V specimen after oxidation at 850℃ for 20 minutes..... 25
Figure 5: Cross section microstructure of the Ti-6Al-4V specimen after oxidation and then boost diffusion treated for 20 hours in vacuum 27
Figure 6: Distribution of Oxygen along the depth from the surface for sample oxidised at 850℃ for 20 minutes and boost diffused for 7 ho urs..... 28
Figure 7: Change in oxide thickness during the boost process at 850℃ 28
Figure 8: Cross section microstructure of oxidised sample at 850℃ for 20 minutes and boost diffused at 850℃ for 20 hours (Zhang et al. 2007)..... 29
Figure 9: Theoretical anodic polarization scan..... 32
Figure 10: Linear Polrization Resistance 33
Figure 11: Tafel Slope Calculation (ASTM G3 – 89. 1989). 35
Figure 12: Potentiodynamic polarization curve for Ti-6Al-4V in Hank's solution (Luiz de Assis et al. 2006). 40
Figure 13: Voltage and Current as a function of time..... 45
Figure 14 Vector in terms of X and Y Coordinates..... 46
Figure 15: Vector in terms of angle θ and magnitude |Z| 47
Figure 16: Vector in terms of Real (I') and Imaginary (I") Coordinates 47
Figure 17: Equivalent Circuit for a Single Electrochemical Cell known as a Randles Cell..... 50
Figure 18: Nquist Plot for a Simple Electrochemical System 52
Figure 19: Bode Plot for a Simple Electrochemical System 53
Figure 20: Equivalent circuit proposed for Ti-6Al-4V..... 54
Figure 21: Equivalent circuit used for the two-layer oxide film on untreated Ti6Al4V, and schematic representation of the oxide film on Ti6Al4V, demonstrating how pores in the porous layer are sealed due to electrolyte filling (Wang et al. 2003). 56
Figure 22: Bode Plot of Ti after anodic polarization at 0V (●), 0.5V (■), 1V (▲), in the presence of chloride ions 58
Figure 23: Picture of the Princeton Flat Cell, utilized in electrochemical testing..... 63
Figure 24: Potentiodynamic scan of a 430 Stainless Steel specimen in 1.0 N H_2SO_4. 64
Figure 25: High magnification view of polished untreated Ti-6Al-4V prior to testing. 66
Figure 26: Thermally Oxidised Ti-6Al-4V corrosion specimen prior to testing. 67
Figure 27: High magnification view of polished thermally oxidised Ti-6Al-4V prior to testing. 67

Figure 28: OBDH Ti-6Al-4V specimen post boost diffusion treatment prior to polishing. 68
Figure 29: Micrograph of OBDH specimen after: (a) the removal of 15µm of the surface (b) the removal of 30µm of the surface. 69
Figure 30: Micrograph of Oxygen Boost Diffusion Hardened Ti-6Al-4V after removal of residual oxide by polishing. 70
Figure 31: Hardness profile of the Untreated and Treated Ti-6Al-4V. 71
Figure 32: Comparison of open circuit potentials after long term immersion times of Untreated, Thermally Oxidised and OBDH Ti-6Al-V specimens in 3.5 wt.% NaCl. .. 72
Figure 33: Potentiodynamic scans of untreated Ti-6Al-4V in 3.5 wt.% NaCl solution initiated at -0.5V below OCP. 74
Figure 34: Potentiodynamic scans of untreated Ti-6Al-4V in 3.5 wt.% NaCl solution initiated at -1.0V_{SCE} 75
Figure 35: Comparison of potentiodynamic scans of -0.5V below OCP (BLUE) and -1.0V_{SCE} (RED) for Untreated Ti-6Al-4V. 76
Figure 36: Potentiodynamic scans of thermally oxidised Ti-6Al-4V in 3.5 wt.% NaCl solution initiated at -0.5V below OCP. 77
Figure 37: Potentiodynamic scans of thermally oxidised Ti-6Al-4V in 3.5 wt.% NaCl solution initiated at -1.0V_{SCE}. 78
Figure 38: Comparison of potentiodynamic scans of -0.5V below OCP (BLUE) and -1.0V_{SCE} (RED) for Thermally Oxidised Ti-6Al-4V. 79
Figure 39: Potentiodynamic scans of OBDH Ti-6Al-4V in 3.5 wt.% NaCl solution initiated at -0.5V below OCP. 80
Figure 40: Potentiodynamic scans of OBDH Ti-6Al-4V in 3.5 wt.% NaCl solution initiated at -1.0V_{SCE} 81
Figure 41: Potentiodynamic scans of OBDH Ti-6Al-4V specimens removed from the furnace without any further polishing, in 3.5 wt.% NaCl solution, initiated at -0.5V below OCP. 82
Figure 42: Comparison of potentiodynamic scans of -0.5V below OCP polished (BLACK) and unpolished (RED) and -1.0V_{SCE} (BLUE) for Untreated Ti-6Al-4V. 83
Figure 43: Comparison of potentiodynamic scans of Untreated (BLUE), Thermally Oxidised (RED) and OBDH (BLACK) Ti-6Al-V in the scan range of -0.5V below OCP. 85
Figure 44: Comparison of potentiodynamic scans of Untreated (BLUE), Thermally Oxidised (RED) and OBDH (BLACK) Ti-6Al-V in the scan range of -1.0V_{SCE} 85
Figure 45: Micrograph showing the contrast between the corroded surface and the non exposed protected region of an untreated Ti-6Al-4V specimen 87
Figure 46: Micrograph showing an increased magnification view of general corrosion occurring on the exposed Untreated Ti-6Al-4V surface. 88
Figure 47: Micrograph showing the contrast between the corroded surface and the unaffected area of an OBDH test sample 88

Figure 48: Micrograph showing an increased magnification view of general corrosion occurring on the exposed OBDH Ti-6Al-4V surface. 89
Figure 49: Equivalent Circuit modelled for untreated and treated Ti-6Al-4V. 91
Figure 50: Nquist plot for untreated Ti-6Al-4V at OCP. 92
Figure 51: Bode Magnitude |Z| and Bode Phase (Angle) plots for untreated Ti-6Al-4V at OCP. 92
Figure 52: Overlays of OCP and potential varied Nquist plots from -0.5V – 3.0V_{SCE} for untreated Ti-6Al-4V. 93
Figure 53: Overlays of OCP and potential varied Bode phase plots from -0.5V – 3.0V_{SCE} for untreated Ti-6Al-4V. 94
Figure 54: Nquist plot for TO Ti-6Al-4V at OCP. 95
Figure 55: Bode Magnitude |Z| and Bode Phase (Angle) plots for TO Ti-6Al-4V at OCP. 95
Figure 56: Overlays of OCP and potential varied Nquist plots from -0.5V – 3.0V_{SCE} for TO Ti-6Al-4V. 96
Figure 57: Overlays of OCP and potential varied Bode phase plots from -0.5V – 3.0V_{SCE} for TO Ti-6Al-4V. 97
Figure 58: Nquist plot for OBDH Ti-6Al-4V at OCP. 98
Figure 59: Bode Magnitude |Z| and Bode Phase (Angle) plots for OBDH Ti-6Al-4V at OCP. 98
Figure 60: Overlays of OCP and potential varied Nquist plots from -0.5V – 3.0V_{SCE} for OBDH Ti-6Al-4V. 99
Figure 61: Overlays of OCP and potential varied Bode phase plots from -0.5V – 3.0V_{SCE} for OBDH Ti-6Al-4V. 100
Figure 62: Potentiodynamic curve of untreated Ti-6Al-4V (left axis) overlayed with the porous layer resistance, R_1 (right axis), as a function of applied potential for untreated Ti-6Al-4V. 102
Figure 63: Potentiodynamic curve of untreated Ti-6Al-4V (left axis) overlayed with the barrier layer resistance, R_2 (right axis), as a function of applied potential for untreated Ti-6Al-4V. 103
Figure 64: Potentiodynamic curve of untreated Ti-6Al-4V (left axis) overlayed with the porous layer capacitance, Q_1 (right axis), as a function of applied potential for untreated Ti-6Al-4V. 104
Figure 65: Potentiodynamic curve of untreated Ti-6Al-4V (left axis) overlayed with the barrier layer capacitance, Q_2 (right axis), as a function of applied potential for untreated Ti-6Al-4V. 105
Figure 66: Potentiodynamic curve of TO Ti-6Al-4V (left axis) overlayed with the porous layer resistance, R_1 (right axis), as a function of applied potential for TO Ti-6Al-4V. 106
Figure 67: Potentiodynamic curve of TO Ti-6Al-4V (left axis) overlayed with the barrier layer resistance, R_2 (right axis), as a function of applied potential for TO Ti-6Al-4V. 107

Figure 68: Potentiodynamic curve of TO Ti-6Al-4V (left axis) overlayed with the porous layer capacitance, Q_1 (right axis), as a function of applied potential for TO Ti-6Al-4V. 108
Figure 69: Potentiodynamic curve of TO Ti-6Al-4V (left axis) overlayed with the barrier layer capacitance, Q_2 (right axis), as a function of applied potential for TO Ti-6Al-4V. 109
Figure 70: Potentiodynamic curve of OBDH Ti-6Al-4V (left axis) overlayed with the porous layer resistance, R_1 (right axis), as a function of applied potential for OBDH Ti-6Al-4V. 110
Figure 71: Potentiodynamic curve of OBDH Ti-6Al-4V (left axis) overlayed with the barrier layer resistance, R_2 (right axis), as a function of applied potential for OBDH Ti-6Al-4V. 111
Figure 72: Potentiodynamic curve of OBDH Ti-6Al-4V (left axis) overlayed with the porous layer capacitance, Q_1 (right axis), as a function of applied potential for OBDH Ti-6Al-4V. 112
Figure 73: Potentiodynamic curve of OBDH Ti-6Al-4V (left axis) overlayed with the barrier layer capacitance, Q_2 (right axis), as a function of applied potential for OBDH Ti-6Al-4V. 113
Figure 75: Nquist plot for untreated Ti-6Al-4V at $-0.5V_{SCE}$. 145
Figure 76: Bode Magnitude and Bode Phase plots for untreated Ti-6Al-4V at $-0.5V_{SCE}$. 145
Figure 77: Nquist plot for untreated Ti-6Al-4V at at $0.0V_{SCE}$. 146
Figure 78: Bode Magnitude and Bode Phase plots for untreated Ti-6Al-4V at $0.0V_{SCE}$. 146
Figure 79: Nquist plot for untreated Ti-6Al-4V at $0.5V_{SCE}$. 147
Figure 80: Bode Magnitude and Bode Phase plots for untreated Ti-6Al-4V at $0.5V_{SCE}$. 147
Figure 81: Nquist plot for untreated Ti-6Al-4V at $1.0V_{SCE}$. 148
Figure 82: Bode Magnitude and Bode Phase plots for untreated Ti-6Al-4V at $1.0V_{SCE}$. 148
Figure 83: Nquist plot for untreated Ti-6Al-4V at $1.5V_{SCE}$. 149
Figure 84: Bode Magnitude and Bode Phase plots for untreated Ti-6Al-4V at $1.5V_{SCE}$. 149
Figure 85: Nquist plot for untreated Ti-6Al-4V at $2.0V_{SCE}$. 150
Figure 86: Bode Magnitude and Bode Phase plots for untreated Ti-6Al-4V at $2.0V_{SCE}$. 150
Figure 87: Nquist plot for untreated Ti-6Al-4V at $2.5V_{SCE}$. 151
Figure 88: Bode Magnitude and Bode Phase plots for untreated Ti-6Al-4V at $2.5V_{SCE}$. 151
Figure 89: Nquist plot for untreated Ti-6Al-4V at $3.0V_{SCE}$. 152
Figure 90: Bode Magnitude and Bode Phase plots for untreated Ti-6Al-4V at $3.0V_{SCE}$. 152

Figure 91: Nquist plot for TO Ti-6Al-4V at -0.5V_{SCE}..... 153
Figure 92: Bode Magnitude and Bode Phase plots for TO Ti-6Al-4V at -0.5V_{SCE}. .. 153
Figure 93: Nquist plot for TO Ti-6Al-4V at 0.0V_{SCE}..... 154
Figure 94: Bode Magnitude and Bode Phase plots for TO Ti-6Al-4V at 0.0V_{SCE}. ... 154
Figure 95: Nquist plot for TO Ti-6Al-4V at 0.5V_{SCE}..... 155
Figure 96: Bode Magnitude and Bode Phase plots for TO Ti-6Al-4V at 0.5V_{SCE}. ... 155
Figure 97: Nquist plot for TO Ti-6Al-4V at 1.0V_{SCE}..... 156
Figure 98: Bode Magnitude and Bode Phase plots for TO Ti-6Al-4V at 1.0V_{SCE}. ... 156
Figure 99: Nquist plot for TO Ti-6Al-4V at 1.5V_{SCE}..... 157
Figure 100: Bode Magnitude and Bode Phase plots for TO Ti-6Al-4V at 1.5V_{SCE}. . 157
Figure 101: Nquist plot for TO Ti-6Al-4V at 2.0V_{SCE}..... 158
Figure 102: Bode Magnitude and Bode Phase plots for TO Ti-6Al-4V at 2.0V_{SCE}. . 158
Figure 103: Nquist plot for TO Ti-6Al-4V at 2.5V_{SCE}..... 159
Figure 104: Bode Magnitude and Bode Phase plots for TO Ti-6Al-4V at 2.5V_{SCE}. . 159
Figure 105: Nquist plot for TO Ti-6Al-4V at 3.0V_{SCE}..... 160
Figure 106: Bode Magnitude and Bode Phase plots for TO Ti-6Al-4V at 3.0V_{SCE}. . 160
Figure 107: Nquist plot for OBDH Ti-6Al-4V at -0.5V_{SCE}. 161
Figure 108: Bode Magnitude and Bode Phase plots for OBDH Ti-6Al-4V at -0.5V_{SCE}.
..... 161
Figure 109: Nquist plot for OBDH Ti-6Al-4V at 0.0V_{SCE}..... 162
Figure 110: Bode Magnitude and Bode Phase plots for OBDH Ti-6Al-4V at 0.0V_{SCE}.
..... 162
Figure 111: Nquist plot for OBDH Ti-6Al-4V at 0.5V_{SCE}..... 163
Figure 112: Bode Magnitude and Bode Phase plots for OBDH Ti-6Al-4V at 0.5V_{SCE}.
..... 163
Figure 113: Nquist plot for OBDH Ti-6Al-4V at 1.0V_{SCE}..... 164
Figure 114: Bode Magnitude and Bode Phase plots for OBDH Ti-6Al-4V at 1.0V_{SCE}.
..... 164
Figure 115: Nquist plot for OBDH Ti-6Al-4V at 1.5V_{SCE}..... 165
Figure 116: Bode Magnitude and Bode Phase plots for OBDH Ti-6Al-4V at 1.5V_{SCE}.
..... 165
Figure 117: Nquist plot for OBDH Ti-6Al-4V at 2.0V_{SCE}..... 166
Figure 118: Bode Magnitude and Bode Phase plots for OBDH Ti-6Al-4V at 2.0V_{SCE}.
..... 166
Figure 119: Nquist plot for OBDH Ti-6Al-4V at 2.5V_{SCE}..... 167
Figure 120: Bode Magnitude and Bode Phase plots for OBDH Ti-6Al-4V at 2.5V_{SCE}.
..... 167
Figure 121: Nquist plot for OBDH Ti-6Al-4V at 3.0V_{SCE}..... 168
Figure 122: Bode Magnitude and Bode Phase plots for OBDH Ti-6Al-4V at 3.0V_{SCE}.
..... 168

LIST OF TABLES

Table 1: Material Properties of Titanium and its allotropes (Askeland & Phule 2006). 19
Table 2: Alloying elements in Ti-6Al-4V 20
Table 3: Material Properties of Ti-6Al-4V 21
Table 4: Impedance Equations describing their particular Circuit Elements .. 49
Table 5: Polishing procedure to achieve mirror finish in preparation for electrochemical testing. 59
Table 6: Polishing procedure for the removal of OBDH oxide, in preparation for electrochemical testing. 61
Table 7: Open Circuit Potentials of Untreated and Treated Ti-6Al-4V. 73
Table 8: Potentiodynamic Data for untreated and treated Ti-6Al-4V. 86
Table 9: Corrosion Rates for untreated and treated Ti-6Al-4V. 89
Table 10: Tabulated EIS data at Ecorr and offset potentials versus reference (0.0V). 101

1 INTRODUCTION

1.1 Motivation

The demand for higher performance and weight reduction has been the main drive for the substitution of steel components with those made from titanium alloys. This is because titanium alloys possess a combination of attractive properties in terms of high strength to weight ratio, exceptional corrosion resistance and excellent biocompatibility. Therefore, titanium alloys have been utilized in a wide range of applications in the fields of aerospace, chemical industry, marine and biomedical devices.

However, titanium alloys are characterized by their poor tribological properties (especially in sliding contact), which has been a severe barrier to tribological applications (Zhang et al. 2006). Many surface engineering techniques have been applied to titanium alloys to improve the tribological properties by reducing friction and improving hardness. It is now well established that attractive case-hardening of titanium alloys can be achieved by surface alloying with oxygen. The oxygen atoms dissolve in solid solution and stabilize the hexagonal-close-packed (HCP) α-phase with concomitant increase in resistance to dislocation movement and hence increase in surface hardness. Effective case hardening of the metal is achieved through a two step process commonly known as oxygen boost diffusion hardening (OBDH), which involves a combination of thermal oxidation and oxygen diffusion into the titanium substrate. The OBDH treatment relies on the formation of an adherent oxide layer on the surface, which subsequently decomposes and releases oxygen to diffuse into the substrate forming an interstitial solid solution. In doing so, the oxide layer acts as an oxygen reservoir for the boost-diffusion process. This technique has been investigated extensively and was found to effectively increase the wear performance of titanium alloys (Zhang et al. 2007).

On the other hand titanium exhibits excellent corrosion resistance due to the natural formation of a stable, strongly adherent protective oxide layer on the metals surface. Therefore, it needs to be speculated that modifying the surface (through the heat treatments) will also influence the corrosion behaviour of the metal. Consequently, the necessity to characterize the corrosion behaviour of the surface treated alloys arises, with a view to compare the behaviour to the untreated alloys.

1.2 Research Objectives

Therefore, the following research questions are addressed:

- How does the OBDH and TO treatments affect the electrochemical character of the surface layer/s of the titanium alloy when compared to the untreated metal?
- Is the open circuit corrosion potential (OCP) influenced by surface treatment condition when immersed in a corrosive medium?
- Does the OBDH and TO treatments affect the passivity of the titanium alloy when compared to untreated surfaces?
- Can potentiodynamic and electrochemical impedance (EIS) techniques be used in a complimentary manner to analyse the corrosion behaviour of surface treated Ti-6Al-4V specimens

2 LITERATURE REVIEW: TITANIUM

2.1 Titanium

Titanium was first discovered in 1791 by William Gregor and given the name Titanium after the Titans of Greek mythology. The element Ti occurs in a number of mineral deposits as oxides, principally rutile and ilmenite, and is widely distributed in the Earth's crust. The titanium metal is then extracted from these principle mineral ores via the Hunter process or the more commonly used Kroll process.

Titanium possesses many attractive and desired properties such as good strength-to-weight ratio, excellent corrosion resistance in neutral and oxidising environments, and the ability to attain great strength increases through alloying and, in some of its alloys, by heat treatments.
Other advantages for specific applications include:

i) low density,
ii) low coefficient of thermal expansion
iii) good oxidation resistance at intermediate temperatures
iv) good toughness
v) low heat treating temperature during hardening

These attractive properties make the uses of titanium are widespread. Due to specific properties such as high corrosion resistance, titanium alloys are used extensively in prosthetic devices such as artificial heart pumps and load bearing bone or hip-joint replacements. Other especially desired properties include the metals high tensile-to-density ratio including high resistance to crack propagation, fatigue resistance and ability to withstand moderately high temperatures without creeping. These material properties make titanium alloys a highly demanded commodity in aerospace and marine applications. Its usage spreads to the automotive industry as well as contributing its uses in the petrochemical industry, in the production of heat exchangers and reactors, to the sporting goods industry, in the manufacture of bicycles, golf clubs and tennis rackets. Taking into account the metals aesthetic appeal for jewellery applications, it is clearly obvious of the importance of titanium and the metals abundant usage in both industry and commercial enterprises.

2.2 Allotropy of Titanium

Titanium's properties are determined mainly by their heat treatments and alloying content. The metal's allotropic behaviour allows the metal to exist in different forms at room temperature when appropriately alloyed and/or heat treated. Commercially pure

titanium has an alpha (α) structure up to a temperature of 882℃, above which it undergoes an allotropic transformation from hexagonal-close-packed (HCP) α into a body-centered-cubic (BCC) beta (β) structure which remains stable to melting point (Qazi et al. 2002). This high temperature change brings about a alteration in properties where the α-phase is required for hardness and the β-phase increases the materials formability.

2.3 Titanium alloys

All elements which are in the range of 0.85 – 1.15 of titanium's atomic radius are able to alloy substitutionally with significant solubility. Elements which alloy with titanium interstitially are less than 0.59 the atomic radius of titanium e.g. H, N, O, C.

In the figure below, titanium and its alloys has been divided into four separate sections for ease of presentation. **Figure 1** characterizes titanium into unalloyed titanium and three groups of titanium alloys based on metallurgical differences, which in turn result in differences in material properties.

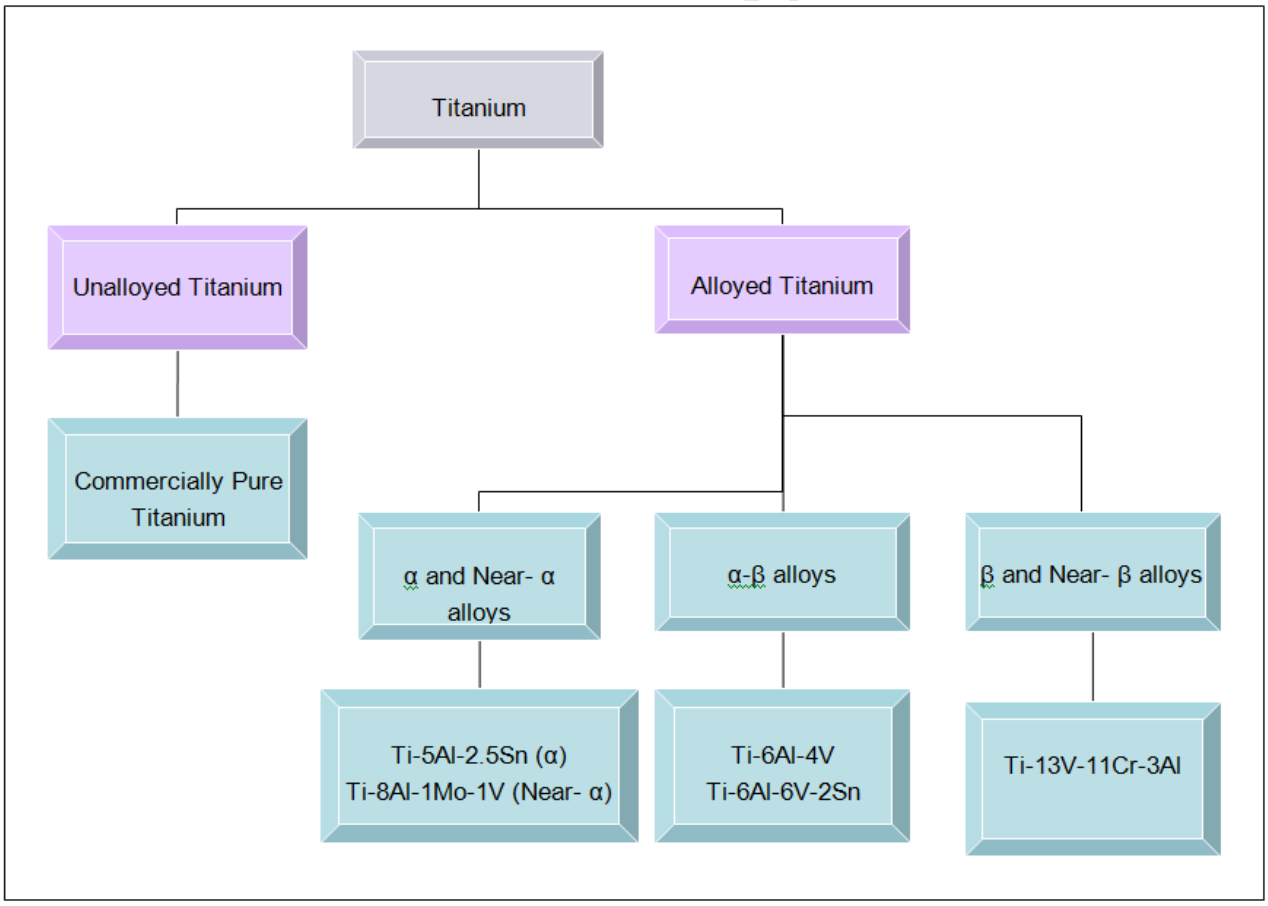

Figure 1: Flow chart of titanium and its allotropes.

2.3.1 Phase Stabilization

The ease at which titanium dissolves solutes makes it difficult to design precipitation hardened alloys, but these alloyed solutes have an effect on stabilizing either the α or β phases. Addition of these solutes or alloying elements alters the transus temperatures achieving a wide range of physical and mechanical properties.

Some elements stabilize the α-phase forming an α-alloy at equilibrium conditions as displayed in Graph (i) of **Figure 2**. A β-alloy contains enough β stabilizers such that 100% β is retained upon quenching above the β transus temperature demonstrated by the Graph (ii) in **Figure 2**. Controlling the amounts of α and β stabilizing elements will result in an α-β alloy at room temperature displayed in Graph (iii) of **Figure 2** (Qazi et al. 2002).

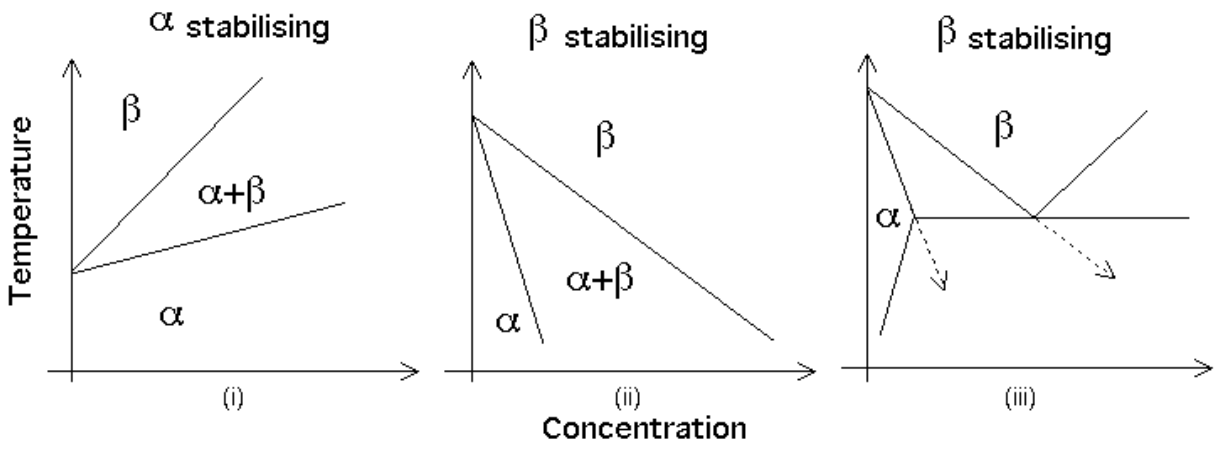

Figure 2: Phase diagrams of titanium alloys (Qazi et al. 2002).

Alpha stabilizers include Al as the most common α-stabilizer as well as C, O and N, whereas elements such as Mo, Cu, and V stabilize the β-phase. Mn, Cr and Fe produce a eutectoid reaction reducing the temperature at which the α-β transformation occurs and results in a two phase α-β structure at room temperature. Additions of Sn and Zr provides solid solution strengthening without affecting the transformation temperature (Askeland & Phule 2006).

2.3.2 Property changes through phase stabilization

The microstructure of the alloy under equilibrium conditions will determine its properties. Near α and α-alloys exhibit superior corrosion resistance, but with limited usage such as medical implants due to their low ambient temperature strength. The presence of two phases in the α-β alloy is responsible for the higher strength of this alloy type. The β-alloy and metastable β-alloys exhibits a combination of good properties such as high strength, good formability, superior corrosion resistance as well as high hardenability, making this alloy a good candidate for complete biomedical joint replacement (M. Long & H.J. Rack 1998). **Table 1** demonstrates how titanium's allotropes compare to each other (Askeland & Phule 2006).

Material	Tensile Strength (MPa)	Yield Strength (MPa)	% Elongation
Commercially Pure Ti			
99.5% Ti	240	170	24
99% Ti	551	480	15
Alpha Ti Alloys			
5% Al – 2.5% Sn	860	780	15
Beta Ti Alloys			
13% V – 11% Cr – 3% Al	1300	1200	5
Alpha-beta Ti alloys			
6% Al – 4% V	950	880	8

Table 1: Material Properties of Titanium and its allotropes (Askeland & Phule 2006).

2.4 Ti-6Al-4V alloy

Ti-6Al-4V is known as the “workhorse” alloy of the titanium industry as it accounts for more than 50% of titanium usage making it the most commonly used titanium alloy.
Ti-6Al-4V exists as an α-β alloy at room temperature with the ability to achieve moderate strength increases through heat treatments. The pseudo-binary phase diagram, displayed in **Figure 3**, clearly depicts the region in which the α-β Ti-6Al-4V alloy forms, which is stable at room temperature.

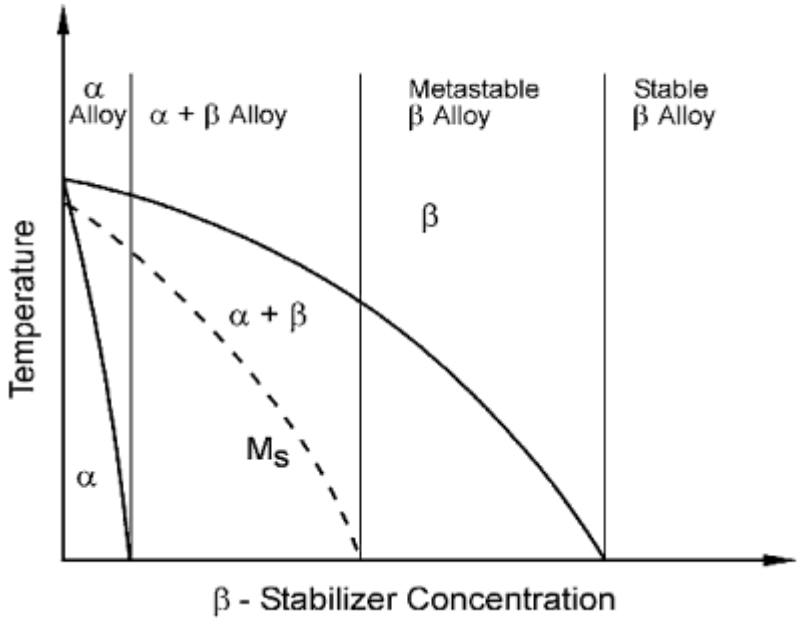

Figure 3: Ti-6Al-4V pseudo-binary phase diagram (Lutjering & Williams 2007).

With its high strength, light weight, corrosion resistance and formability, Ti-6Al-4V has become a world standard in aerospace applications. Even though the alloy is limited to service temperatures of below 350℃ and not recommended for use in wear applications, it can be considered in any application which requires high strength to weight ratio at low to moderate temperatures (Carpenter 2000).The weight percent alloying elements are tabulated in **Table 2** (Boyer et al. 1994) and an overview of the materials properties are presented in **Table 3** (Boyer et al. 1994, Metals Handbook 1990).

Component	Al	Fe	O	Ti	V
Weight %	6	Max 0.25	Max 0.2	Balance	4

Table 2: Alloying elements in Ti-6Al-4V (Boyer et al. 1994).

Property	Metric
Density	4.43 g.cm^3
Hardness (Vickers)	349
Modulus of Elasticity	113.8 GPa
Ultimate Tensile Strength	950 MPa
Yield Strength	880 MPa
% Elongation	8%
Thermal Conductivity	6.7 W/m-K

Table 3: Material Properties of Ti-6Al-4V (Boyer et al. 1994, Metals Handbook 1990).

3 LITERATURE REVIEW: SURFACE ENGINEERING OF TITANIUM ALLOYS

The ever increasing demands for higher performance and changing service conditions have been the driving force for the replacement of steel with titanium alloys. However, poor tribological properties limit its uses in applications involving wear conditions. The poor tribological performance of titanium alloys is related to their inherent characteristics, especially the surface nature of the alloy. Addressing this problem would require surface modification or changing the surface nature of the alloy i.e. surface engineering of titanium alloys (Dong & Li 2000). For this reason many surface engineering techniques have been applied to titanium and its alloys; techniques such as physical vapour deposition (PVD), laser surface treatments, plasma spraying, plasma immersion ion implantation, plasma nitriding, chemical vapour deposition (CVD) and oxygen boost diffusion hardening (OBDH) have been used to improve the surface properties of the metal and thereby increasing performance under wear conditions (Zhang et al. 2007).

3.1 Effect of Thermal Oxidation on Ti-6Al-4V

When assessing whether a material is suitable for wear applications, a surface engineered material must have low friction and anti-wear performance; adequate bond strength to the substrate to resist adhesive failure; and strong support from the substrate to prevent cohesive failure due to plastic deformation in the substrate (Bloyce et al. 1998).

Oxygen, like nitrogen and carbon, can significantly harden titanium alloys through the formation of titanium oxide. Much interest in titanium oxide has been sparked due to the increasing understanding of the mechanism of oxidation. A treatment in which thermal oxidation has been used to enhance the tribological performance of Ti-6Al-4V has been developed by Dong and Li (2000). It involves the formation of the lubricious rutile oxide layer that significantly reduces the friction of the thermally oxidised material. When two surfaces are in contact, asperities on the surface undergo elastic and plastic deformation to accommodate the stress. It is this plastic deformation between the contacting surfaces which make an important contribution to friction and wear. The friction and wear between the surfaces can be significantly reduced if the contacts between the surfaces are predominantly elastic. Thermally oxidising the material effectively limits the degree of plastic deformation and increases elastic contact which favours low adhesion between the contacting surfaces and hence reduces friction (Bloyce et al. 1998).

At ambient temperatures, Ti-6Al-4V also undergoes oxidation forming the naturally occurring thin oxide layer. However, during the oxidising treatment a fast accumulation of oxygen on the surface of Ti-6Al-4V occurs at high temperatures such as 500 - 900℃ (Bloyce et al. 1998), forming a thick oxide layer with satisfactory adhesion to the substrate. During the oxidation process various oxides form depending on the composition of the metal. For Ti-6Al-4V the oxides TiO_2, Al_2O_3 and V_2O_5 form during thermal oxidation treatments (Long and Rack 1998). Vanadium is found to be detrimental to the formation of the oxide layer whereas, if the content is high enough, aluminium is beneficial where the formation of the stable α-Al_2O_3 occurs (Gulyeryuz & Cimenoglu 2009).

Formation of a thick adherent oxide layer is greatly dependent on the temperature as well as the oxidation time, where the adjustment and control of these two parameters can result in a desirable layer (Dong and Li 2000). Increasing the time and temperature results in a higher hardness and the formation of a thicker oxide; however, stratification of the oxide occurs and the oxide layer delaminates from the metal. Although high surface hardness is achievable through thermal oxidation, oxide layer scaling damages the surface integrity of the metal and therefore, limits the use of thermal oxidation for surface hardening of titanium.

The limitations found in thermal oxidation can be greatly overcome using the novel method of Oxygen Boost Diffusion Hardening (OBDH) in which an adherent oxide layer is formed on the surface with a boost diffusion zone underneath.

3.2 Oxygen Boost Diffusion Hardening

It was found that the thermal oxidation treatment improved the rolling-sliding wear resistance under light to moderate loads (Dong and Li 2000). The relatively thin oxide layer with a limited diffusion zone showed some strength; however, inevitable scaling and delamination due to the high value of the Pilling-Bedworth ratio (Johns 2006) limited the formation of a thick oxide and deep case.

Therefore, an Oxygen Boost Diffusion Hardening (OBDH) process has been developed which consists of two steps namely:

i) Thermal oxidation of titanium specimens in oxygen
ii) Diffusion treatment of the pre-oxidised samples in a vacuum

Step (i) results in the formation of an adherent layer of optimum thickness followed by step (ii) which commences the boost diffusion step whereby oxygen from the oxide layer diffuses into the metal and thus increases the diffusion hardened zone initiated by the thermal oxidation step. This process results in a deeply hardened titanium

surface without evoking scaling or oxide spallation which is common during long oxidation times at high temperatures (Zhang et al. 2007, Dong and Li 2000).

3.2.1 Step (i): Thermal Oxidation

Thermal oxidation is conducted at elevated temperatures in an oxygen rich environment. During this step two processes occur simultaneously; namely oxide formation and interstitial strengthening of the metal during which oxygen atoms are constantly diffusing into the metal.

Luo et al. (2004) established that the high affinity of titanium for oxygen is due to the similar bond energies between the Ti-Ti bonds and the Ti-O bonds. In the work carried out by Zhang et al. (2007), a series of thermal oxidizing treatments were performed on the Ti-6Al-4V alloy at temperatures in the range off 600 – 850℃ with time being varied. The rate of oxidation accumulation at 850℃ was found to be much higher than that at 800℃. Zhang et al. (2007) found that the weight increase of the Ti-6Al-4V sample oxidised at 800℃ for 60 minutes was 0.661mg.cm^{-2} where as the sample oxidised at 850℃ for 20 minutes was 0.7642mg.cm^{-2}. Dong and Li (2000) established that oxidation treatments which were done at 850℃ for less than 40 minutes resulted in a reasonably compact and adherent oxide layer. However, a longer soaking time at this temperature or a higher temperature resulted in a flaky oxide layer. A linear relationship between treatment time and weight gain was found at this temperature where eventually Dong and Li (2000) determined the optimum thermal oxidation treatment for Ti-6Al-4V occurred at 850℃ for 30 minutes (Zhang et al. 2007). The cross section of a Ti-6Al-4V specimen with a 4µm thick oxide layer (which formed during an oxidation treatment done at 850℃ for 20 minutes long) can be observed in **Figure 4** (Zhang et al. 2008).

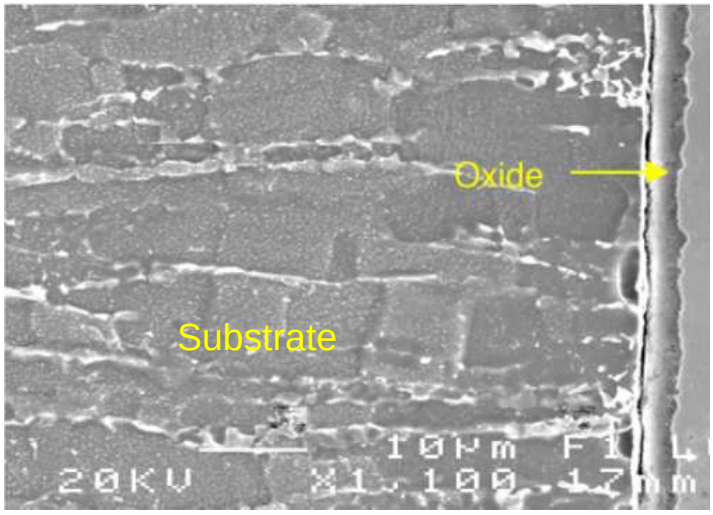

Figure 4: Cross section microstructure of the Ti-6Al-4V specimen after oxidation at 850℃ for 20 minutes (Zhang et al. 2006).

3.2.1.1 Oxide layer formation

Oxide formation occurs through the diffusing of oxygen atoms into the metal. The movement of Ti atoms are limited due to microstructure defects, causing the oxide layer to grow inwards (Luo et al. 2004).

Burnell-Gray et al. (1994) found that during thermal oxidation at temperatures in the range of 650 – 850℃ the oxides TiO_2 and Al_2O_3 grew in alternate layers about the metal substrate. The amount of these alternating layers increased with temperature and exposure time. Initial formation of TiO_2 occurs due to the significantly higher titanium activity compared to the aluminium activity. Ti and Al atoms diffuse outwards from the substrate where as O atoms diffuse into the substrate through the oxides. The inward diffusion of oxygen at the oxide/substrate combines with the outwards diffusion of titanium to form TiO_2. The drop in partial pressure of oxygen at the oxide/gas interface favours the formation of TiO_2. However, experimentally Al_2O_3 nucleates, and grows laterally to form the Al_2O_3 layer resulting in the Ti atoms now being "trapped" in this region allowing for the Al_2O_3 layer to be more kinetically favoured to form at the oxide/gas interface. This process allows for the formation and growth of the TiO_2 and Al_2O_3 layers.

Differences in expansion coefficients between the oxide and substrate initiate cracking which limits the diffusion of Ti and Al dramatically. However, O is still allowed to diffuse into the cracked regions increasing the partial pressure of oxygen in this region. Once again the formation of TiO_2 is favoured at the substrate side of the oxide/substrate interface resulting in the formation of a TiO_2 layer. Once the TiO_2 layer is formed Al diffuses to the gas/oxide surface of this newly formed TiO_2 and the

process occurs once again resulting in the alternating layers of TiO_2 and Al_2O_3 being formed. The frequency at which these layers occur is dependent on the exposure time at oxidising temperatures (Burnell-Gray et al. 1994).

3.2.2 Step (ii): Oxygen Boost Diffusion

In step (ii) of the OBDH process it is necessary to vary the diffusion treatment to obtain the desired strength and hardness profile. Dong and Li (2000) found that the optimum boost diffusion step was done at 850℃. The y claimed that temperatures below this required longer treatment times whereas temperatures above this resulted in the oxide layer having poor adhesion to the metal. The optimum treatment time for complete dissociation of the oxide layer was found to be 20 hours (Dong & Li (2000), Zhang et al. (2007)). Zhang et al. (2007) established that a high vacuum of 1×10^{-6} Torr is required for the dissociation of oxygen out of the oxide layer and for the boost diffusion to occur at the interface.

A variation of the boost time from 1 - 40 hours was carried out by Zhang et al. (2007) where during the first several hours it was seen that an intermediate oxide layer at the interface of the oxide layer and the substrate appeared. This suggests that contacts between the oxide and the substrate occurred and oxygen diffusion has taken place through dissociation. After the first 5 hours of boost diffusion the rutile oxide amount was greatly reduced and the formation of sub-oxides appeared which may be TiO, Ti_2O_3 or Ti_3O_4. As the diffusion time increased, the amount of oxide layer on the surface decrease and after 7 hours, consumption of almost the entire oxide layer had taken place (Zhang et al. 2007). **Figure 4** presents the cross section of a Ti-6Al-4V specimen which was oxidised at 850℃ for 20 minutes whereas **Figure 5** displays the cross section of the same Ti-6Al-4V specimen after boost diffusion treatment for 20 hours in vacuum.

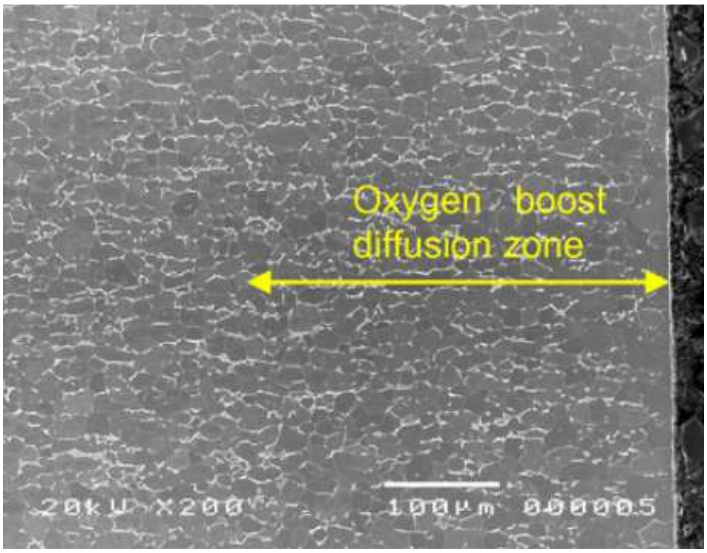

Figure 5: Cross section microstructure of the Ti-6Al-4V specimen after oxidation and then boost diffusion treated for 20 hours in vacuum (Zhang et al. 2006).

3.2.2.1 Oxygen Dissociation

The dissociation process occurs where initially a high oxygen potential exists in the TiO_2 layer at the substrate/oxide interface. As long as this layer is present, it acts as an oxygen reservoir. Initially oxygen dissociates out of the oxide layer across the interface and diffuses into the metal, a process which actively decreases the thickness of the oxide layer until complete dissociation eventually occurs. The extent to which oxygen diffusion occurs, and thus boost diffusion hardening of the substrate, is dependent on the surface adherence of the oxide layer which is why step (i) is absolutely crucial.

The depth the oxygen diffuses from the surface can be detected by energy-dispersive X-ray spectroscopy (EDX) demonstrated in **Figure 6**. This figure depicts how oxygen continually diffuses into the substrate at longer diffusion times **Figure 7** displays the oxide layer thickness during the diffusion process. From the graph it can be clearly observed that once the oxide layer has been fully dissociated, the oxide thickness decreases. Thus the oxygen has been boosted into the substrate forming a hard case in the surface area of the sample (Zhang et al. 2007, Dong and Li 2000).

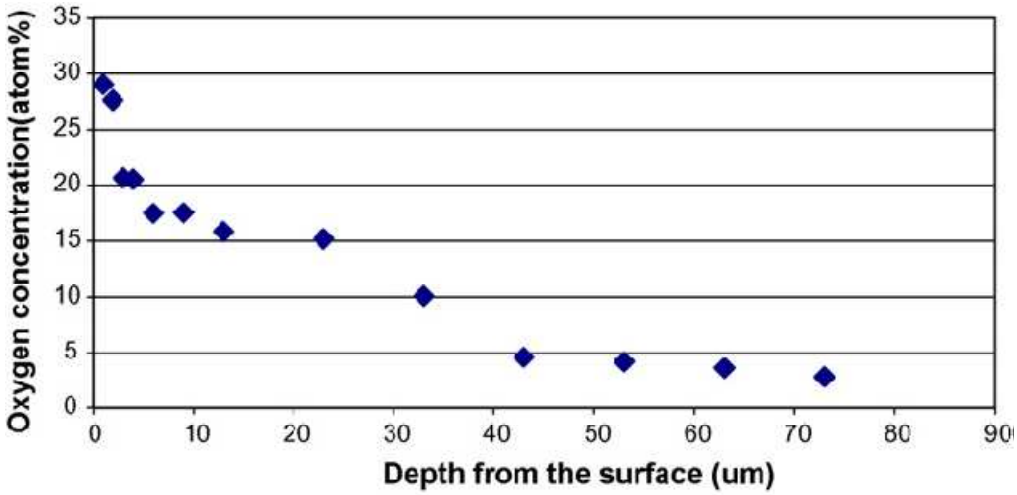

Figure 6: Distribution of Oxygen along the depth from the surface for sample oxidised at 850℃ for 20 minutes and boost diffused for 7 ho urs (Zhang et al. 2007).

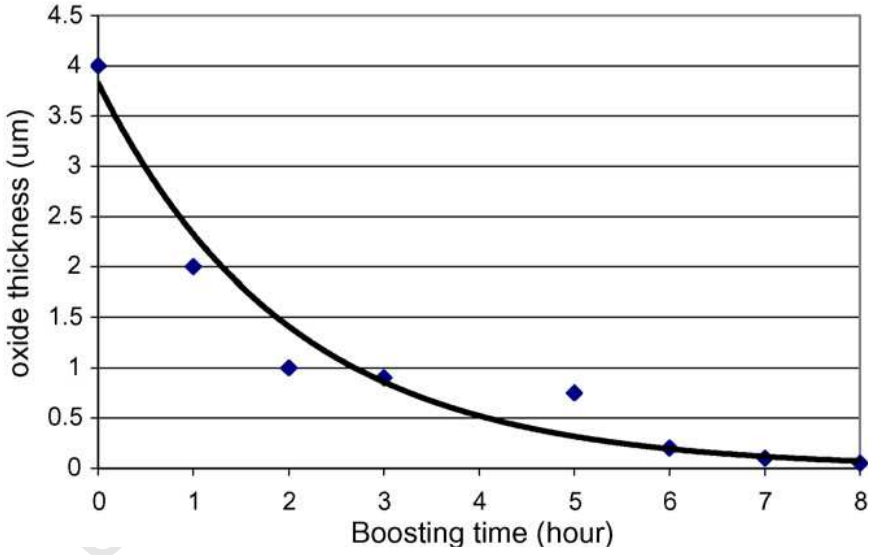

Figure 7: Change in oxide thickness during the boost process at 850℃ (Zhang et al. 2007).

3.2.3 Diffusion Phase Morphology

The area near the surface is the oxygen strengthened α region (Region I in **Figure 8**). This is the region from the surface to a depth varied with diffusion time and temperature where no, or only small amounts of β-phase can be identified. The α-phase is followed by the oxygen strengthened α and β transition phase (region II) which extends several 10 microns deep with a higher amount of the β-phase present.

The phase found after region II is a diffused oxygen affected area with stable α and β phases up to hundreds of microns deep(region III). The area of the substrate which is least affected by the oxygen (region IV) could be affected by the high temperature treatment (Zhang et al. 2007).

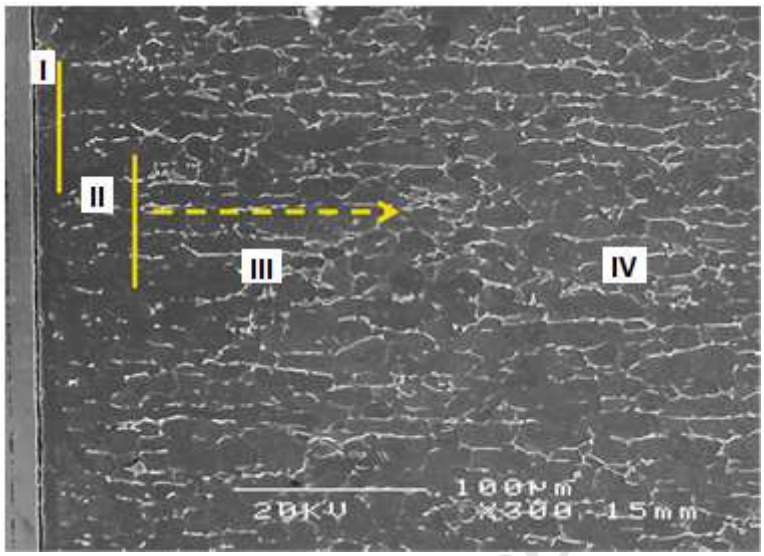

Figure 8: Cross section microstructure of oxidised sample at 850℃ for 20 minutes and boost diffused at 850℃ for 20 hours (Zhang et al. 2007).

4 LITERATURE REVIEW: CORROSION RESISTANCE

Metallic materials react naturally with its environment seeking its energetically preferable state, where for all non-precious metals this state is the metals combined oxide state (Joubert 1988). This oxidation reaction can be defined as corrosion.

Energy is required to refine metals from its natural mineral oxide state. The same amount of energy is emitted during the chemical reaction that produces corrosion returning the metal to this combined oxide state; thus corrosion has been called extractive metallurgy in reverse (Jones 1996).

These corrosion processes can be explained in terms of electrochemical reactions. Therefore, electrochemical techniques using current-potential relations (under controlled conditions) can be used to study corrosion phenomena and yield information on corrosion rates, pitting susceptibility, passivity, cathodic behaviour and other important data (Enos & Scribner 1997, Princeton Applied Research 1982).

4.1 Electrochemical Nature of Aqueous Corrosion

Virtually all metallic corrosion processes involves the transfer of electrons in aqueous solutions. These processes are known as electrochemical reactions.

During electrochemical processes, an anode and a cathode must be present with an ionic and electrical conduction path between them. The ionic conduction path is provided by the solution (the electrolyte) which separates the counter electrode and working electrode. The electrical conduction path can be provided by an external source called a potentiostat. During a potentiodynamic test, the potentiostat controls the driving force for electrochemical reactions to take place on the working electrode. The magnitude of this driving force dictates the process taking place at the anode and the cathode; and the rate of reaction.

Oxidation reactions take place at the anode and can be represented in the following way:

$$M \Leftrightarrow M^{x+} + xe^{-} \qquad [1]$$

M represents the pure metal or alloy and M^{x+} the ion of the metal. The number of electrons transferred in the process is represented by xe^{-}.

Reduction reactions take place at the cathode shown in the following reaction:

$$Z^{x+} + xe^{-} \Leftrightarrow Z \quad [2]$$

Where Z represents a species in solution.

Immersing a metal specimen into a corrosive medium initiates both reduction and oxidation processes on the metals surface; the metal typically oxidizes or corrodes and the solvent is reduced. The metal acts as both a cathode and anode resulting in anodic as well as cathodic currents occurring at the surface; however, corrosion processes occurring are usually a result of anodic currents (Enos & Scribner 1997).

4.2 The Potentiodynamic Polarization Scan

Polarizing the metal by means of a direct current (DC) power supply pushes electrons in a steady direction, changing the potential of the working electrode while monitoring the resulting current. The potentiodynamic polarization test is a polarization technique in which the electrode's potential is varied over a relatively large potential range at a specified rate by the application of a current through the electrolyte (Roberge 2008).

Once the metal specimen (the working electrode) is immersed in the corrosive medium the metal assumes a potential, relative to a reference electrode, known as the corrosion potential (E_{corr}) or open circuit potential (OCP). At this particular potential both anodic and cathodic currents occur at the surface in equal magnitudes, thereby producing no net current. The metal is said to be in equilibrium with the environment.

Once the metal is polarized in the positive or noble direction from E_{corr}, the potential moves from equilibrium and the anodic current predominates at the expense of the cathodic current. This results in anodic polarization where the corrosion rate generally increases. In the case of negative polarization i.e. in the active direction below E_{corr}, the cathodic current dominates resulting in cathodic polarization (Enos & Scribner 1997). The current density values indicate the state of corrosion i.e. the dissolution of metallic ions from the material into the electrolyte (Tamilselev et al. 2007).

Measurements of these polarization characteristics are done experimentally by plotting the current response as a function of applied potential. This curve is known as a potentiodynamic polarization plot. **Figure 9** depicts a theoretical plot of a

polarization scan classified by regions A - E between point 1 and 2 (Enos & Scribner 1997).

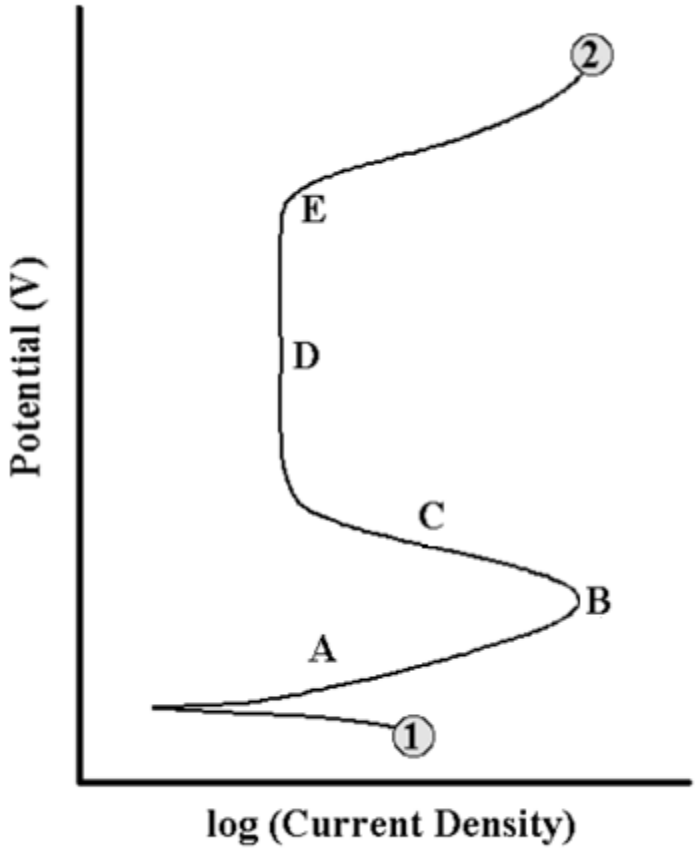

Figure 9: Theoretical anodic polarization scan (Enos & Scribner 1997).

Figure 9 consists of regions A – E which can be described in the following way:

Region A: Known as the active region where the specimen corrodes as the potential increases in the positive (noble) direction.

Region B: In this region it is clearly visible that the rate of corrosion, which is measure by the current, starts to decrease significantly and the onset of passivation occurs. This is due to the formation of an oxide film on the surface of the metal, explained in more detail in later sections. This point can be characterized as the primary passivation potential, E_{pp}, and the critical current density, I_c.

Region C: The rapid decrease of current, as the oxide film on the metal surface passivates, occurs at C

Region D: As the potential increases the current is constant and corrosion occurs at a very slow rate in this region. This is known as the passive region.

Region E: Region E sees the breakdown of the passivating film and is known as the transpassive region.

4.3 Corrosion Rates

4.3.1 Polarization Resistance

Absolute corrosion rates can be determined using the electrochemical technique of polarization resistance and is usually expressed in milli-inches per year (mpy). Polarization resistance or linear polarization shows an excellent correlation to rates obtained by conventional weight loss determination.

This technique is performed by scanning through a potential range close to E_{corr} at a range of generally ± 25mV about E_{corr}. Potential is plotted against the resulting current where the slope of the graph is known as the Polarization Resistance (Figure 10).

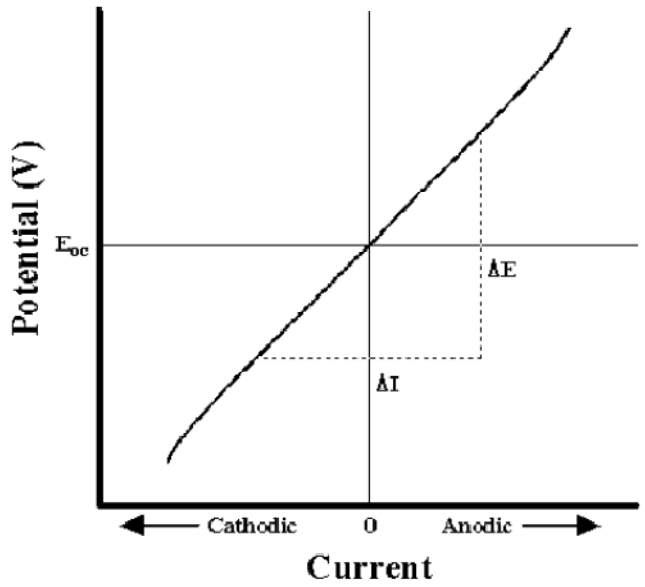

Figure 10: Linear Polrization Resistance (Enos & Scribner 1997).

The corrosion current, I_{corr}, is related to the polarization resistance or slope of the graph through the following equation:

$$R_p = \frac{\Delta E}{\Delta i} = \frac{\beta_a \beta_c}{2.3(i_{corr})(\beta_a \beta_c)} \quad [3]$$

Where:

$\frac{\Delta E}{\Delta I}$	=	polarization resistance
β_a, β_c	=	anodic and cathodic Tafel constants, obtained from Tafel plot analysis
i_{corr}	=	corrosion current

Rearranging equation 1 we obtain:

$$i_{corr} = \frac{\beta_a \beta_c \quad \Delta i}{2.3(\beta_a + \beta_c)\Delta E} \quad [4]$$

Solving for i_{corr} allows for the direct relation to the corrosion rate through the following equation:

$$Corrosion\ Rate\ (mpy) = \frac{0.13 i_{corr}(EW)}{d} \quad [5]$$

Where:

E.W	=	equivalent weight of corroding species (g)
d	=	density of corroding species ($g.cm^{-3}$)

4.3.2 Tafel Plots

Long term corrosion studies such as weight loss determination take days or weeks to compute, which is why electrochemical techniques such as potentiodynamic tests and Tafel plots (which require at most several hours to complete) are used with ever increasing popularity among corrosion engineers.

Similar to linear polarization, Tafel plots are carried out close to E_{corr} at about 300mV on either side of E_{corr} i.e. anodically and cathodically in a step wise manner. The resulting current is plotted on a logarithmic scale demonstrated by **Figure 11.**

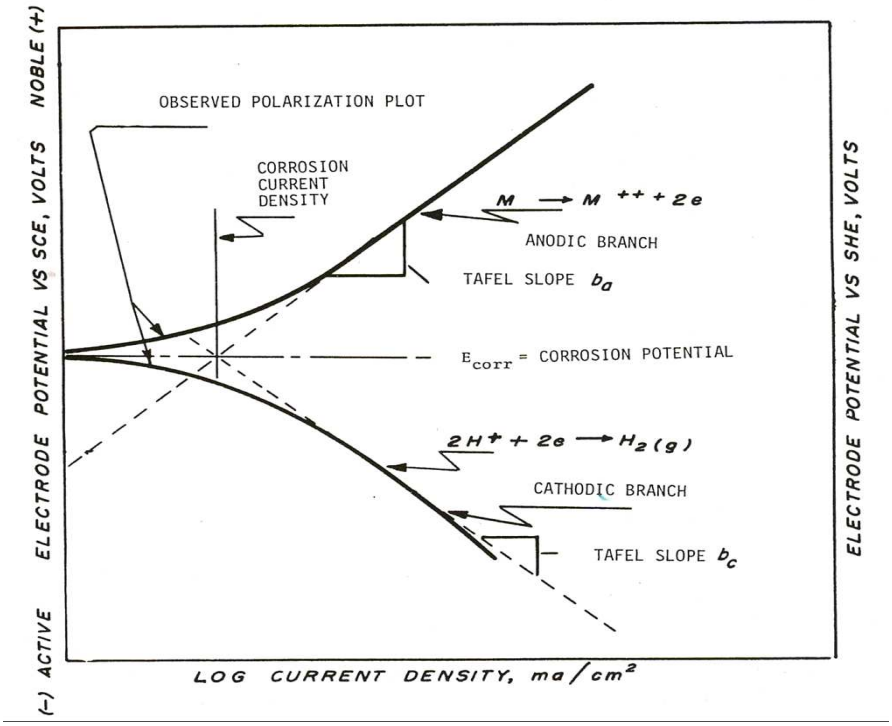

Figure 11: Tafel Slope Calculation (ASTM G3 – 89. 1989).

Using this plot the corrosion current i_{corr} is obtained by extrapolating the linear portion of the curve to E_{corr} as observed in **Figure 11**. The corrosion rate can once again be calculated by Equation 5.

Anodic or cathodic Tafel plots are described by the following equation known as the Tafel equation

$$\eta = \beta log \frac{I}{i_{corr}} \quad [6]$$

Where:

η	=	overvoltage which is the difference between the specimen potential and the corrosion potential
β	=	Tafel constant
I	=	current at overvoltage in

B_a *and* B_c Tafel constants must be calculated for both anodic and cathodic parts of the Tafel plot as illustrated in **Figure 11** (ASTM G3 – 89. 1989).

However, in practice it is not always simple to find a linear region in the Tafel plot, which results in inaccurate determination of β_a and β_c. Limitations in steady state techniques such as Tafel plots have been established by many authors who observe the following occurrences which give rise to errors in the measurement of corrosion intensity:

i) Variation of Tafel slopes with time
ii) Non linear polarization curve in the region of the corrosion potential
iii) High resistivity due to the electrolyte itself or corrosion product layers
iv) Pitting or localized corrosion
v) Variation of corrosion potential during test
vi) Equilibrium potentials of cathodic and anodic reactions are to close to the corrosion potential
vii) Diffusion controlled corrosion reaction, or the metal is passivated
viii) Perturbations in the working electrode/electrolyte interface during measurement
ix) Steady state not reached prior to measurement

These limitations can often be overcome by the use of non steady-state techniques such as Impedance Spectroscopy (Gabrielli 1997).

4.4 Corrosion Resistance of Ti-6Al-4V

Titanium is well known for its superior corrosion resistance properties. However, when subjected to aggressive environments such high temperature reducing acids, titanium and its alloys can exhibit poor corrosion resistance which restricts its use in certain offshore and chemical applications.

Under normal environmental conditions titanium exhibits excellent corrosion resistance due to the natural formation of a very stable, continuous, highly adherent and protective oxide film on the surface (Milosev et al. 2000, Venugopalan et al. 2000, Frauchiger et al. 1997). Research has shown that any surface treatment which will initiate a thicker and tougher protective oxide film on the surface will improve the corrosion resistance of titanium; processes such as anodising or thermal oxidation (Bloyce 1998). Comparative investigations have shown that thermal oxidation offers better protective performance than anodised and pickled conditions.

Thermal oxidation when compared to anodised films produces a thick, highly crystalline rutile oxide film whereas anodising forms anatase and hydrated oxides of low crystallinity on the surface. Rutile is inert and resistant to attack by hot reducing agents whereas anatase is readily attacked and dissolved in the harsh acidic

environment. The thermal oxide film forms when titanium is heated in air to temperatures ranging from 450 - 900℃ for times ran ging above 2 – 10 minutes. The resulting rutile TiO_2 film measurably improves the corrosion resistance to dilute acids, cathodic charging and the hydrogen absorption under gaseous hydrogen conditions. However, these thermally oxide films provide effective corrosion protection to titanium surfaces only if the integrity of the film can be maintained. This proves to be difficult due to the easily damaged oxide film, by mechanical impact, surface wear and plastic deformation.

Therefore, a thin oxide film with low wear resistance will provide little corrosion resistance where mechanical damage is likely. It is important to improve the chemical and mechanical performance of protective oxide films where corrosion is a design concern. Other methods of generating an oxide film include plasma nitriding and palladium-treated thermal oxidation (Bloyce 1998, Tait 1994).

4.4.1 Characterization of Ti-6Al-4V oxide layer

Understanding surface properties such as the formation of a stable passive oxide layer is critical to designing and engineering of medical devices and new biomaterials. Combining electrochemical methods with surface analytical techniques provides information on the composition, thickness and structure of the surface oxide layer (Milosev et al. 2000).

Several authors have proven that upon air exposure Ti-6Al-4V spontaneously formed a passive oxide layer on the surface of the metal (Pham et al. 1997, Wieland et al. 1997, Hernardez de Gatica et al. 1993, Sodhi et al. 1991,). The oxide layer has a thickness which varies between 2nm (Ask et al. 1988) and 7nm (Pham et al. 1997) and is composed of predominantly TiO_2.

Through the use of X-ray photoelectron spectroscopy (XPS), the influence of many treatments on Ti-6Al-4V have been studied (Pham et al.. 1997, Schmiedgen et al. 1997, Wieland et al. 1997, Hernardez de Gatica et. al 1993) with all reports again confirming that the oxide layer formed on the surface of the metal was predominantly TiO_2, with small amounts of suboxides TiO and Ti_2O_3 closer to the metal/oxide interface. Al and V was also reported by Sodhi et al. (1991) to be present throughout the oxide layer, where it was observed that V in the passivated layer was reduced (1 wt%), while Al was greatly enhanced (26 wt%). Others, Ask et al. (1988), reported only the presence of Al and not V in the outer most surface. Sundararajan et al. (1998) also observed oxidized Al but no oxidized V in the oxide layer whereas Okazaki et al. (1998) found small amounts of oxidized V in this layer. It is therefore evident that the presence of V in the oxide layer was relatively ambiguous. Maeusli et

al. (1986) also added to the ambiguity by not observing the presence of V in the outer most surface by means of XPS or Auger electron spectroscopy (AES); however, V was detected by secondary ion mass spectroscopy (SIMS). Therefore, due to the detection limits of XPS and AES and low concentration, V was not observed in the oxide layer in previous reports but it was confirmed to be present with low concentration detection techniques such as SIMS.

The oxidation states present (in the oxide layer) for Al was established to be Al_2O_3 and between V_2O_3 and V_2O_5 for V (Sodhi et al. 1991, Ask et al. 1988). However, these elements (Al and V) could also be present as ions at substitutional or interstitial sites in the TiO_2 matrix (Ask et al. 1988).

It was apparent that the use of XPS revealed information about the oxide layer present on the Ti-6Al-4V alloy, but besides XPS, Electrochemical Impedance Spectroscopy (EIS) was used to characterize the passive oxide layer by its electronic properties and correlate these properties to the chemical composition of said layer (Dolata et al. 1996, Pan et al. 1996, Da Fonseca et al. 1994, Tomkiewicz 1979).

4.4.2 Corrosion resistance of Thermally Oxidised Ti-6Al-4V

In a study carried out to determine the corrosion resistance of thermally oxidised samples, Ti-6Al-4V specimens were subjected to temperatures of 600℃ and 650℃ for times ranging from 12 – 60 hours. It was found that a protective layer of rutile and/or anatase oxide was formed with an oxygen diffusion zone beneath it (Bloyce 1998).

It is known that as the oxidation time increases so does the thickness of the oxide layer as well as the oxygen diffusion zone. However, when the oxidation temperature increased from 600℃ to 650℃ there was a significa nt increase in the oxide layer formation rate, thus a thicker oxide layer formed in the same time constraint. Also as the temperature increased so did the roughness of the oxide layer. Therefore, increasing temperature can produce a thicker oxide layer which is a well known fact, but this increase in temperature may put the whole oxide layer in a more stressed condition as a result of intrinsic and thermal effects. The formation of a defected oxide layer provides an easy diffusion path for metal ions and oxygen allowing further oxidation to progress in an uncontrollable way. Since the corrosion resistance of the oxide layer depends on its chemical stability and defect free structure, these defects (microcracks and pores) may be responsible for the failure of oxidised surfaces. Once immersed in a corrosive environment, aggressive ions penetrate towards the oxide-metal interface causing oxide layers to gradually flake off from the substrate as fragments due to corrosion at the substrate-oxide interface. From this observation it

proves that the presence of these defects due to high oxidation temperatures provides a path for the corrosive solution to reach the interface.

Samples which were oxidised at 600℃ for shorter times i.e.12 hours showed a different behaviour to that of the other samples. These samples formed a relatively thin oxide layer consisting of both rutile and anatase. Anatase, as stated, is readily attacked and dissolved in reducing agents whereas rutile is inert and resistant to the aggressive environment. Dissolution of the anatase left areas of the substrate unprotected causing accelerated corrosion to occur on the unprotected surfaces. Increasing the oxidation time resulted in higher amounts of rutile in the oxidised layer which increased the protective nature of the layer. The formation of less defective oxide structures containing more rutile also formed at longer oxidation times for an oxidation temperature of 600℃ (Bloyce 1998).

4.5 Electrochemical Polarization of Ti-6Al-4V

Luiz de Assis et al. (2006) carried out potentiodynamic polarization scans on Ti-6Al-4V as well as two other Ti alloys in Hank's solution from -0.8V to 3.0V versus the saturated calomel electrode (SCE), at a scan rate of 1mv/s and observed the behaviour of all three alloys **Figure 12**. The curves were observed to be S-shaped where initially the current density decreased rapidly from potentials of $-0.6V_{SCE}$ corresponding to the onset of an oxide film formation on the alloy (Blackwood & Chooi 2002, Sul et al. 2002, Milosev et al. 2000, Yeroklin et al. 2000, Robin et al. 1999)

Partial stabilization of current density indicates, at this range of potentials below E_{corr}, the formation of a protective film in agreement with low i_{corr} values. However, at potentials greater than E_{corr} a sharp increase in the current density suggested that the initial film was replaced by a less protective passive film.

The increase of current density with increasing potential was suggested to occur due to these potential increases not being accompanied by corresponding thickening of the oxide film. Or, it could be due to oxidation processes involving the oxidation of TiO or Ti_2O_3 to TiO_2 which is discussed in more detail in the next section. The film was initially less protective but stabilized approximately above $100mV_{SCE}$. The newly stabilized oxide film is different to the film formed initially at lower potentials (Luiz de Assis et al. 2006). This behaviour of passivity in this region of practically constant current indicates the oxide film growth and the thickness of the anodic oxide film increases linearly with applied potential. This region is known as the passive region (Schmidt & Azambuja 2006).

The current density for Ti-6Al-4V once again increased at approximately 2.0V_{SCE} and then stabilized once again at a current density of 10^{-5}A.cm^{-2}(Luiz de Assis et al. 2006)

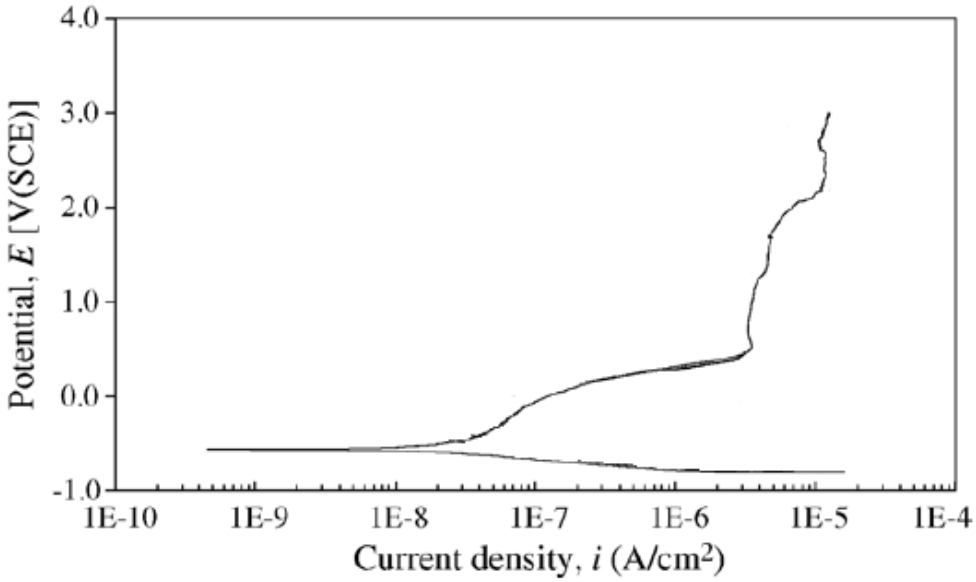

Figure 12: Potentiodynamic polarization curve for Ti-6Al-4V in Hank's solution (Luiz de Assis et al. 2006).

Another interesting finding, reported by several authors (Ramires & Guastaldi 2002, Raetzer-Sheibe 1978, Beck 1973) was the effect of the presence of halides in solution. Raetzer-Sheibe (1978) established that there is a tendency for chemisorptions of halide ions on the oxide/electrolyte interface which may explain the changes in the repassivation behavior of Ti-6Al-4V in a halide containing solution such as NaF, where fluoride ions are strongly adsorbed on the TiO_2 surface. Bech (1973) studied the pitting potential for titanium in Cl^-, I^- and Br^- solutions and according to his observations he found that in a neutral chloride solution, Ti^{3+} was the dominant dissolved species close to an corroding pit exposed to a chloride solution. Whereas Ramires and Guastaldi (2002) demonstrated that pitting did not occur neither did film breakdown after polarization up to 3.0V_{SCE} in 0.15mol/l NaCl solution.

4.5.1 Composition of oxide layer at varying potentials

Milosev et al. (2000) studied the composition of the oxide layer when polarized to various potentials in physiological solution using XPS. It was reported that after oxidation at lower potentials (0V_{SCE}), four different contributions to the passive

surface layer were present which were Ti, TiO, Ti_2O_3 and TiO_2. As the oxidation potential had increased to values greater than $0.5V_{SCE}$, the intensity of the metallic Ti and suboxide species i.e. TiO and Ti_2O_3, decreased whereas that of TiO_2 increased. The intensity of TiO, however, started to disappear at potentials greater than $0.25V_{SCE}$ compared to Ti_2O_3 which remained over the potential range, but was greatly reduced as the potentials increased above $0.5V_{SCE}$.

Milosev et al. (2000) reported that electrochemical polarisation caused the oxidation of Al as well, where at low potentials aluminium was found predominantly in the oxidized state i.e. Al_2O_3. As the potential increased above $1.25V_{SCE}$ metallic Al disappeared. As established earlier, the detection of vanadium was not possible by XPS. Milosev et al. (2000) concluded that the composition of the surface oxide layer as a function of oxidation potential is presented as atomic fractions of Ti, Al and O, containing predominantly TiO_2, and deduced that theoretically the oxide should contain 33 at% Ti and 67 at% O. However, the reported findings, depending on the oxidation potential, showed Ti to be present in the range of 21.5 - 23.6 at% which was lower than expected and was attributed to the incorporation of 4.0 – 8.4 at% of Al_2O_3 into the passive oxide layer.

5 LITERATURE REVIEW: DIFFERENCES IN DC AND AC CURRENT

5.1 Faradaic Current and Corrosion

Electrons which form an electric current come from ionizing atoms producing a type of current termed a Faradaic current. Certain factors resist the flow of this faradaic current and so slowing down the corrosion process.

When a metal specimen (termed the working electrode) is immersed in a corrosive environment, the metal atoms at the surface ionize forming ions which must detach themselves and move into solution. The restriction effect of these processes on the current is known as the Faradaic Resistance, R_f. The R_f occurs at the interface of the electrolyte and working electrode. Ions which are bulky and not able to flow through metal (i.e. electrons) move through the electrolyte. The equivalent resistance to this movement is known as the Electrolyte Resistance (R_e) also commonly known as the Solution Resistance (R_s) (Kauffman 1997).

5.2 The Electric Double Layer

If the surface of the metal, once immersed in a corrosive environment, is studied we observe that the metal becomes negatively charged on the inside and covered with a positive Adsorbed Fixed Layer on the outside.

Positive and negative ions exist in solution and the positive Adsorbed Fixed layer attracts negative ions which form a layer around the fixed layer called the Diffuse Mobile Layer, which is loosely held together by electrostatic attractions. Ions enter and leave this layer and the net charge is negatively balanced by the positive fixed layer. The absorbed fixed layer and the diffuse mobile layer together are known as the Electric Double Layer. This double layer acts like a capacitor between the adsorbed fixed layer and the diffuse mobile layer, charging and discharging like an electrolytic capacitor would. The capacitor can be described as a piece of nonconducting plastic (known as a dielectric) between two metallic conducting plates (Kauffman 1997).

5.3 Direct Current (DC) and the Electric Double Layer

In DC testing such as potentiodynamic testing, it was noted that the DC power supply pushes electrons in a steady direction. For a steady flow of current into the metal specimen (i.e. a steady withdrawal of electrons) the electrode becomes

positive and repels adsorbed ions causing more surface ions to ionize thus causing the electrode to corrode. The desorbed ions move through the diffuse mobile layer and eventually into solution causing faradaic current to flow. DC voltage produces a net current flow through the double layer from one 'plate' to the other. The double layer thus acts as a 'leaky' capacitor (Kauffman 1997).

5.4 Alternating Current (AC) and the Electric Double Layer

Compared to DC, an AC power supply pushes then pulls electrons in and out of the metal specimen at the supply frequency resulting in no net current flowing. The double layer capacitor charges and discharges causing the diffuse mobile layer to oscillate (i.e. attracted and repelled) at the AC frequency. Therefore, with AC the double layer behaves like a perfect capacitor because there is no net current flow and no 'leakage and there is no chemical reaction or corrosion occurring (Kauffman 1997). AC voltage is utilized in Electrochemical Impedance Spectroscopy (EIS) and this non destructive feature is one of many features which make EIS such an attractive means for corrosion studies.

6 LITERATURE REVIEW: ELECTROCHEMICAL IMPEDANCE SPECTROSCOPY (EIS)

Through EIS you can represent an electrochemical cell using electronic models, since it is well known that electrodes undergoing electrochemical reactions are typically analogous to an electronic circuit. By using established AC circuit theory, one can take advantage of this analogy and characterize the electrochemical cell in terms of its equivalent circuit. In essence, impedance data correlates to a particular circuit or circuits which consist of circuit elements that apply to physical or chemical properties of the electrode in question.

6.1 THEORY

Electrochemical Impedance Spectroscopy theory describes the response of a circuit to an alternating current or voltage as a function of frequency. In DC theory the concept of resistance is well-known as the ability of a circuit to resist the flow of current, and is defined by Ohms law in the following equation:

$$R = \frac{E}{I} \quad [7]$$

Where:

E	=	potential	(V)
I	=	current	(A)
R	=	resistance	(Ω)

But use of this well known relationship is limited to an ideal resistor. An ideal resistor has properties which:

i) follows Ohms law at all current and voltage levels.
ii) resistance value is independent of frequency.
iii) AC current and voltage signals through a resistor are in phase with each other (Gamry Instruments. 2007).

Many real world systems exhibit a much more complex behaviour than the simple one circuit element of resistance thus introducing a new concept of impedance.
In AC theory where, unlike DC theory, the frequency is now a non-zero value and the equation becomes:

$$Z = \frac{E_{ac}}{I_{ac}} \quad [8]$$

Impedance is defined by Z in Equation 8. Unlike resistance, Z is not limited by the simplified properties listed for ohms law and represents not only resistors, but capacitors and inductors as well which all have the ability to impede the flow of electrons in AC circuits. We can associate these circuit elements of an AC electric circuit to slow electrode kinetics, slow preceding chemical reactions and diffusion in an electrochemical cell, which all impede the flow of electrons (Loveday et al. 2004).

Impedance can be expressed as a complex number with resistance being the real component. The capacitance and inductance is the imaginary component given the name reactance for the combined two. The reactance component not only effects the magnitude of an alternating current but also its time dependant characteristics i.e. its phase. **Figure 13** shows the time relationship and its dependency on frequency through a sine wave voltage applied to an electrochemical cell with the corresponding current response (Princeton Applied Research 1985).

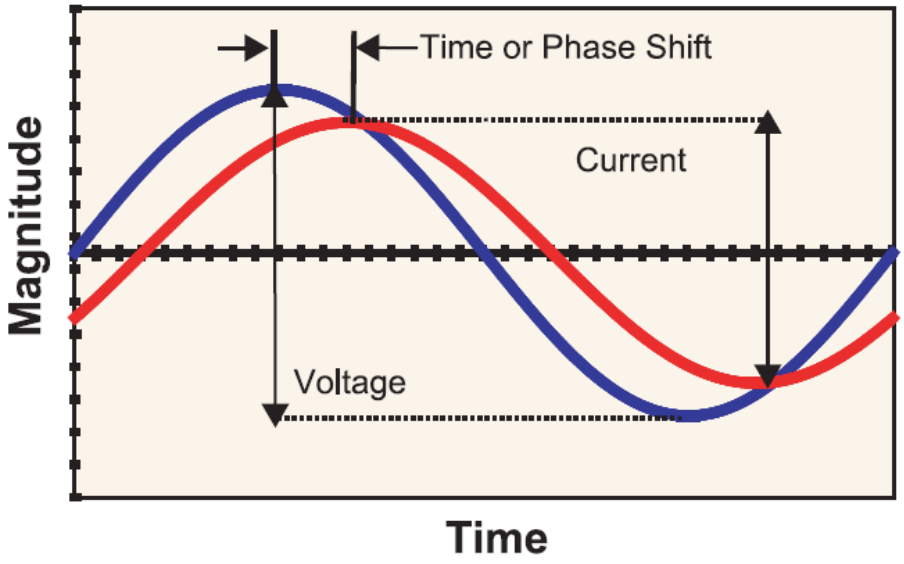

Figure 13: Voltage and Current as a function of time (Loveday et al. 2004).

The time shift due to the slow response of this system can be expressed as an angle called the phase angle (θ). However, in the case of a purely resistive network, the two waveforms would be in phase i.e. the waveforms would not be shifted. The magnitude of the impedance (in ohms) of the system can be expressed by ratio of the voltage sine wave (in volts) to the current sine wave (in amperes). The magnitude of the impedance, |Z|, the phase angle, θ, and the frequency in hertz are all required to characterize the impedance of a system (Loveday et al. 2004).

6.2 Vector Analysis

A convenient way of characterizing an AC waveform is through vector analysis, where the wave can be described in terms of amplitude and phase characteristics.

i) X & Y coordinates
ii) Angle (θ) and magnitude (Z)
iii) Real (I') and Imaginary (I'')

The current sine wave can be described by the following equation:

$$I(t) = A\sin(\omega t + 0) \quad [9]$$

Where:

I(t)	=	instantaneous current
t	=	time
A	=	maximum amplitude
ω	=	frequency in radians per seconds = 2πf (f = frequency in hertz)
θ	=	phase shift in radians

The resultant current waveform (**Figure 13**) can be presented by vector analysis shown in **Figure 14 – Figure 16**.

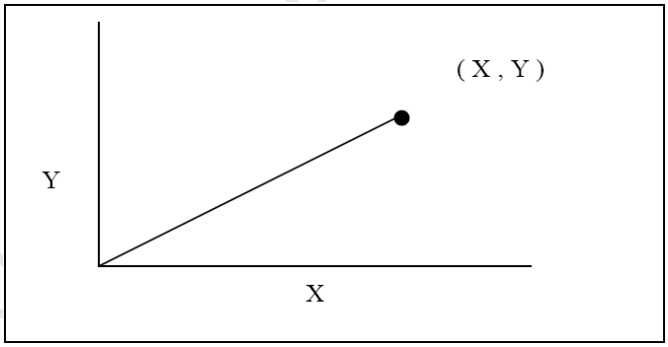

Figure 14 Vector in terms of X and Y Coordinates (Princeton Applied Research 1985).

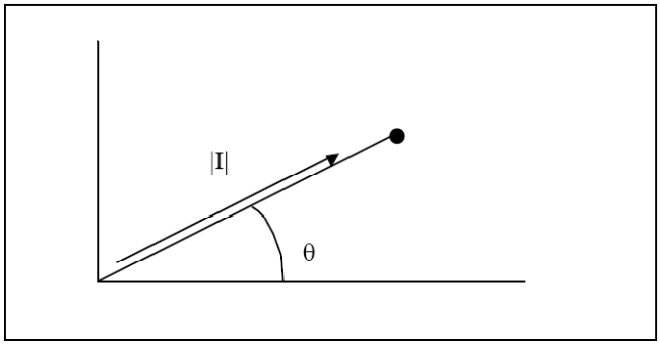

Figure 15: Vector in terms of angle θ and magnitude |Z| (Princeton Applied Research 1985).

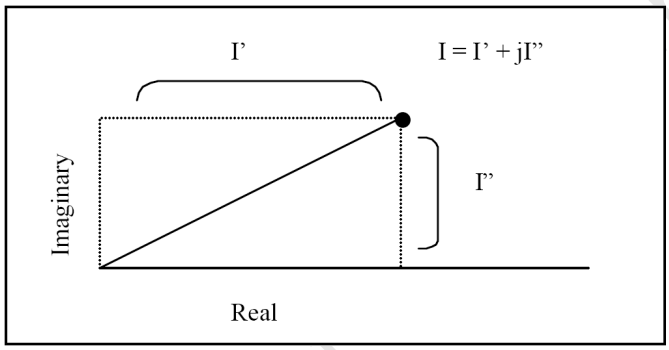

Figure 16: Vector in terms of Real (I') and Imaginary (I") Coordinates (Princeton Applied Research 1985).

Figure 14 – Figure 16 demonstrates that the current waveform vector can be described in a number of ways. **Figure 14** displays the end point of the vector described in terms of x-y coordinates from the in phase x component and the out of phase y component, whereas **Figure 15** defines the vector by phase angle (θ) and current magnitude |I|. The third approach and most convenient for numerical axis is presented in **Figure 16,** where the axes are defined as real and imaginary components. These components can be utilized as a single complex number notation in complicated equations. An AC current vector can then be defined as the sum of both the imaginary and real components in the following equation:

$$I_{total} = I' + I"j \qquad [10]$$

Where:

$j = \sqrt{-1}$

Figure 14, **Figure 15** and **Figure 16** are just three different ways to express the position of the point:

i) (x–y) pair
ii) Phase angle/Magnitude
iii) Real/Imaginary component

Using Equation 8, the impedance vector which is the quotient of the voltage and current vectors can be calculated in the following way:

Remember: $$Z = \frac{E_{total}}{I_{total}}$$

Where (for AC voltage): $$E_{total} = E' + E^{"}j \quad [11]$$

And (for AC current): $$I_{total} = I' + I^{"}j \quad [12]$$

Therefore (for Impedance): $$Z_{total} = \frac{E'+E\mathrm{j}}{\mathrm{I'+I}j} \quad [13]$$

Where the absolute magnitude of the impedance, which is the length of the vector in **Figure 14**, **Figure 15** and **Figure 16**, can be expressed as:

$$|Z| = \sqrt{(Z')^2 + (Z^{"})^2} \quad [14]$$

And the phase angle can be defined by:

$$\tan\theta = \frac{Z'}{Z^{"}} \quad [15]$$

(Princeton Applied Research 1985)

6.3 Equivalent Circuit Diagrams

As previously stated, resistors, capacitors and inductors can be represented as circuit elements which are used to form a circuit diagram which represents properties of a material. Each circuit element has an impedance expression presented in **Table 4**.The impedance of a resistor has no imaginary component at all and the phase shift is 0° meaning that the current is in phase with the voltage. Conversely the impedance of a capacitor has no real component and the current is always 90° out of phase with the voltage.

Circuit Element	Impedance Equation
RESISTOR 	$Z = R + 0j$ $j = \sqrt{-1}$
CAPACITANCE 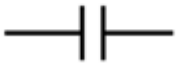	$Z = 0 - j/\omega C$ $\omega = 2\pi f$

Table 4: Impedance Equations describing their particular Circuit Elements (Princeton Applied Research 1985).

A simple corrosion system called a Randles cell can be represented by a parallel capacitor and resistor in series with a second resistor (**Figure 17**). The resistor in series (R_s) with the parallel resistor and capacitor is known as the solution or electrolyte resistance and refers to the resistance of the solution between the working and reference electrodes. The R_s value is typically a few ohms if the electrolyte's salt concentration is a few percent (Loveday et al. 2004).

The parallel resistance (R_p) is known as the polarization resistance or charge transfer resistance (Equation 3), which refers to the resistance at the working electrode/electrolyte interface. Polarization resistance determines the rate of the corrosion reaction. The means by which the corrosion rate is calculated from the polarization reaction will be dealt with in following sections. For a coated metal this value refers to the resistance of the coating, and is a property of the material and depends on the thickness and composition of the coating.

The capacitance (C_{DL}) is known as the double layer capacitance. The C_{DL} occurs at the interface of the electrode and the electrolyte and can provide information on the adsorption and desorption phenomena. In certain systems C_{DL} indicates the integrity of an organic coating rather than the double layer capacitance. For a coated metal the C_{DL} refers to the capacitance of the coating and can be characterized by the dielectric constant and thickness of the coating material (Loveday et al. 2004, Princeton Applied Research 1985).

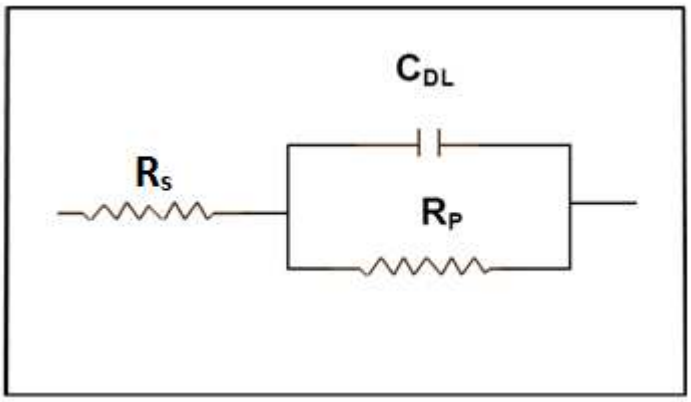

Figure 17: Equivalent Circuit for a Single Electrochemical Cell known as a Randles Cell (Princeton Applied Research 1985).

6.3.1 Circuit Behaviour

The impedance of resistors are constant and do not vary with frequency; however, the impedance of capacitors do, with an inversely proportional relationship to frequency. When the cell is exposed to low frequencies (DC), the C_{DL} does not conduct and the impedance of the capacitor is nearly infinite. The capacitor acts as an open circuit i.e. as if it were not there. The only resistance is provided by R_p and R_s which are in series, therefore the current is not divided and the resulting resistance looks like the combination of the two resistors. Thus the effective impedance of the two series resistors is the sum of the individual resistors. This combined resistance is displayed accordingly when plotted on impedance plots discussed in section 6.4 (Loveday et al. 2004).

The current reaches its maximum when the voltage is changing the fastest. The magnitude of the current is a frequency dependant value so the higher the frequency, the faster the voltage changes, and the higher the magnitude of the current. From Equation 8 the high currents at high frequencies lead to smaller impedances of the capacitor. Ultimately at zero frequency (DC voltage) the current is zero since there is a non conductor present in a capacitor, and the impedance is at its maximum. Therefore, at high frequencies the impedance of the capacitor becomes smaller and at some frequency the impedance reaches a value which is smaller than R_p. The current then flows preferably through the capacitor C_{DL} effectively shorting out R_p removing it from the circuit, leaving R_s as the only constant impedance. The Randle cell is now controlled almost entirely by R_s. C_{DL} can be said to act as a zero ohm impedance or a piece of wire at high frequencies.

At intermediate frequencies the capacitor plays a part in the circuit and contributes to the overall impedance. The overall impedance will be between the high frequency limit (R_s) and the low frequency limits (R_s and R_p). At either limits the phase is nearly zero whereas at intermediate frequencies the phase angle approaches -90° which is the phase angle for a capacitor. The imaginary component is now significant and the cells impedance becomes frequency dependant (Gamry Instruments 2007, Loveday et al. 2004, Princeton Applied Research 1985).

6.4 Impedance Plots and Interpretation

Upon completion of an EIS test at a specified frequency range, the raw data obtained is as follows:

i) The real component of voltage (E')
ii) The imaginary component of voltage (E")
iii) The real component of current (I')
iv) The imaginary component of current (I")

Using this data the total impedance (Z) and phase shift (θ) can be computed among other impedance functions.

Impedance plots are used to discover the true behaviour of a real chemical system by representing data in a clear and informative way to extract meaningful values which correspond to the modelled equivalent circuit. A variety of plots exist each with specific advantages revealing certain characteristics of a given chemical system (Princeton Applied Research 1985).

6.4.1 The Nquist Plot

The Nquist plot (**Figure 18**), also known as the Cole-Cole plot or complex plane plot, is a popular format for displaying impedance data, where the imaginary impedance component (Z" on the y-axis) is plotted versus the real component (Z' on the x-axis) at each excitation frequency.

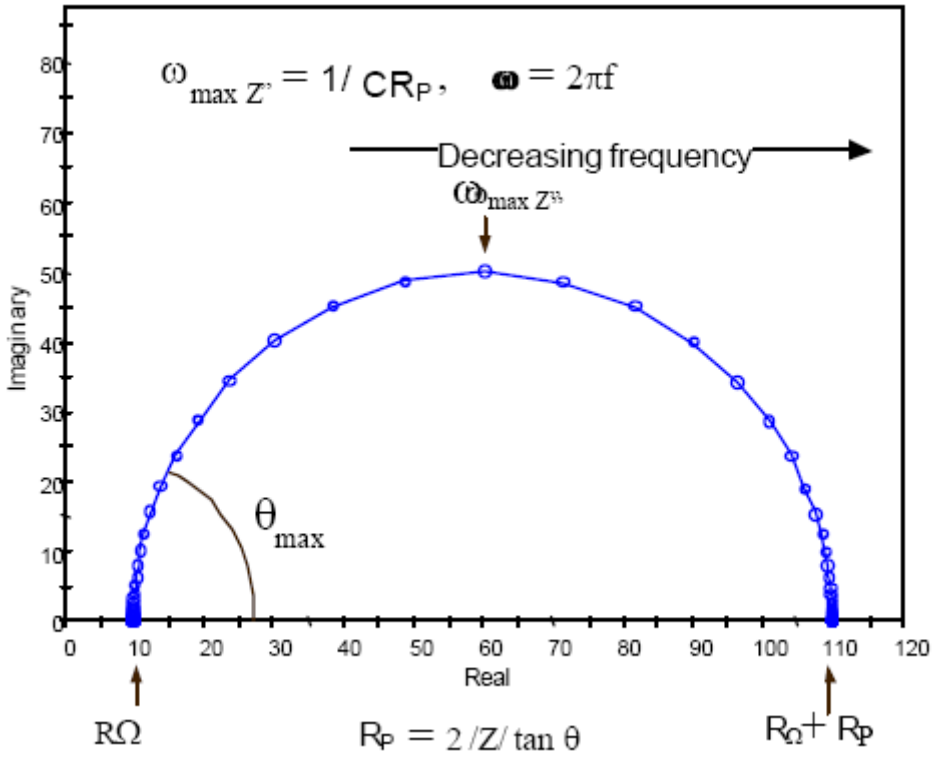

Figure 18: Nquist Plot for a Simple Electrochemical System (Princeton Applied Research 1985).

For a simple Randles cell, the high frequency response was almost entirely due to the solution resistance (R_s or R_Ω) which is observed at the high frequency end of the Nquist plot i.e. the leftmost end, where the semi-circle touches the x-axis. The cells low frequency response is due to R_Ω and R_p and is at the rightmost end of the plot where the semi-circle once again touches the x-axis.

Using the Nquist plot to represent impedance data can be advantageous as it is easy to read the solution resistance as well as the polarisation resistance off the plot where the semi-circle touches the x-axis. However, a major disadvantage in using this plot is that the frequency does not appear explicitly i.e. cannot be read directly off the axes, and the capacitance can only be calculated once the frequency information is known. The frequency at the apex of the semi-circle ($\omega_{(\theta max)}$) in **Figure 18** can be used to calculate the capacitance as long as the R_p is known (Gamry Instruments 2007, Loveday et al. 2004, Princeton Applied Research 1985).

6.4.2 The Bode Plot

The impedance data represented in the Nquist plot for a simple electrochemical system is shown in the corresponding Bode plot (**Figure 19**). This plot shows two curves: the actual impedance (calculated by Equation 14) and the phase shift (θ) of the impedance, each as a function of frequency. The major advantage of presenting data in the form of a Bode plot is that frequency appears as one of the axis making the effect of frequency on the impedance easily observed. The plot uses logarithm axes to plot wide ranges on both axes.

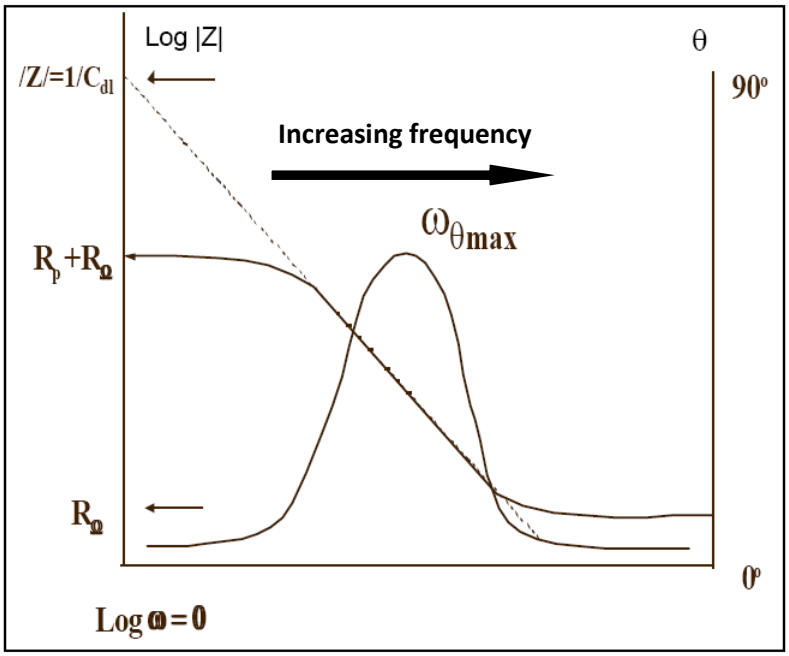

Figure 19: Bode Plot for a Simple Electrochemical System (Princeton Applied Research 1985).

The R_p and R_Ω values are shown on the Log |Z| axis, where at the highest frequency the solution resistance dominates the impedances (demonstrated in **Figure 19**) and the value can be read off the plot at the horizontal plateau. Log (R_p + R_Ω) can be read from the y-axis at the lowest frequency plateau. At intermediate frequencies, where the curve is a straight line with a gradient of -1, the capacitance of the double layer can be calculated by extrapolating the straight line to the log |Z| axis shown in **Figure 19**. The capacitance can be calculated using the following relationship:

$$|Z| = \frac{1}{C_{DL}} \qquad [16]$$

The Bode phase angle (θ) plot is included in the Bode plot where at high and low frequencies the phase angle is zero because the Randles cell is resistor like, but at

intermediate frequencies the phase angle increases as the reactance increases i.e. imaginary component of the impedance increases. At the phase plot maximum i.e. $\omega_{(\theta max)}$ where the phase shift of the response is at its maximum, the double layer capacitance can be calculated by the following equation:

$$\omega_{\theta max} = \sqrt{\left(\frac{1}{C_{DL}\, R_p}\right)\left(1 + \frac{R_p}{R_s}\right)} \qquad [17]$$

The Bode plot is advantageous over Nquist plots when data scatter prevents adequate fitting of Nquist semi-circles and also to avoid long measurement times associated with low frequency polarization resistance determinations. The Bode plot can also provides a means of better extrapolation of data from higher frequencies.

So in general the Bode plot illustrates a much clearer view of the electrochemical system frequency dependant behaviour than if the Nquist plot is used (Gamry Instruments 2007, Loveday et al. 2004, Princeton Applied Research 1985).

6.5 Electrochemical Impedance Evaluation of Ti-6Al-4V

Numerous studies (Songur et al. 2009, Souto et al. 2003, Luiz de Assis et al. 2006, Milosev et al. 2000, Gonzalez & Mirza-Rosca 1999, Kolman & Scully 1994) have reported that the behavior of Ti-6Al-4V alloys impedance plots conforms to the equivalent circuit as depicted in **Figure 20**.

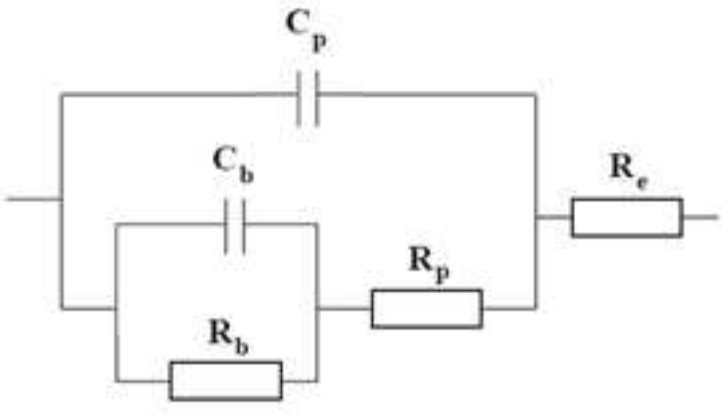

Figure 20: Equivalent circuit proposed for Ti-6Al-4V.

The circuit elements are defined as follows:

C_1/C_p: Polarization capacitance or capacitance of the porous layer

C_2/C_b: Double layer capacitance or barrier layer capacitance

$R_s/R_e/R_\Omega$: Solution resistance

R_1/R_p: Polarization resistance or porous layer resistance

R_2/R_b: Charge transfer resistance or barrier layer resistance

Throughout the following text the use of shorthand symbols will be used alternating between symbols such as R_1 and R_p. In some cases $R_{1(p)}$ is used which represents the same element; however, some authors prefer to define these elements differently. So the symbol for R_1 becomes $R_{1(x)}$ where 1 attaches the symbol to the first resistor in Figure 19, and 'x' within the brackets denotes the symbol defined by the author from which the text is referenced.

For a two time constant model (displayed for Ti-6Al-4V), the impedance spectra can be divided into two distinct frequency regions. The high frequency time constant is due to the uncompensated solution resistance and the impedance resulting from the penetration and movement of the electrolyte through a porous film. The low frequency response accounts for the processes taking place at the substrate/electrolyte interface. This behavior is characteristic to metallic materials covered by a porous oxide film in a corrosive environment (Souto et al. 2003).

Pan et al. (1996) observed that when exposed to corrosive environment such as phosphate buffered saline (PBS) solution, Ti-6Al-4V impedance spectra displays behavior characteristic of a thin oxide film on the surface, displaying near-capacitive response indicated by a phase angle close to -90° over a large frequency range. Pan et al. (1996) reported that this behavior remained constant even after long exposure times i.e. 30 days, indicative of a rather stable oxide film. The equivalent cell depicted in **Figure 20** was proposed for Ti-6Al-4V by Pan et al. (1996). Additionally Pan et al. (1996) found that because the outer porous layer was thin and the pores filled with solution, the contribution of this layer to the electrochemical properties is rather small and that the impedance response is mostly dominated by the inner barrier layer.

Wang et al. (2003) found that when Ti-6Al-4V is immersed into simulated body fluid (SBF) $R_{2(b)}$ is very high whereas $C_{2(b)}$ is relatively low decreasing slowly with long term immersion times (i.e. 8 weeks) reaching a steady state. The decrease was argued to be attributed to the slow growth of the titanium oxide film, indicating long term stability of the thin passive film in SBF. The initially low $R_{1(p)}$ increases with exposure time indicating that the pores may be filled only with electrolyte depicted in **Figure 21** (Wang et al. 2003).

Mansfeld 1993 argued that the circuit in **Figure 20** modeled a two time constant or two-layer model of an oxide film with an unsealed anodic oxide film (Thompson & Campbell 1994). For unsealed pores it is generally agreed (Mansfeld 1993) that the pores in the outer porous layer (represented by $R_{1(p)}$ and $C_{1(p)}$ in **Figure 21**) are filled with electrolyte and is a good fit for a two time constant model. However, if the oxide is sealed, the pores are filled with hydrated compounds which are caused by the presence of an additional corrosive species, such as the addition of H_2O_2 to PBS solution. In this case the hydrates need to be taken into account in the equivalent circuit for a better fit of the EIS spectra. The sealing of pores can be accommodated by an additional capacitor to the circuit (Baltat-Bazia et al. 1992).

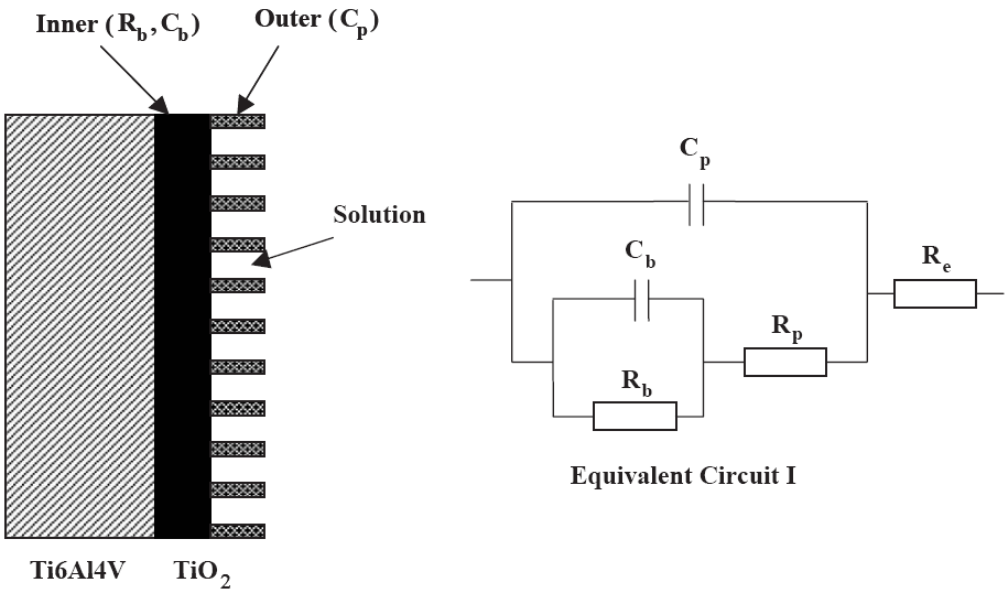

Figure 21: Equivalent circuit used for the two-layer oxide film on untreated Ti6Al4V, and schematic representation of the oxide film on Ti6Al4V, demonstrating how pores in the porous layer are sealed due to electrolyte filling (Wang et al. 2003).

Ramires and Guastaldi (2001) observed that the impedance response (in 0.9% NaCl) is dependent on the film thickness. If thin films are formed on the Ti surface, the diffusional impedance or diffusional process through the oxide film occurs at a sufficiently high frequency causing the Nquist plot to appear to be a single semi circle, fitting a single time constant impedance spectrum. Theoretically this is not the case for Ti-6Al-4V which fits a two time constant spectrum and therefore a second capacitive semicircle should be visible at low frequencies (<0.1Hz). Ramires and Guastaldi (2001) claimed that the shape of the second contribution was considered as a distorted semi circle intersecting the Re(Z) axis at frequencies below 0.001Hz. This second response related to the slow mass transport process whereas the initial contribution or semicircle is due to the kinetics of the metal-metal ion reaction.

Ramires and Guastaldi (2001) thus confirmed the presence of two time constants in the 100KHz – 1mHz frequency range.

Schmidt and Azambuja (2006) characterized the oxide film formed in the presence of various tested halides, by conducting EIS tests with Ti and Ti-6Al-4V in citric acid solution (with and without halides) at varied potentials. Spectra recorded for chloride containing citric acid polarized to varied potentials of 0, 0.5, 1.0 V_{SCE} displayed supporting evidence of at least two overlapped time constants which related to the strong adsorption process of chloride ions on the oxide film (**Figure 22)**. Schmidt and Azambuja (2006) observed that when polarized to 0V, the phase angle in the Bode plot (**Figure 22**) was found to be near 45° at the lower frequency limit showing a process of diffusion is present. When polarized to 1.0V the phase angle shifted to 10° indicating the increase in the film's porosity. The data was once again found to be a good fit to the equivalent circuit proposed in **Figure 20** consisting of an inner barrier layer and outer porous layer.

Luiz de Assis et al. (2006) presented Bode plots showing phase angles approaching -90° indicating highly capacitive behavior which is typical of a compact passive oxide film (Gonzalez & Mirza-Rosca 1999). This observation confirmed the work done by Schmidt and Azambuja (2006) depicted in **Figure 22**. It was suggested that according to the proposed equivalent circuit in **Figure 20** the inner barrier layer resistance ($R_{2(b)}$) was significantly larger than the outer porous layer resistance ($R_{1(p)}$). This indicated that the extent of the protection provided is due to the inner barrier layer; however, the ability to osseointegrate in biomedical implants is apparently attributed to the outer porous layer (Lavos-Valereto et al. 2004).

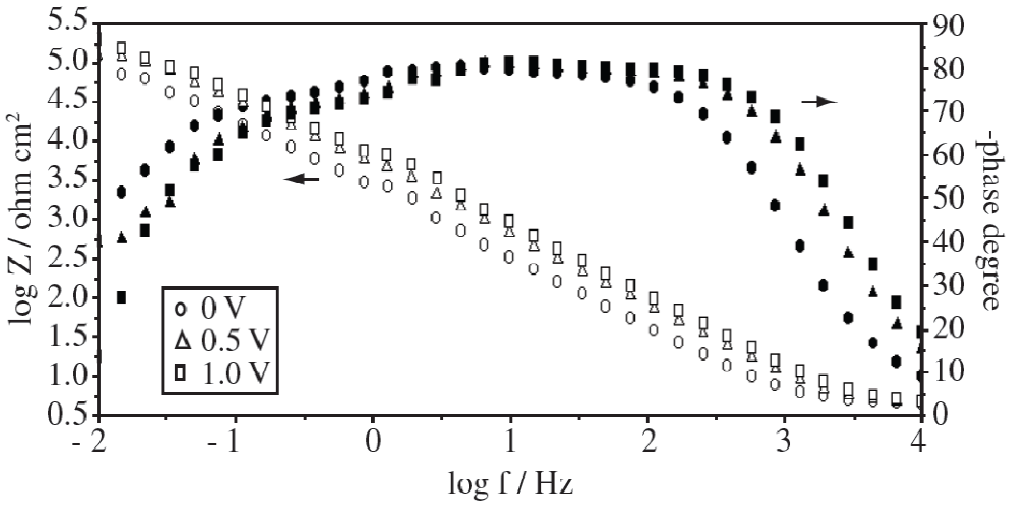

Figure 22: Bode Plot of Ti after anodic polarization at 0V (●), 0.5V (■), 1V (▲), in the presence of chloride ions (Schmidt and Azambuja 2006).

Tamilselev et al. (2007) suggested that a constant phase element (CPE) be used in place of capacitance. The CPE takes into account the fact that experimentally the oxide film never shows the theoretically expected phase shift of -90° and a slope of -1, which occurs for an ideal dielectric. Thus the dissipation factor 'n' associated with them. The CPE relates to the adsorbed species and takes into account diffusion processes and surface roughness (Rammelt & Reinhard 1990).

7 EXPERIMENTAL PROCEDURE

7.1 Materials used

Ti-6Al-4V rod was supplied by Goodfellow Cambridge Ltd. Test specimens were sectioned in to 16mm^2 cylindrical discs varying in thickness from 8 – 10mm for use in electrochemical testing.

7.2 Specimen Preparation

Due to the importance of the surface condition with regards to corrosion testing, proper care had to be carried out with surface preparation. Therefore, all specimens in its untreated form were polished prior to any heat treatments or electrochemical testing. To ensure a flat surface required for the Flat Cell, both sides of the untreated specimens were hand ground using 500 grit SiC grinding paper. The specimens were then hot mounted in clear acrylic resin for 5 minutes heating, followed by 5 minutes cooling while under a 20kN force. After which, the specimens were polished with an automated polisher using SiC grinding paper of decreasing roughness from 500 grit, 800 grit and 1200 grit to 4000 grit.

A mirror finish was acquired once polished with a MD NAP under attack solution using the procedure demonstrated in **Table 5**.

Polishing Medium	**Lubricant**	**Force (N)**	**Time (min)**	**Rotational Speed (RPM)**
MD NAP	Colloidal silica	30	10	150
MD NAP	*Attack Solution	30	10	150
MD NAP	Water	30	10	150

Table 5: Polishing procedure to achieve mirror finish in preparation for electrochemical testing.

*Attack solution used was made up of 50mL colloidal silica solution and 10mL hydrogen peroxide and used for the removal of metal deformed through scratching during the grinding and polishing stages.

Specimens were then removed from the resin, degreased using detergent on cotton wool and then rinsed in water. This was followed by an ultrasonic cleansing in ethanol for 5 minutes and hot air drying.

7.3 Heat treatments

Ti-6Al-4V specimens were tested in three conditions i.e. untreated, thermally oxidized and oxygen boost diffusion hardened condition. Thermal oxidation was carried out in a box furnace at 850℃ in air for 30 minutes and fu rnace cooled to room temperature at a heating and cooling rate of 5℃/min.

As discussed previously, the OBDH treatment is carried out in two steps, in a tube furnace allowing for both oxidation and diffusion processes. Initially the specimens were pulse oxidized in 99% pure O_2 for 30 minutes at 850℃. Oxygen was allowed to flow in the chamber for 1 minute, followed by a 9 minute soak period at atmospheric pressure. This pulsed oxidation process was carried out two more times, until the total oxidation time reached 30 minutes. The second diffusion step was carried out in vacuum at $4x10^{-5}$mbar for 20 hours at 850℃.

7.4 Hardness Testing

A Matsusawa MXT-CX7 Optical Microhardness Tester was used for microhardness measurements on all specimens. A static load of 50 gram force utilizing a pyramid shaped diamond indenter was used for indentations on cross sectioned treated and untreated specimens, generating hardness values displayed in **Figure 31**. Five indents at each distance from the surface were carried out, and an average hardness at each depth was calculated.

7.5 Electrochemical Testing

7.5.1 Specimen preparation for corrosion testing

Electrochemical testing was carried out on untreated samples in the polished condition. Thermally oxidized (TO) specimens were hand polished using 3µm diamond paste on a ø20cm MD-NAP polishing pad with a DP-blue lubricating solution (supplied by Struers), to decrease the surface roughness but not to remove the thick surface oxide layer.

Some potentiodynamic tests were carried out on unpolished OBDH specimens as well; however, the bulk of the potentiodynamic testing was done on polished OBDH

specimens. The main objective was to remove the oxide scale on the specimens to achieve a mirror finish without removing too much material. It was found that the removal of ~40µm ±9µm per sample was sufficient to achieve a metallic mirror finish, while still retaining a high hardness (see **Figure 31**). The removal of surface material was achieved using the automated polisher, where samples mounted in clear acrylic resin were polished individually using the procedure displayed in **Table 6**.

Polishing Medium	**Lubricant**	**Force (N)**	**Time (s)**	**Rotational Speed (RPM)**
1200 gritt SiC paper	Water	10	90	150
MD NAP	Colloidal silica	30	600	150
MD NAP	Attack Solution	30	300	150

Table 6: Polishing procedure for the removal of OBDH oxide, in preparation for electrochemical testing.

The technique displayed in **Table 6** was derived using a microscope and cross sectioned OBDH specimen, to determine the amount of material removed. During the grinding in the 1200 grit SiC stage, the amount of material removed was monitored at 30 second intervals. A micrometer was also utilized as a secondary precaution to monitor amount of material removed by checking the thickness of the sample at four different points on the specimen surface.

To ensure electrical contact through the metal for electrochemical testing of treated specimens, the surface of the disc specimens opposite to the test surface were ground down to the bare metal, removing any oxides which would possibly inhibit current flow.

7.5.2 Preparation of Electrolyte

The electrolyte used in all testing was 3.5 wt.% NaCl, made up using distilled water. To ensure accuracy and consistency, analytical reagent grade chemicals were used at all times. Cleaning procedures were stringent and caution was taken in mixing the electrolyte to avoid contamination.

7.5.3 Potentiostat

Potentiodynamic and impedance testing was carried out using the VersaSTAT 3 teamed with the V3-Studio software package. The VersaSTAT 3 is a potentiostat/galvanostat with an optional frequency response analyzer contained in a single unit.

The Wenking Model LT-78 potentiostat was used for the determination of the long term immersion open circuit potential (OCP) versus time scans.

7.5.4 Reference Electrode

A saturated calomel electrode (SCE) was used as the reference electrode having a potential of 0.241V with reference to the standard hydrogen electrode.

7.5.5 The Corrosion Cell

The Flat Cell was utilized in all electrochemical testing (**Figure 23**). The body of the Flat Cell is constructed of a Pyrex glass cylinder body clamped horizontally between two end plates. One end plate houses the counter electrode and the other end plate houses the working electrode. The Luggin well houses the reference electrode, with a fixed Teflon Luggin capillary protruding from the bottom of the well. A Teflon gasket exposes 1 cm^2 area of the working electrode to the electrolyte in the glass cylinder body.

All connections were sealed using parafilm to ensure no leaks, or contamination and to reduce the probability of oxygen entering the cell, and thus into the electrolyte during tests. Electrode precipitate from the chloride solution and corrosion product tends to form on the electrode connections; therefore, connections were monitored and kept clean at all times. The Teflon gasket was replaced once the onset of corrosion occurred beyond the 1cm^2 exposed surface area. The luggin capillary was constantly monitored for the presence of air bubbles, which were removed by tapping the cell or pressing down on the reference electrode, thereby pushing the air bubbles out the capillary.

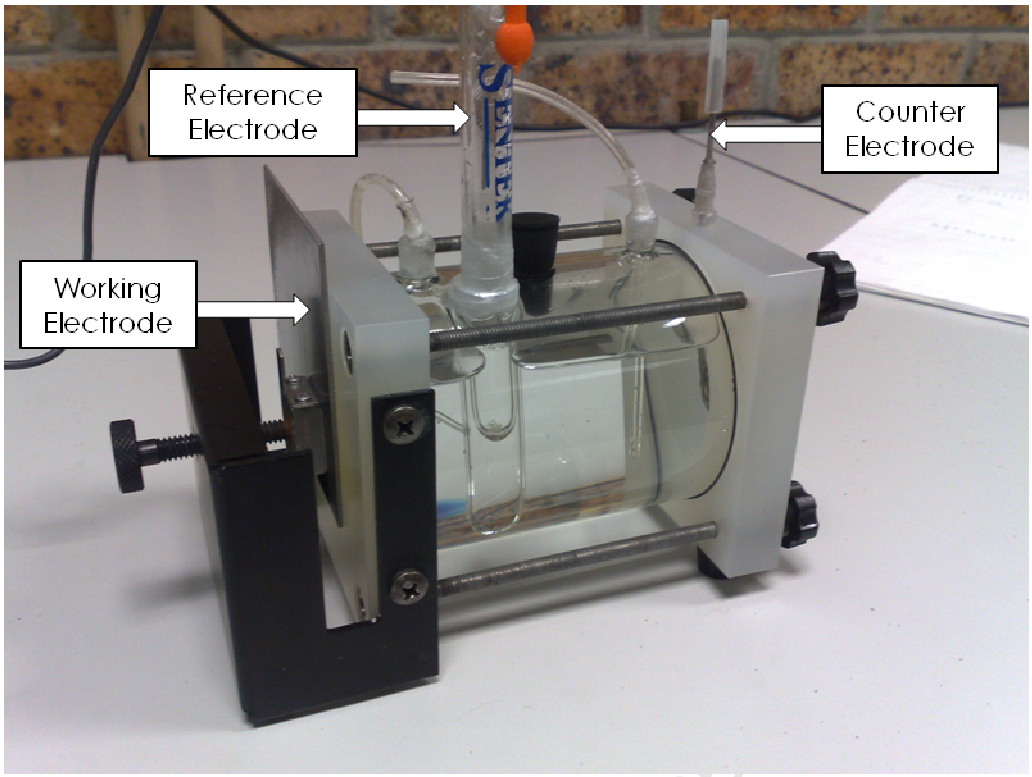

Figure 23: Picture of the Princeton Flat Cell, utilized in electrochemical testing.

7.5.6 Standard Test

The standard test method describes an experimental procedure which can be used to check one's experimental technique and to ensure proper functioning of the instrumentation. The test was performed using a AISI 430 specimen in 1N H_2SO_4 resulting in the curve displayed in **Figure 24**. This curve can be compared to curves presented in the ASTM standard G5-94 (ASTM G5 – 94 2004).

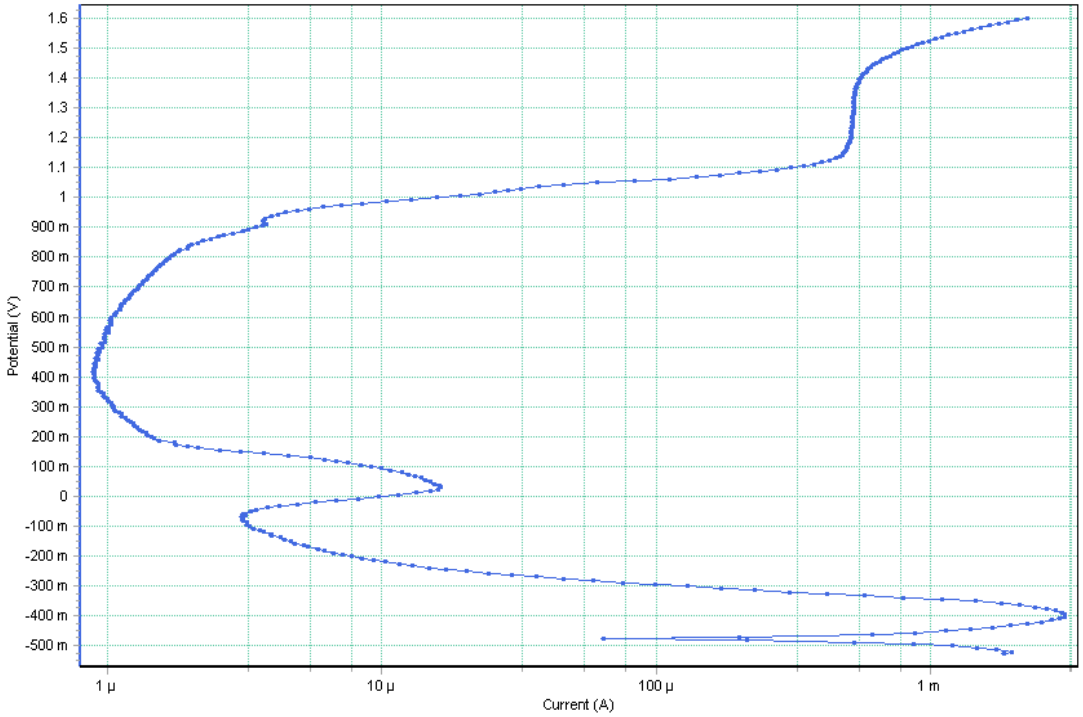

Figure 24: Potentiodynamic scan of a 430 Stainless Steel specimen in 1.0 N H_2SO_4.

7.5.7 Open Circuit Potential (OCP) versus Time Tests

Long term immersion OCP tests were carried out in 3.5 wt.% NaCl, in a non deaerated solution. Potentials were monitored, initially at each hour for the first 8 hours and then at 24 hour intervals. The cell was consistently monitored for any areas where chloride ions precipitated and stirring of the electrolyte was carried out if precipitation did occur.

7.5.8 DC tests: Potentiodynamic scans

Potentiodynamic scans of untreated and treated specimens were carried out in 3.5 wt.% NaCl. An initial deaeration was carried out prior to polarization by bubbling nitrogen through the solution for a period of 60 minutes, to reduce the oxygen in solution. The temperature was maintained at room temperature by monitoring the temperature before and after tests. Polarization was initiated below OCP at a scan rate of 1mV/s in the anodic direction for all tests.

7.5.9 DC tests: Tafel plots

Tafel plots were carried out in a deaerated 3.5 wt.% NaCl solution over a potential range of ±250mV with respect to the free corrosion potential (OCP). The corrosion rates were calculated using the V3 Studio software. The procedure for calculation of Tafel constants and corrosion rates are explained in section 4.3.

7.5.10 AC tests

EIS testing was carried out in a deaerated 3.5 wt.% NaCl solution, at a scan frequency range of 100kHz to 10mHz using a perturbation amplitude of 10mV. Impedance tests were carried out at OCP, and at offset potentials of -0.5, 0.0, 0.5, 1.0, 1.5, 2.0, 2.5 and 3.0V_{SCE}. The resulting data was interpreted as the plots discussed in section 6.4.

The spectra were then circuit modelled (as explained in section 6.3) using the ZSimpwin (Version 3.21) modeling software, where the best fit between the measured data and the calculated data was computed. The fitting quality was evaluated by the chi-squared (χ^2) values and were found to be in the order of between 10^{-3} – 10^{-4}.

7.6 Microscopy

Optical light microscope images were acquired utilizing a Nikon optical light microscope fitted with a Leica EC3 camera. Images were taken of the surface of the polished specimens, prior to testing and after electrochemical testing.

7.7 Scanning Electron Microscopy (SEM)

The Leica Stereoscan 440 was used to examine the microstructures of untreated and treated specimens. SEM images were used to display the presence of alpha and beta grains as well as reveal the surface morphology of the TO specimens.

8 RESULTS

The results section presents data obtained from tests carried out on untreated and treated Ti-6Al-4V specimens.

8.1 Microstructure

8.1.1 Untreated Ti-6Al-4V

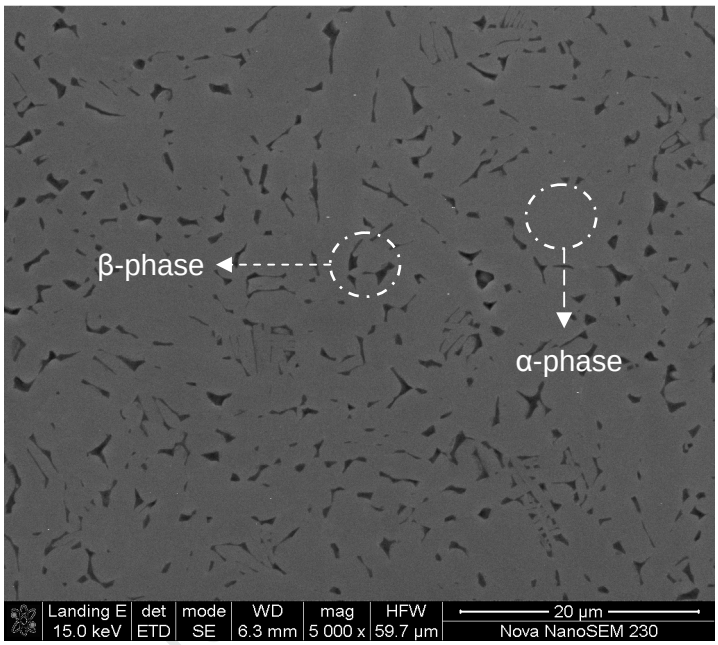

Figure 25: High magnification view of polished untreated Ti-6Al-4V prior to testing.

Figure 25 presents the microstructure of the untreated metal showing a high magnification view of the specimen's surface morphology. The micrograph displays the sample's polished state that was prepared for corrosion testing, attaining a surface roughness of 0.08 ±0.02µm for the R_a value. A typical microstructure for Ti-6Al-4V is exhibited in **Figure 25**, where the darker dispersed grains represent the BCC β-phase titanium and the lighter areas represent the HCP α-phase titanium grains.

8.1.2 Thermally Oxidised Ti-6Al-4V

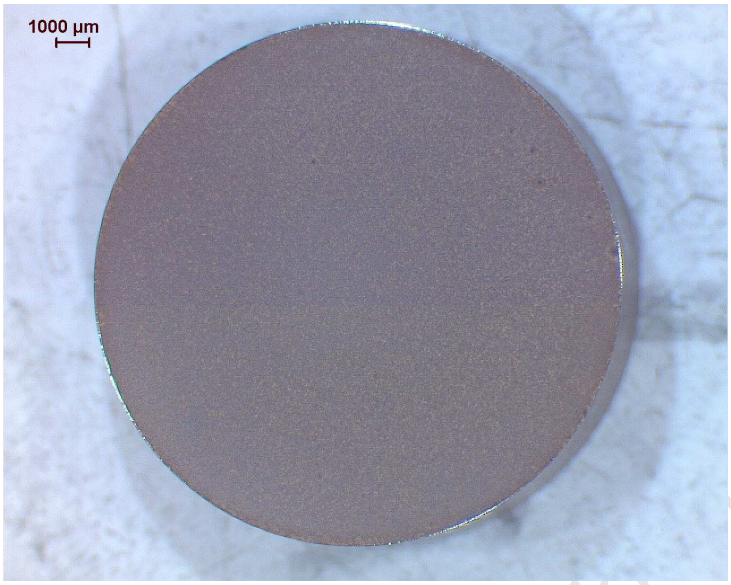

Figure 26: Thermally Oxidised Ti-6Al-4V corrosion specimen prior to testing.

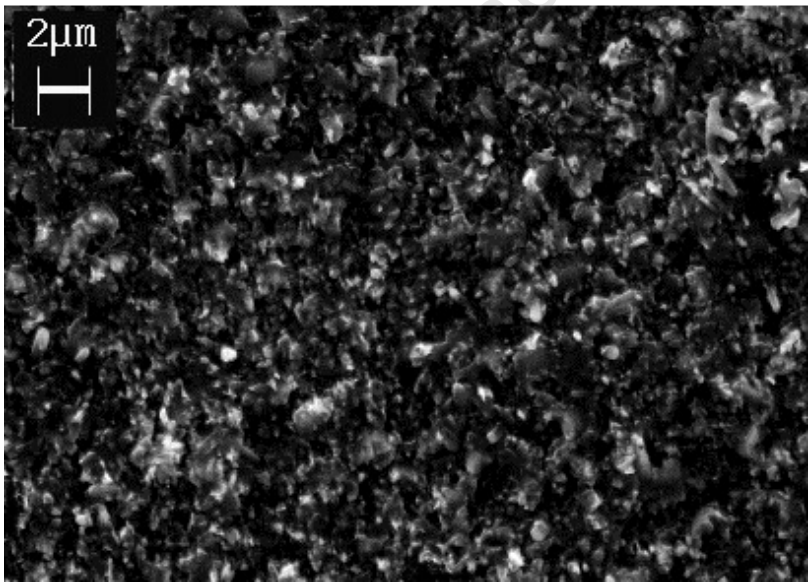

Figure 27: High magnification view of polished thermally oxidised Ti-6Al-4V prior to testing.

Oxidation of the untreated metal is carried out in air in a box furnace forming an oxide with a mottled reddish brown appearance, displayed by the thermally oxidised Ti-6Al-4V specimen in **Figure 26**. Polishing of the oxide layer was carried out to decrease the surface roughness to a desirable value for a more uniform surface condition required for consistency in corrosion testing. Prior to the oxidation treatment proper care is taken during polishing of the untreated metal, so that the extent of plastic deformation will be too small to cause any significant change in the oxidation

kinetics/mechanism. Post oxidation polishing, using 3µm diamond paste for one minute resulted in a decrease in surface roughness from 0.34 ±0.03µm to 0.08 ±0.02µm for the R_a value.

Figure 27 presents a high magnification view (SEM image) of a polished thermally oxidised sample. Examination of the surface morphology revealed a dark spongy almost flake-like appearance.

8.1.3 Oxygen Boost Diffusion Hardened (OBDH) Ti-6Al-4V

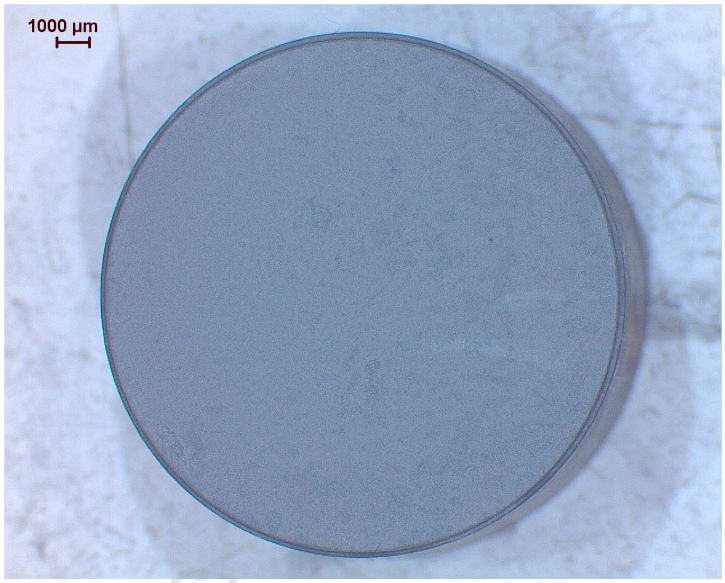

Figure 28: OBDH Ti-6Al-4V specimen post boost diffusion treatment prior to polishing.

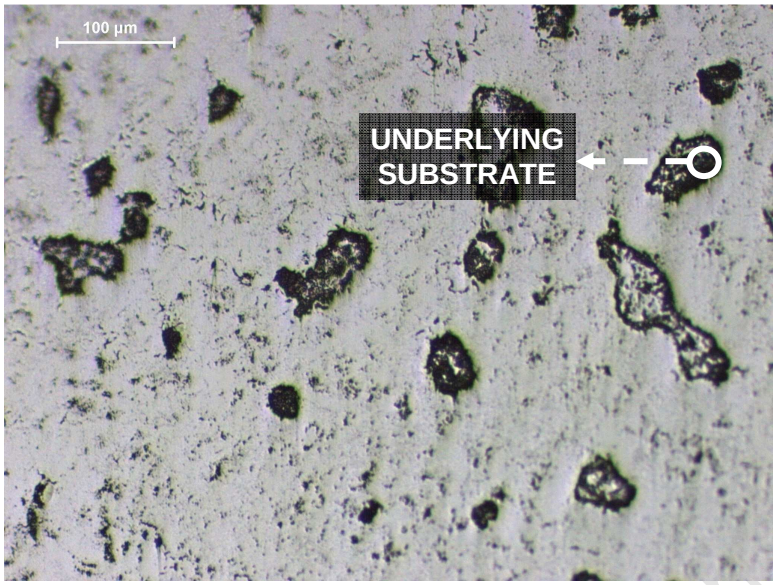

(a)

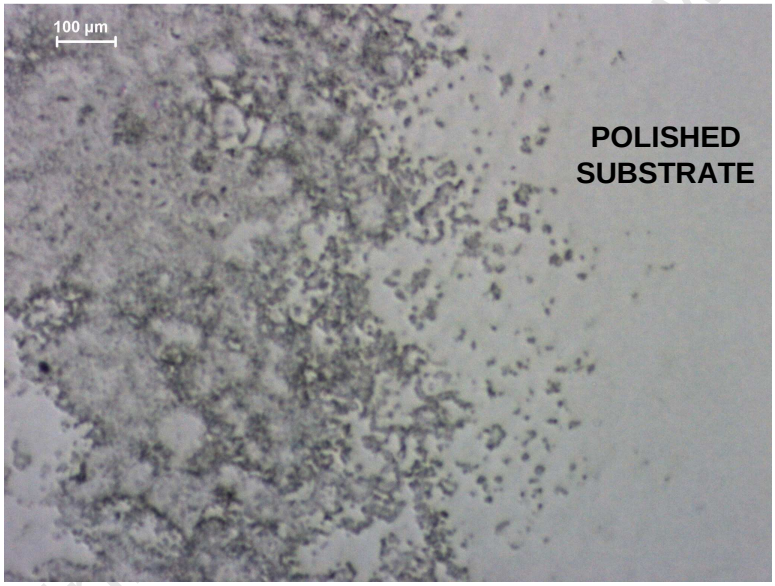

(b)

Figure 29: Micrograph of OBDH specimen after: (a) the removal of 15µm of the surface (b) the removal of 30µm of the surface.

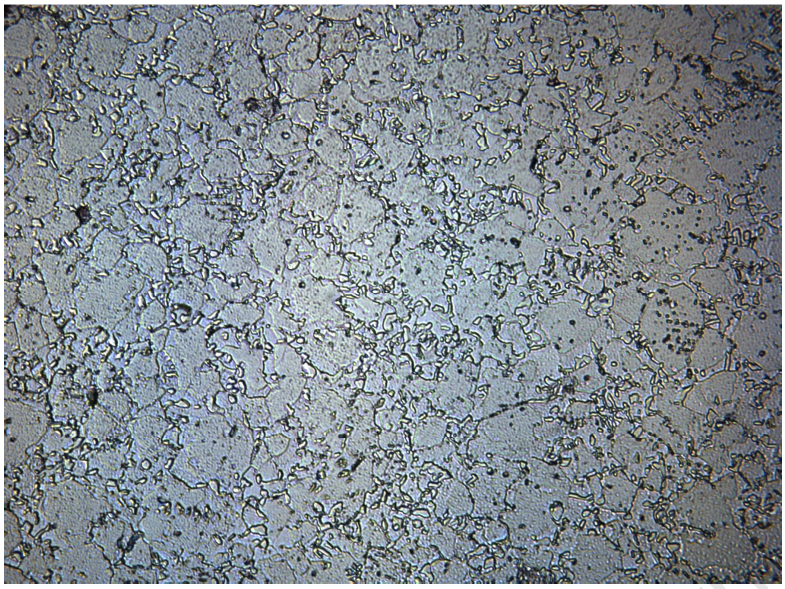

Figure 30: Micrograph of Oxygen Boost Diffusion Hardened Ti-6Al-4V after removal of residual oxide by polishing.

Figure 28 displays the image of an OBDH specimen after the boost diffusion hardening treatment prior to polishing, where the specimen now takes on a silver grey colour. The optical micrograph after polishing to a metallic mirror finish is displayed in **Figure 30**, where the surface roughness attained is the same as that of the untreated metal i.e. 0.08 ±0.02µm for the R_a value. The polished mirror finish surface required for corrosion testing, was achieved after the removal of 40µm ±9 µm of the surface. The specimen displayed in **Figure 30** was etched to better distinguish between the light alpha and dark beta phases.

Figure 29a displays the surface condition after the removal of 15µm of the surface, where a metallic finish was not yet achieved. A hazy white layer is displayed on the surface, with areas revealing the underlying substrate which is increasingly exposed with further removal of material from the surface. **Figure 29b** represents the surface after removal of 30µm of material, where a polished surface is starting to appear (for example on the right-hand side of **Figure 29b**).

8.2 Hardness Profile

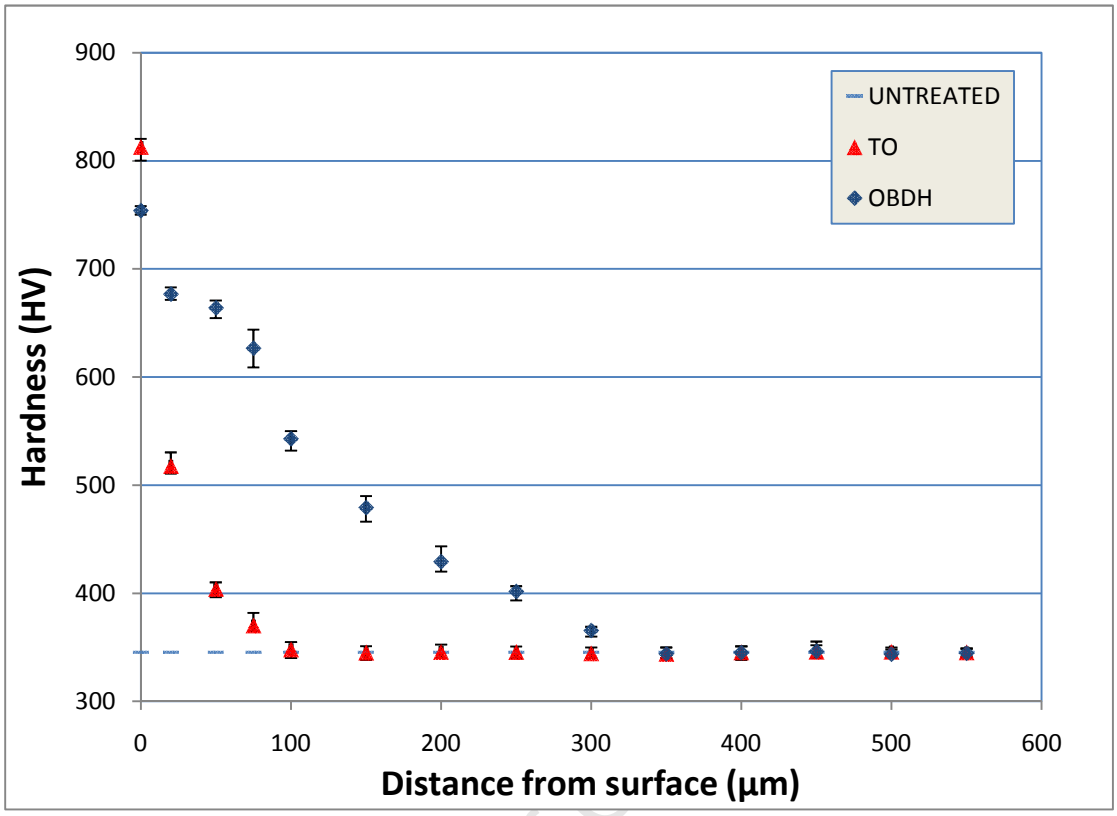

Figure 31: Hardness profile of the Untreated and Treated Ti-6Al-4V.

The hardness profiles of untreated and treated Ti-6Al-4V specimens are displayed in **Figure 31.** The Vickers hardness decreases as the distance from the surface increases for the TO and OBDH specimens, whereas the hardness remains constant for the bulk untreated specimen. Initially the TO specimens have a high hardness at the surface, which decreases rapidly with increasing depth into the diffusion zone. Eventually bulk hardness is reached at around 100µm from the surface. The OBDH specimens have a slightly lower hardness (at the surface) than the TO specimen. However, the OBDH specimen retains its high hardness deeper into the substrate (with an increased oxygen diffusion zone) and the bulk hardness is only reached around 350µm from the surface. Error bars show the standard deviation calculated from the five hardness reading taken at each depth.

9 RESULTS: DC ANALYSIS

9.1 Long Term Immersion OCP (Open Circuit Potential)Tests

Long term testing was performed on untreated, and treated Ti-6Al-4V specimens (Thermally oxidised (TO) and oxygen boost diffusion hardened (OBDH) specimens) in a non deaerated 3.5 wt.% NaCl electrolyte. The potentials of each specimen were monitored on a daily basis until such time that the OCP demonstrated sufficient stability.

9.1.1 Comparison of OCP tests

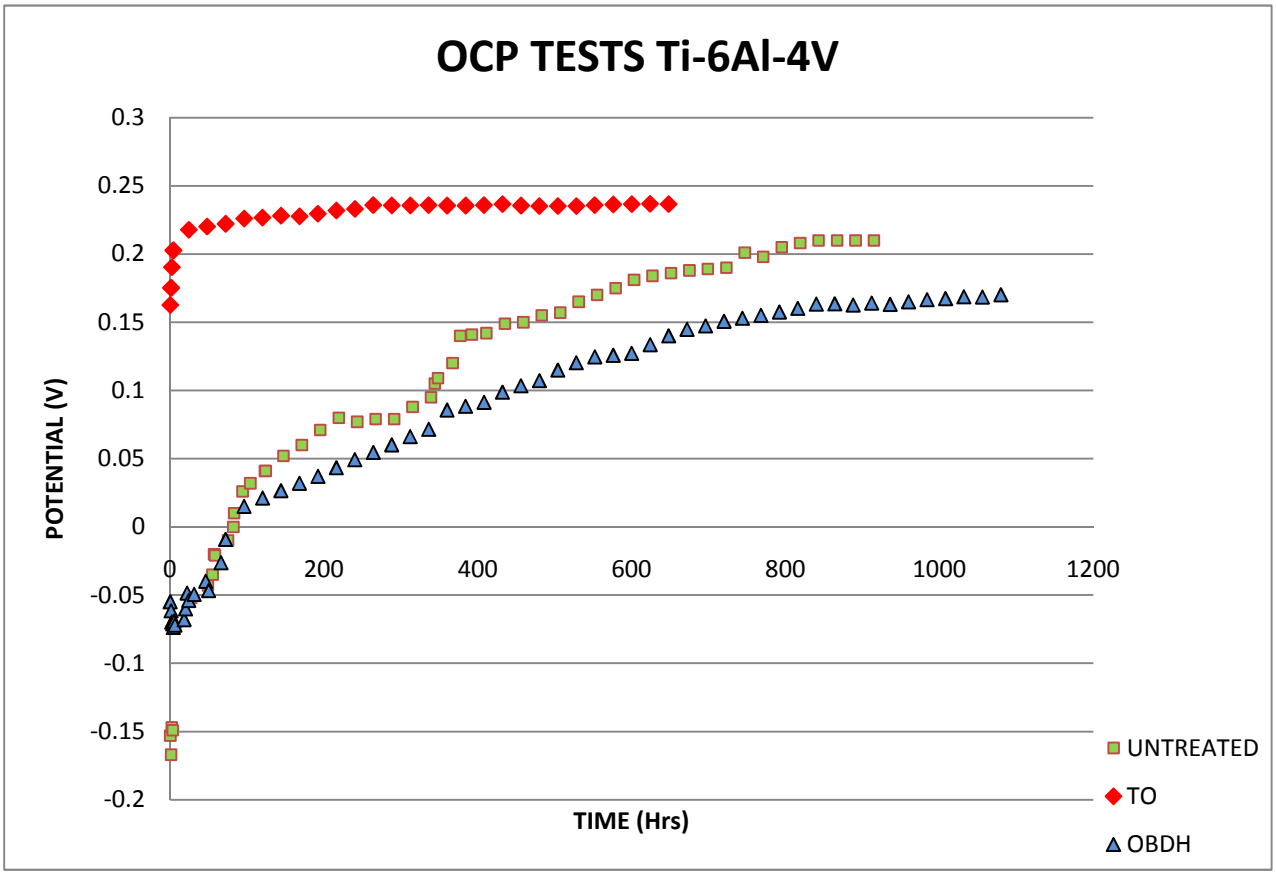

Figure 32: Comparison of open circuit potentials after long term immersion times of Untreated, Thermally Oxidised and OBDH Ti-6Al-V specimens in 3.5 wt.% NaCl.

The effect of time on the OCP value of the three specimens is displayed in **Figure 32**. Changes in potential after initial immersion in the electrolyte until final stabilization are summarized in **Table 7**. For untreated specimens and OBDH specimens the potential increases gradually with time becoming more anodic (noble) throughout the duration of the test until the potential stabilizes at values noted in **Table 7**. In the case of TO specimens an initial fast increase in potential leads to a more anodic (noble) potential which stabilizes and remains at this final potential for

the remainder of the test. The initial potential for the TO specimen is much higher compared to the untreated and OBDH specimens. However, all three specimens stabilize at final potentials very close to one another (**Table 7**), with the TO specimen stabilizing much faster compared to the time taken for the untreated and OBDH specimens to stabilize.

TEST	Initial Potential (V)	Stabilization Potential (V)	Time to Stabilization (hours)	Rise in Potential (V)
Untreated	-0.153	0.210	819	0.363
T.O	0.163	0.237	264	0.074
O.B.D.H	-0.055	0.170	912	0.225

Table 7: Open Circuit Potentials of Untreated and Treated Ti-6Al-4V.

9.2 Potentiodynamic Analysis

Potentiodynamic polarization scans were carried out on untreated and treated Ti-6Al-4V specimens. Samples were appropriately polished (see Section 1) prior to testing to reduce surface impurities and minimize surface roughness.

(***Arrows on graphs in Section 9.2 are an indication of specific parameters which characterize the behaviour of the material during the potentiodynamic scan. The average values of the parameters are summarized in **Table 8**.)

9.2.1 Untreated Ti-6Al-4V

Potentiodynamic scans performed on untreated Ti-6Al-4V specimens were carried out at a scan rate of $1mV.s^{-1}$ in 3.5 wt.% NaCl solution in the following scan ranges:

i) -0.5V below open circuit potential (OCP) to $4.0V_{SCE}$ and

ii) $-1.0V_{SCE}$ to $4.0V_{SCE}$.

i) Initial potential = -0.5V below OCP

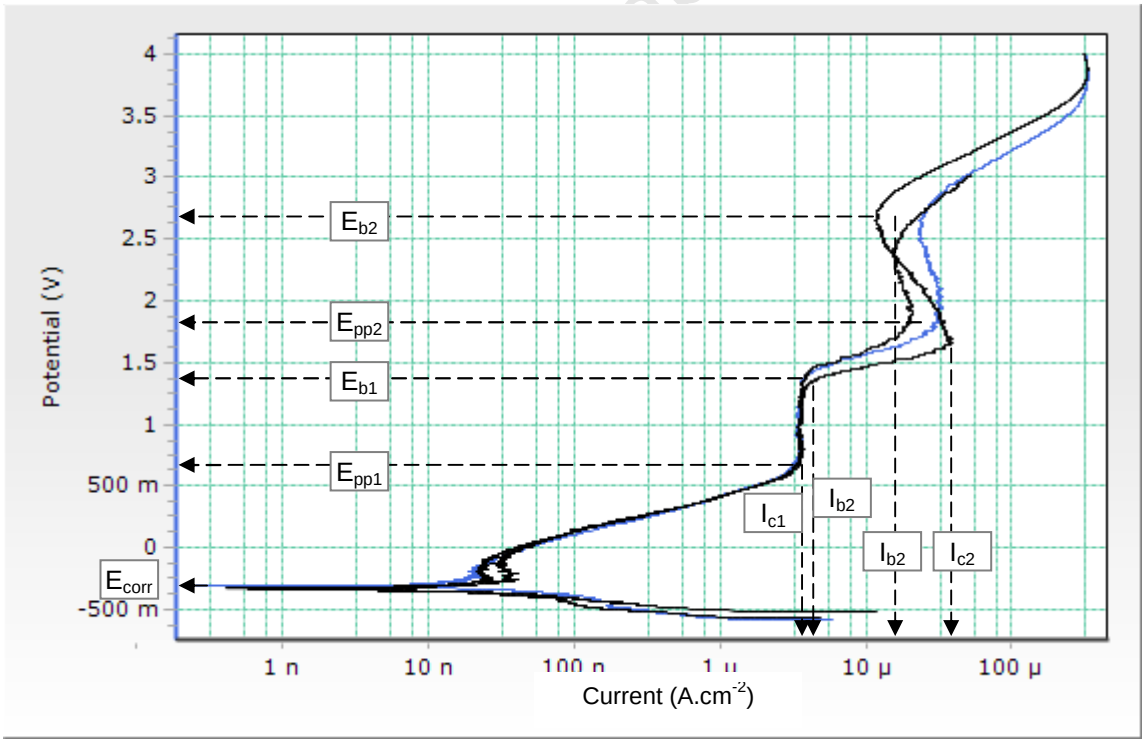

Figure 33: Potentiodynamic scans of untreated Ti-6Al-4V in 3.5 wt.% NaCl solution initiated at -0.5V below OCP.

ii) Initial potential = -1.0V_{SCE}

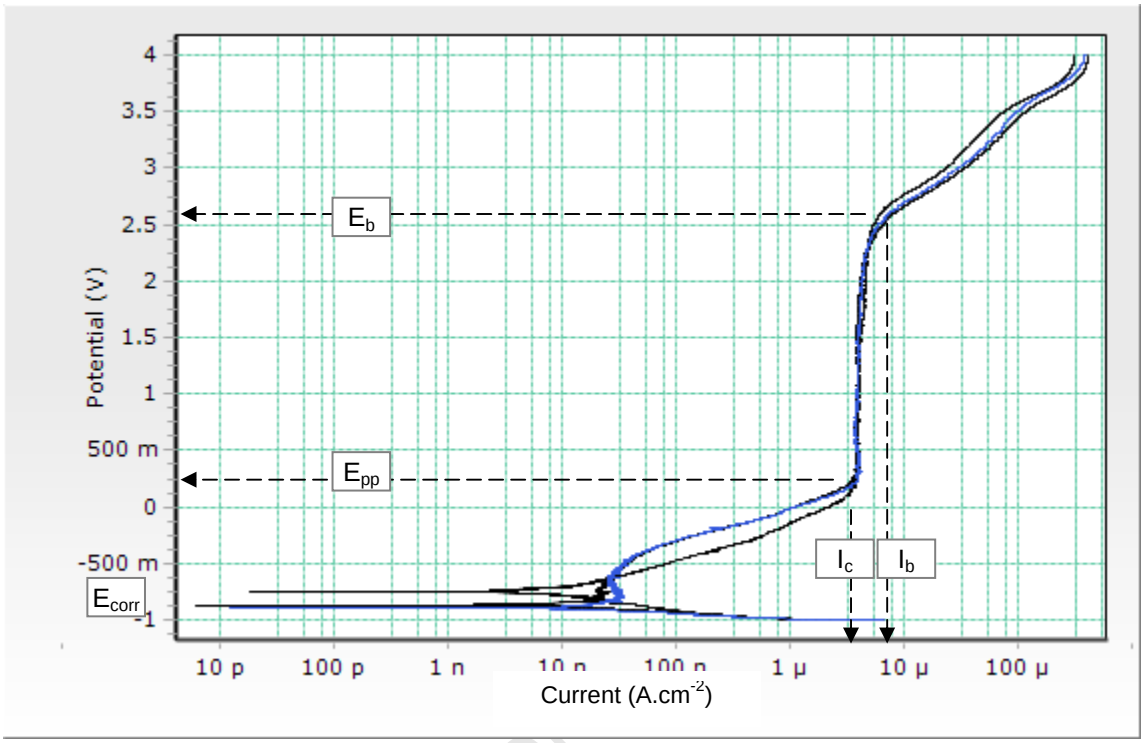

Figure 34: Potentiodynamic scans of untreated Ti-6Al-4V in 3.5 wt.% NaCl solution initiated at -1.0V_{SCE}.

Figure 33 shows the potentiodynamic scan of an untreated polished Ti-6Al-4V specimen. The scan starts in the cathodic region at ~ 600mV_{SCE}. The current density initially decreases as the sample is polarized towards the corrosion potential (E_{corr}) and corresponding corrosion current I_{corr}. Once the metal is polarized in the positive or noble direction from E_{corr}, the current density starts to increase indicating the onset of oxidation. A potential is then reached where the current density rapidly decreases known as the primary passivation potential (E_{pp1}) and critical current density (I_{c1}). As the potential continues to increase after the E_{pp1} the current density remains almost constant over a wide range of potentials in the region known as the passive region where the corrosion rate is very low. The oxide layer breaks down at the initial breakdown potential (E_{b1}) and then repassivates to form part of the passive region. The passive region finally ends at the second breakdown potential (E_{b2}). Values for E_{corr}, E_{pp}, E_{b1}, E_{b2} and passive region range are shown in **Table 8**.

Figure 34 displays a similar scan to **Figure 33** but instead of polarizing the sample from -0.5V below OCP, the sample is polarized from -1.0V_{SCE}. The effect of starting the scan at a lower potential is instantly visible. The E_{corr} values are notably lower.

Another obvious difference is the passive region, where the current density remains constant over a wider potential range when compared to specimens polarized at -0.5V below OCP. The initial breakdown potential (E_{b1}) was not observed evident in **Figure 33**. **Table 8** displays the E_{corr}-values as well as the passivation and breakdown potentials, including the corresponding current density values.

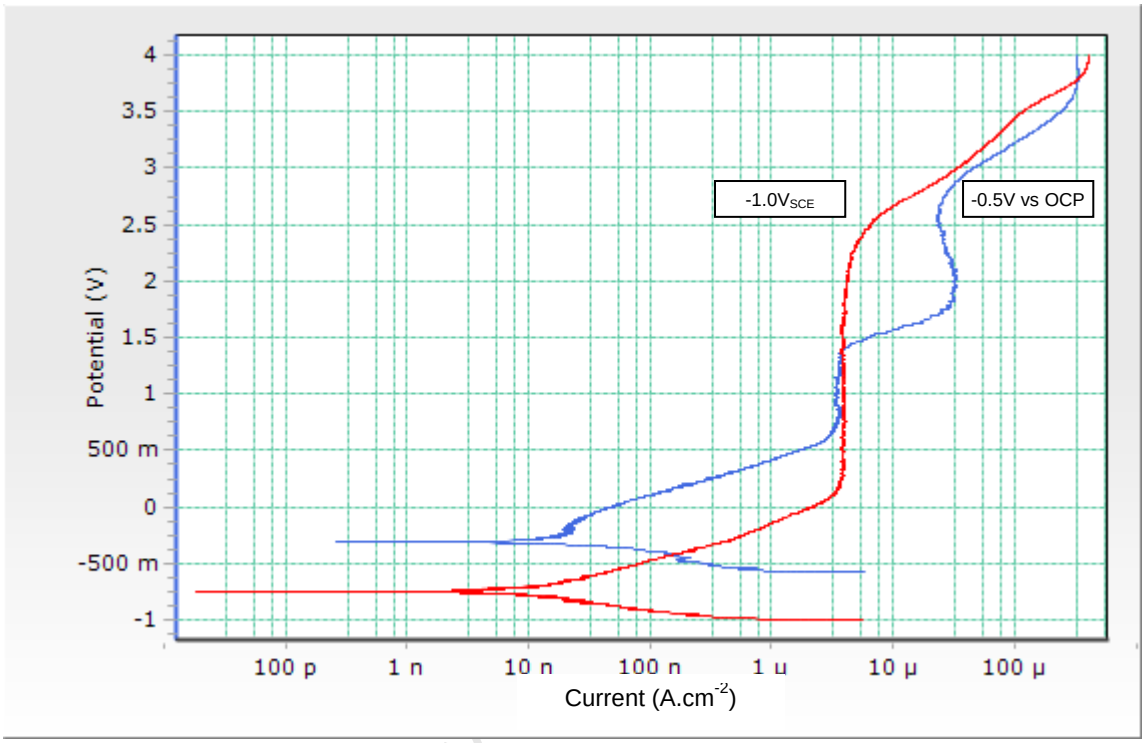

Figure 35: Comparison of potentiodynamic scans of -0.5V below OCP (BLUE) and -1.0V$_{SCE}$ (RED) for Untreated Ti-6Al-4V.

Comparison of **Figure 33** (Blue curve) and **Figure 34** (Red curve) is displayed in **Figure 35** to demonstrate the difference in polarization behaviour. A more active initial polarization of -1.0V_{SCE} results in a lower E_{corr}, E_{pp} as well E_{b1}-value; however, the corresponding current density values remain similar in both curves (see **Table 8**).

9.2.2 Thermally Oxidised Ti-6Al-4V

Potentiodynamic scans done on thermally oxidised Ti-6Al-4V specimens were carried out at a scan rate of 1mV.s^{-1} in 3.5 wt.% NaCl solution in the following scan ranges:

i) -0.5V below open circuit potential (OCP) to 4.0V_{SCE} and

ii) -1.0 V_{SCE} to 4.0V_{SCE}.

i) Initial potential = -0.5V below OCP

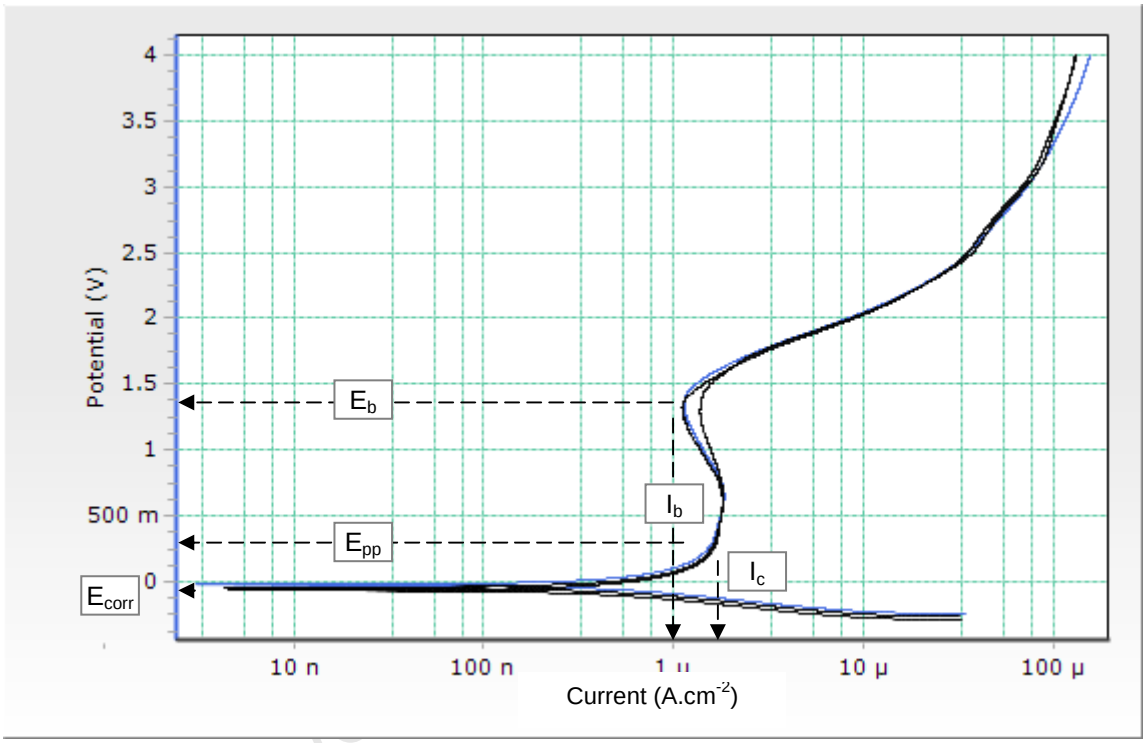

Figure 36: Potentiodynamic scans of thermally oxidised Ti-6Al-4V in 3.5 wt.% NaCl solution initiated at -0.5V below OCP.

ii) Initial potential = -1.0V_{SCE}

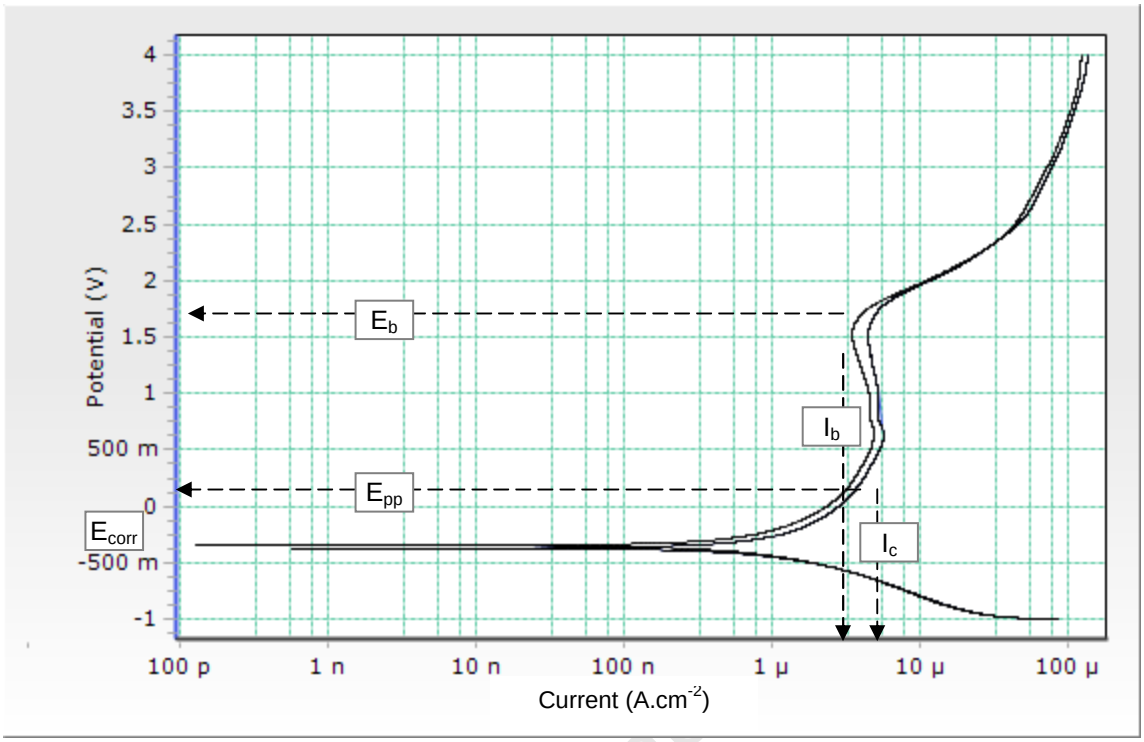

Figure 37: Potentiodynamic scans of thermally oxidised Ti-6Al-4V in 3.5 wt.% NaCl solution initiated at -1.0V_{SCE}.

The potentiodynamic scan for a thermally oxidised Ti-6Al-4V specimen is displayed in **Figure 36** and **Figure 37**. Once again the polarization scan starts in the cathodic region where the specimen is polarized to a potential more active than the free corrosion potential or OCP of the specimen. **Figure 36** shows the specimen polarized from -0.5V below OCP, whereas **Figure 37** illustrates the behaviour when polarized from -1.0V_{SCE}. The shapes of the two scans are very similar but vary in critical values. The E_{corr}-value for **Figure 36** is noticeably higher than that of **Figure 37**. Polarizing the metal further causes the metal to passivate, where the current density decreases over a range of potentials, until the metal finally breaks down at E_b (see **Table 8**). However, repassivation is not evident even after further polarization up to 4V_{SCE}.

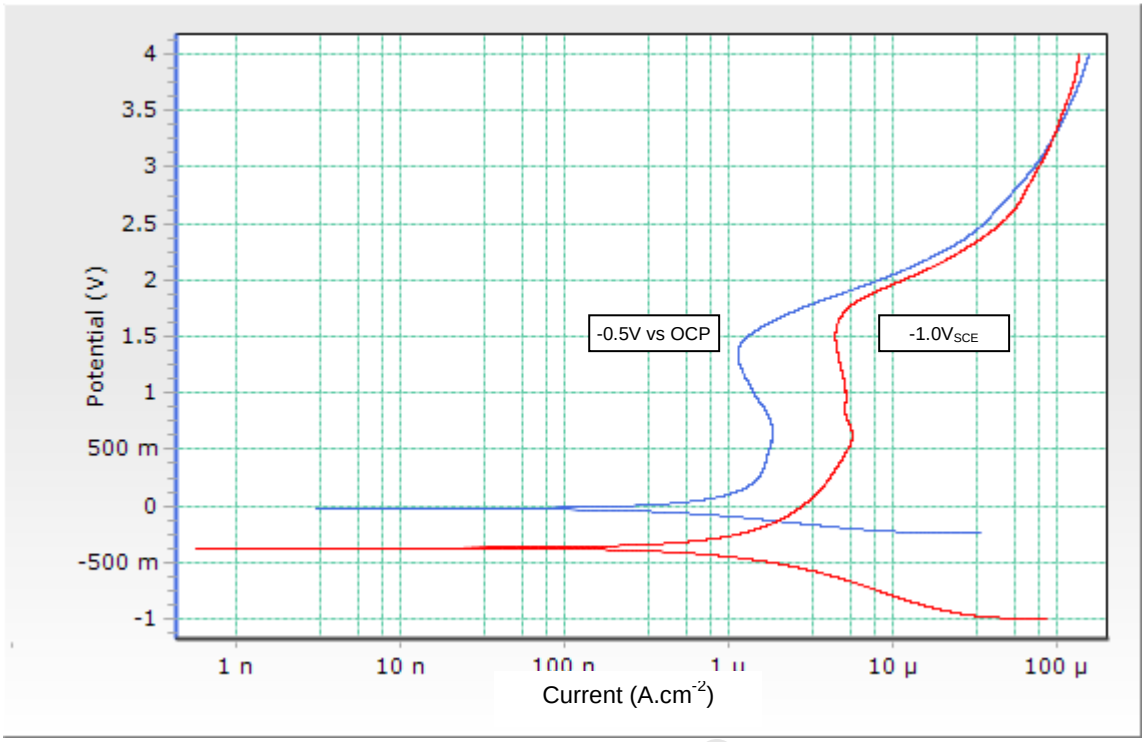

Figure 38: Comparison of potentiodynamic scans of -0.5V below OCP (BLUE) and -1.0V$_{SCE}$ (RED) for Thermally Oxidised Ti-6Al-4V.

Figure 38 presents a comparison of the two thermally oxidised scans, **Figure 36** (Blue curve) and **Figure 37** (Red curve). The most apparent observation reveals that initiating polarization in the active region closer to OCP displays a higher E_{corr} value and lower current density values, thus exhibiting a better corrosion resistance. However, the metal appears to passivate at very similar potentials (see **Table 8**); but a slightly higher E_b is evident for specimens polarized from more active potentials (i.e. -1.0V$_{SCE}$), thus indicating a larger passive region.

9.2.3 Oxygen Boost Diffusion Hardened (OBDH) Ti-6Al-4V

Potentiodynamic scans were carried out on OBDH specimens which were polished to a metal finish, thereby removing the oxide layer on the surface and testing the oxygen enriched boosted diffusion zone.

An additional test was also carried out on OBDH specimens which were removed from the furnace without any further polishing thereafter. In doing so, the aim was to indicate the difference in electrochemical properties of the oxide layer on the OBDH specimen compared to the TO specimen. This additional test would also display the difference between surface oxide and the boost diffusion zone under the surface oxide.

Thus, potentiodynamic scans done on OBDH Ti-6Al-4V specimens were carried out (at a scan rate of 1mV.s^{-1} in 3.5 wt.% NaCl solution) in the scan ranges as follows:

i) -0.5V below open circuit potential (OCP) to 4.0V_{SCE},
ii) -1.0 V_{SCE} to 4.0V_{SCE} and
iii) -0.5V below open circuit potential (OCP) to 4.0V_{SCE} for unpolished OBDH specimens.

i) Initial potential = -0.5V below OCP (Polished)

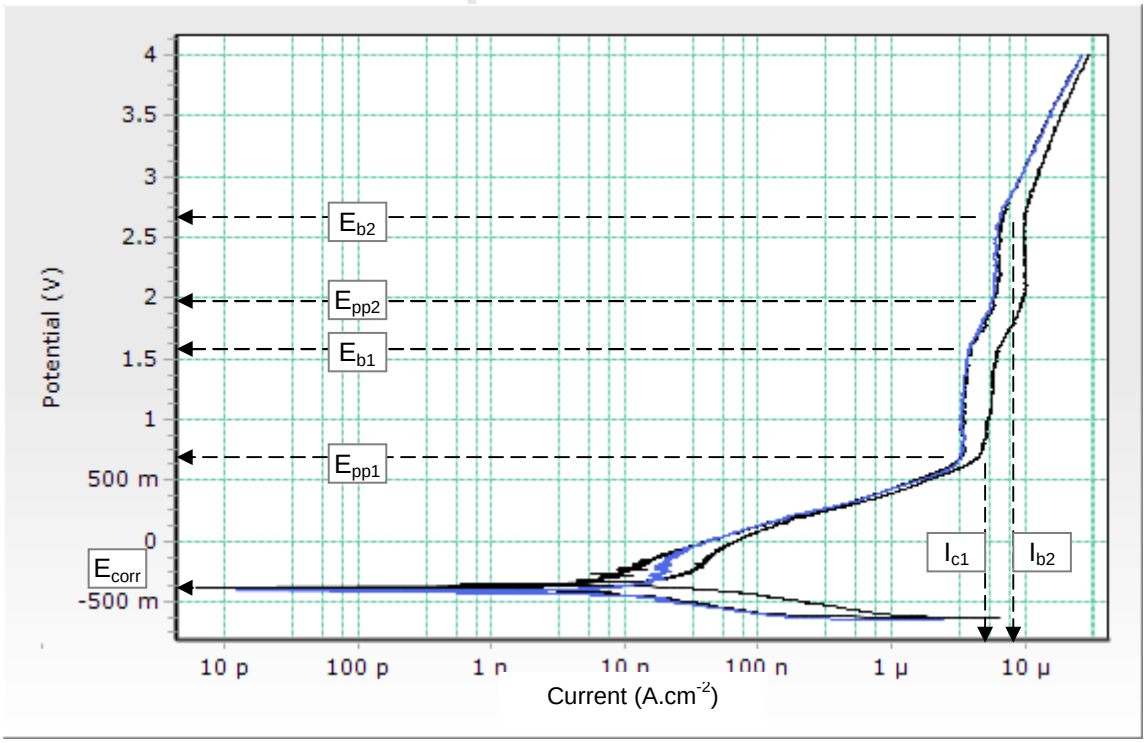

Figure 39: Potentiodynamic scans of OBDH Ti-6Al-4V in 3.5 wt.% NaCl solution initiated at -0.5V below OCP.

ii) Initial potential = -1.0V_{SCE} (Polished)

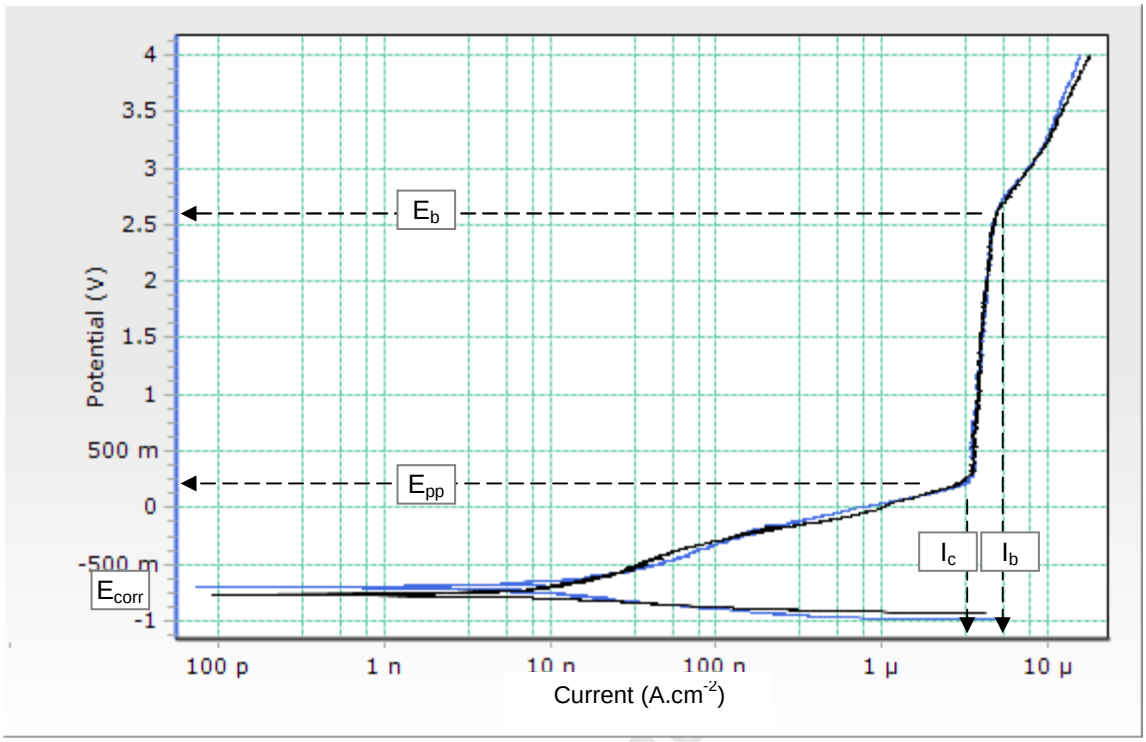

Figure 40: Potentiodynamic scans of OBDH Ti-6Al-4V in 3.5 wt.% NaCl solution initiated at -1.0V_{SCE}.

Potentiodynamic scans of OBDH specimens (**Figure 39** and **Figure 40**) demonstrate a similar behaviour to the respective untreated specimens (**Figure 33** and **Figure 34**). Polarizing the specimen from -0.5V below OCP results in E_{corr} values similar to that displayed by the untreated metal, in **Figure 33**. Passivation and breakdown potentials and current values are noted in **Table 8**. Once again polarizing from -0.5V below OCP results in oxide film breakdown and repassivation in the passive region. On the other hand, polarizing in the more active region of -1.0V_{SCE} results in a lower E_{corr} and E_{pp}-value and a more consistent passive region, with no visible disturbance of the current density in the passive range.

iii) Initial potential = -0.5V below OCP (Unpolished)

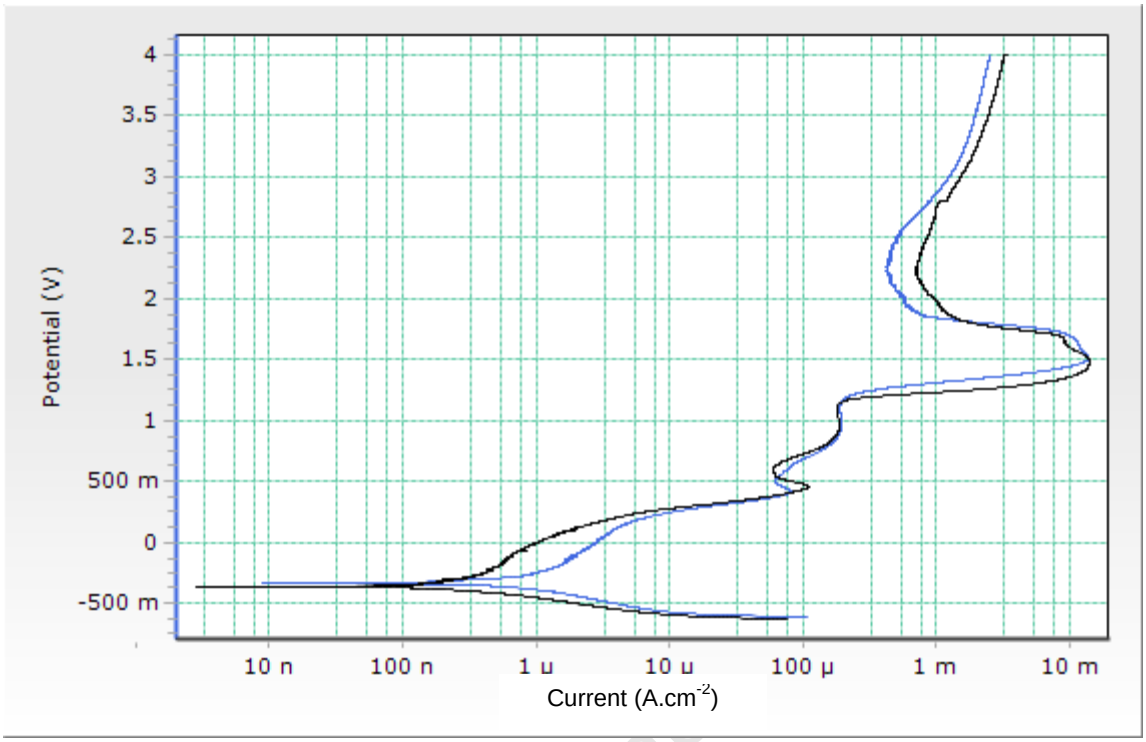

Figure 41: Potentiodynamic scans of OBDH Ti-6Al-4V specimens removed from the furnace without any further polishing, in 3.5 wt.% NaCl solution, initiated at -0.5V below OCP.

Tests carried out on OBDH specimens without any prior polishing resulted in the curve displayed in **Figure 41**. The curve provides evidence of the inhomogeneous surface, with constant breakdown and repassivation of the oxide layer (see **Table 8**). A consistent passive region is not evident, as demonstrated by the polished specimens.

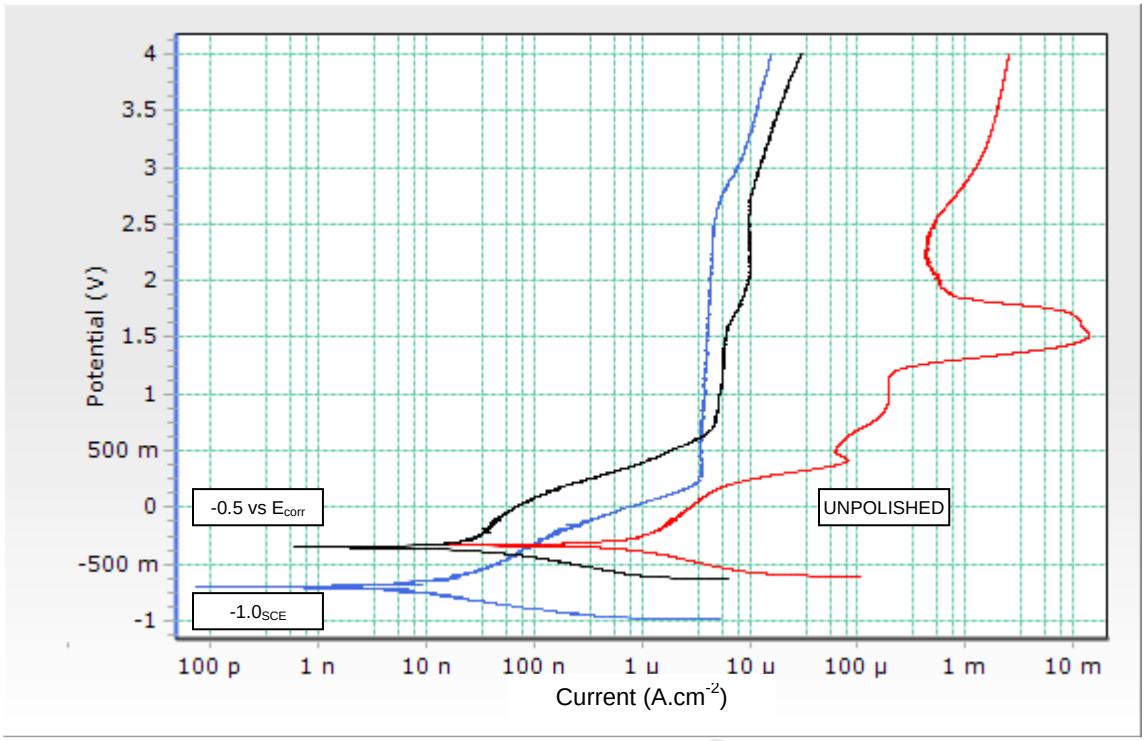

Figure 42: Comparison of potentiodynamic scans of -0.5V below OCP polished (BLACK) and unpolished (RED) and -1.0V_{SCE} (BLUE) for Untreated Ti-6Al-4V.

Figure 42 presents an overlay of all curves obtained for OBDH specimens. Initial observations reveal the difference in E_{corr} values for the two polished samples, where the blue curve (Initial potential **=** -1.0V_{SCE}) has a noticeably lower E_{corr} and E_{pp1} compared to the black curve (Initial potential = -0.5V below OCP) and the red curve (unpolished specimen). However, the current density values of the polished specimens follow a similar trend, whereas the unpolished specimen is shifted to the right of the other two curves, indicating a higher corrosion current and a visibly less stable oxide layer. Clearly the blue curve (Initial potential **=** -1.0V_{SCE}) shows the most consistent passive layer and a slightly larger passive region (see **Table 8**).

9.2.4 Comparison of Treated with Untreated Ti-6Al-4V

This section describes the differences in behaviour displayed for the three specimens being tested i.e.

i) Untreated Ti-6Al-4V
ii) Thermally Oxidised Ti-6Al-4V
iii) Oxygen Boost Diffusion Hardened Ti-6Al-4V

Figure 43 and **Figure 44** presents the three curves overlayed on the same set of axes, to illustrate the differences in potentiodynamic behaviour. **Figure 43** displays tests carried out at an initial potential of -0.5V below OCP. OBDH specimens display very similar potentiodynamic behaviour to the untreated metal from below E_{corr} all the way to the passive region. Differences between specimens become more apparent in the passive region. Untreated specimens demonstrate a larger shift in current density during the initial breakdown potential and repassivate at a higher current density than that of the OBDH specimen. The OBDH specimen, however, shows a small shift in current density at the initial breakdown potential. The E_{b2} is more obvious for the untreated specimen and occurs at a higher current density when compared to the OBDH specimen. Once E_{b2} of the OBDH specimen is reached the corrosion rate undergoes a gradual increase. When comparing the untreated and OBDH specimens to the TO specimen there are notable differences in behaviour. Thermally oxidized specimens exhibit a higher E_{corr}-value as well as a lower E_{pp1}-value. These values occur at a lower current density indicating a lower corrosion rate. The TO specimen's breakdown potential is similar to that of the untreated and OBDH specimens E_{b1}; however, once the TO specimen breaks down it does not repassivate, as displayed for the untreated and OBDH specimens. Once the TO specimen breaks down, it undergoes a rapid increase in current density with potential. This results in the TO specimen exhibiting the smallest passive region of the three specimens.

Figure 44 is an overlay of tests carried out at -1.0V_{SCE}. Once again the similarity in behaviour of the untreated metal to the OBDH specimen is apparent. However, the passive region for both is more uniform with very little or no disturbance over the passive range. Thereafter (after breakdown potential), the difference between the two specimens is evident demonstrated by the changes in current density, as discussed for **Figure 43**. The TO specimen shows once again a higher E_{corr}-value, but now a very similar E_{pp1}-value to that of untreated and OBDH specimens (**Table 8**). The TO specimen breaks down at a slightly higher potential than in **Figure 43**, but still much sooner than untreated and OBDH specimens. Thus, the TO specimen has the smallest passive region once again. Also, the (TO) I_{c1} and passive region current density values occur at a higher current density than in **Figure 43**, now conforming more to the untreated and OBDH specimens.

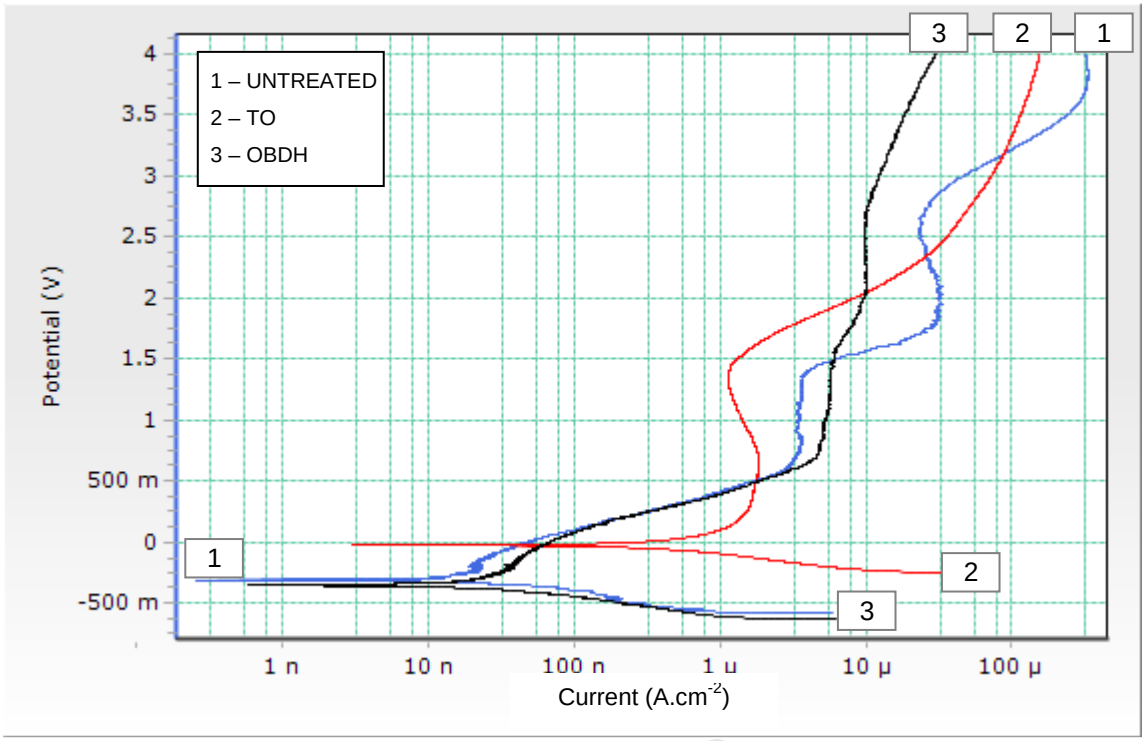

Figure 43: Comparison of potentiodynamic scans of Untreated (BLUE), Thermally Oxidised (RED) and OBDH (BLACK) Ti-6Al-V in the scan range of -0.5V below OCP.

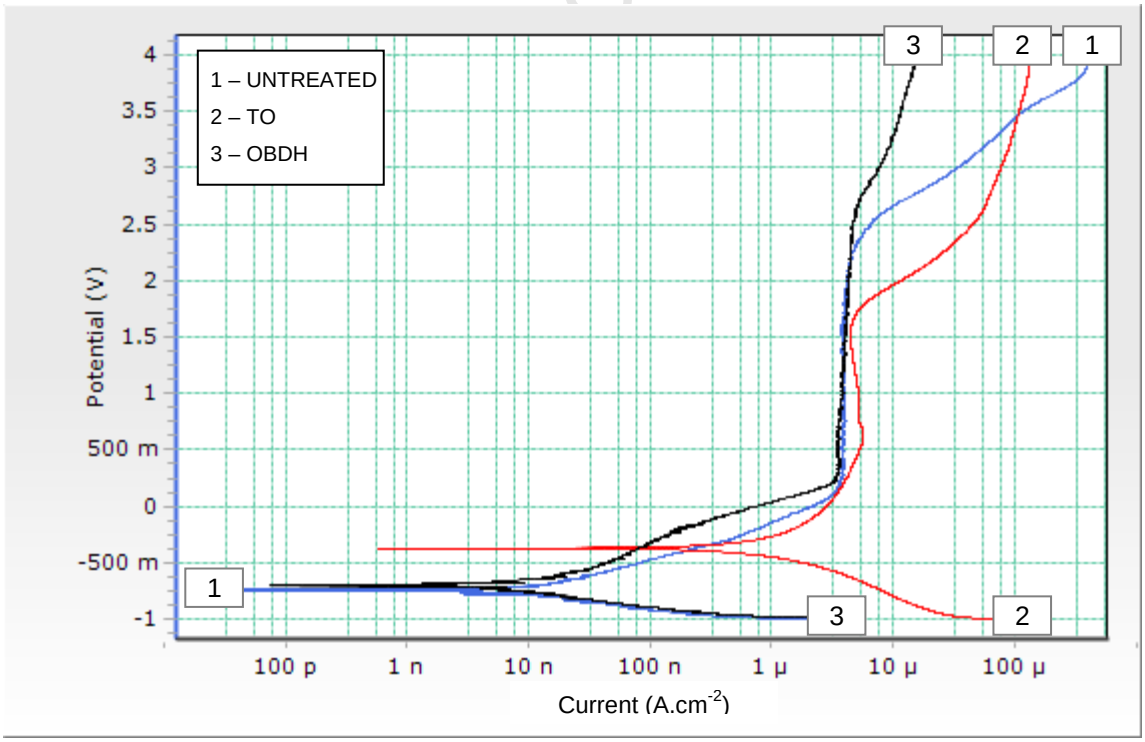

Figure 44: Comparison of potentiodynamic scans of Untreated (BLUE), Thermally Oxidised (RED) and OBDH (BLACK) Ti-6Al-V in the scan range of -1.0V_{SCE}.

Test	Scan Range (V)	OCP (V)	E_{pp1} (V)	E_{b1} (V)	E_{pp2} (V)	E_{b2} (V)	Pass Range (V)	i_{c1} (A)	i_{b1} (A)	i_{c2} (A)	i_{b2} (A)	i_{corr} (A)
UNTREATED	($-0.5_{vs\ OCP}$, 4)	-0.309	0.582	1.4	1.75	2.75	2.168	3.24E-06	3.24E-06	3.30E-05	2.25E-05	-5.43E-09
	(-1.0_{SCE}, 4)	-0.748	0.059	-	-	2.38	2.321	3.31E-06	-	-	4.55E-06	
THERMALLY OXIDISED	($-0.5_{vs\ OCP}$, 4)	-0.068	0.159	-	-	1.4	1.241	1.51E-06	-	-	1.02E-06	-1.40E-07
	(-1.0_{SCE}, 4)	-0.372	0.152	-	-	1.711	1.559	5.30E-06	-	-	3.70E-06	
OBDH	($-0.5_{vs\ OCP}$, 4)	-0.351	0.658	1.6	1.96	2.69	2.032	4.56E-06	6.40E-06	9.30E-06	9.30E-06	-3.54E-09
	(-1.0_{SCE}, 4)	-0.706	0.204	-	-	2.56	2.356	3.25E-06	-	-	4.71E-06	
$OBDH_{(unpolished)}$	($-0.5_{vs\ OCP}$, 4)	-0.335	0.397	1.22	1.45	2.52	2.123	8.10E-05	1.91E-04	1.37E-02	5.10E-04	

Table 8: Potentiodynamic Data for untreated and treated Ti-6Al-4V.

9.3 Corrosion Micrographs

Micrograph images of untreated and OBDH surfaces are presented in this section. The micrographs were captured at the end of the potentiodynamic scan and thus indicate the surface appearance after the successive active/passive transitions and final breakdown (where applicable) of the passive film.

Micrographs of TO specimens are omitted as it was not possible to display using a light optical microscope. Corrosion was not found to be evident on the oxide surface of the TO specimen.

9.3.1 Untreated Ti-6Al-4V

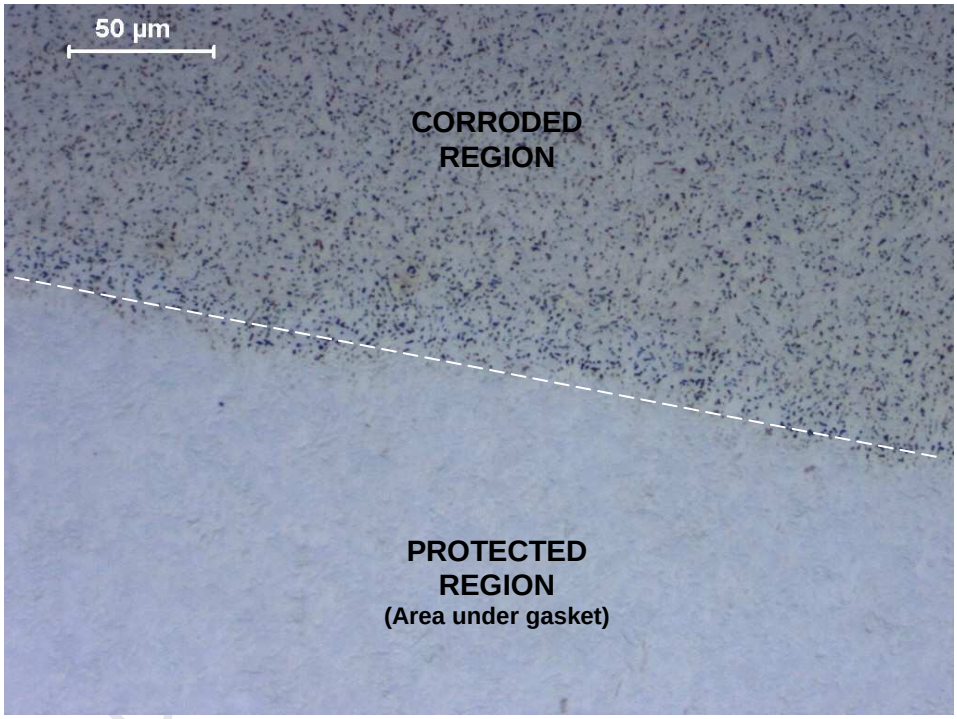

Figure 45: Micrograph showing the contrast between the corroded surface and the non exposed protected region of an untreated Ti-6Al-4V specimen.

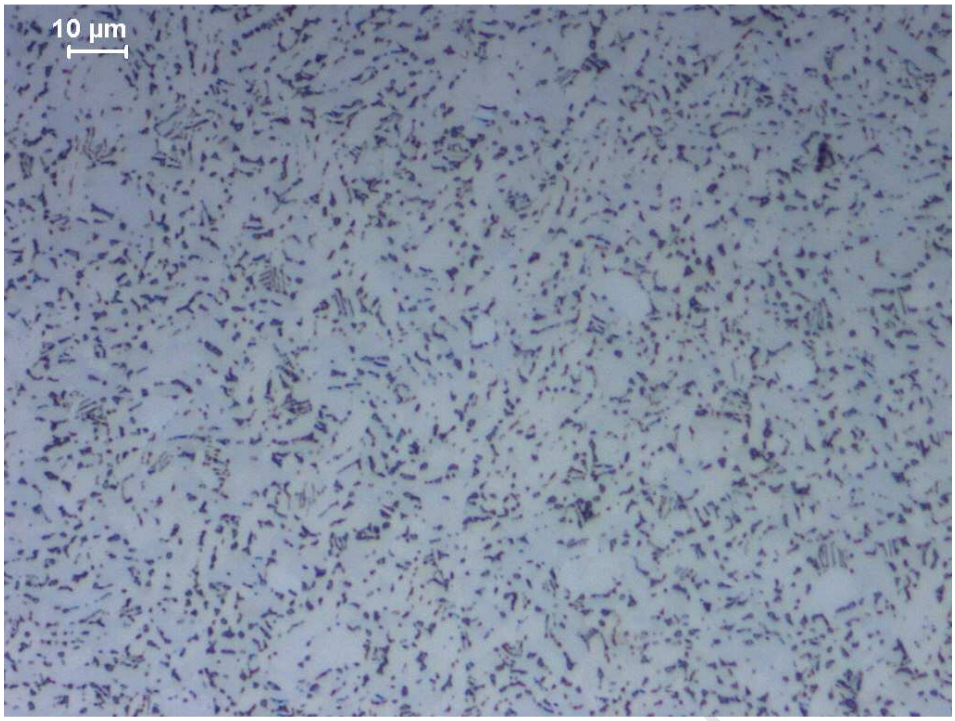

Figure 46: Micrograph showing an increased magnification view of general corrosion occurring on the exposed Untreated Ti-6Al-4V surface.

9.3.2 OBDH Ti-6Al-4V

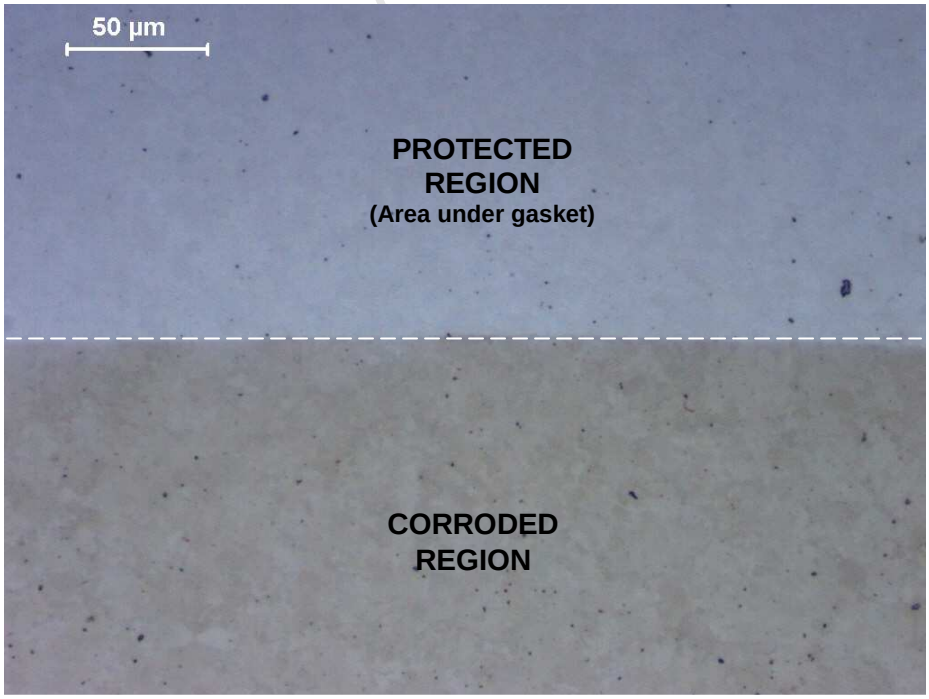

Figure 47: Micrograph showing the contrast between the corroded surface and the unaffected area of an OBDH test sample

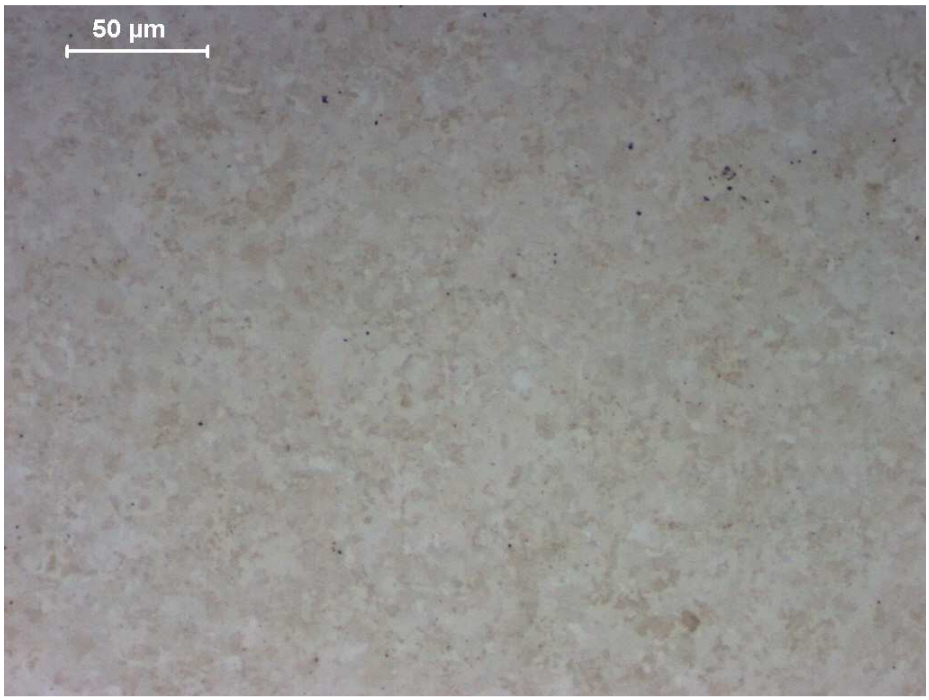

Figure 48: Micrograph showing an increased magnification view of general corrosion occurring on the exposed OBDH Ti-6Al-4V surface.

9.4 Corrosion Rates

The corrosion rates for untreated and treated Ti-6Al-4V specimens were calculated through Tafel Plots. **Table 9** summarizes the I_{corr} values used in the calculation of the final corrosion rate of each specimen.

SPECIMEN	i_{corr} (A)	Corr Rate (MPY)
UNTREATED	-9.55E-09	4.16E-03
TO	-1.40E-07	6.48E-02
OBDH	-6.15E-09	2.70E-04

Table 9: Corrosion Rates for untreated and treated Ti-6Al-4V.

10 RESULTS: AC ANALYSIS (EIS)

The following section displays the electrochemical impedance behaviour of untreated and treated (i.e. TO and OBDH) Ti-6Al-4V specimens. Impedance data are represented by Nquist, Bode Magnitude and Bode phase plots. The data are divided into three different sections for each specimen, namely:

i) OCP Impedance Plots
ii) Potential Variation Impedance Plots (see also APPENDIX)
iii) Overlays of Potential Variation Impedance Plots

The OCP impedance plots display Nquist, Bode Magnitude and Bode Phase data at the open circuit potential without prior polarization. The Potential Variation Impedance Plots are a result of polarizing the specimens (to offset potentials of -0.5, 0.0, 0.5, 1.0, 1.5, 2.0, 2.5 and $3.0V_{SCE}$) and display the resulting data in the form of Nquist and Bode plots. These individual plots at each specific potential can be viewed in the Appendix. The focal importance of displaying these plots individually is to represent the fit between the theoretical model and experimental data.

The actual behaviour due to polarization can be better distinguished in the third section, where the Nquist plots are overlayed on the same axis for potentials in the range -0.5 – $3.0V_{SCE}$, including measurement at OCP. This is followed by an overlay of the Bode Phase plot at the same potentials.

The resistance and capacitance values for untreated and treated specimens are noted in **Table 10** of Section 10.5. Section 10.6 demonstrates trends in data with potential variance, giving a more explicable view of the behaviour of each circuit element; thereby providing insight into the corrosion behaviour of untreated and treated specimens.

10.1 Equivalent Circuit Model

The circuit displayed in **Figure 49** was established as the proposed equivalent circuit modelled for untreated and treated Ti-6Al-4V, defined by **Figure 20**. However, the capacitance is replaced by constant phase elements denoted by Q_p and Q_b. The impedance of the Q is defined by:

$$Z_Q = \frac{1}{(jw)^n C}$$

Where j = $\sqrt{-1}$, ω = 2πf, C is a constant representing true capacitance and the exponent 'n' of the constant phase element is related to non-equilibrium current distribution (Hsu et al. 2004).

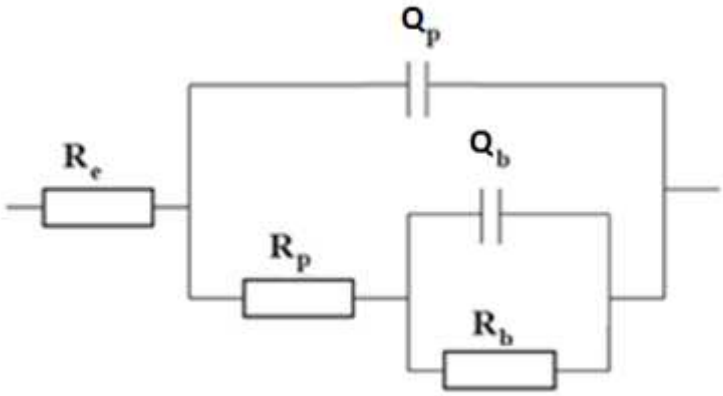

Figure 49: Equivalent Circuit modelled for untreated and treated Ti-6Al-4V.

10.2 Untreated Ti-6Al-4V

10.2.1 OCP impedance plots

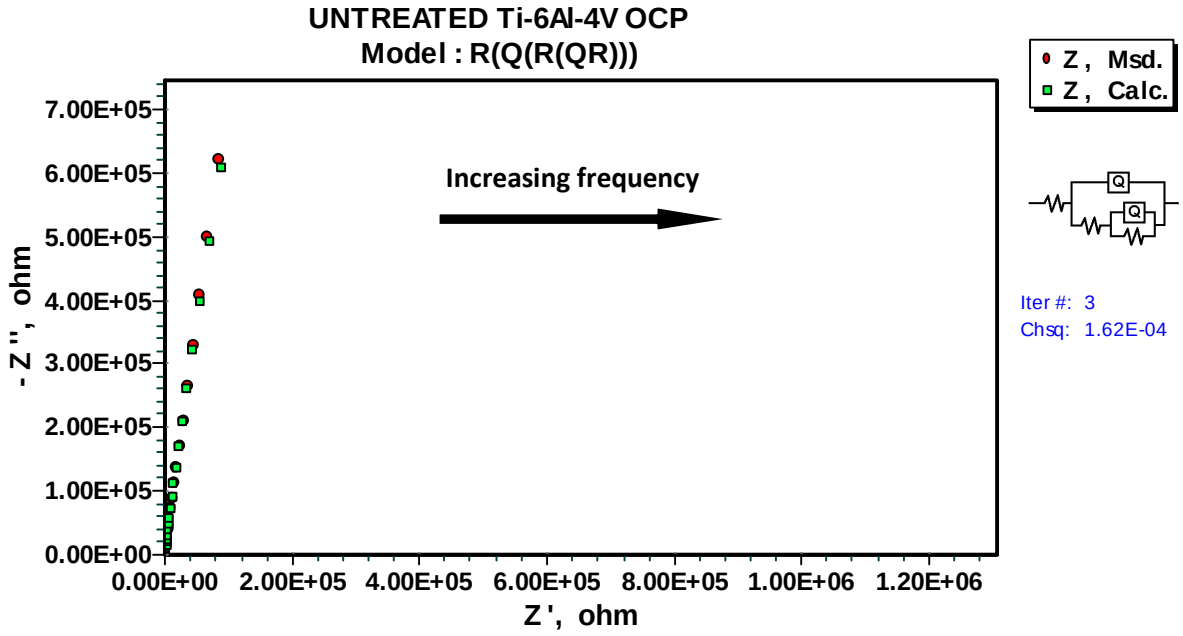

Figure 50: Nquist plot for untreated Ti-6Al-4V at OCP.

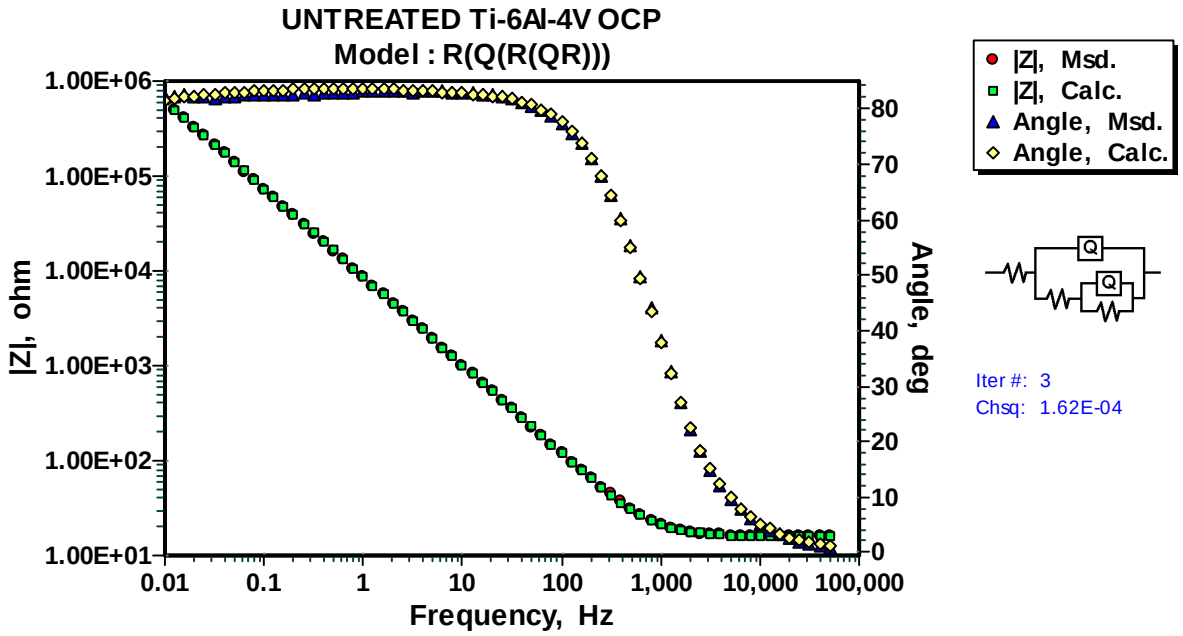

Figure 51: Bode Magnitude |Z| and Bode Phase (Angle) plots for untreated Ti-6Al-4V at OCP.

Figure 50 displays the Nquist plot and **Figure 51** the Bode plots for untreated Ti-6Al-4V specimens at OCP. At OCP the oxide is undamaged therefore the Nquist plot lacks significant data until the development of resistive elements. The behaviour of Nquist and Bode plots for the untreated metal is better characterized in Section 10.6.1.

The theoretical model proposed in **Figure 49** for a metal with an oxide layer, demonstrates an excellent fit to the experimental data in **Figure 50** and **Figure 51**. The chi-square value in the region of 10^{-3} indicates excellent agreement between experimental and theoretical values as well.

10.2.2 Overlays of Potential Variation Impedance Plots

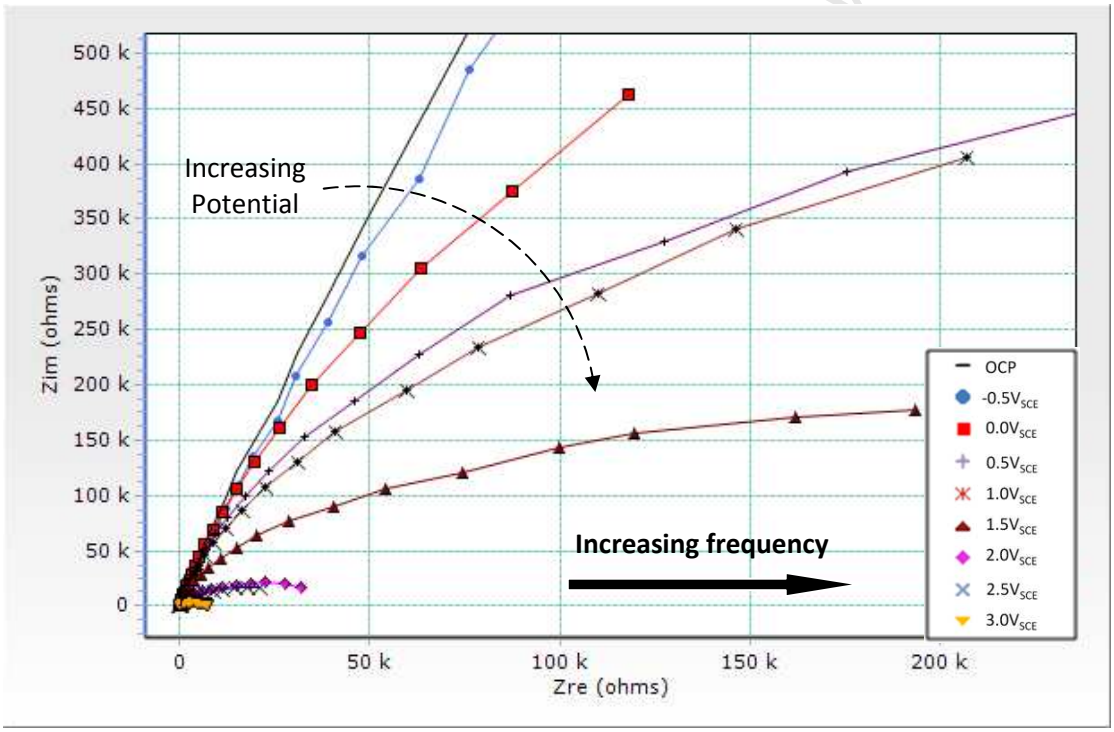

Figure 52: Overlays of OCP and potential varied Nquist plots from -0.5V – 3.0V_{SCE} for untreated Ti-6Al-4V.

Figure 52 presents an overlay of Nquist plots for untreated Ti-6Al-4V specimens, polarized at different offset potentials from -0.5 – 3.0V_{SCE}. The impedance spectra demonstrates an almost capacitive behaviour, with a decrease in the total impedance with increasing polarization. This is made obvious by the depression of the capacitive loop (drop in Z_{im} maxima), displaying a decrease in diameter as the potential is increased. Also, the formation of a more apparent semicircle loop is visible at high

potentials (2.0 – 3.0V_{SCE}), whereas at lower potentials ~ -0.5V_{SCE} a slightly distorted semicircle is initiating.

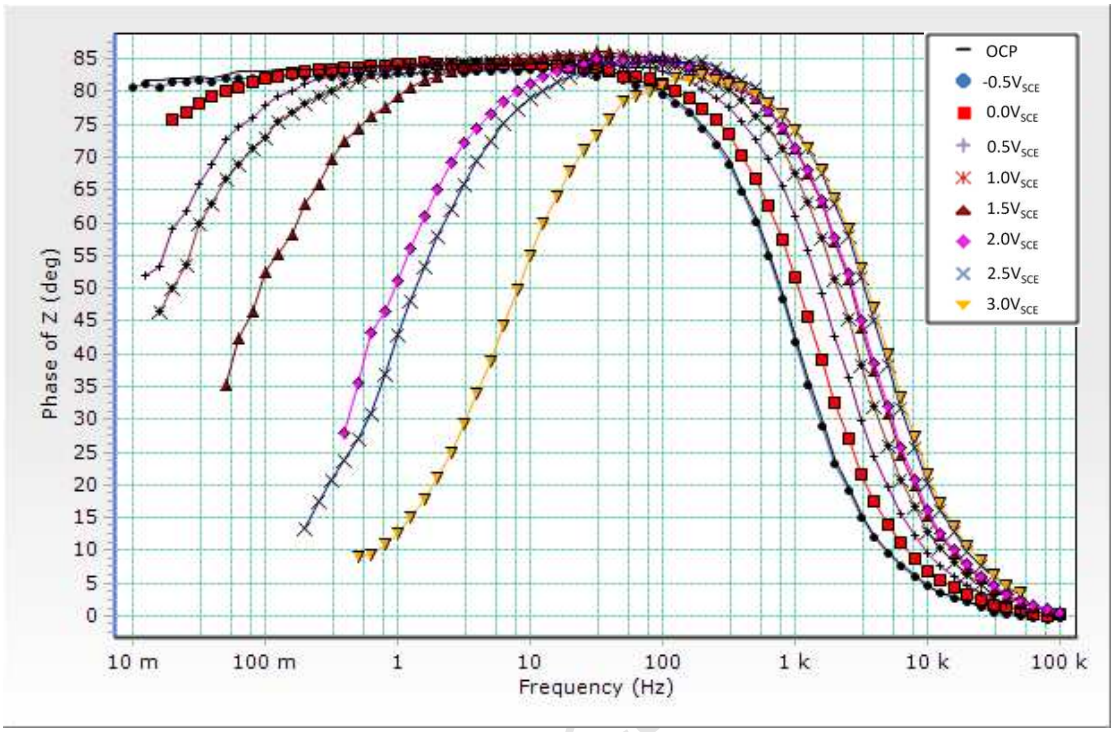

Figure 53: Overlays of OCP and potential varied Bode phase plots from -0.5V – 3.0V_{SCE} for untreated Ti-6Al-4V.

The Bode phase plots of untreated Ti-6Al-4V specimens are illustrated in **Figure 53**, where an overlay of Phase plots at different offset potentials from -0.5 – 3.0V_{SCE} is demonstrated. The test initiates in the high frequency region, where the phase plots (at all polarized potentials) display a phase angle near to 0° in response to the solution resistance R_s. The plot demonstrates a near capacitive response, where the phase angle increases as the frequency decreases, reaching a plateau close to 85° at frequencies close to 100Hz. A certain degree of deviation from ideal capacitive behaviour can be observed, which is common for TiO_2 films. However, the frequency range over which this plateau is sustained is decreased as the potential increases, and for potentials above 2.0V_{SCE} a distinct bell shaped curve is formed. In the low frequency region the phase angle decreases significantly with increasing polarization after 0V_{SCE}.

10.3 Thermally Oxidised Ti-6Al-4V

10.3.1 OCP impedance plots

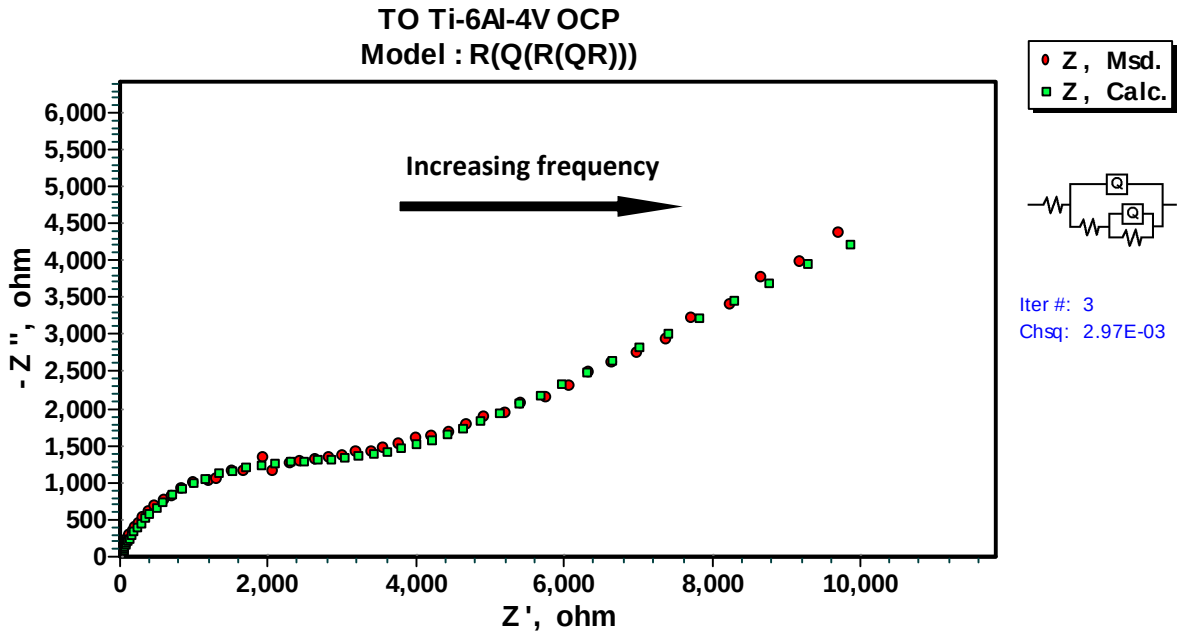

Figure 54: Nquist plot for TO Ti-6Al-4V at OCP.

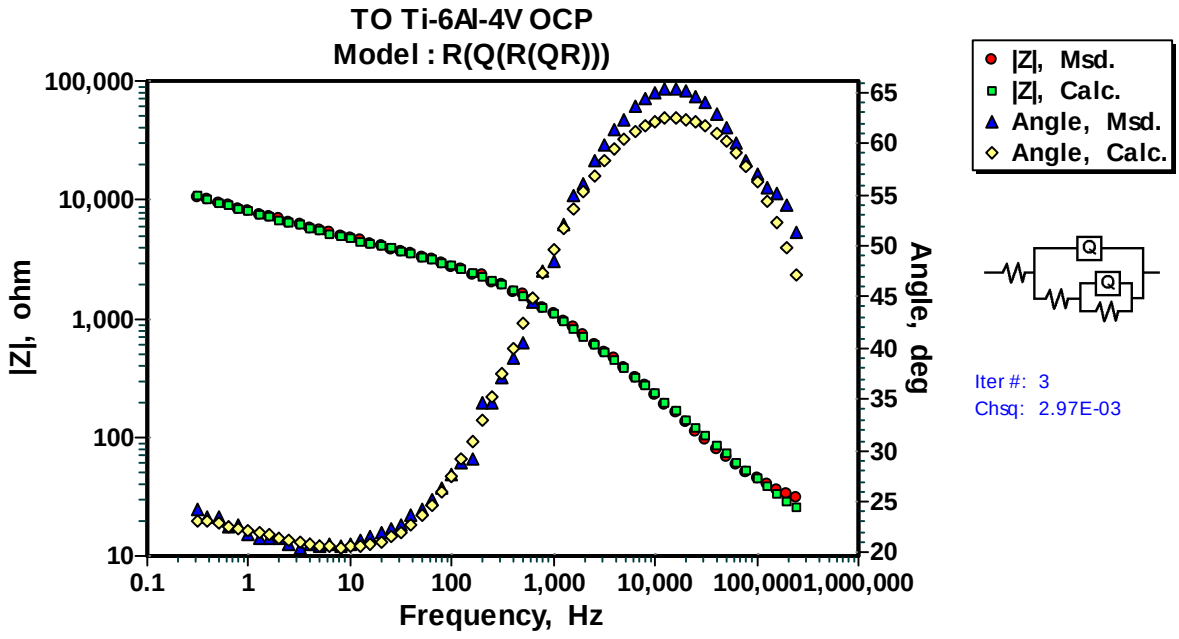

Figure 55: Bode Magnitude |Z| and Bode Phase (Angle) plots for TO Ti-6Al-4V at OCP.

The impedance behaviour of thermally oxidised Ti-6Al-4V specimens at OCP are presented in the Nquist plot (**Figure 54**) and the Bode plots (**Figure 55**), where an excellent fit of the experimental data to the theoretical model is once again demonstrated, with chi-square value in the region of 10^{-3}.

The impedance behaviour of the TO specimen can be easily presented and described by overlaying the plots from potentials -0.5V – 3.0V_{SCE} and at OCP (on the same axis) displayed in Section 10.6.2, where significant differences can be distinguished.

10.3.2 Overlays of Potential Variation Impedance Plots

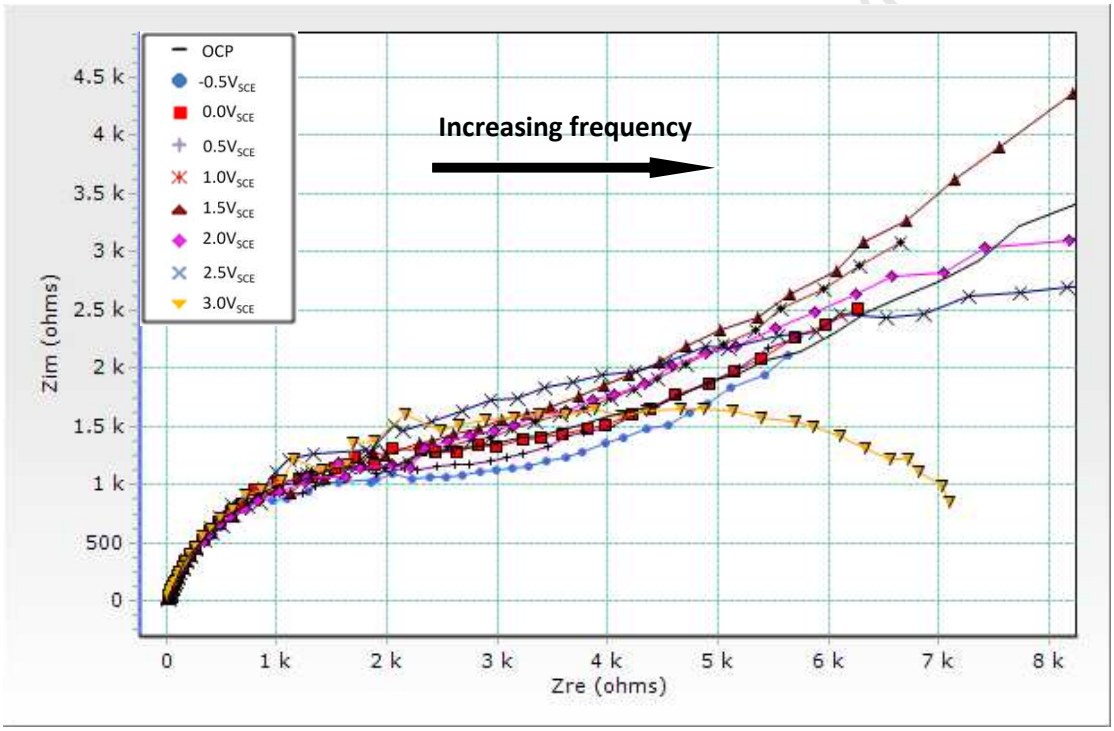

Figure 56: Overlays of OCP and potential varied Nquist plots from -0.5V – 3.0V_{SCE} for TO Ti-6Al-4V.

Figure 56 presents an overlay of Nquist plots for Thermally Oxidized Ti-6Al-4V, polarized at different offset potentials from -0.5 – 3.0V_{SCE}, and at OCP. The impedance spectra show an almost capacitive behaviour, whereby as the potential increases no significant changes occur in the Nquist loop. However, at 3.0V_{SCE} a more apparent semicircle forms and a depression of the capacitive loop is now evident.

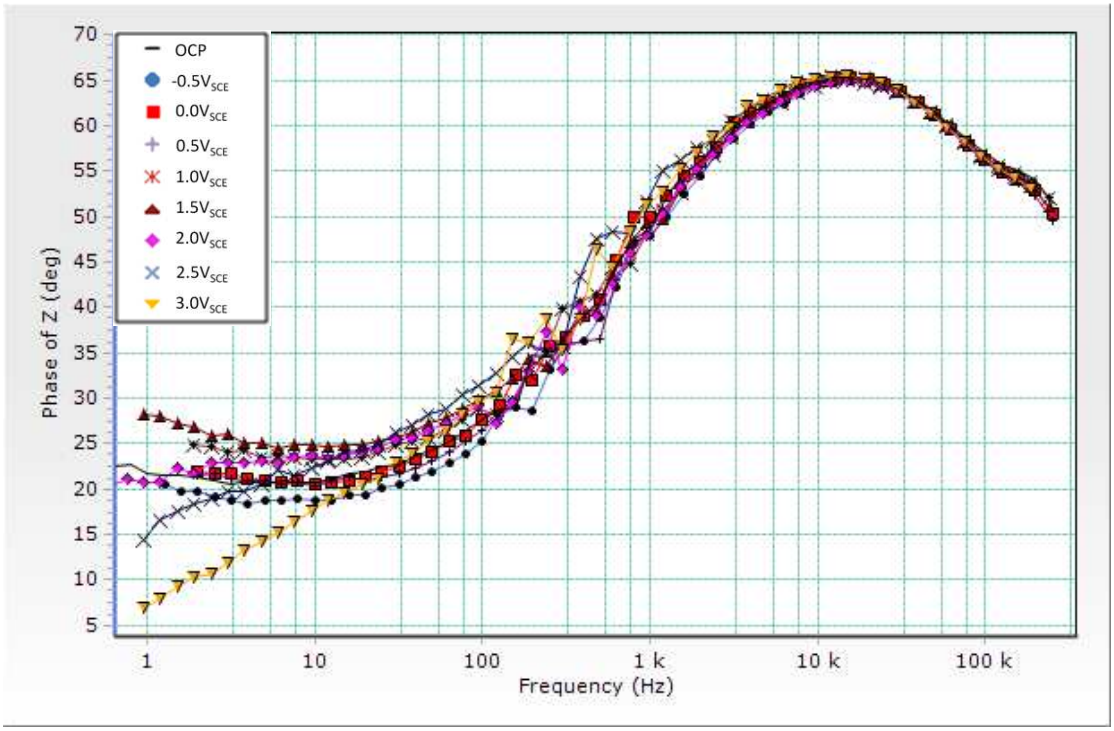

Figure 57: Overlays of OCP and potential varied Bode phase plots from -0.5V – 3.0V$_{SCE}$ for TO Ti-6Al-4V.

An overlay of Bode phase plots polarized at different offset potentials from -0.5 – 3.0V$_{SCE}$ including OCP, is displayed in **Figure 57**. At the start of the test, in the high frequency region, there is no deviation with polarization and the phase angle remains at ~ 50°.The phase plots demonstrate a near capacit ive response, where the phase angle increases as the frequency decreases reaching a plateau around 65°. However, the frequency range at which this phase angle is sustained is small and the same for all potentials (unlike for the untreated and OBDH specimens). Thus, the plots show no significant change with polarization from -0.5 – 2.0V$_{SCE}$. However, when polarized from 2.5 – 3.0V$_{SCE}$ there is a noticeable drop in phase angle in the lower frequency region.

10.4 Oxygen Boost Diffusion Hardened (OBDH) Ti-6Al-4V

10.4.1 OCP impedance plots

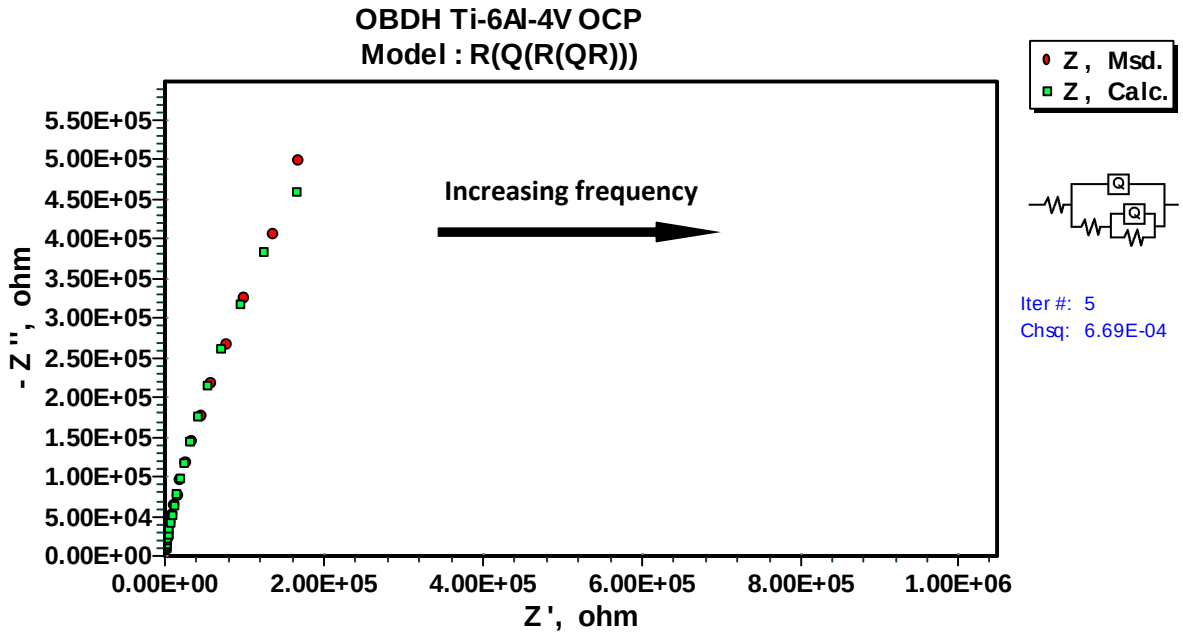

Figure 58: Nquist plot for OBDH Ti-6Al-4V at OCP.

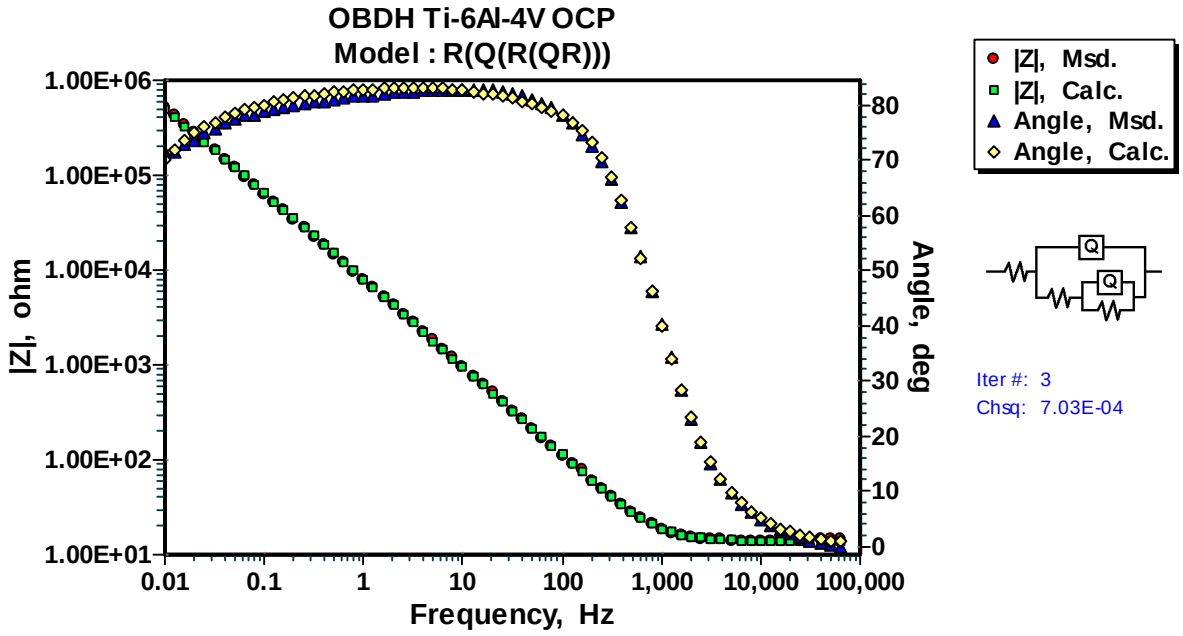

Figure 59: Bode Magnitude |Z| and Bode Phase (Angle) plots for OBDH Ti-6Al-4V at OCP.

As for untreated and TO specimens the experimental data at OCP displays an excellent fit to the theoretical model in the Nquist plot (**Figure 58**) and Bode plot (**Figure 59**), with chi-square values in the region of 10^{-4}. These plots are represented in Section 10.6.3 where the overlays better display significant differences in impedance data due to polarization of the metal.

10.4.2 Overlays of Potential Variation Impedance Plots

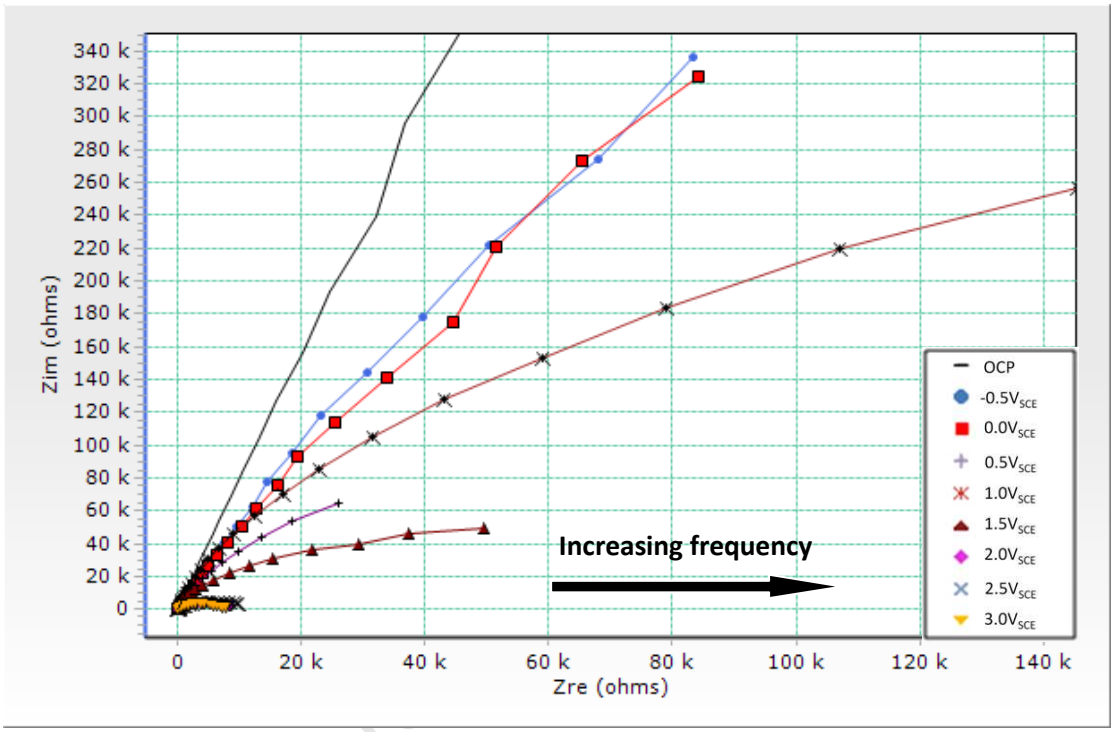

Figure 60: Overlays of OCP and potential varied Nquist plots from -0.5V – 3.0V_{SCE} for OBDH Ti-6Al-4V.

The overlay of Nquist plots for OBDH Ti-6Al-4V specimens is presented in **Figure 60**, where the specimen is polarized at different offset potentials from -0.5 – 3.0V_{SCE}. Similar to that of untreated Ti-6Al-4V, the impedance spectra show an almost capacitive behaviour, where the total impedance decreases as the polarization potential increases. The decrease in impedance values is made apparent by the depression of the capacitive loop (drop in Z_{im} maxima) and the decrease in diameter of the semicircles. At offset potentials > 2.0V_{SCE} more visible semicircles are shown, whereas at potentials < 2.0V_{SCE} only the initiation of a semicircle is evident.

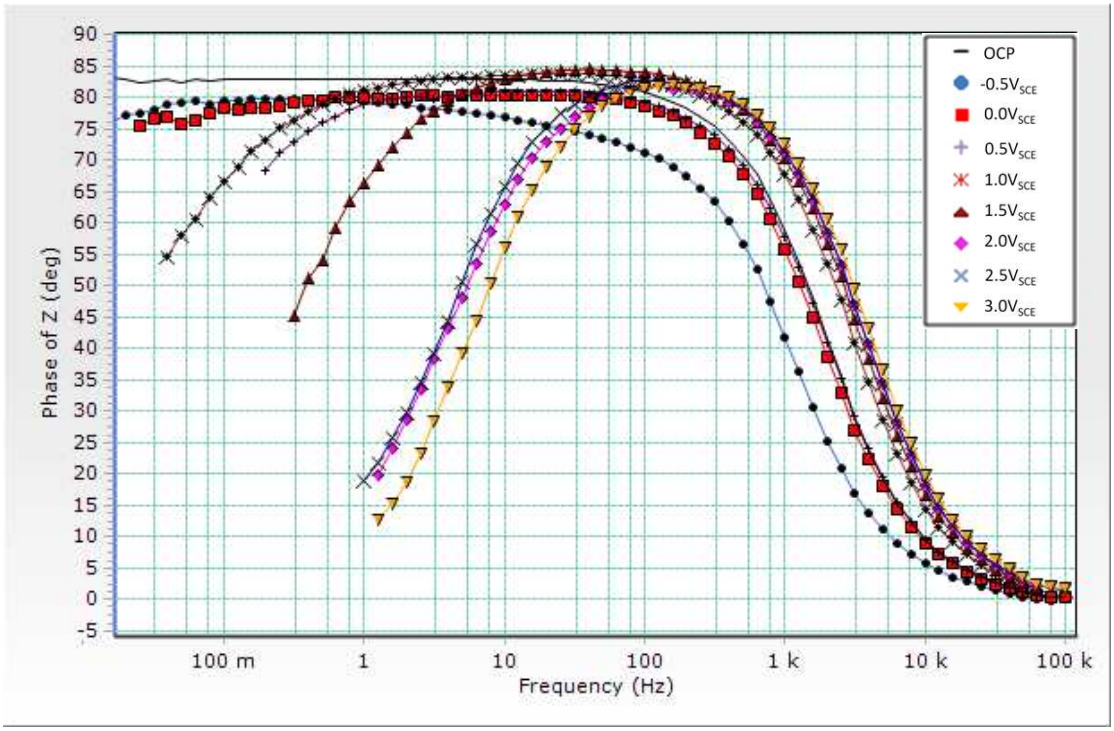

Figure 61: Overlays of OCP and potential varied Bode phase plots from -0.5V – 3.0V_{SCE} for OBDH Ti-6Al-4V.

The overlay of the Bode Phase Plots for the OBDH treated Ti-6Al-4V specimens, polarized at different offset potentials from -0.5 – 3.0V_{SCE} are presented in **Figure 61**. The phase plots for OBDH specimens are very similar to that of the untreated metal. However, the bell shape curves at potentials 2.0 – 3.0V_{SCE} are all very similar and the phase angle does not decrease any further in the low frequency region.

10.5 Evaluation of Impedance Data

The impedance data at OCP, and each offset potential from -0.5V – 3.0V_{SCE} are tabulated in **Table 10**. Trends in the data are more easily distinguished in Section 10.6. The labels for each column are defined as follows:

R_s = Solution resistance
Q_1 = Porous layer CPE
n_1 = Exponent of Q_1
R_1 = Porous layer resistance
Q_2 = Barrier layer CPE
n_2 = Exponent of Q_2
R_2 = Barrier layer resistance

Potential	$R_s(\Omega.cm^2)$	$Q_1(F.cm^{-2})$	n_1	$R_1(\Omega.cm^2)$	$Q_2(F.cm^{-2})$	n_2	$R_2(\Omega.cm^2)$
UNTREATED							
OCP	14.43	1.23E-05	1.00	1372	6.95E-06	0.80	3.50E+06
-0.5_{SCE}	14.43	1.26E-05	1.00	1375	8.30E-06	0.79	2.08E+07
0.0_{SCE}	14.43	1.19E-05	1.00	1300	5.44E-06	0.83	4.32E+06
0.5_{SCE}	14.43	8.63E-06	1.00	1547	2.97E-06	0.82	1.78E+06
1.0_{SCE}	14.43	5.71E-06	1.00	1705	2.55E-06	0.80	6.90E+05
1.5_{SCE}	14.43	5.00E-06	1.00	2605	2.13E-06	0.78	2.84E+05
2.0_{SCE}	14.43	3.85E-06	1.00	2629	1.99E-06	0.81	4.43E+04
2.5_{SCE}	14.43	3.30E-06	1.00	1681	2.04E-06	0.75	3.31E+04
3.0_{SCE}	14.43	3.06E-06	1.00	1225	5.61E-06	0.67	6.42E+03
STD DEV	0.2	5.51E-07	0.00	134.34	1.89E-07	0.03	3.90E+05
TO							
OCP	10.82	8.69E-07	0.76	2518	7.21E-05	0.35	5.95E+04
-0.5_{SCE}	10.82	8.80E-07	0.76	2326	9.16E-05	0.38	1.96E+04
0.0_{SCE}	10.82	9.23E-07	0.76	2819	6.14E-05	0.44	1.95E+04
0.5_{SCE}	10.82	9.13E-07	0.76	2382	7.21E-05	0.42	2.74E+04
1.0_{SCE}	10.82	1.04E-06	0.76	2449	6.32E-05	0.45	3.48E+04
1.5_{SCE}	10.82	9.01E-07	0.76	2452	4.22E-05	0.45	2.22E+04
2.0_{SCE}	10.82	8.97E-07	0.76	2419	4.31E-05	0.49	2.05E+04
2.5_{SCE}	10.82	9.23E-07	0.76	2863	2.56E-05	0.53	9.99E+03
3.0_{SCE}	10.82	8.75E-07	0.76	2863	1.57E-05	0.59	5.48E+03
STD DEV	0.92	2.18E-08	0.0007	59.62	2.23E-06	0.04	8.13E+02
OBDH							
OCP	14.82	1.23E-05	1.00	1571	6.97E-06	0.79	3.60E+06
-0.5_{SCE}	14.82	1.35E-05	1.00	1213	6.81E-06	0.81	1.60E+07
0.0_{SCE}	14.82	1.04E-05	1.00	1367	5.42E-06	0.80	6.21E+06
0.5_{SCE}	14.82	7.14E-06	1.00	1680	3.13E-06	0.83	4.09E+06
1.0_{SCE}	14.82	4.65E-06	1.00	1121	2.83E-06	0.80	1.30E+06
1.5_{SCE}	14.82	3.85E-06	1.00	1280	2.23E-06	0.76	2.08E+05
2.0_{SCE}	14.82	3.36E-06	1.00	1362	2.40E-06	0.77	3.20E+05
2.5_{SCE}	14.82	2.83E-06	1.00	1417	1.61E-06	0.76	1.57E+05
3.0_{SCE}	14.82	2.71E-06	1.00	1291	1.48E-06	0.76	5.73E+04
STD DEV	0.39	1.61E-07	0.00	96.19	2.69E-07	0.03	1.37E+06

Table 10: Tabulated EIS data at Ecorr and offset potentials versus reference (0.0V).

10.6 E.I.S Trends with Potential Variation

The various parameters obtained from the EIS tests (see **Table 10**) are superimposed on the potentiodynamic curves for the respective untreated and surface treated conditions. Unlike the potentiodynamic curves, the EIS parameters are plotted as discrete points at the respective polarization potentials. To reduce any modifications of the surface through cathodic charging, testing closer to OCP has been the preferred mode of testing. Therefore, potentiodynamic tests initiated at -0.5V below OCP have been used in this section as opposed to the alternative potentiodynamic scans which were initiated at -1.0V_{SCE}.

10.6.1 Untreated Ti-6Al-4V

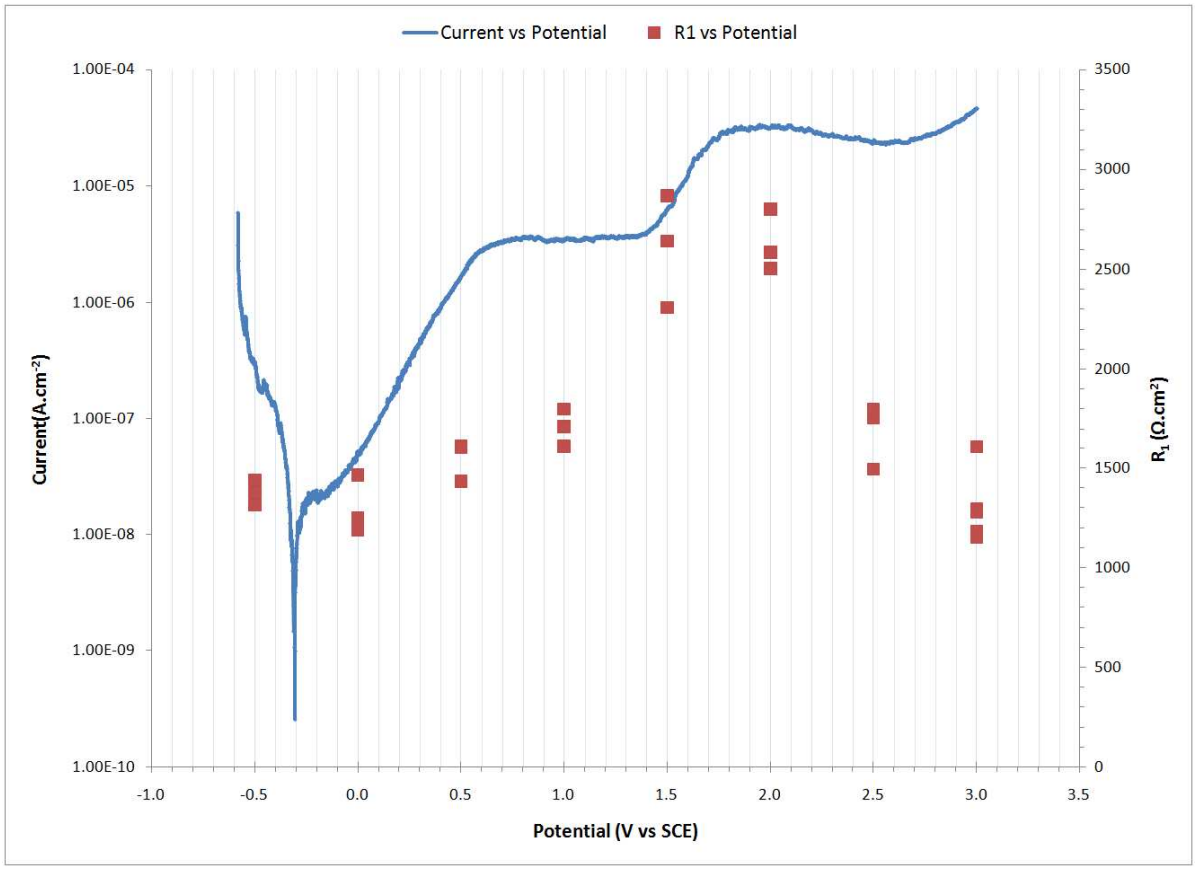

Figure 62: Potentiodynamic curve of untreated Ti-6Al-4V (left axis) overlayed with the porous layer resistance, R_1 (right axis), as a function of applied potential for untreated Ti-6Al-4V.

Figure 62 presents an overlay of a potentiodynamic scan and the porous layer resistance (R_1) of an untreated Ti-6Al-4V specimen. Initially from -0.5V_{SCE} (with increasing potential) the potentiodynamic scan shows a decrease in current density until E_{corr} is reached. The current density then increases until ~0.6V_{SCE}, whereas the

accompanying R_1 curve changes only slightly from -0.5 – 0.0V_{SCE}. The porous layer resistance (R_1) then gradually starts to increase, sustaining a constant positive gradient over the region where the potentiodynamic scan starts to plateau. At 1.0V_{SCE} a considerable increase in R_1 occurs, which coincides with the passive layer formation of the potentiodynamic scan. From 1.5 – 2.0V_{SCE}, the potentiodynamic scan displays an increase in the current density until repassivation, where the curve plateaus once again. R_1 increases in this potential range, followed by a significant decrease from potentials 2.0 – 2.5V_{SCE}. However, the potentiodynamic scan remains in the passive region between 2.0 – 2.5V_{SCE}, breaking down after 2.5V_{SCE}. This breakdown, and hence increase in current density, now coincides with the decreasing R_1 at these potentials.

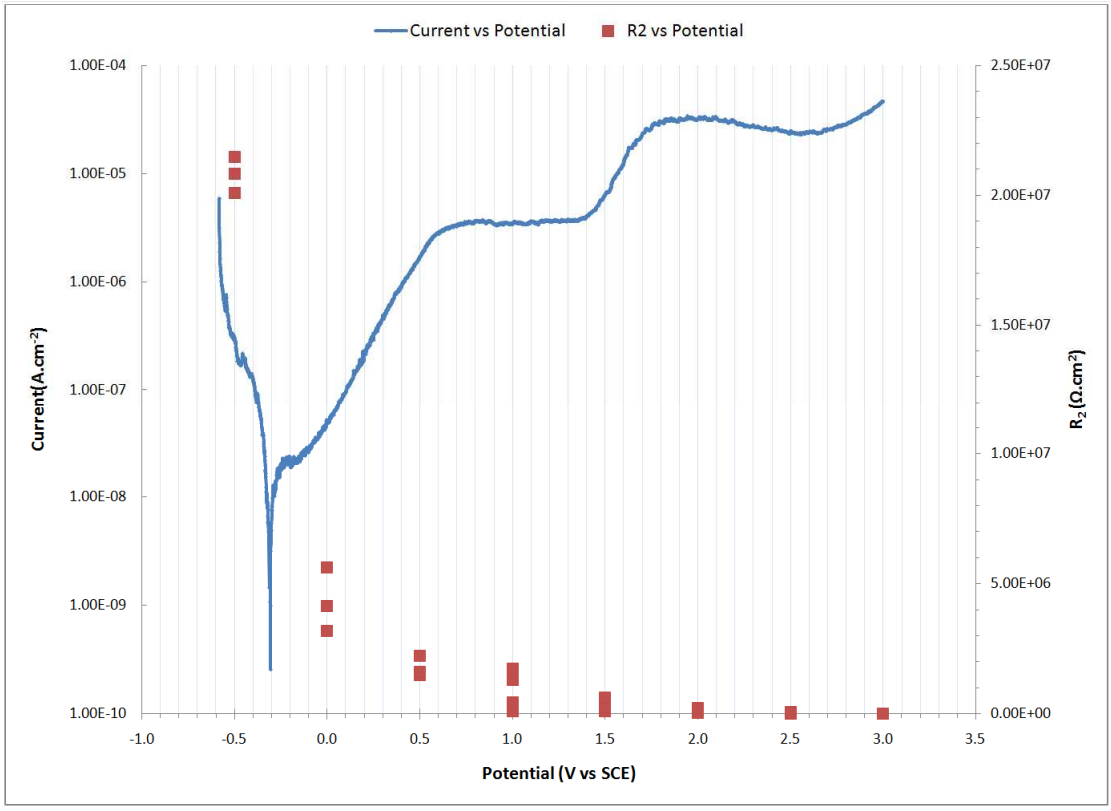

Figure 63: Potentiodynamic curve of untreated Ti-6Al-4V (left axis) overlayed with the barrier layer resistance, R_2 (right axis), as a function of applied potential for untreated Ti-6Al-4V.

Figure 63 displays the barrier layer resistance versus potential overlayed with the respective potentiodynamic scan. Unlike the variance experienced by the porous layer resistance (R_1) in **Figure 62**, the barrier layer resistance (R_2) drops rapidly at the start of the potentiodynamic scan from the cathodic region (**Figure 63**). Although the R_2-value continues to drop as the potential increases, the rate of change decreases significantly. R_2 undergoes minimum changes, if any, and remains almost

constant when polarized from 2.0 – 3.0V_{SCE} (see **Table 10**), whereas the potentiodynamic curve remains passive and then undergoes an increase in current density after 2.5V_{SCE}.

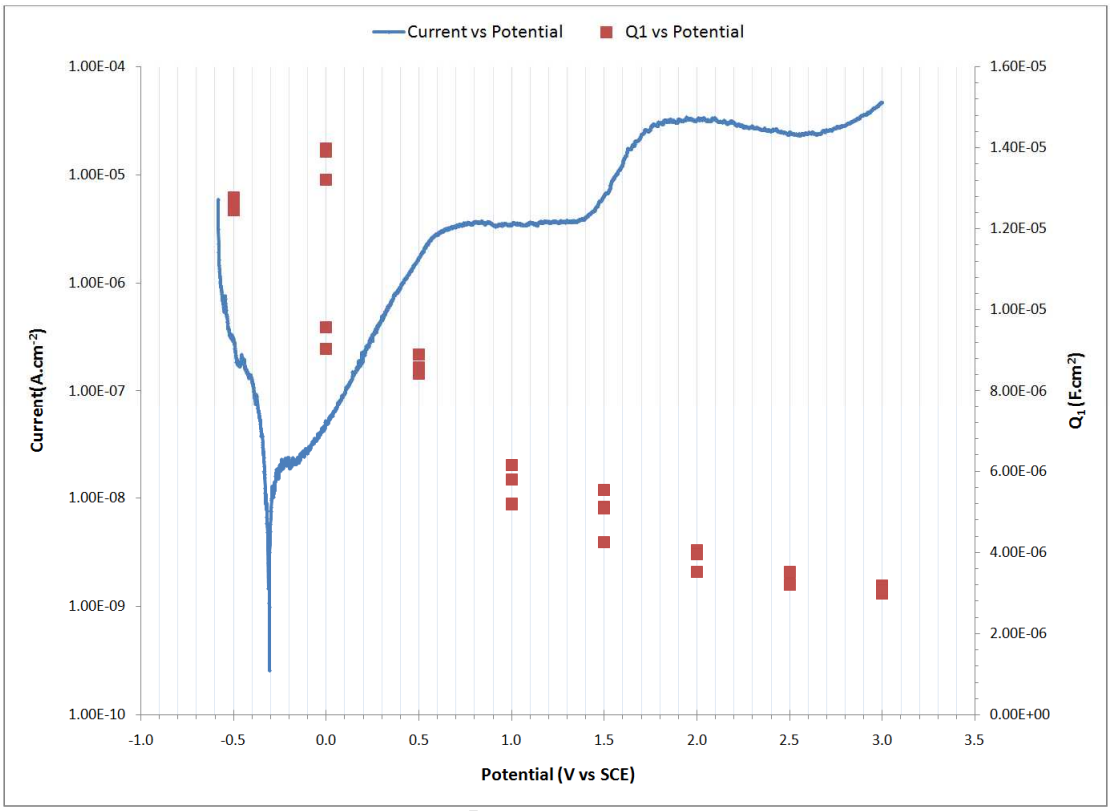

Figure 64: Potentiodynamic curve of untreated Ti-6Al-4V (left axis) overlayed with the porous layer capacitance, Q_1 (right axis), as a function of applied potential for untreated Ti-6Al-4V.

Initially the porous layer capacitance (**Figure 64**) is high and fluctuates in the range -0.5 – 0.0V_{SCE}. As the metal passivates (~0.6V_{SCE}), an accompanying change in the Q_1 behaviour is visible, whereby Q_1 continues to decrease as the potential increases. However, the rate of change decreases considerably. The change in rate of Q_1 coincides with the increase in current density of the potentiodynamic scan. In the range of 2.0 – 3.0V_{SCE} the graph seems to reach a very low rate of decrease (see **Table 10**) with Q_1 nearing stabilization.

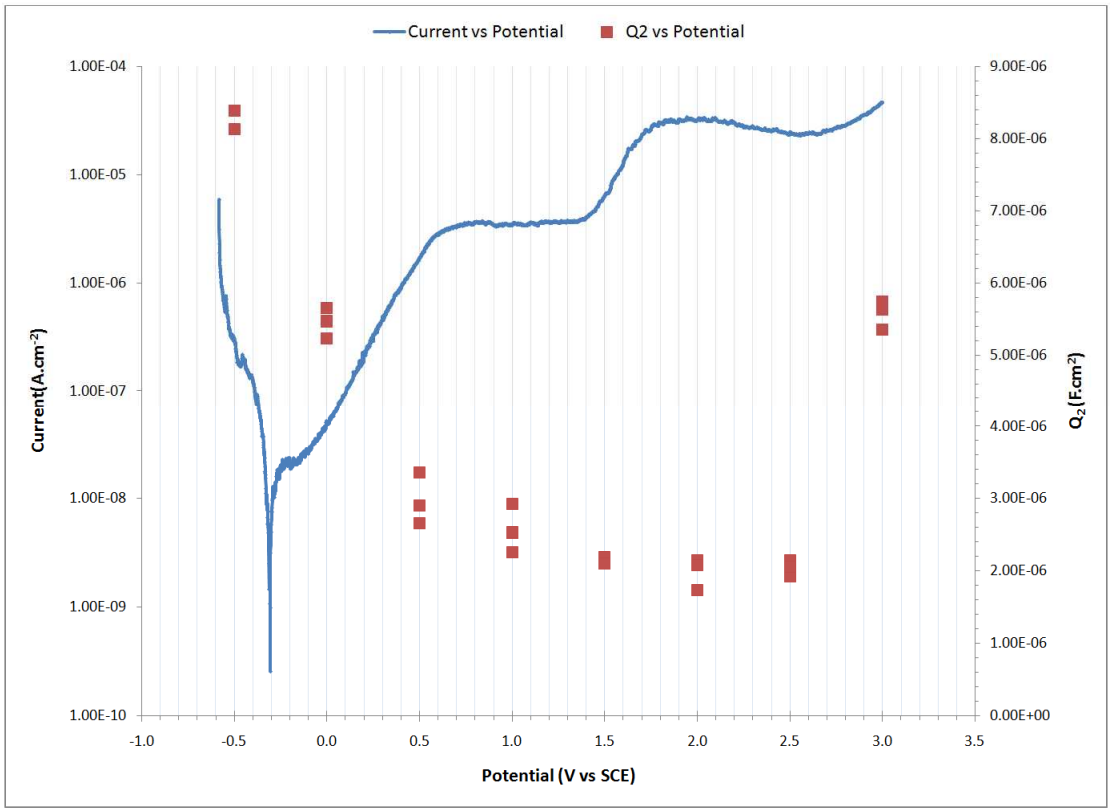

Figure 65: Potentiodynamic curve of untreated Ti-6Al-4V (left axis) overlayed with the barrier layer capacitance, Q_2 (right axis), as a function of applied potential for untreated Ti-6Al-4V.

Figure 65 displays the effect of polarization on the behaviour of the barrier layer capacitance (Q_2). As for Q_1, the behaviour of the double layer capacitance is initially high and decreases at a constant rate from potentials -0.5 – $0.5V_{SCE}$, until which time the rate of change decreases significantly coinciding with changes in current density. The behaviour remains similar to Q_1 until the 2.5 – $3.0V_{SCE}$ range, where the capacitance undergoes a steep increase in value coinciding with the increase in current density of the potentiodynamic scan.

10.6.2 Thermally Oxidised (TO) Ti-6Al-4V

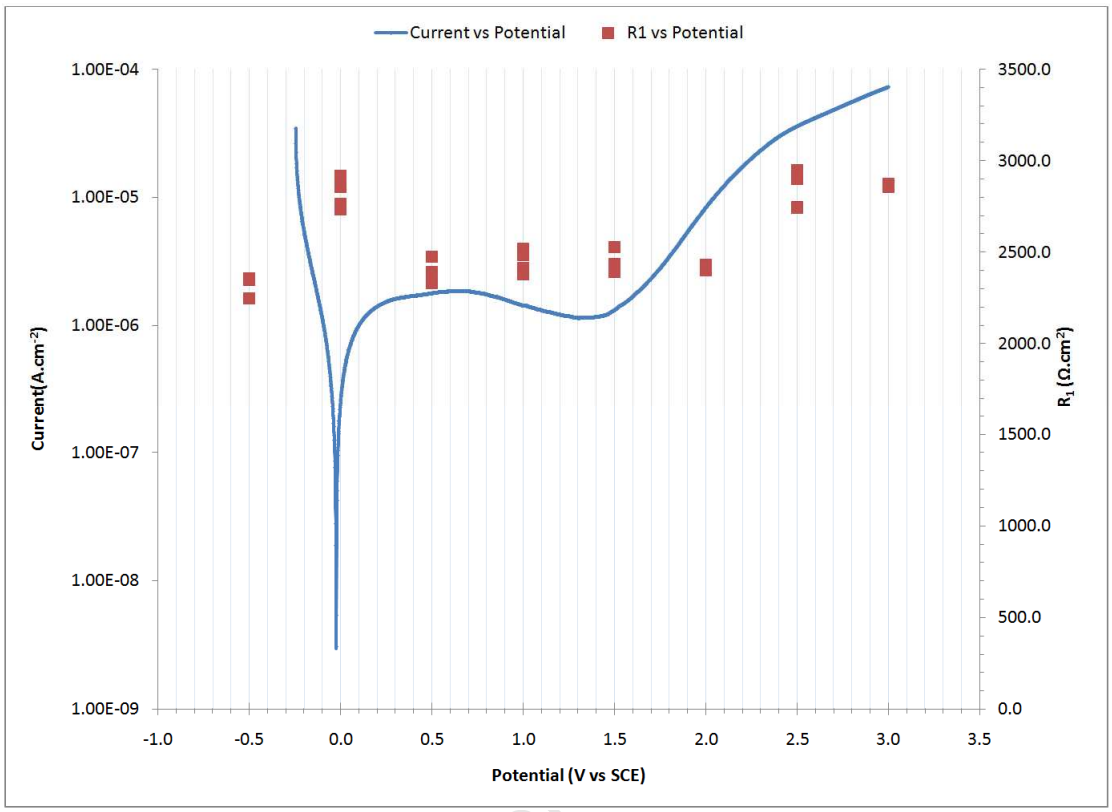

Figure 66: Potentiodynamic curve of TO Ti-6Al-4V (left axis) overlayed with the porous layer resistance, R_1 (right axis), as a function of applied potential for TO Ti-6Al-4V.

Figure 66 illustrates how polarization affects the porous layer resistance (R_1) of thermally oxidized Ti-6Al-4V. In the -0.5 – $0.0V_{SCE}$ polarization range, the potentiodynamic scan reaches its E_{corr} value, whereas the accompanying R_1 curve displays a slight increase followed by a decrease (between 0.0 – $0.5V_{SCE}$) to values around the initial R_1 values. This decrease coincides with the passivation of the TO specimen in the potentiodynamic scan, where the current density remains about constant until $1.5V_{SCE}$. The R_1 curve remains constant with minimum deviations until $2.0V_{SCE}$, where the resistance starts to increase slightly. This increase coincides with the increase in current density of the potentiodynamic scan.

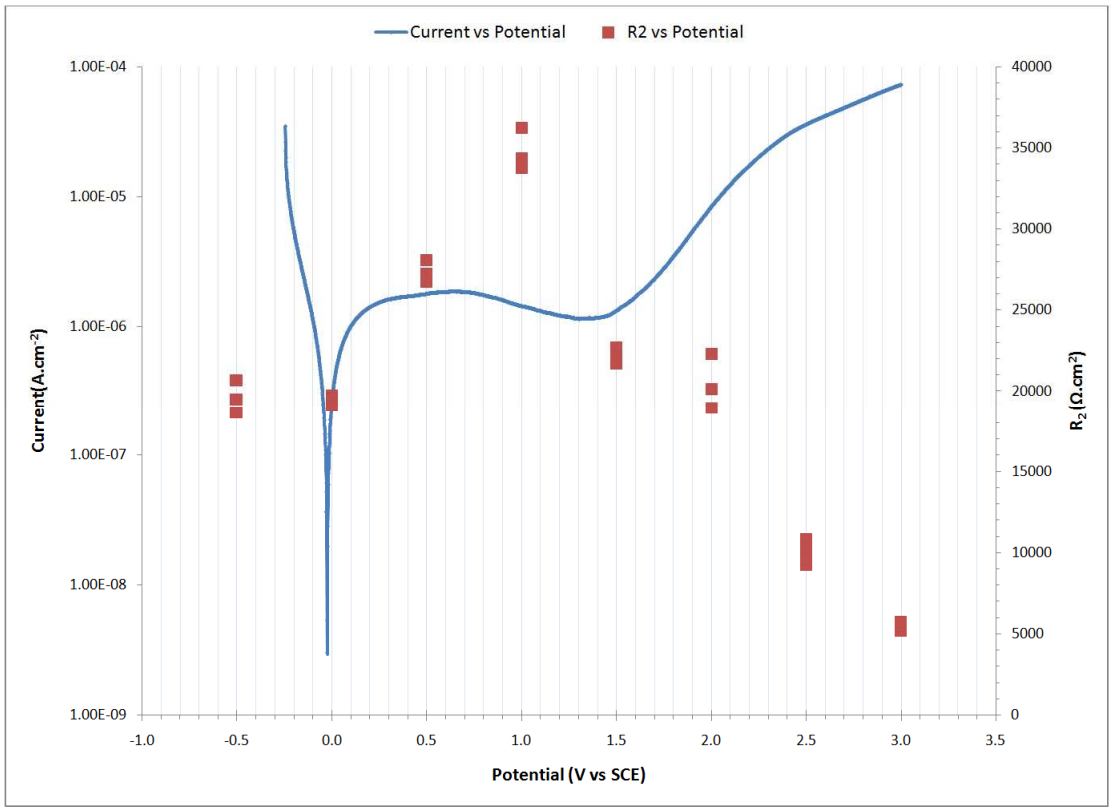

Figure 67: Potentiodynamic curve of TO Ti-6Al-4V (left axis) overlayed with the barrier layer resistance, R_2 (right axis), as a function of applied potential for TO Ti-6Al-4V.

The barrier layer resistance (R_2), presented in **Figure 67,** shows no significant changes in the polarization range from -0.5 – 0.0V_{SCE}. From potentials 0.0 – 1.0V, the resistance value increases steeply, coinciding with the formation of a passive region in the potentiodynamic curve. The R_2 curve undergoes a significant decrease once the TO specimen breaks down, coinciding once again with the increasing current density.

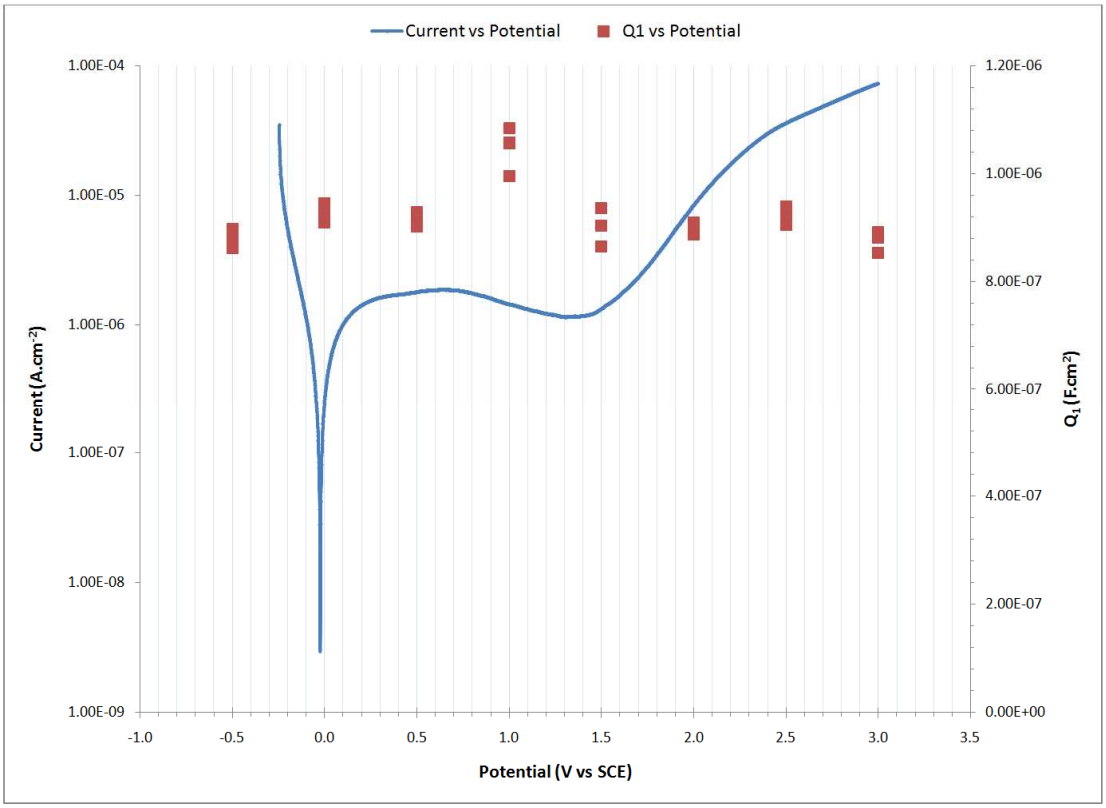

Figure 68: Potentiodynamic curve of TO Ti-6Al-4V (left axis) overlayed with the porous layer capacitance, Q_1 (right axis), as a function of applied potential for TO Ti-6Al-4V.

The porous layer capacitance (Q_1) demonstrates no significant changes across the potential range (**Figure 68**). Slight deviations in the curve appear, however, there is no evidence to support that these deviations signify a change in the TO metals capacitance.

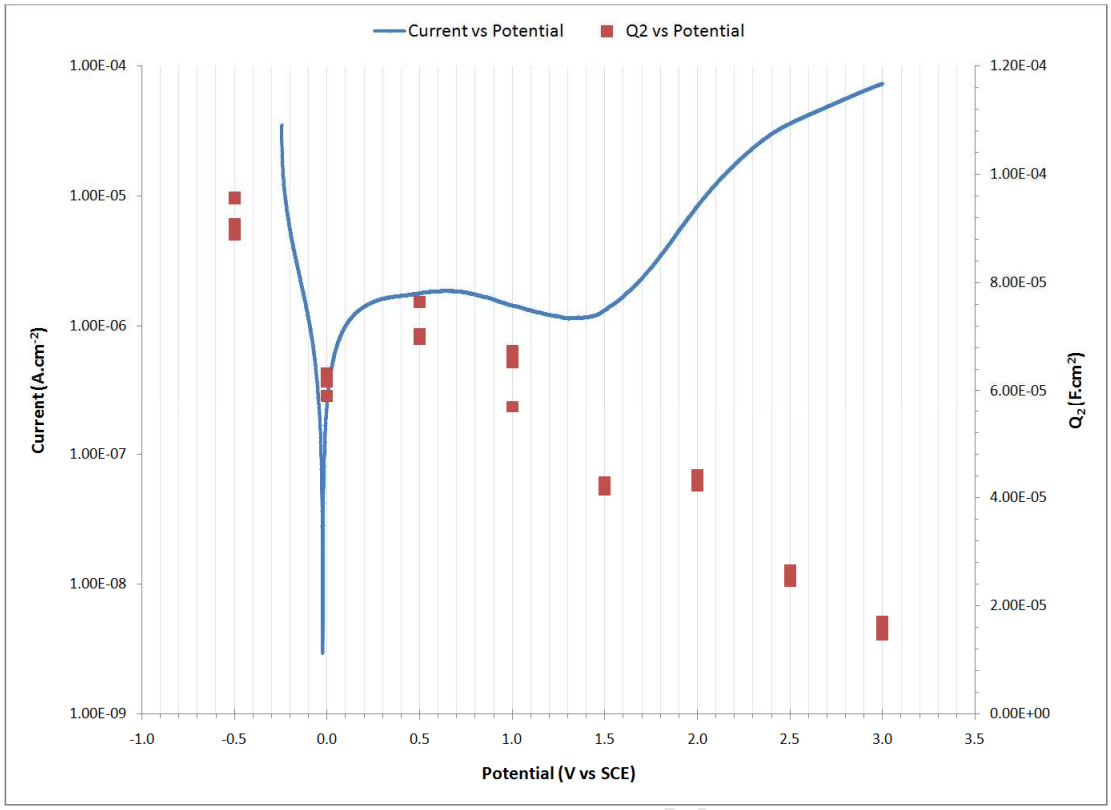

Figure 69: Potentiodynamic curve of TO Ti-6Al-4V (left axis) overlayed with the barrier layer capacitance, Q_2 (right axis), as a function of applied potential for TO Ti-6Al-4V.

Figure 69 illustrates the behaviour of the barrier layer capacitance (Q_2). A general trend in the curve displays a constant decrease in capacitance over the full polarization range; however, closer examination of the curve reveals increases in Q_2 with increases in current density. This occurs from 0.0 – 0.5V_{SCE}, before the metal passivates, and from1.5 – 2.0V_{SCE}, when the metal breaks down. Since this behaviour is highly reproducible, it is believed that the disturbance in the general downward trend of Q_2 values with increasing potential is significant.

10.6.3 Oxygen Boost Diffusion Hardened (OBDH) Ti-6Al-4V

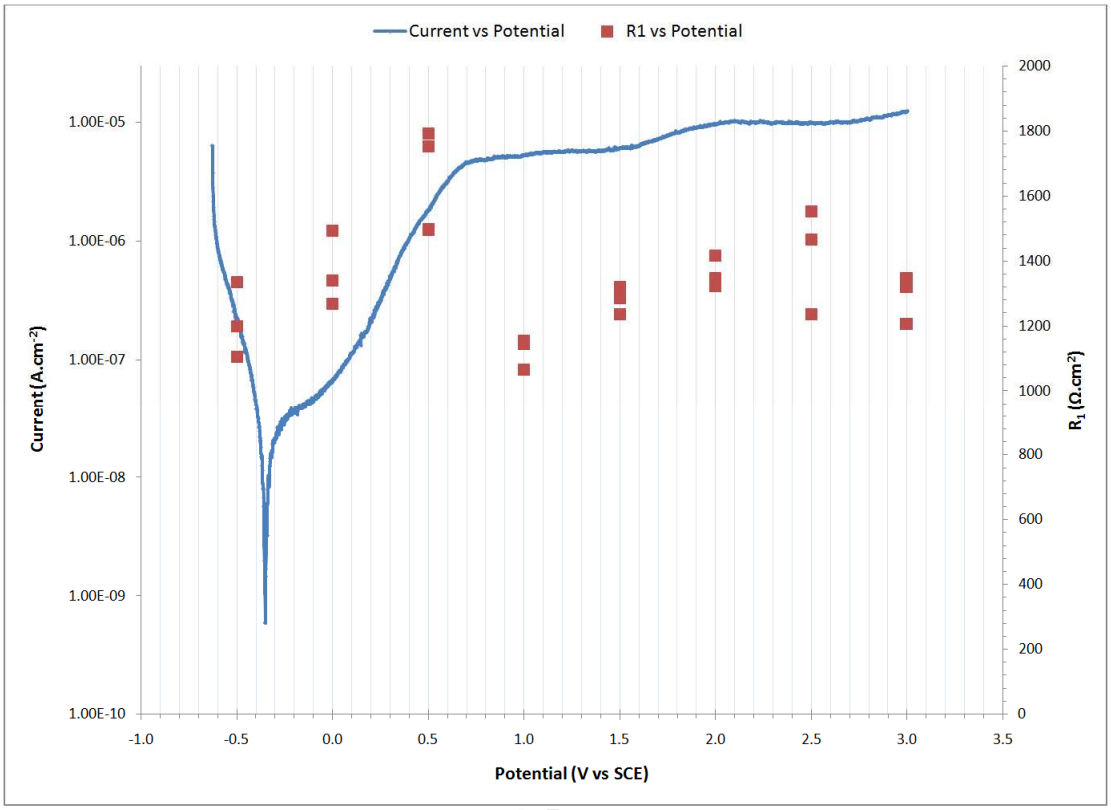

Figure 70: Potentiodynamic curve of OBDH Ti-6Al-4V (left axis) overlayed with the porous layer resistance, R_1 (right axis), as a function of applied potential for OBDH Ti-6Al-4V.

Figure 70 displays how the OBDH porous layer resistance (R_1) behaviour coincides with the respective potentiodynamic scan. In the potential range -0.5 – 0.5V_{SCE} the OBDH specimen reaches E_{corr}, whereas R_1 undergoes an increasing trend. After 0.5V_{SCE}, R_1 decreases significantly, which coincides with the formation of the passive region in the potentiodynamic scan. Apart from a very minor breakdown and repassivation between potentials 1.5 – 2.0V_{SCE}, the specimen remains fairly passive until final polarization potential of 3.0V_{SCE}. The porous resistance increases, with increasing potential, from 1.0 – 2.0V_{SCE}. This behaviour coincides with the passive region of the potentiodynamic scan.

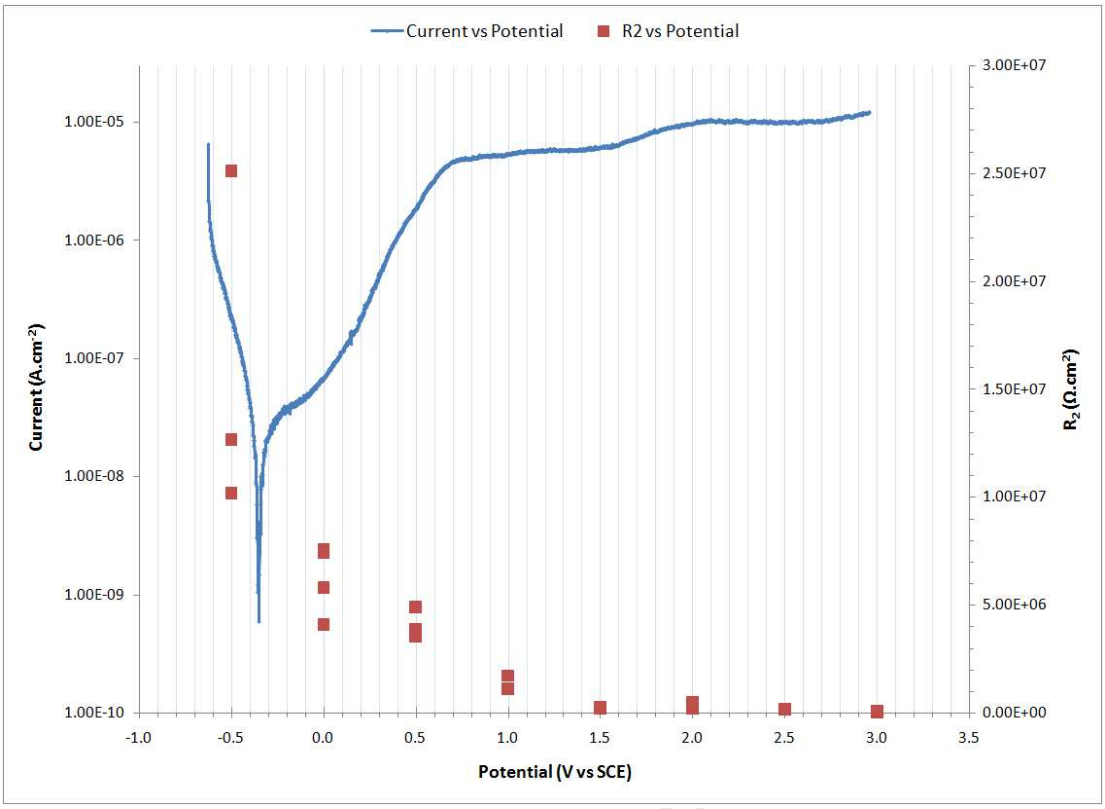

Figure 71: Potentiodynamic curve of OBDH Ti-6Al-4V (left axis) overlayed with the barrier layer resistance, R_2 (right axis), as a function of applied potential for OBDH Ti-6Al-4V.

The barrier layer resistance (R_2) behaviour is presented in **Figure 71,** and is very similar to that of the untreated metal. As for the untreated metal, the R_2 drops significantly at the start of the potentiodynamic scan from the cathodic region. Although the R_2-value continues to drop as the potential increases, the rate of change decreases and the R_2-values stabilize after $1.5V_{SCE}$ (see **Table 10)**.

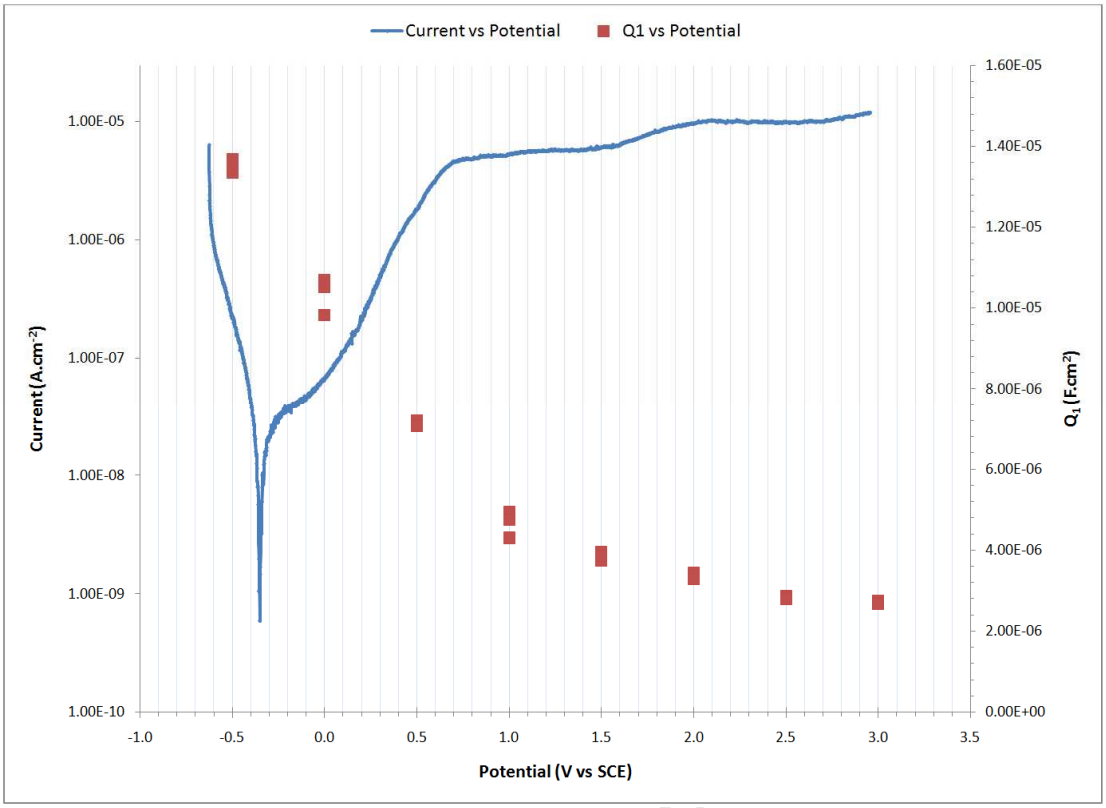

Figure 72: Potentiodynamic curve of OBDH Ti-6Al-4V (left axis) overlayed with the porous layer capacitance, Q_1 (right axis), as a function of applied potential for OBDH Ti-6Al-4V.

A constant decrease in the porous layer capacitance (Q_1) can be observed in **Figure 72**, which is very similar to the behaviour displayed by the untreated metal. From approximately 1.0V_{SCE}, the rate of change diminishes substantially coinciding with the passivation of the metal seen in the potentiodynamic scan.

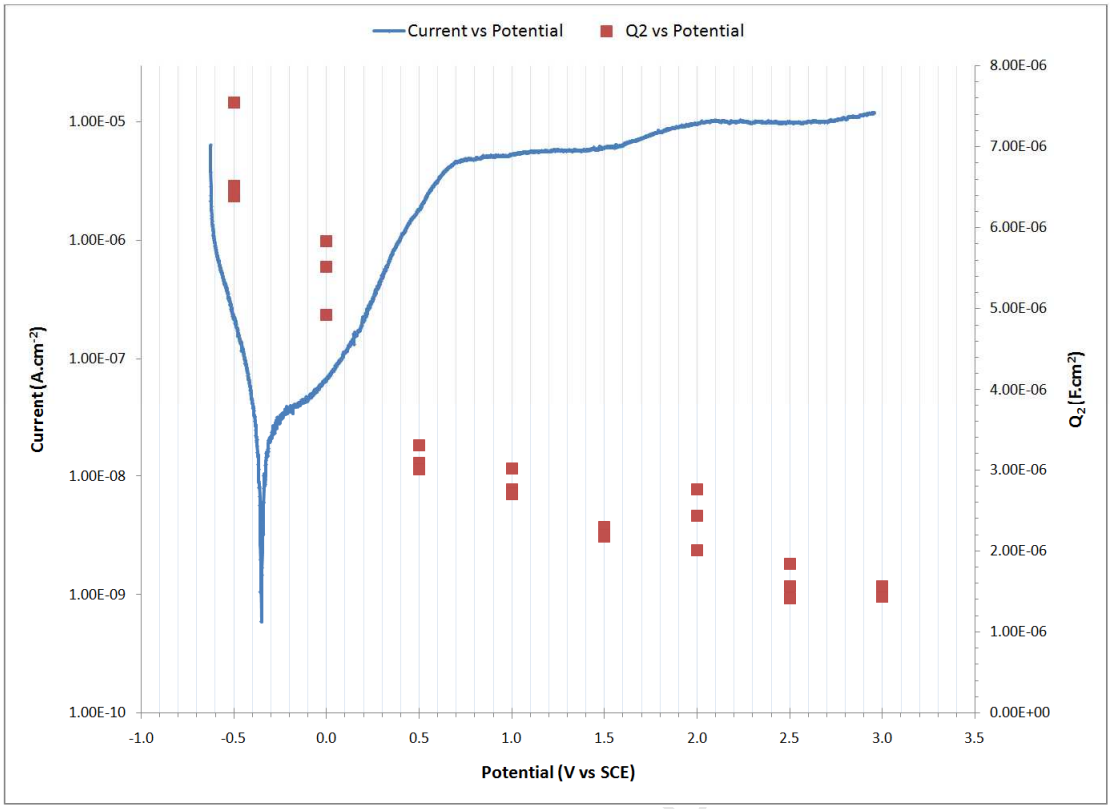

Figure 73: Potentiodynamic curve of OBDH Ti-6Al-4V (left axis) overlayed with the barrier layer capacitance, Q_2 (right axis), as a function of applied potential for OBDH Ti-6Al-4V.

Figure 73 represents the barrier layer capacitance (Q_2) which, once again, demonstrates similar behaviour to that of the untreated metal. The Q_2 undergoes a steady decrease for the duration of the test. However, from 1.5 – 2.0V_{SCE}, Q_2 fluctuates. This point coincides with the minor increase in current density of the potentiodynamic scan, where the passive layer breaks down and repassivates.

11 DISCUSSION

11.1 Microstructure analysis

11.1.1 Untreated Ti-6Al-4V

The SEM micrograph of the untreated specimen reveals two distinct microstructural constituents in the alloy; a lighter matrix representing the HCP α-phase, with darker dispersed grains representing BCC β-phase titanium. This is the typical two phase structure observed for Ti-6Al-4V (**Figure 25**).

11.1.2 Thermally Oxidized (TO) Ti-6Al-4V

The reddish brown appearance of the thermally oxidized specimens (**Figure 26)** occurs due to the increase in the thickness of the surface oxide layer, and the consequent change in the interference of the incident light radiation. The oxide layer is composed mainly of rutile (TiO_2) oxide with a different structure and composition to the passive layer that generally appears on clean metal in an ambient environment.

Figure 27 presents a typical SEM image for thermally oxidized Ti-6Al-4V which indicates an open structure with an almost flake-like appearance at high magnification. This appearance suggests that the oxide layer could be porous to the electrolyte during corrosion testing.

11.1.3 Oxygen Boost Diffusion Hardened (OBDH) Ti-6Al-4V

An oxygen boost treated Ti-6Al-4V specimen is presented in **Figure 28,** where the sample takes on a silver grey colour, different to the rust like brown appearance of the TO specimen. The difference is due to the diffusion of oxygen into the substrate and the dissociation of the oxide layer formed during the initial oxidation step.

Initial polishing, with removal of ~15 µm of surface material, displayed a white hazy surface (**Figure 29a**), which is suggested to be part of the oxygen strengthened α-region. This α-region spans from the surface of the OBDH specimen to low depth into the metal substrate, and consists of hardly or no beta phase, giving this region its high hardness displayed in **Figure 31**. **Figure 30** represents the optical micrograph after polishing to achieve a metallic mirror finish, which required the removal of 40µm ±9µm of the surface. The etched specimen clearly reveals the two distinct microstructural constituents i.e. the lighter matrix representing the HCP α-phase and the darker grains representing BCC β-phase titanium. However, even after the removal of a significant amount of surface material, the OBDH specimens which are

used for electrochemical testing are still well within the boost diffusion zone (see **Figure 31**).

11.2 Hardness Profile

Figure 31 displays the hardness profile for the untreated and treated Ti-6Al-4V specimens. The oxide of the TO specimen shows the highest surface hardness of 812Hv ±7.93Hv, which decreases rapidly with depth. This is due to the shallow oxygen diffusion zone, reaching the original bulk hardness at ±100µm into the surface. The majority of hardness decrease occurs during the first 20µm below the TO surface. The OBDH specimen displays a slightly lower surface hardness (754Hv ± 3.9Hv) than the TO specimen, but a significantly larger hardness than the untreated specimen (345Hv). The OBDH specimen retains its hardness over a large range (Zhang et al. 2007), and a total hardened layer of approximately 350µm in depth was achieved due to the large oxygen diffusion zone. Therefore, the boost diffusion process showed a deeper case-hardening effect than that of the thermal oxidation process.

Oxygen is a strong α-stabilizing element resulting in the oxygen-rich near-surface α-region. The initial hardness was achieved due to this oxygen hardened α-region. The substrate retains a high hardness deep into the oxygen strengthened α – β region with increased amount of β phase, which extends several tens of microns deep into the substrate. The gradual decrease in hardness occurs in the region of stable α – β phase, which extends up to hundreds of microns until the bulk hardness is eventually reached (Zhang et al. 2007).

Oxygen has a high solubility in titanium and the isolated oxygen released from TiO_2 is unlikely to escape from the material, and it is trapped in the OBDH substrate. The oxygen concentration in the substrate close to the oxide-substrate interface increases and the oxide becomes visibly different to that of the TO and untreated specimen. Oxygen, being one of the most effective solid solution strengtheners in titanium, diffuses into the metal and can occupy both substitutional and interstitial sites, causing inherent lattice distortions, thereby inhibiting dislocation mobility. The oxygen atoms are more stable around dislocations than in the rest of the lattice, resulting in “atmospheres” of atoms to form around these dislocations. Once dislocations are forced out of the atmosphere, the atoms rearrange themselves. This causes a distortion of the lattice that represents an increase in elastic energy. This additional energy is added to the stress required to move the dislocation, thereby increasing the overall energy required for dislocation movement. The result is that these atmospheres inhibit the movement of dislocations, making the material stronger and harder (Zhang et al. 2006).

12 DISCUSSION: ELECTROCHEMICAL ANALYSIS

One of the most attractive properties of Ti-6Al-4V alloys is its exceptional corrosion resistance, which is provided by a very thin naturally occurring surface oxide composed mostly of titanium oxide. This oxide film is self-healing in various environments; however, the Ti-6Al-4V alloy is susceptible to localized breakdown in the forms of pitting and crevice corrosion. Corrosion in this alloy is affected by the integrity of the passive layer, the environment and the heat treatment. Heat treatments can bring about large increases in the corrosion resistance of the alloy, if carried out at the optimum temperatures.

12.1 Long Term Immersion OCP (Open Circuit Potential) Tests

Comparisons of the free corrosion potential versus time of untreated and treated Ti-6Al-4V specimens are displayed in **Figure 32**. The corrosion behaviour was monitored until stabilization of the OCP had been reached. The changes in potential, after initial immersion into electrolyte until final stabilization of the potential, can be noted in **Table 7**. For untreated and OBDH specimens, the potential increases gradually with time becoming more anodic (noble) throughout the duration of the test, until the potential stabilizes. For the untreated metal, an initial potential of -0.153V_{SCE} increases with time stabilizing at 0.210V_{SCE} after 819 hours. The OBDH specimen increases from an initial potential of -0.055V_{SCE} to 0.170V_{SCE}, after 912 hours. These increases in potential are related to thickening of the oxide film which improves the corrosion protection ability in the 3.5 wt.% NaCl environment.

The thermally oxidised specimen reached equilibrium in the fastest time, almost immediately, increasing with time from an initial potential of 0.163V_{SCE} to 0.237V_{SCE}, which is the lowest rise in potential of the three conditions. This is due to the already present thick highly corrosion resistant thermally oxidised layer on the surface of the metal. Further oxidation of the TO specimen in the chloride environment is reduced or does not occur, compared to the untreated and OBDH specimens. The TO specimen exhibits the highest initial OCP; however, all three specimens stabilize at a final OCP relatively close together (see **Table 7**). This very inert surface oxide impedes/prevents the movement of electrons, therefore reducing any significant changes in current density, after the OCP stabilizes.

All OCP curves are shifted in the positive direction in the presence of chloride ions, confirming that chloride ions interfere with passivation of the metal. The potential increase also indicates that all specimens become thermodynamically more stable with time. This shift in the noble direction furthermore represents a lowering of the

corrosion rate by reducing the driving force for the cathodic reaction and increasing the thickness of the passive oxide film.

The corrosion potential or E_{corr} values displayed in the potentiodynamic curves are significantly lower than those obtained from the OCP measurements. This behaviour is expected, due to the fact that the potentiodynamic tests were initiated at a cathodic potential relative to the corrosion potential. This causes the naturally formed passive film on the surface to be partially or completely removed at the start of the test, due to the highly reducing initial potentials.

12.2 Potentiodynamic Analysis

Potentiodynamic scans for untreated and treated Ti-6Al-4V specimens are presented in **Figure 33** – **Figure 44**.

12.2.1 Untreated Ti-6Al-4V

Potentiodynamic scans of untreated Ti-6Al-4V specimens initiated closer to OCP (i.e. -0.5V below OCP) are displayed in **Figure 33**. The initial decrease in current density observed below E_{corr} indicates the formation of an initial oxide film as observed by Luiz de Assis et al. (2006). However, from potentials above ~0.2V the current density sharply increases indicating that the initial film is being broken down, therefore, leading to a less protective oxide. This increase in current density is due to anodic oxidation processes involving the oxidation of TiO or Ti_2O_3 to TiO_2. An increase in potential is not accompanied by the corresponding thickening of the oxide film, until final stabilization of the film occurs at E_{pp1}, and corresponding i_{c1}-value (see **Table 8**). The newly stabilized oxide layer brings about the passive region where the current density is practically constant, indicating that the growth of the oxide film and the thickness of the film increases linearly with potential.

The passive region is observed to contain two apparent passive regions, also reported by Luiz de Assis et al. (2006), which are separated by an initial breakdown and repassivation region. The metal passivates at E_{pp1} and remains passive for 0.818V until breaking down and then repassivating for a further 1.0V, resulting in a total passive region of 2.168V (see **Table 8**). The initial breakdown and repassivation which occurs prior to final breakdown, appears due to metastable pits forming. As observed in **Figure 33**, the current briefly increases as the pits nucleate and begin to grow and the dissolution of the initial passive layer occurs. After a short growth period, these metastable pits repassivate and the current once again decreases rapidly forming a second less passive region at a higher current density. The metal eventually breaks down at E_{b2} (see **Table 8**), due to dissolution of the oxide layer.

Figure 34 demonstrates the effect of polarizing at a lower initial potential i.e. -1.0V_{SCE}. The metal behaves similar to that demonstrated in **Figure 33**, until the metal reaches its initial passivation potential (E_{pp1}). The most notable difference is the potential range at which the metal remains passive with no or minimum changes in the current density. This occurs where the oxide layer passivates at E_{pp1}, and remains passive until the metal finally breaks down, with no second breakdown and repassivation potentials as demonstrated in **Figure 33**.

An overlay of **Figure 33** and **Figure 34** is displayed in **Figure 35,** where a comparison in behaviour can be observed. A significant difference in the E_{corr} value is visible, which is suggested to be due to when polarizing at a more active potential, the surface of the Ti-6Al-4V is cathodically "cleaned" of its naturally occurring oxide layer. The removal of this oxide layer results in the Ti atoms being exposed directly to the electrolyte, without the protection by the TiO_2 layer; thereby, decreasing the metals rest potential.

Another obvious difference is that **Figure 34** reaches E_{pp1} at a much earlier potential, but breaks down at a lower potential (E_{b2}). The passive region is therefore significantly larger than that displayed in **Figure 33**. The differences are suggested to be because of the initial cathodic removal of the naturally occurring oxide layer, which is due to the highly reducing initial potential. This provides a new, smoother flat surface where a more compact uniform oxide layer can be formed on.

12.2.2 Thermally Oxidized (TO) Ti-6Al-4V

Figure 36 – Figure 38 presents the potentiodynamic scans of TO Ti-6Al-4V specimens; where **Figure 36** displays specimens polarized from -0.5V below OCP and **Figure 37** presents specimens polarized at a more active initial potential of -1.0V_{SCE}.

Figure 36 displays a corrosion potential (E_{corr}) close to 0.0V_{SCE}, which is nobler than that of the untreated specimen. This behaviour is anticipated for TO specimens, which possess a thick rutile oxide layer. The curve displays that of an S-shaped potentiodynamic curve, where initial decrease in current density occurs at active potentials due to the surface oxide layer. Once E_{corr} is reached, the current density once again increases due to oxidation at the barrier layer of the TO specimen. The E_{pp1}-value is reached almost immediately, due to the already present inner barrier layer. However, the passive region only lasts for 1.24V where the metal eventually breaks down at E_{b2} (see **Table 8**). A similar behaviour in the curve is demonstrated in **Figure 37**. However, in **Figure 38** a visible drop in E_{corr}, between the two tests, is noted.

The resistance of the oxide layer is dependent on the chemical and mechanical stability of the layer. The mechanical stability is affected by defects, which are micro cracks or pores, which are responsible for failure of the oxidised surface. The lower than anticipated passive region for an oxidised surface is suggested to be because of the defective and porous oxide layer. Therefore, aggressive ions in the electrolyte diffuse or penetrate through the pores of the outer porous oxide layer towards the oxide metal interface, initiating localized corrosion forming pits at the interface. This occurs through the formation of a galvanic cell at the interface, where the more noble ceramic oxide coating will tend to act as a cathode and the metal substrate the anode. The exposed area will then anodically dissolve and then further extend along the coating/substrate interface and finally, leading to the removal of the coating by flaking (Bloyce et al. 1998). However, flaking-off of the oxide layer from the metal substrate was not evident for the polarization range used. The behaviour displayed in the TO specimen potentiodynamic scan is also evident in impedance studies which will be discussed at a later stage.

Therefore, it is important to note that the corrosion resistance of the oxide layer/metallic substrate is mainly determined by the density and distribution of defects in the coating, the nature of the coating/substrate interface and the passivation ability of the substrate. It is proposed that the corrosion resistance of the TO specimens (in this study) is mainly dependent on the substrate and not the surface oxide, due to the poor corrosion properties displayed at high polarizing potentials. Reducing the defects in the coating and optimising the oxidation treatment would produce a denser coating, thereby improving the corrosion resistance immensely.

12.2.3 Oxygen Boost Diffusion Hardened (OBDH) Ti-6Al-4V

The effect of polarization on OBDH specimens is displayed in **Figure 39 – Figure 41**. **Figure 39** represents the scan acquired when initial polarization is carried out from -0.5V below OCP. The shape of the curve resembles that of the untreated metal. Once again polarization at a more active potential brings about a lower E_{corr}-value displayed in **Figure 40** and a more stable passive region with almost no changes in current density.

The untreated and OBDH specimens polarized at more active potentials (i.e. -1.0V_{SCE}) showed minimum deviations in behaviour. However, a noticeable difference occurs in the passive region for specimens polarized from -0.5V below OCP. An initial breakdown and repassivation occurs in this region for the OBDH specimen as

well; however, not as prominent as that displayed for the untreated specimen (**Figure 33**). This difference is better differentiated in **Figure 43**.

Figure 41 displays the potentiodynamic behaviour of an OBDH specimen without prior polishing before corrosion testing. From the deviations in current density and low E_{corr}-value, it is evident that the oxide layer formed reacts different to the chloride media than when the metal is polished to a metallic finish. The porous and defective oxide scale present on the surface serves as a pathway for aggressive ions in the electrolyte to penetrate the pores reaching the metal oxide interface, initiating localized corrosion beneath the oxide layer. Even though there is an oxygen diffusion zone, the oxide layer formed at the metal-oxide interface is inhomogeneous and vulnerable to localized attack, thus giving rise to large increases in current density. The unpolished metal does, however, show decreases in current density owing to oxide layer formation but this layer is unstable with unreliable integrity with regards to improving corrosion resistance. Therefore, OBDH specimens were polished for further testing to determine the corrosion resistance of the diffusion hardened layer as opposed to the corrosion behaviour of the residual oxidised surface.

An overlay of tests conducted on OBDH specimens is displayed in **Figure 42**. Once again polarizing at more active potentials (i.e. $-1.0V_{SCE}$) demonstrates the lowest E_{corr}-value, but the largest passive region of 2.37V. The sample polarized closer to OCP in **Figure 39** displays a slightly lower passive region of 2.03V. The unpolished specimen shows no apparent passive region and the entire potentiodynamic scan of the unpolished specimen sits at a much higher current density, indicating its lower corrosion resistance when compared to the other two curves. Actively polarizing the specimen from two different initial potentials does not, however, significantly change the final breakdown potential of the specimens (see **Table 8**).

12.2.4 Comparison of treated with untreated Ti-6Al-4V

All values at points discussed in this section are tabulated in **Table 8**.

Figure 43 and **Figure 44** presents overlays of the potentiodynamic behaviour of untreated and treated Ti-6Al-4Vspecimens. Tests initiated at -0.5V below OCP are presented in **Figure 43,** where the E_{corr} for the untreated metal was found to be very similar to the E_{corr} of the OBDH specimens. However, the TO specimens demonstrated a significantly larger E_{corr} as expected for the specimens with a thick inert oxide layer on the surface. As the samples are polarized, the TO specimens passivate first, much sooner than the untreated and OBDH specimens, for reasons already suggested. In addition, the current density of the TO passive region is visibly lower than the untreated and OBDH specimens.

All three conditions undergo an initial breakdown (E_{b1}) at very similar potentials. However, even though the TO specimen breaks down at a lower current density, the oxidized specimen does not repassivate and the current density increases at a considerable rate. This verifies this breakdown as the final breakdown. The untreated and OBDH specimens repassivate to extend the initial passive region. The most apparent difference between the untreated and OBDH specimen is visible in the passive region. Even though the metal breaks down at similar E_{b1} and i_{b1} values, the difference is visible in the E_{pp2} values and more importantly in the i_{c2} values. The untreated metal repassivates at a higher current density suggesting a greater dissolution of the initial passive layer occurs. This generates a less passive second region which finally breaks down at E_{b2}. This breakdown is accompanied by a substantial increase in current density and corrosion rate, as the metal is polarized to potentials above E_{b2}. The OBDH specimen demonstrates a smaller peak in current density at the initial breakdown potential (E_{b1}), indicating that the oxygen boosted Ti-6Al-4V specimen is more efficient in preventing the dissolution of the passive layer formed. This is proposed to be associated with the high oxygen content below the surface of the metal, thereby producing a more passive oxide layer. Increasing the probability of TiO_2 formation at higher potentials enhances the corrosion resistance of the substrate below the surface oxide. This behaviour is also evident in the EIS results.

Once the OBDH specimen breaks down, the current density increases at a low rate depicting a low corrosion rate even after dissolution of the passive layer. This corrosion rate is significantly lower than that of the untreated metal. The TO specimen exhibits the highest increase in current density after breaking down (E_{b2}), indicating the lowest corrosion resistance at high potentials, of the three conditions.

Figure 44 displays the potentiodynamic behaviour when polarized at more active potentials (i.e. -1.0V_{SCE}), resulting in a more pronounced passive region. Once again the E_{corr}-value of the TO specimen is significantly higher than that of the other two specimens, but lower than the E_{corr} values obtained in **Figure 43**. All specimens show only one passivation and breakdown potential, unlike that displayed in **Figure 43**. The TO specimen once more breaks down first, though now at a similar current density to the untreated and OBDH specimen, resulting in a larger passive region. Even though the untreated and OBDH specimens break down at a lower potential (E_{b2}) than that displayed in **Figure 43**, they display larger more stable passive regions, therefore, showing better corrosion resistance.

The ease of passivation of the metal can be deduced as the difference in the E_{pp1} and E_{corr} values (see **Table 8**). The lower the difference, the easier the specimen passivates. The TO specimen passivates the easiest owing to its already present thick oxide layer. It is well known that materials susceptible to pitting corrosion (such as titanium alloys), possess a characteristic pitting potential at which a sudden increase in current density will occur. This sudden increase in current density was not observed at the final breakdown potential for untreated and OBDH specimens, and pitting corrosion was not present on the surface. However, this sudden increase in current density was present for TO specimens once E_b was reached, again suggesting localized corrosion i.e. pitting corrosion below the porous oxide at the oxide-substrate interface.

12.3 Corrosion Micrographs

Ti-6Al-4V displays a two phase equiaxed microstructure, therefore making the alloy susceptible to corrosion as the compositional difference across the grain boundaries increase. A galvanic cell is formed between the two phases due to the enrichment of Aluminium in the alpha phase and Vanadium in the beta phase. As a result, corrosion occurs preferably at the grain boundaries for both untreated and polished OBDH specimens (displayed in **Figure 45 – Figure 48**) and the phase structure is efficiently revealed by a process not unlike etching.

The morphology of the corroded surfaces of untreated and OBDH specimens (**Figure 45 – Figure 48**) after corrosion studies verified that the alloy was corroded uniformly, indicating that the mode of degradation was due to uniform corrosion (Gurrappa 2003). The presence of pitting was not evident, hence breakdown of the metal did not occur due to localized corrosion in this potential range i.e. -0.5 – 4V_{SCE}.

12.4 Corrosion Rates

The corrosion rates and corrosion current densities (i_{corr}) measured for untreated and treated Ti-6Al-4V specimens are noted in **Table 9**. Corrosion rate determination was done through Tafel extrapolation. The corrosion rates and i_{corr}-values, for the untreated and treated specimens are relatively very low due to Ti-6Al-4V's general excellent corrosion resistance and passivating ability. The corrosion rates observed are in the order of:

TO > untreated > OBDH specimens.

The corrosion rate of the OBDH treated specimen is approximately 3.5 times lower than the untreated condition , whereas the corrosion rate of the TO specimen is approximately 24 times greater than the untreated condition.

The data thus revealed that the oxygen content beneath the surface has a reasonable effect on the corrosion rate between the untreated and the OBDH specimen. The boosted specimen shows a lower corrosion rate, due to its higher corrosion resistance, evident in both potentiodynamic polarization and impedance measurements. Therefore, between untreated and treated specimens, the OBDH specimens exhibit the lowest corrosion rate overall.

13 DISCUSSION: AC ANALYSIS (EIS)

The equivalent circuit for Ti-6Al-4V is found to best fit the circuit displayed in **Figure 49**, as proposed for a metal with an oxide layer on the surface (Pan et al. 1996). This circuit is similar to the equivalent circuit representing the oxide layer on anodized aluminium (Mansfeld and Kendig 1988). The circuit consists of circuit elements which represent the outer porous layer i.e. the oxide layer, and the inner barrier layer i.e. the metal-substrate interface. The capacitance of these layers was better characterized by employing a constant phase element (CPE). The CPE takes into account the fact that experimentally, the represented layers (porous layer and barrier layer) never shows the theoretically expected phase shift of 90° and a slope of -1, which occurs for an ideal dielectric. The dissipation factor 'n' associated with the CPE, accommodates diffusion processes and adsorbed species.

An excellent fit was found between the proposed theoretical model and the experimental data, with low chi-square values in the region 10^{-3} – 10^{-4} indicating an excellent agreement in values as well. Apart from the excellent fit produced by the data, another reason for employing the same circuit for both untreated and treated specimens is so that simple and necessary comparisons can be made between circuit elements of different specimens. In doing so, the corrosion resistance can be characterized according to the different treatment conditions.

13.1 Overlays of Untreated and Treated Ti-6Al-4V

The EIS technique is based upon the application of an alternating current from high to low frequencies at a specific potential. It is important to note that extending the lower frequency range could result in better definition of the Nquist semicircle; however, a more defined semicircle does not suggest better quality results, as it is the modelling that determines valuable EIS data. Also, making EIS measurements at very high (>100 000Hz) and very low frequencies (<0.01Hz) is evidently extremely difficult as well as time consuming. In the case of low frequencies, the measurement may be able to be made but is, however, not a meaningful one. At times, data collected at frequencies below 1Hz were found to be erratic and scattered, which may not be measurements characteristic of the oxide layer or corrosion reaction. Therefore, erratic data and scattered points at these low frequencies (<1Hz) were not included as it did not illustrate the behaviour of the test specimen in question.

To properly describe the impedance behaviour of the Ti-6Al-4V specimens, comparisons between Nquist and Bode plots will be discussed in conjunction with the plots displaying the impedance behaviour as a function of potential (Section 10.6). This demonstrates how the EIS data compares to the potentiodynamic behaviour. In

that way, any assumptions made by discussing one curve or plot can be confirmed by supporting evidence of another.

13.2 EIS analysis of untreated Ti-6Al-4V

13.2.1 Nquist Plot Analysis

Nquist overlay plots for untreated specimens (**Figure 52**) exhibit very similar behaviour to that of OBDH Nquist overlay plots (**Figure 60**). Total impedance decreases with increasing polarization. This is indicated by a depression in the capacitive loop (drop in Z_{im} maxima), resulting in a lower diameter of the semicircles i.e. a decrease in the x-intercept at high frequency.

Upon initial exposure to the electrolyte, the oxide layer acts as a perfect capacitor, displaying excellent protective properties at low polarizing potentials. Therefore, plots at OCP and low potentials display large diameters, owing to a large initial resistance. The Nquist plot of an undamaged oxide layer lacks significant data, as displayed by plots at OCP for both untreated and OBDH specimens. The plots will remain uninteresting until the development of resistive elements, which occurs when polarizing the specimen to higher potentials.

As the polarization increases a clearer semicircle starts to form, which for Ti-6Al-4V is an indication of oxidation occurring rather than degradation of the underlying metal. Polarizing the sample from 2.0 -3.0V_{SCE} results in a large decrease in the Nquist loop, now conforming to the semicircle of a Randle-like cell. This depicts the formation of a more porous film, where a pathway for the electrolyte to the underlying metal is starting to form and a decrease in the pore resistance should be apparent (displayed in **Figure 62**).

It is possible that had the Ti-6Al-4V specimen been polarized to higher potentials inducing further more apparent corrosion to occur, the formation of two semi-circles is proposed to appear in the Nquist plot. In this case, the semi circle at high frequencies is due to the porous layer capacitance (C_p) and the semi circle at lower frequencies would depict the barrier layer capacitance (C_b). However, distortions resulting in deformed broader semicircle loops (**Figure 52**) were established to also be due to the two time constant impedance spectra, whereby, the high frequency intercept is due to the solution resistance (R_s) and the low frequency behaviour accounts for all processes taking place at the substrate/electrolyte interface. This behaviour is also typical of a metallic material covered by a porous film exposed to an electrolytic environment. Therefore, the presence of two visible semicircles is not

always apparent and is evident from Nquist plots for both the untreated and treated specimens (Ramires and Guastaldi 2001).

13.2.2 Bode Phase Plot Analysis

The Bode phase plot is illustrated in **Figure 53**, where an overlay of phase plots at different offset potentials from -0.5 – 3.0V_{SCE} is demonstrated. The high frequency response at all offset potentials is attributed to R_s, displaying a phase angle near 0°. The OCP impedance measurements show a near capacitive response, where the phase angle reaches a plateau close to 85°, sustaining this value over a large frequency range. This behaviour is characteristic of a rather stable oxide layer (Hsu et al. 2004). The broad (phase angle) peak is suggested to be indicative of the interaction of two time constants, the outer porous layer and the inner barrier layer.

The behaviour of the phase plot remains similar to the OCP curve, when polarized from -0.5 – 0.0V_{SCE}. As the potential is increased from -0.5 – 1.5V_{SCE}, the maximum phase angle shifts to higher frequencies and the films resistance R_1 is found to increase. This increase in R_1 is also evident in **Figure 62**. The decrease in phase angle (with increasing potential) at frequencies below 100mHz indicates that oxidation of the passive film is occurring and the film is different to that formed at OCP. The frequency range at which the phase angle remained close to 85° remains high until 1.5V_{SCE}. However, at 2.0V_{SCE} a distinct bell-shaped curve is observed, and the phase angle in the low frequency region decreases. This is an indication that the oxide layer once again undergoes a change, where a more porous film starts forming. This porous film is more susceptible to corrosion, whereby the electrolyte has an easier path to the metal substrate. This, results in a decrease in the resistance to charge transfer at the corrosion interface, indicated by a drop in R_2-values (see **Table 10**). Hence, the decrease in the phase angle relates to increases in the films porosity (Schmidt and Azambuja 2006).

The overlapping of the phase plots from the high frequency region to the low frequency region indicates a strong adsorption process of chloride ions on the oxide film during the polarization process (Schmidt and Azambuja 2006). At potentials where the phase angle is ~85°, it is plausible to suppose chloride adsorption took place on the oxide outer layer and thereby sealing the pores (**Figure 21**). Sealed pores increases the metals porous layer resistance displayed in **Figure 62** (Wang et al. 2003).

13.2.3 Untreated Ti-6Al-4V EIS Trends

Figure 62 displays the trend in the porous layer resistance with increasing potential, which provides insight into the impedance behaviour of the oxide layer compared to potentiodynamic behaviour.

At potentials -0.5V_{SCE} and 0.0V_{SCE}, only a minimum change in the porous layer resistance occurs. This does not signify that no changes occur in the porous resistance between these points. As the potential increases from 0.0 – 1.0V_{SCE} the potentiodynamic scan shows an increase in current density, until the passive region is reached. This increase in current density is evident in the Nquist plot's depression of the capacitive loop, and the Bode plot's decrease in phase angle, as explained previously. The porous layer resistance increases in this potential range (from 0.0 – 1.0V_{SCE}), due to the oxide layer passivating and the sealing of pores (see Error! Reference source not found.).

From potentials 1.0 – 1.5V_{SCE}, R_1 undergoes a considerable increase, signifying increased passivity of the oxide layer. When the oxide film becomes thickened, with the possible presence of sealed pores, the corrosion resistance can reach a high level and further dissolution of the oxide layer is prevented over a wide polarizing potential range demonstrated as the passive region. The increase in R_1 coincides with this passive region, where the current density reaches a plateau. The metal undergoes its initial breakdown from ~1.5 – 2.0V_{SCE}, resulting in a significant decrease in the R_1. The passive layer repassivates once again; however, the porous layer resistance continues to decrease even though the current density seems to stabilize. This is an indication of the formation of a more porous and less passive oxide layer (from 2.0 – 3.0V_{SCE}) different from the initial passive oxide formed where a path for the electrolyte to the underlying metal is starting to form. The same behaviour is evident in Nquist and Bode phase plots for untreated specimens (previously discussed) for the same potential range (2.0 – 3.0V_{SCE}).

Figure 63 displays the impedance trend for the inner barrier layer resistance (R_2). The most obvious observation is the visible decrease in resistance throughout the polarization range; however, R_2 remains significantly high until polarized to 1.5V_{SCE} (see **Table 10**). This implies a very high corrosion resistance i.e. a low rate of titanium release and oxide growth.

A common behaviour for passive films on titanium is for an increase in R_2 to occur and is attributed to regrowth of the inner layer and a self healing process, which is not apparent in **Figure 63**. The reasoning for this is as follows. Initially R_2 is high and decreases when polarized from -0.5V_{SCE}, which may be due to the cathodic partial or complete removal of the naturally formed oxide film on the surface of the metal. The

remaining oxide is somewhat porous or defective, if present at all. This substrate thus becomes exposed, and vulnerable to attack by chloride ions in the electrolyte. Consequently the barrier layer resistance at the substrate-oxide interface decreases.

However, as the polarizing potential increases, the oxide once again grows (through oxidation occurring on the metals surface) to produce a thicker, more compact passive oxide film. The porous oxide may become hydrated and ions from the NaCl electrolyte may easily be incorporated into the pores and precipitate further. When these pores are filled by hydrated or precipitated compounds (**Figure 21**) the thickened oxide film can become highly protective, thereby increasing the metals corrosion resistance at the substrate-oxide interface.

From potentials 1.5 – 3.0V_{SCE}, R_2 undergoes a significant decrease coinciding with the initial breakdown of the metal. As discussed previously, the oxide layer undergoes a change to form a more porous and less passive oxide layer. The significant drop in R_2 after this potential (see **Table 10**) is attributed to the electrolyte penetrating the pores of the oxide layer, thereby affecting the barrier layer at the metal-oxide interface.

The behaviour of the porous layer capacitance (Q_1), displays a decreasing trend with increasing polarization potential (**Figure 64**). This is expected for a metal with a protective oxide layer and passivating capabilities. However, the rate of change differs, denoting a change in the composition of the porous layer. Changes in the rate coincide with the passivation and breakdown of the metal.

The trend displayed by the barrier layer capacitance (Q_2) demonstrates similar behaviour to that of Q_1 (**Figure 65**). The capacitance undergoes a decreasing trend with increasing polarization potential, which corresponds to the slow growth of the titanium oxide film attaining passivity (Wang et al. 2003). Changes in current density coincide with changes in the decreasing Q_2 rate; however, the barrier layer capacitance remains relatively low (see **Table 10**) regardless of the trend. This denotes excellent corrosion resistance of the Ti-6Al-4V specimen. When polarized from 2.5 to 3.0V_{SCE}, Q_2 undergoes a sharp increase, indicative of the metal now breaking down. The electrolyte is suggested to now contact the metal substrate, resulting in corrosion to occur at the metal oxide interface, therefore displaying a change in the metal substrate's capacitance.

13.3 EIS analysis of OBDH Ti-6Al-4V

The OBDH Ti-6Al-4V specimen shows substantially similar behaviour to that of the untreated metal. It should be noted that ~40 - 50µm of the surface layer has been removed to expose a metallic mirror finish; however, even at this depth the hardness of the OBDH specimen is significantly higher than that of the untreated specimen (**Figure 31**). This verifies the effect of high oxygen concentration within the OBDH specimen. Therefore, differences observed between the untreated and the OBDH specimen can be considered to be caused by this difference in oxygen concentration between them. Only the differences between the two specimens are pointed out in the following discussion of the OBDH impedance data.

13.3.1 Nquist Plot Analysis

A significant difference in the Nquist plot (between the untreated and OBDH specimen), occurs when the OBDH specimen is polarized from 2.0 – 3.0V_{SCE} (**Figure 60**). In this potential range, the behaviour of the OBDH capacitive loops closely resembles one another and the semicircle loops are almost on top of each other (overlapping), which is not observed for the untreated specimen. This behaviour indicates that a minimum decrease in total impedance occurs in this potential range (2.0 – 3.0V_{SCE}). Therefore, the OBDH porous resistance should not display large changes from 2.0 to 3.0V_{SCE}, evident in **Figure 70**. This observation is consistent in the Bode phase analysis as well.

13.3.2 Bode Phase Plot Analysis

The Bode Phase plot observed for the OBDH specimen (**Figure 61)** resembles the behaviour of the untreated specimen from -0.5 – 2.0V_{SCE}. The phase angle maximum was measured at approximately 75 - 85°. The phase angle maxima sustain a high value (~75 - 85°) over a high frequency range, indicating that the passive oxide layer behaves as an efficient barrier to corrosion. This results in a high resistance to charge transfer at the corrosion interface, which is evident by the high R_2 values (see **Table 10**).

Similar to the Nquist plot, the impedance behaviour of the OBDH specimen from 2.0 – 3.0V_{SCE} is quite similar, indicating a minimum change in total impedance after this potential. The passive oxide layer becomes more porous with increasing offset potential; however, not to the extent displayed by the untreated specimen. Therefore, a large decrease in the resistance to charge transfer (R_2) does not occur when polarized from 2.0 -3.0V_{SCE} (see **Table 10**). The barrier layer resistance (R_2) remains

high even after breakdown of the metal (compared to untreated and TO specimens) indicating a higher corrosion resistance at high potentials.

13.3.3 OBDH Ti-6Al-4V EIS Trends

Figure 70 displays the trend in the behaviour of the porous layer resistance (R_1) exhibited by OBDH Ti-6Al-4V specimens. There is a significant difference in the R_1 trend when compared to the untreated specimen, indicating that the boosted oxygen has an effect on the substrate. The data points at each offset potential (-0.5 – $0.5V_{SCE}$) are fairly scattered due to different tests; however, the increasing trend seems to be constant between samples. The increase is attributed to the high oxygen content in the substrate (due to the boost diffusion treatment), where beneath the metal surface (in the diffusion zone) a large number of oxygen-rich titanium compounds form. These oxygen-rich compounds are suggested to have a significant effect on the measured R_1-value by forming part of the porous layer, thereby increasing the passivity of the metal when polarization is initiated. Therefore, R_1 remains high even prior to the passive region.

The R_1 undergoes a sharp decrease once polarized to $1.0V_{SCE}$, which coincides with the passive region of the potentiodynamic scan. This decrease is due to the now newly passivated oxide layer, which possesses a different chemical composition to the oxygen-rich titanium compounds formed beneath the surface. Therefore, a different R_1 is displayed, as this is now the oxide layer being detected and evaluated. Consequently, R_1 displays a lower resistance than that of the initial oxides, but gradually increases again as a more passive layer anodically forms (from 1.0 – $2.0V_{SCE}$). From potentials 2.0 – $3.0V_{SCE}$, R_1 does not undergo a significant decrease as it did for the untreated specimen. This behaviour is evident in both Nquist and Bode Phase plots (for OBDH specimens), thereby providing more evidence that a more stable and less porous oxide layer forms on the OBDH specimen.

Apart from the trend behaviour of the porous layer resistance between potentials -0.5 – $3.0V_{SCE}$, the untreated specimen demonstrates a higher maximum R_1-value (see **Table 10**). The untreated specimen also displays an overall higher R_1-value from potentials 1.0 – $3.0V_{SCE}$, whereas the OBDH specimen displays higher R_1 values between potentials -0.5 – $0.5V_{SCE}$, as well as a higher porous resistance at E_{corr}. The OBDH specimen also forms a more stable, less porous oxide layer at high potentials (2.0 – $3.0V_{SCE}$).

The inner barrier layer resistance (R_2) of the OBDH specimen exhibits similar behaviour to that of the untreated specimen (**Figure 71**). The similarities in the R_2 values are observed when polarized from -0.5 – $1.5V_{SCE}$; however, from 2.0 – $3.0V_{SCE}$ the OBDH specimen does not undergo a significant decrease, as displayed

by the untreated specimen (see **Table 10**). This behaviour has been discussed previously for Nquist and Bode phase plots of the OBDH specimen, and provides further evidence of the formation of a less porous more compact oxide. This less porous oxide limits the pathway for electrolyte to penetrate the pores and contact the underlying substrate, thereby increasing the resistance to charge transfer at the corrosion interface.

The capacitance of the OBDH specimen (**Figure 72** and **Figure 73**) exhibits exceptionally close behaviour to that displayed by the untreated metal (**Table 10**). The only difference in behaviour is displayed for the inner barrier layer capacitance (Q2), when polarized from 2.5 – 3.0V_{SCE}. The Q_2-value of the OBDH specimen remains low due to the less porous oxide formed on the surface, thereby hindering the movement of electrolyte to the underlying metal. Therefore, no increase in capacitance is observed.

13.4 EIS Analysis of TO Ti-6Al-4V

Nquist overlays for thermally oxidised Ti-6Al-4V specimens are displayed in **Figure 56**. Polarization of the TO specimen from -0.5 – 2.5V_{SCE}, results in no depression of the capacitive loops, as seen for untreated and OBDH specimens. However, at 3.0V_{SCE}, a depression in the loop and a decrease in diameter of the semicircle occurs, thereby indicating a decrease in total impedance. Apart from the depression of the capacitive loop in the low frequency region, the Nquist plots are practically uninformative, displaying behaviour analogous to that observed at OCP.

The Bode Phase overlay plots observed for TO specimens (**Figure 57**) show particularly different behaviour to that of untreated and OBDH specimens. At the start of the test (in the high frequency region), the phase angle is near 50° at all offset potentials and OCP, in response to the solution resistance (R_s). The slight deviation in the Bode phase loop before the phase maximum is reached, confirms the existence of two time constants i.e. the outer porous layer and the inner barrier layer. At frequencies below 10 000Hz, the phase plot reaches a maximum phase angle around 67°, noticeably lower than that of untreated and OBDH specimens, which is not characteristic of an oxide layer. Another indication of the uncharacteristic behaviour is the very small range of frequencies at which the phase angle remains high and the low phase angles at all offset potentials and OCP in the low frequency region. This uncharacteristic behaviour of the oxide layer indicates that the oxide of the TO specimen is not very effective at providing good protection due the highly porous oxidised layer.

Overall, the Bode phase plot as well as the Nquist plot of the TO specimen, indicates that the oxidised layer is very porous prior to polarization; therefore, displaying poor protective properties. No changes in the impedance behaviour can be reported from the plots as the polarization increases. This is suggested to be because the oxide layer present was formed during the thermal oxidation heat treatment, and is present prior to polarization. Throughout the polarization process the same porous layer is being assessed. Whereas, for untreated and OBDH specimens the nature and chemical composition of the oxide layer changes due anodic polarization; therefore, bringing about changes in the total impedance. This behaviour is supported by trends in EIS data (of the TO specimen) discussed in the next section.

However, what is evident by the Bode phase plot is that at the low frequency limit of the plot the phase angle reaches values of below 30°, indicating that a process of diffusion is present as proposed by Schmidt and Azambuja (2006). This is also evident in the low 'n' values displayed in **Table 10**. A possible explanation for the impedance behaviour displayed is due to the formation of Al-enriched oxide zones present in the oxide due to thermal oxidation treatment. The existing rutile layer provides a high corrosion resistance; however, the presence of alumina (Al_2O_3) nuclei lowers the resistance acting as diffusion easy paths through which the electric signal preferentially passes until reaching the metal substrate (Garcia-Alonso et al. 2002).

13.4.1 TO Ti-6Al-4V EIS Trends

The porous layer resistance (R_1) for thermally oxidised specimens is displayed in **Figure 66**. The oxide layer present on the TO specimen is formed during the thermal oxidation treatment, and undergoes minimum changes through electrochemical polarization. This behaviour is indicated by the R_1 trend, as well as Nquist and Bode phase plots.

Peaks in the R_1 trend is observed at offset potentials $0.0V_{SCE}$ and $2.5 – 3.0V_{SCE}$. These peaks are suggested to be caused by the possible presence of sealed pores, as demonstrated by the untreated specimens. However, the presence of sealed pores does not attribute to the corrosion resistance in the case of TO specimens, as the metal still shows an increase in current density from $2.5 – 3.0V_{SCE}$. The effect of polarization is better demonstrated when characterizing the inner barrier layer resistance (R_2).

The trend of R_2 is presented in **Figure 67**, where (unlike the untreated and OBDH specimen) polarization has a visible effect on the TO specimen. The corrosion resistance of TO specimen is hardly dependent on the thermal oxide layer, but

predominantly on the electrochemical activity occurring at the substrate-oxide interface. The main reason for this outcome is due to the porosity of the thermal oxide layer, where the pores present are sufficiently large enough to allow for penetration of electrolyte and result in a path to the underlying metal substrate. The interaction at the corrosion interface produced changes in the inner barrier layer resistance, whereby localized corrosion is suggested to occur as demonstrated by the low R_2 values (relative to the untreated and OBDH specimens).

This passive region of the potentiodynamic scan brings about increases in R_2 from 0.0 – 1.0V_{SCE}, due to the inner barrier layer passivating. Growth of this passive layer results in a more protective layer. Breakdown of this passive layer (evident by the increase in current density) results in a sharp decrease in R_2 (from 1.5 – 3.0V_{SCE}). Therefore, even though the outer oxide layer is inert and expected to be highly resistant (displays the highest R_1-value in **Table 10**) it does not add to the corrosion resistance of the TO specimen but conversely decreases the corrosion resistance. The decrease in corrosion resistance is brought about by localized corrosion occurring at the substrate-oxide interface. This outcome is only deduced for the thermal oxidation treatment and specimen preparation used in this study, and not at all to ascertain that thermal oxidation lowers corrosion resistance. It is apparent that producing a more compact (less porous) oxide would provide a high corrosion resistance.

The porous layer capacitance (Q_1) of the TO specimen is displayed in **Figure 68**, where the behaviour shows no significant changes throughout the polarization range. This is due to the same thermal oxide layer being measured, as discussed for R_1. The overall Q_2 of the TO specimen is the lowest of the untreated and treated specimens, as anticipated for a thick oxide layer. However, as suggested previously, the outer porous layer inactivity is an indication that the inner barrier layer plays the determining role of the specimen's corrosion resistance.

Figure 69 displays the inner barrier layer capacitance (Q_2). The capacitance undergoes a decreasing trend with increasing polarization potential .Changes in current density coincide with changes in the decreasing Q_2 rate. The TO specimen exhibits the highest Q_2 (compared to untreated and OBDH specimens), indicating that the electrolyte has penetrated the oxide's pores resulting in increased activity at the substrate/oxide interface.

13.5 Evaluation of EIS data integrity

The data tabulated in **Table 10** displays the impedance values at OCP and each offset potential. The trends in R_1, R_2, Q_1 and Q_2 have been discussed previously. The solution resistance (R_s) for both untreated and OBDH specimens are very similar, as anticipated due to the same surface being tested. These specimens show n_1 values of 1, indicating that the CPE (Q_1) acts as a true capacitor. Whereas, values of n_2 are lower for both the untreated and OBDH specimens, which is attributed to adsorbed species, taking into account diffusion processes and surface roughness. Nevertheless, n_2 remains relatively high close to that of a true capacitor.

The TO specimen differs in R_s-value, indicating that the equivalent circuit proposed in **Figure 49** might require an additional circuit element. Another indication of this is the low 'n' values, in particular the low n_2 value. Milosev et al. (2000) proposed that if 'n' is ~ 0.5, then the diffusion mass transport control is the rate determining step, indicating that a process of diffusion is present. It is important to note that the CPE (Q) takes into account diffusion processes and surface roughness. A low 'n' value as well as the low phase angles displayed in the TO Bode phase plots, indicates a diffusion process is most likely taking place. Therefore, the addition of the Warburg impedance element to **Figure 49** could accommodate for this diffusion process.

14 CONCLUSIONS

14.1 Surface treated Ti-6Al-4V

The oxygen boost diffusion hardening (OBDH) and thermal oxidation (TO) treatments were successfully carried out, resulting in an increase of the surface hardness of Ti-6Al-4V specimens. The OBDH treatments demonstrate the ability to develop a hardened alpha case below the surface to a depth of approximately 350µm, until hardness of the untreated metal was reached. This is significantly higher than the ~100µm oxygen diffusion zone displayed by the TO specimens. The increase in hardness is attributed to the amount of oxygen diffused into the substrate, whereby as the amount of oxygen within the lattice increases so does the hardness of the alloy. Therefore, in conclusion, the OBDH process showed a deeper hardness profile than the TO process.

14.2 Potentiodynamic (DC) Analysis

The DC electrochemical techniques utilized in this study led to the following conclusions:

- Long term immersion OCP tests displayed an increase in potential over time stabilizing at a higher final potential, indicating passivation of an oxide layer for untreated and treated Ti-6Al-4V specimens.

- The potentiodynamic response of untreated and treated Ti-6Al-4V specimens displayed low corrosion current densities in 3.5 wt.% NaCl indicating passivity in this electrolyte.

- The OBDH treated specimens displayed very similar potentiodynamic behaviour to the untreated specimen with a corrosion rate approximately 3.5 times lower than the untreated condition.

- The corrosion resistance of the TO specimens was found to display the lowest corrosion resistance with a corrosion rate approximately 24 times greater than the untreated condition.

- The corrosion resistance of the TO specimen was mainly dependent on the substrate and not the porous surface oxide.

- The OBDH specimens formed the most compact passive layer, demonstrating the lowest corrosion rate. Due to the high oxygen reservoir beneath the surface,

the oxide layer formed resulted in a highest corrosion resistance even at high potentials.

14.3 Electrochemical Impedance Spectroscopy (AC) Analysis

The AC electrochemical impedance techniques utilized led to the following conclusions:

- The theoretical model proposed for a metal with an oxide layer shows an excellent fit to the experimental data. The chi-square value in the region of 10^{-3} indicates excellent agreement between experimental and theoretical values.

- High impedance values were obtained for untreated and treated Ti-6Al-4V specimens, suggesting a high corrosion resistance of this alloy in the 3.5 wt.% NaCl. This result supports the passive behaviour of the alloys, consistent with OCP tests and potentiodynamic analysis.

- The TO specimen demonstrated different impedance behaviour to the untreated and OBDH specimens. The corrosion resistance displayed by the TO specimens was mainly due to the inner barrier layer and not attributed to the outer porous thermally oxidised layer.

- This porous oxide layer of the TO specimen was therefore not sufficiently compact to provide adequate corrosion resistance (from aggressive chloride ions) over the entire polarization range.

- Impedance analysis indicates that the untreated and OBDH specimens behaved in a similar way. However, the OBDH specimen provides a superior corrosion resistance over the entire polarization range, indicated by a consistent barrier layer resistance (R_2), even at high potentials.

- The impedance results are in good agreement with the electrochemical polarization data, as the OBDH Ti-6Al-4V specimen was found to provide superior overall corrosion performance in both instances.

- Therefore, EIS analysis supports the differences exhibited by potentiodynamic scans, validating the electrochemical behaviour of untreated and treated Ti-6Al-4V specimens.

15 REFERENCES

Ask, M., Lausmaa & Kasemo, B. (1988). Preparation and surface spectroscopic comparison of sputtered Ti, Ti6Al4V, and passivated bulk metals for use in cell culture techniques. J Vac Sci Technol A, A9, pp. 1329 – 1333.

Askeland D. R. & Phulé, P. P. (2006). The science and engineering of materials, 5th edition, Ontario, Bill Stenquist.

ASTM G5 – 94. (2004). Standard Reference Test Method for making Potentiostatic and Potentiodynamic Anodic Polarization Measurements, Annual Book of ASTM Standards, 03.02, pp. 71 – 77.

ASTM G3 – 89. (1989). Standard Practice for Conventions Applicable to Electrochemical Measurements in Corrosion Testing, Annual Book of ASTM Standards, 14.02, pp. 54 – 61.

Baltat-Bazia, A., Celati, N., Keddam, M., Takenouti, H. & Wiart, R. (1992). Mater. Sci. Forum, 359, pp. 111 – 112.

Boukamp, B. (1989). Proc. 9th. Euro. Congr. Corros., FU-252.

Beck, T.R. (1973). ibid, 120, n 10, pp. 1317.

Beck, T.R. (1973). J. of Electrochem. Soc., 120, n 10, pp. 1310.

Boyer, R., Welsch, G. & Collings, E. W. (1994). Materials Properties Handbook: Titanium Alloys, eds. ASM International. Materials Park, OH.

Blackwood, D.J. (2002). Biomaterials: past successes and future problems. in: Proceedings of the 15th International Corrosion Congress, Paper No 4, Granada, Spain

Blackwood, D.J. & Chooi, S.K.M. (2002). Corros. Sci., 44, pp. 395.

Bloyce, A., Qi, P.Y., Dong, H. and Bell, T. (1998). Surface modification of titanium alloys for combined improvements in corrosion and wear resistance. Surface and Coatings Technology, 107, pp. 125 – 132.

Boukamp, B. (1989). Proc. 9th. Euro. Congr. Corros., FU-252.

Burnell-Gray et al (1994). Air oxidation behaviour of Ti-6Al-4V between 650 and 850℃. Corrosion Science , 36, 4, pp. 631 – 642.

Carpenter (2000). Technical Datasheet, http://cartech.ides.com/datasheet.aspx?i=103&e=269&c=TechArt.

Da Fonseca, C., Bouden, S. & Da Cunha Belo, M. (1994). Characterization of titanium passivation films by in situ ac impedance measurements: an XPS analysis. J Electroanal Chem, 379, pp. 173 – 180.

Dolata, M., Kedzierawski, P. & Augustynski, J. (1996). Comparative impedance spectroscopy study of rutile and anatase TiO_2 film electrodes. Electrochim Acta, 41, pp. 1287 – 1293.

Dong, H. & Li, X.Y. (2000) Oxygen boost diffusion for the deep-case hardening of titanium alloys. Materials Science and Engineering, A280, pp. 303 - 310.

Enos, D.G. & Scribner, L.L. (1997). The Potentiodynamic Polarization Scan. Solartron Ltd, Technical Report 33.

Frauchiger, L., Taborelli, M. & Descouts, P. (1997). Appl. Surf. Sci., 115, pp. 232.

Gabrielli, C. (1997) Use and Application of Electrochemical Impedance Techniques.

Kauffman, A.M. (1997). Undersatanding Electrochemical Cells. Solartron Ltd, Technical Report 17.

Gamry Instruments. (2007). Basics of Electrochemical Impedance Spectroscopy.

Tamilselev, S., Murugaraj, R. & Rajendran, N. (2007). Electrochemical impedance spectroscopic studies of titanium and its alloys in saline solution. Materials ad Corrosion, 58, No. 2, pp. 113 – 120.

Garcia-Alonso, M.C., Saldana, L., Valles, G., Gonzalez-Carrasco, J.L., Gonzalez-

Cabrero, J., Martinez, M.E., Gil-Garay, E. & Munuera, L. (2002) In vitro corrosion behaviour and osteoblast response of thermally oxidised Ti6Al4V alloy, Biomaterials, 24, pp19 – 26.

Gonzalez, J.E.G. & Mirza-Rosca, J.C. (1999) . Journal of Electroanal. Chem., 471, pp. 109.

Gulyeryuz, H. & Cimenoglu, H. (2009). Oxidation of Ti-6Al-4V alloy. Journal of Alloys and Compounds, 472, pp. 241 – 246.

Hernardez de Gatica, N.L., Jones, G.L. & Gardella, Jr J.A. (1993). Surface characterization of titanium alloys sterilized for biomedical applications. Appl Surf Sci, 68, pp. 107 – 121.

Hsu, R.W., Yang, C., Huang, C. & Chen, Y. (2004). Electrochemical corrosion properties of Ti-6Al-4V alloy in biological environment. Materials Science and Engineering, A 380, pp. 100 – 109.

Johns, S.M. (1996). Wear resistance of plasma immersion ion implanted Ti6Al4V. Surface and Coatings Technology, 85, pp. 7-14.

Jones, D.A. (1996). Principles and Prevention of Corrosion 2nd Edition. Prentice Hall

Joubert, K.J. (1988). The influence of tempering on the corrosion resistance of newly developed steels. M.Sc thesis. Department of Material Engineering, University of Cape Town.

Khan, M.A., Williams, R.L. & Williams, D.F. (1996). In vitro corrosion and wear of titanium alloys in the biological environment. Biomaterials, 17, pp. 2117 – 2126.

Kolman, D.G. & Scully, J.R. (1994). ibid, 141, n 10, pp. 2633.

Kolman, D.G. & Scully, J.R. (1993). J. of Electrochem. Soc., 140, n 10, pp. 2771.

Lavos-Valereto, I.C., Wolynec, S., Ramires, I., Guastaldi, A.C., Costa, I. & Mater, J. (2004). Sci. :Mater. Med, 55.

Long, M. & Rack, H.J. (1998). Titanium alloys in total joint replacement : a materials science perspective. Biomaterials Journal,19, pp. 1621 - 1639.

Loveday, D., Peterson, P. & Rodgers, B. (2004) Evaluation of organic coatings with electrochemical impedance spectroscopy. JCT Coatings Tech.

Luiz de Assis, S., Wolynec, S. & Costa, I. (2006) Corrosion characterization of titanium alloys by electrochemical techniques. Electrochimica Acta, 51, pp. 1815 – 1819.

Luo, J., et al (2004). The computer simulation of the boost diffusion oxidation process for the deep-case hardening of titanium alloys. J. Phys. IV France, 120, pp. 259 – 268.

Lutjering, G. & Williams, J.C. (2007). Titanium, 2nd edition, New York, Springer.

Maeusli, P-A., Bloch, P.R., Geret, V. (1986). Biological and biomechanical performance of biomaterials. Amsterdam: Elsevier, pp. 57

Mansfeld, F. (1993). Analysis and interpretation of EIS data for metals and alloys. Solartron-Schlumberger, Chapter 4, Technical Report 26.

Mansfeld, F. & Kendig, M.W. (1988 J. Electrochem. Soc., 135, pp.828.

Marino, C.E.B., Biaggio, S.R., Rocha-Filho, R.C. & Bocchi, N. (2006). q on Ti6Al4V alloy in chloride medium. Electrochimica Acta, 51, pp. 6580 – 6583.

Marinovic, A., Metikos-Hukovic, M. & Milosev, I. (2000). Stress generation during the growth of anodic oxide films on titanium-aluminium alloys, 50th ISE Meeting presentation.

Metals Handbook. (1990) - Properties and Selection: Nonferrous Alloys and Special-Purpose Materials, ASM International, 2, 10th Ed.

Milosev, I., Metikos-Hukovic, M. & Strehblow, H.-H. (2000). Passive film on orthopaedic TiAlV alloy formed in physiological solution investigated by X-ray photoelectron spectroscopy. Biomaterials, 21, pp. 2103 – 2113

Okazaki, Y. & Gotoh, E. (2005). Comparison of metal release from various metallic biomaterials in vitor. Biomaterials, 26, pp. 11 – 21.

Okazaki, Y., Tateishi, T. & Ito,Y. (1997). Corrosion resistance of implant alloys in pseudo physiological solutions and role of alloying elements in passive fims. Mater Trans JIM, 38, pp. 78 – 84.

Pan, J., Thierry, D. & Laygraf, C. (1996). Electrochemical Impedance Spectroscopy study of the passive oxide film on titanium for implant application. Electrochimica Acta, 41, pp. 1143 – 1153.

Pham, M.T., Zygaow, I. & Matz, W. (1997). Corrosion behaviour ad microstructure of titanium implanted with α and β stabilizing elements. Thin Solid Films, 3, pp. 251 – 259.

Princeton Applied Research. (1985). Basics of Electrochemical Impedance Spectroscopy. Princeton Applied Research, Application Note AC-1

Princeton Applied Research (1982) Basics of Corrosion Measurements. Princeton Applied Research, Application Note AC-1.

Qazi, J. I., Rahim, J., Senkov O. N. and F. H. Froes. (2002). Phase Transformations in the Ti-6Al-4V-H System, Journal of Metals, 54, pp. 68-71.

Raetzer-Sheibe, H.J. (1978) Corrosion, 34, n 12, pp 437.

Ramires, I & Guastaldi, A.C. (2002). Quim. Nova, 25, n 1, pp. 10.

Ramires, I & Guastaldi, A.C. (2001). Electrochemical study of the corrosion of Ti-Pd and Ti-6Al-4V electrodes in sodium chloride solutions. Biomecanica, 9, 1, pp. 61 – 65.

Rammelt U. & Reinhard G. (1990). On the applicability of a constant phase element (CPE) to the estimation of roughness of solid metal electrodes. Electrochim. Acta., 35, 6, pp 1045.

Roberge, P. (2008). Chapter 5 Corrosion Kinetics and Applications of Electrochemistry to Corrosion.

Robin, A., Sandim, H.R.Z. & Rosa, J.L. (1999). Corros. Sci., 41, pp. 1333.

Schmidt A.M. & Azambuja D.S. (2006). Electrochemical Behaviour of Ti and Ti6Al4V in aqueous solutions of citric acid containing halides. Materials Research, 9, n 4, pp. 387 – 392.

Schmidt, A.M. & Azambuja, D.S. (2003). Effect of Flouride Ions on Ti6Al4V Alloy Passivation in Lactated Ringer's Serum. Materials Research, 6, No. 2, pp. 227 – 231.

Schmiedgen, M.; Baretzky, B.; Schminke, A.; Schmidt, H. (1997). X-ray photoelectron spectroscopy characterization of ion-implanted Ti-6Al-4V. Paper presented at the ECASIA '97, pp. 143 – 146.

Schultze, J.W. & Kudelka, S. (1997). Investigations of passivity. The Electrochem Soc Interface, 6, pp. 28 – 31.

Sodhi, R.N.S., Weninger, A., Davis, J.E. & Sreenivas, K. (1991). X-ray photoelectron spectroscopic comparison of sputtered Ti, Ti6Al4V, and passivated bulk metals for use in cell culture techniques. J Vac Sci Technol A, A9, pp. 1329 – 1333.

Songur, M., Celikkan, H., Gokmese, F., Simsek, S.A., ltun, N.S. & Aksu, M.L. (2009). Electrochemical corrosion properties of metal alloys used in orthopaedic implants. J Appl Electrochem, 39, pp. 1259 - 1265.

Souto, R.M., Laz, M.M. & Reis, R.L. (2003). Degradation characteristics of hydroxyapatite coatings on aorthopaedic TiAlV in simulated physiological media investigated by electrochemical impedance spectroscopy. Biomaterials, 24, pp. 4213 – 4221.

Sul, Y.-T., Johansson, C.B., Petronis, S., Kroger, A., Wennerger, A. & Albrektsson, T. (2002). Biomaterials, 23.

Sundararajan, T., Kamachi Mudali, U., Mair, K.G.M., Rajeswari, S. & Subbiyan, M. (1998). Surface characterization of electrochemically formed passive film on nitrogen implanted Ti6Al4V alloy. Mater Trans JIM, 39, pp. 756 – 761.

Tait, W.S. (1994). An Introduction to Electrochemical Corrosion Testing for Practicing Engineers and Scientists. Ph. D thesis. Department of Material Engineering, University of Cape Town

Thompson, I. & Campbell. (1994). Interpreting Nquist responses from defective coatings on steel substrates. Corros Sci, 36, pp187-198.

Tomkiewicz, M. (1979). Relaxation spectrum analysis of semiconductor-electrolyte interface – TiO_2. J Electrochem Soc, 126, pp. 2220 – 2225.

Venugopalan, R., Wimer, J.J., George, M.A. & Lucas, L.C. (2000). Biomaterials, 21, pp. 1669.

Wang, C., Wang, M. & Zhou, X. (2003). Nucleation and growth of apatite on chemically treated titanium ally: an electrochemical impedance spectroscopy study. Biomaterials, 24, pp. 3069 – 3077.

Wieland, M., Sittig, C. & Textor, M. (1997). Surface compostion and topography of titanium alloy implants. Paper presented at the ECASIA '97, pp. 139 – 124.

Yeroklin, A.L., Nie, Y., Leyland, A. & Mathews, A. (2000). Surf. Coat. Technol., 130, pp. 195.

Zhang, Z. X., Dong, H., Bell, T. and Xu, B. (2008). The effect of deep-case oxygen hardening on the tribological behaviour of a-C:H DLC coating on Ti6Al4V alloy. Journal of Alloy and Compounds, 464, pp. 519-525.

Zhang, Z. X., Dong, H., Bell, T. and Xu, B. (2007). The effect of treatment condition on boost diffusion of thermally oxidized titanium alloy. Journal of Alloys and Compounds, 431, pp. 93 – 97.

Zhang, Z. X., Dong, H., Bell, T. and Xu, B. (2006). The load bearing capacity of hydrogen-free Cr-DLC coatings on deep-case oxygen hardened Ti6Al4V. Surface and Coatings Technology, 200, pp. 5237-5244.

16 APPENDIX

Sections 16.1, 16.2 and 16.3 display the Nquist and Bode plots for untreated, TO and OBDH Ti-6Al-4V specimens respectively. The appendix displays the individual Nquist and Bode plots of untreated and treated specimens at each offset potential from -0.5V to $3.0V_{SCE}$. At all offset potentials the best fit, between the experimental and theoretical curve, was always attained by employing the circuit proposed in **Figure 49**. Chi-square value between 10^{-3} - 10^{-4} which indicates excellent agreement between the experimental and theoretical data.

16.1 Untreated Ti-6Al-4V Potential Variation Impedance Plots

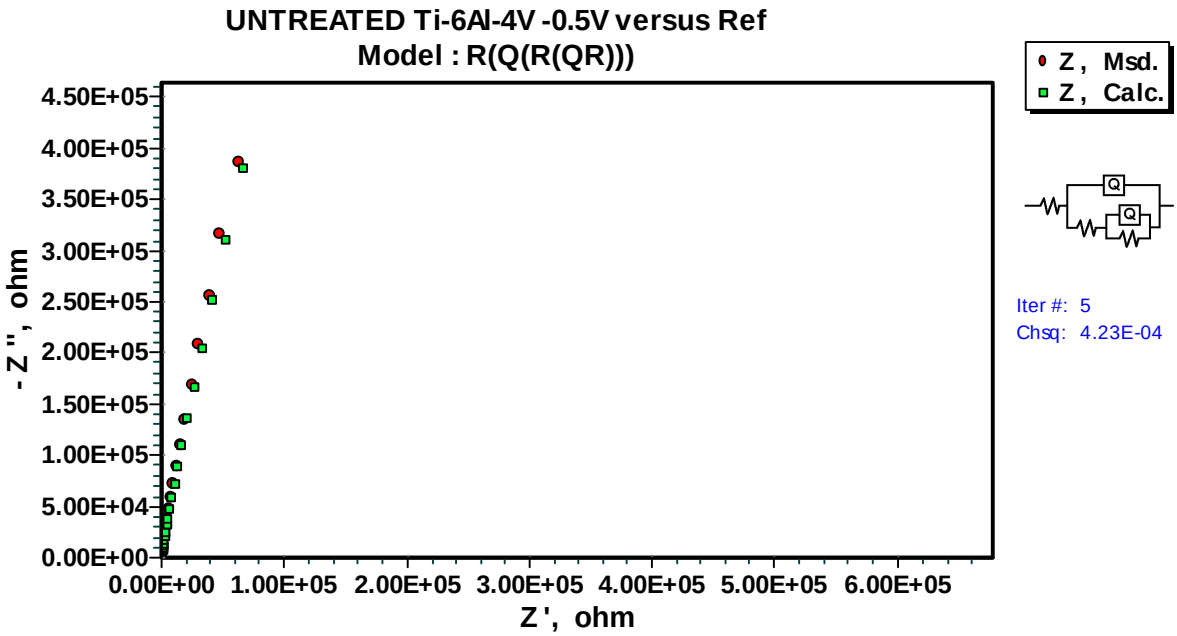

Figure 74: Nquist plot for untreated Ti-6Al-4V at -0.5V_{SCE}.

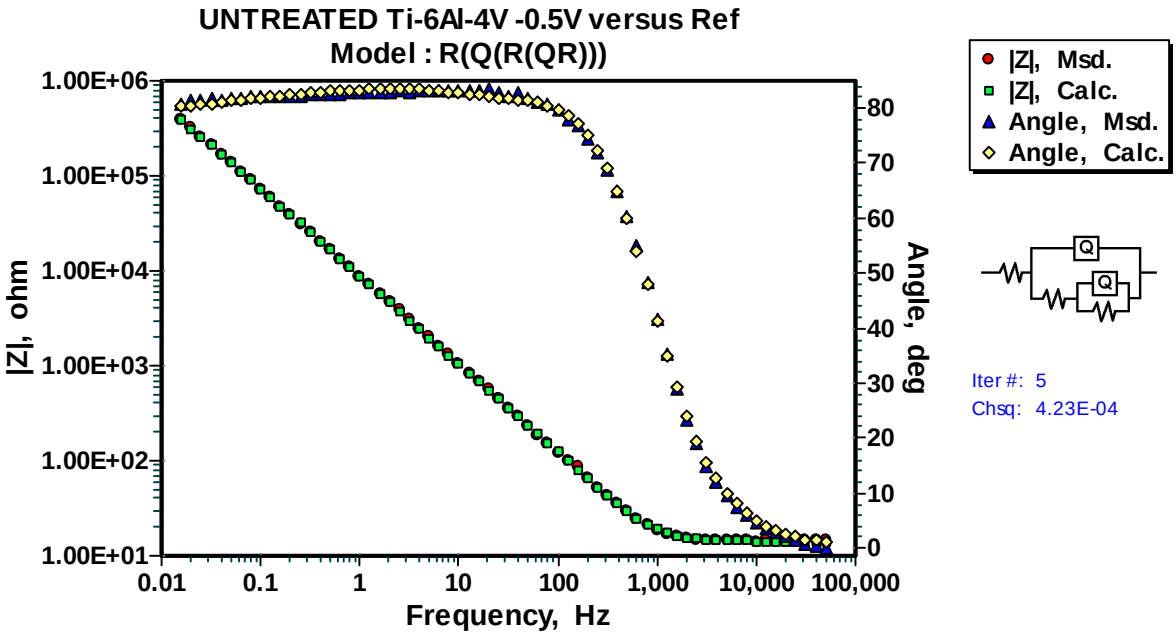

Figure 75: Bode Magnitude and Bode Phase plots for untreated Ti-6Al-4V at -0.5V_{SCE}.

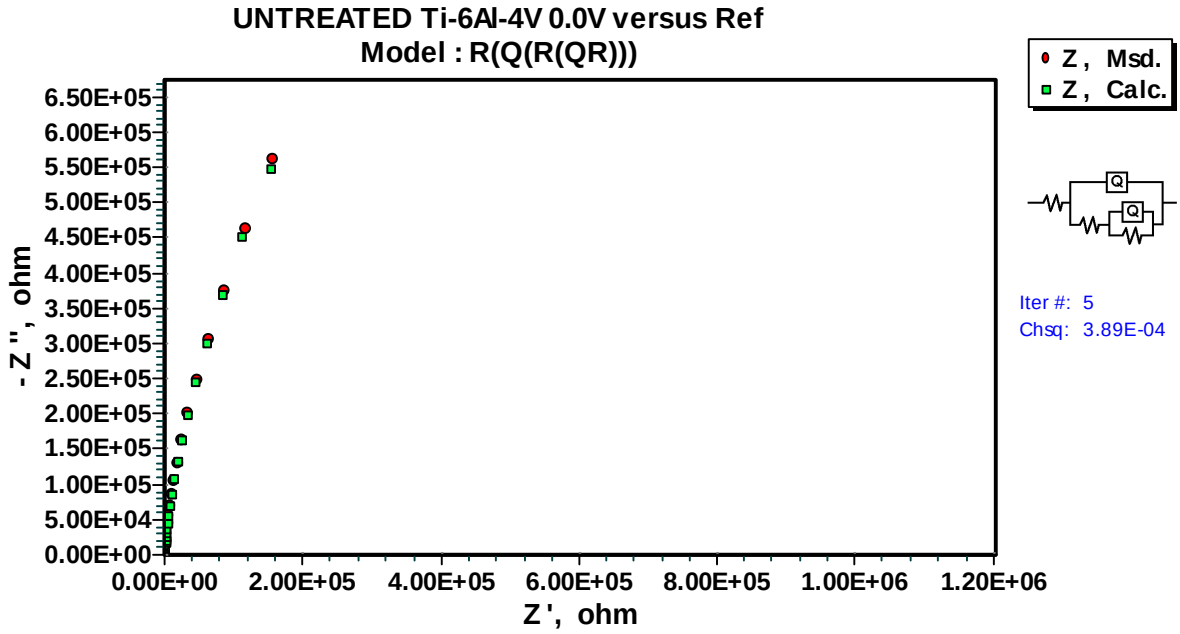

Figure 76: Nquist plot for untreated Ti-6Al-4V at at 0.0V_{SCE}.

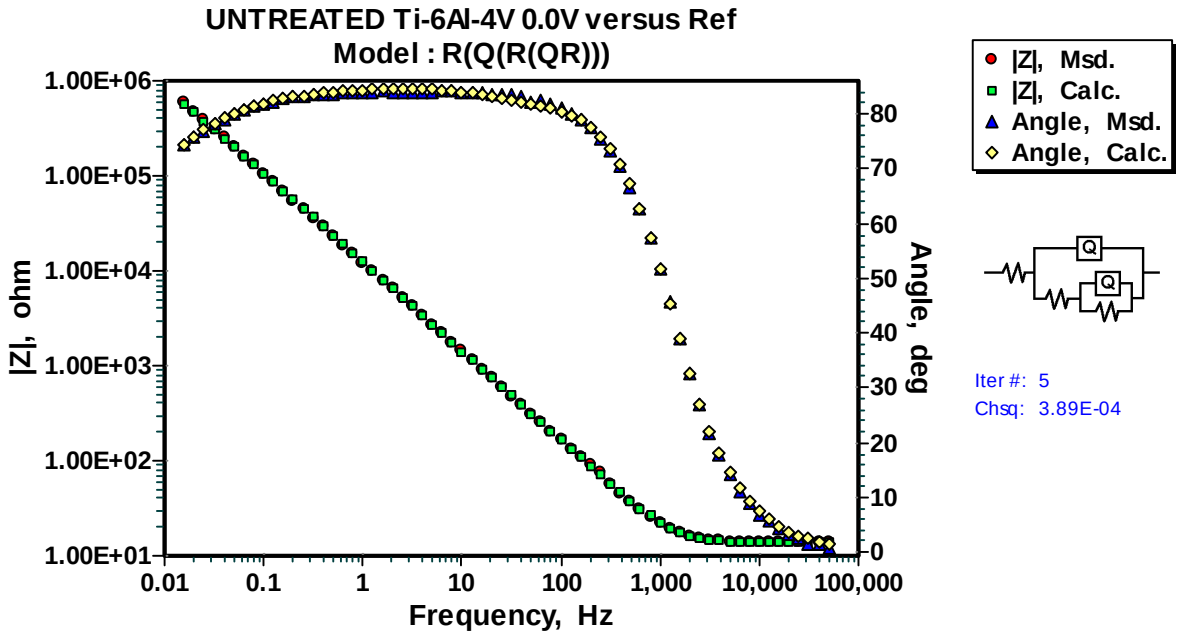

Figure 77: Bode Magnitude and Bode Phase plots for untreated Ti-6Al-4V at 0.0V_{SCE}.

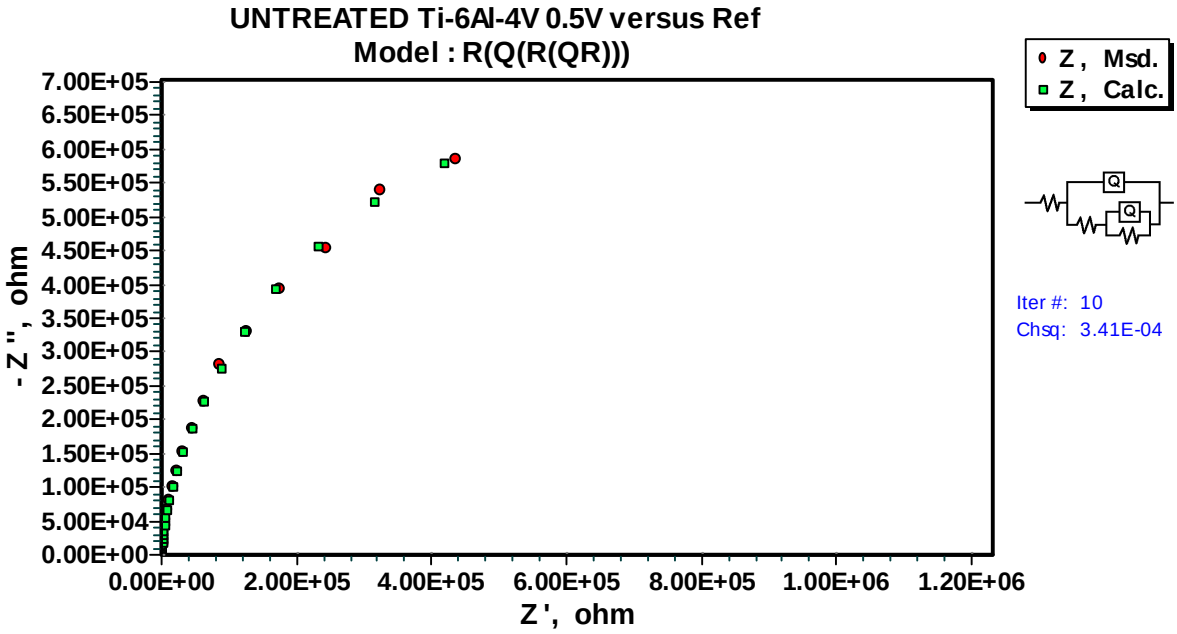

Figure 78: Nquist plot for untreated Ti-6Al-4V at 0.5V_{SCE}.

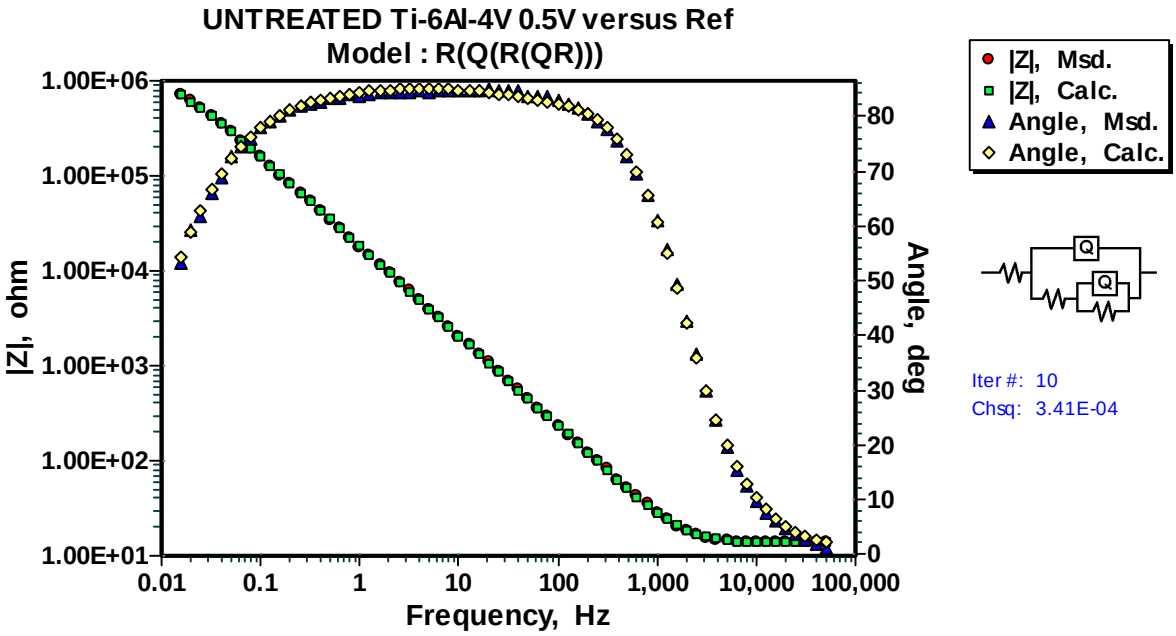

Figure 79: Bode Magnitude and Bode Phase plots for untreated Ti-6Al-4V at 0.5V_{SCE}.

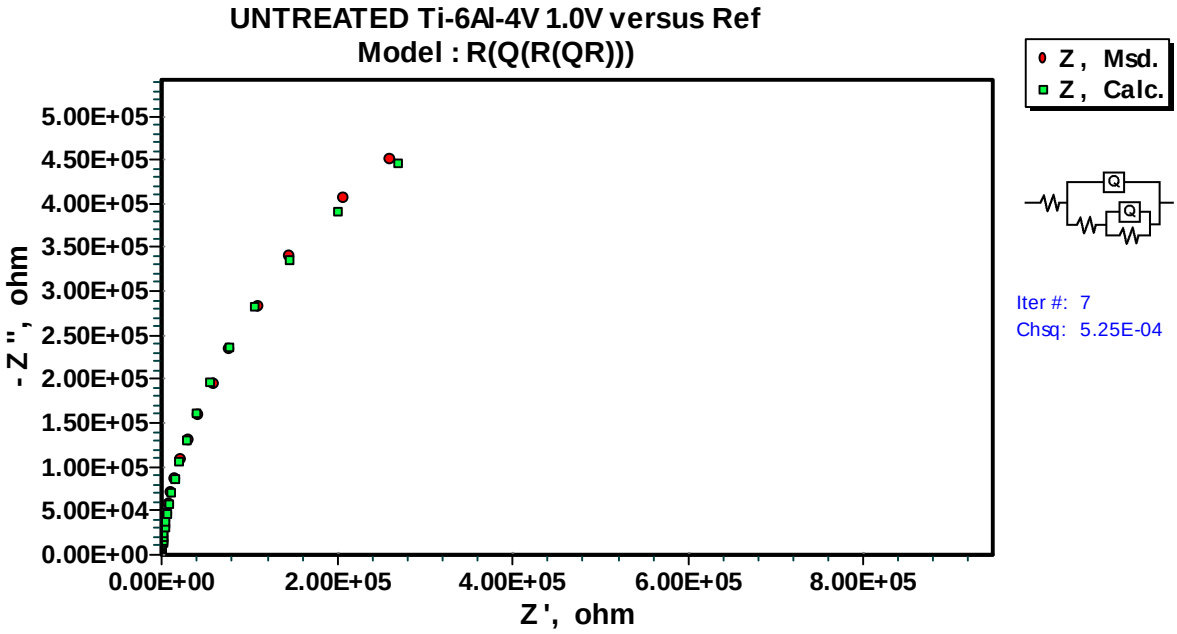

Figure 80: Nquist plot for untreated Ti-6Al-4V at 1.0V_{SCE}.

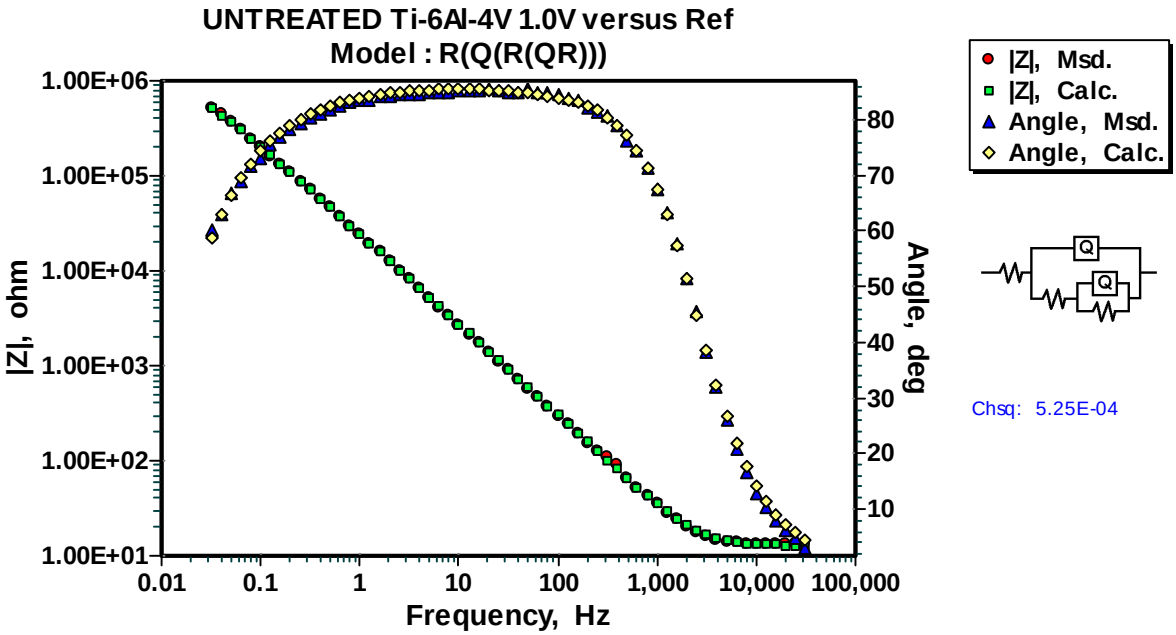

Figure 81: Bode Magnitude and Bode Phase plots for untreated Ti-6Al-4V at 1.0V_{SCE}.

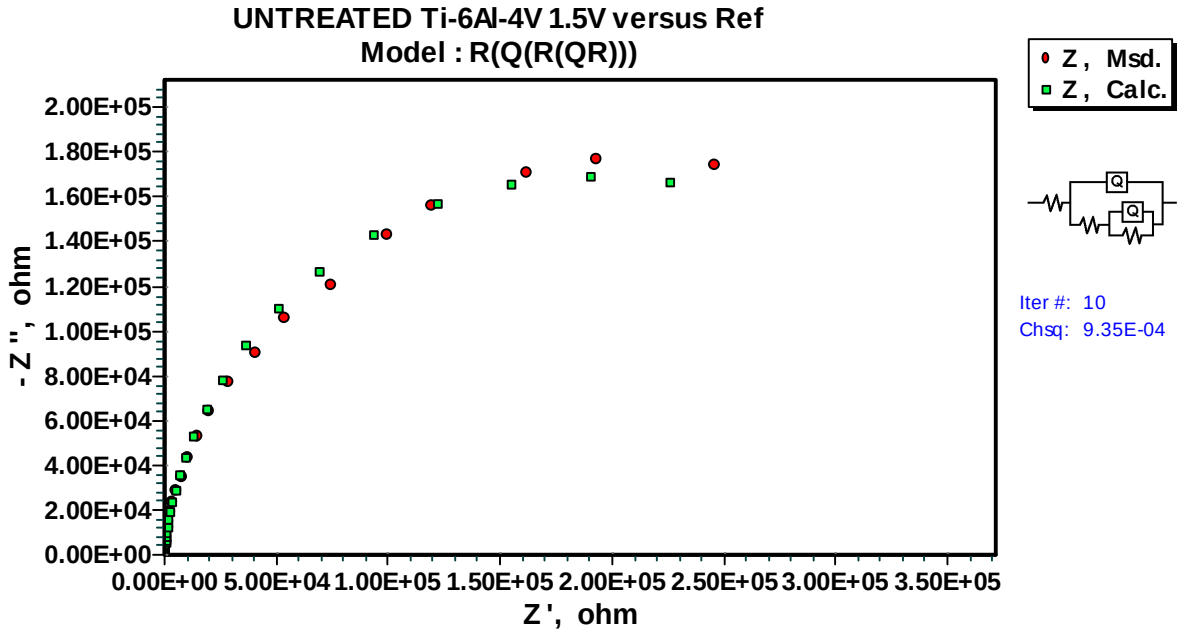

Figure 82: Nquist plot for untreated Ti-6Al-4V at $1.5V_{SCE}$.

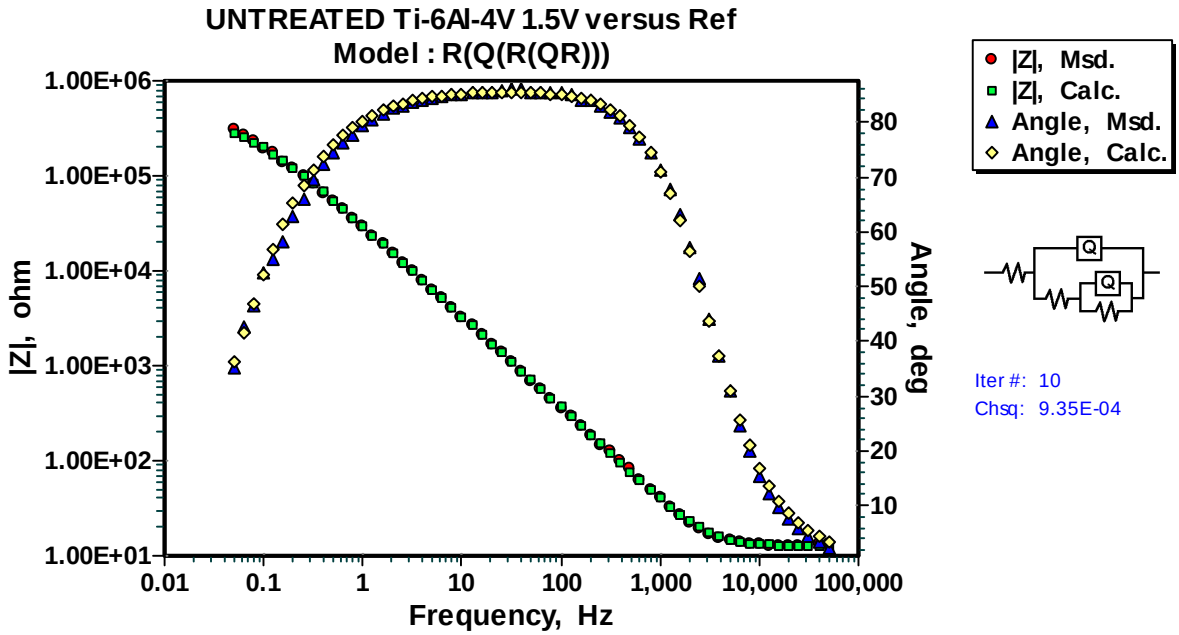

Figure 83: Bode Magnitude and Bode Phase plots for untreated Ti-6Al-4V at $1.5V_{SCE}$.

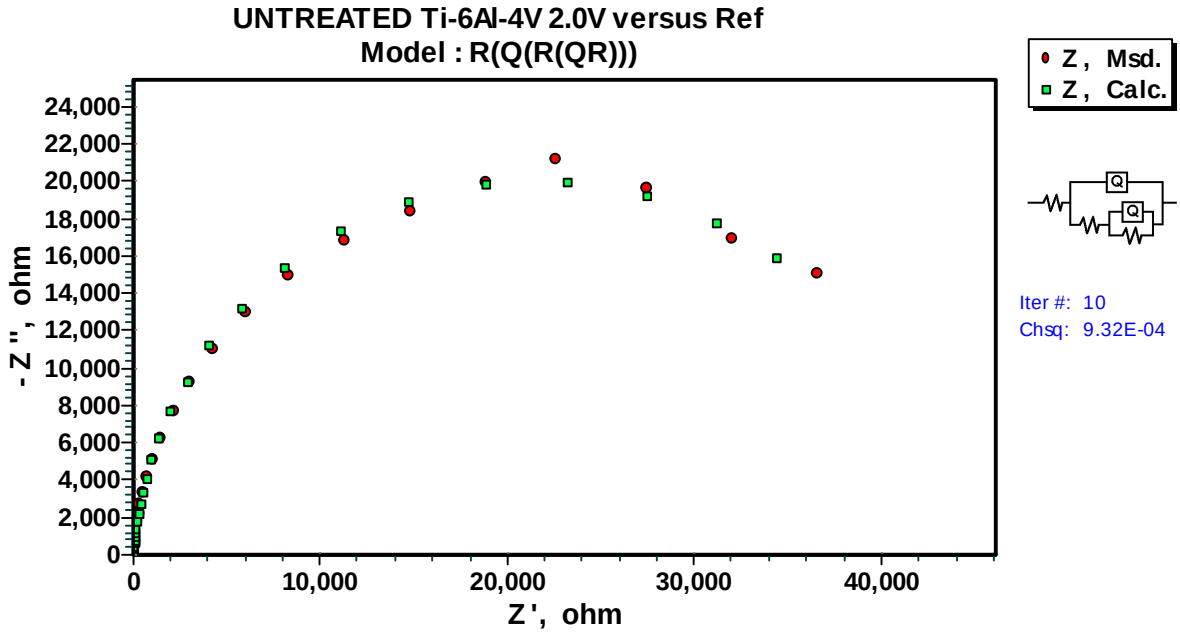

Figure 84: Nquist plot for untreated Ti-6Al-4V at 2.0V_{SCE}.

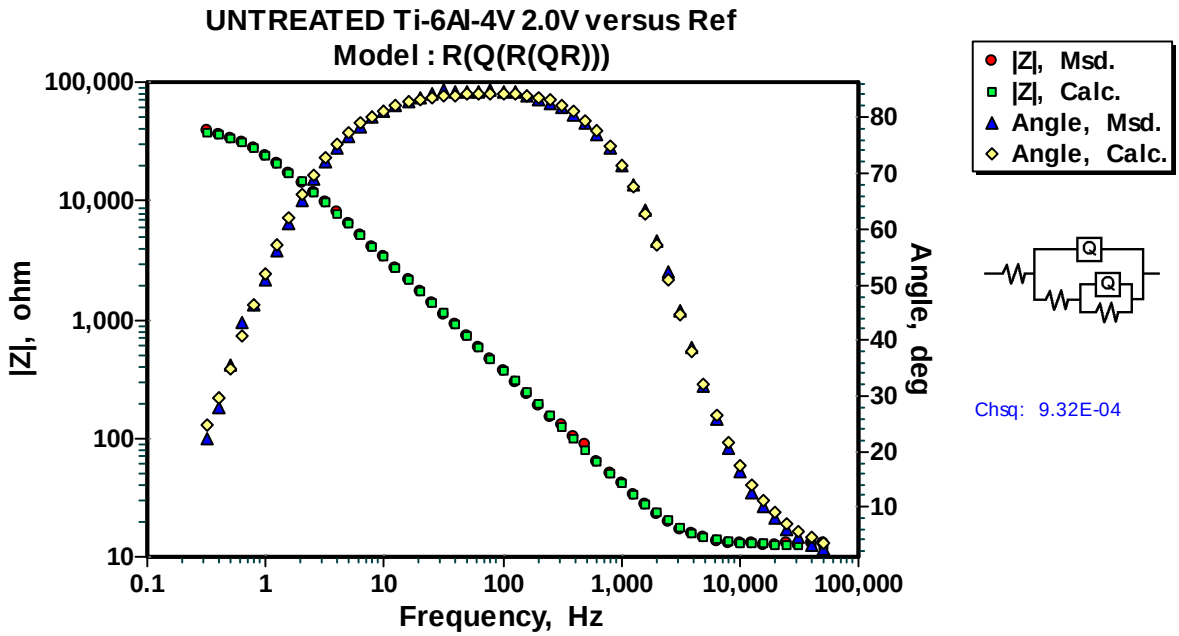

Figure 85: Bode Magnitude and Bode Phase plots for untreated Ti-6Al-4V at 2.0V_{SCE}.

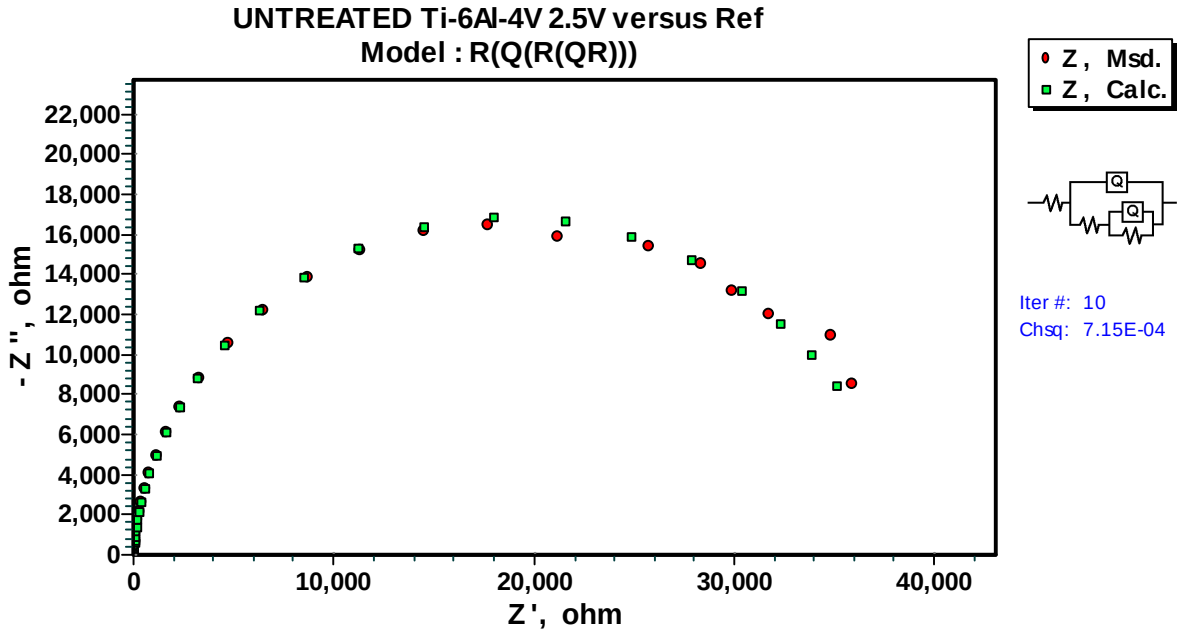

Figure 86: Nquist plot for untreated Ti-6Al-4V at 2.5V_{SCE}.

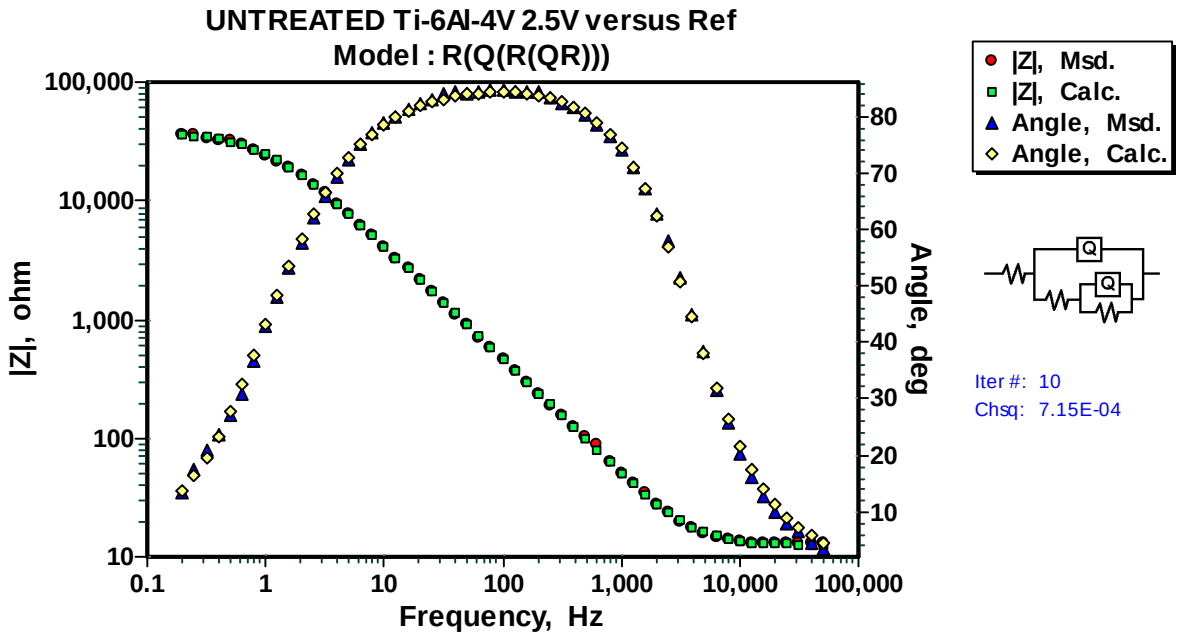

Figure 87: Bode Magnitude and Bode Phase plots for untreated Ti-6Al-4V at 2.5V_{SCE}.

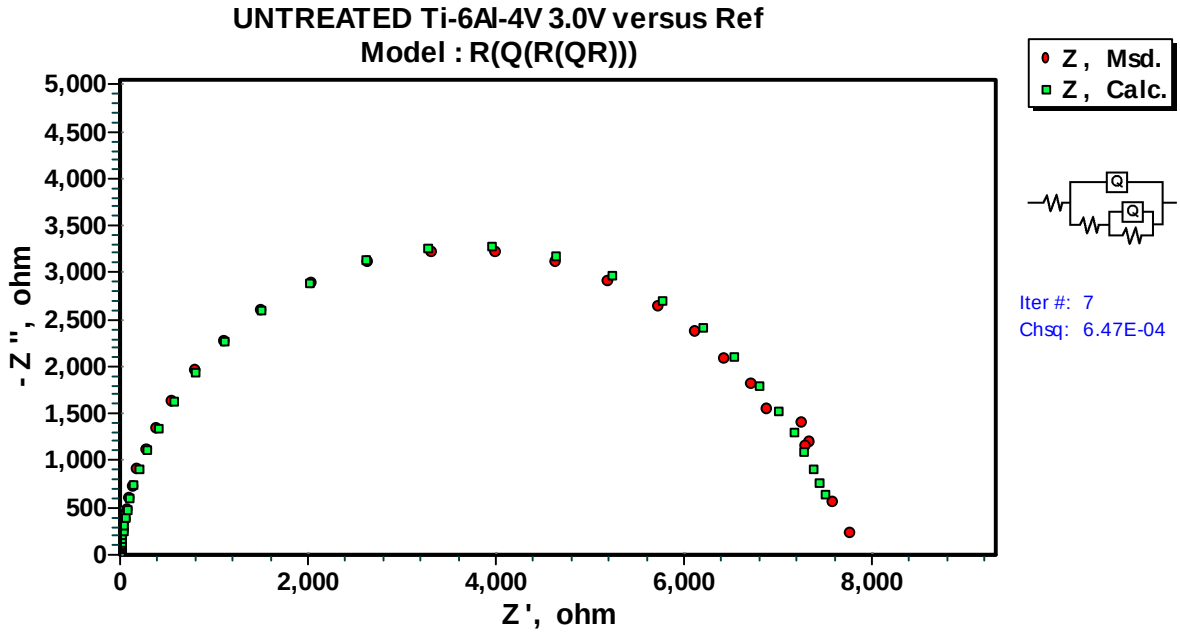

Figure 88: Nquist plot for untreated Ti-6Al-4V at 3.0V_{SCE}.

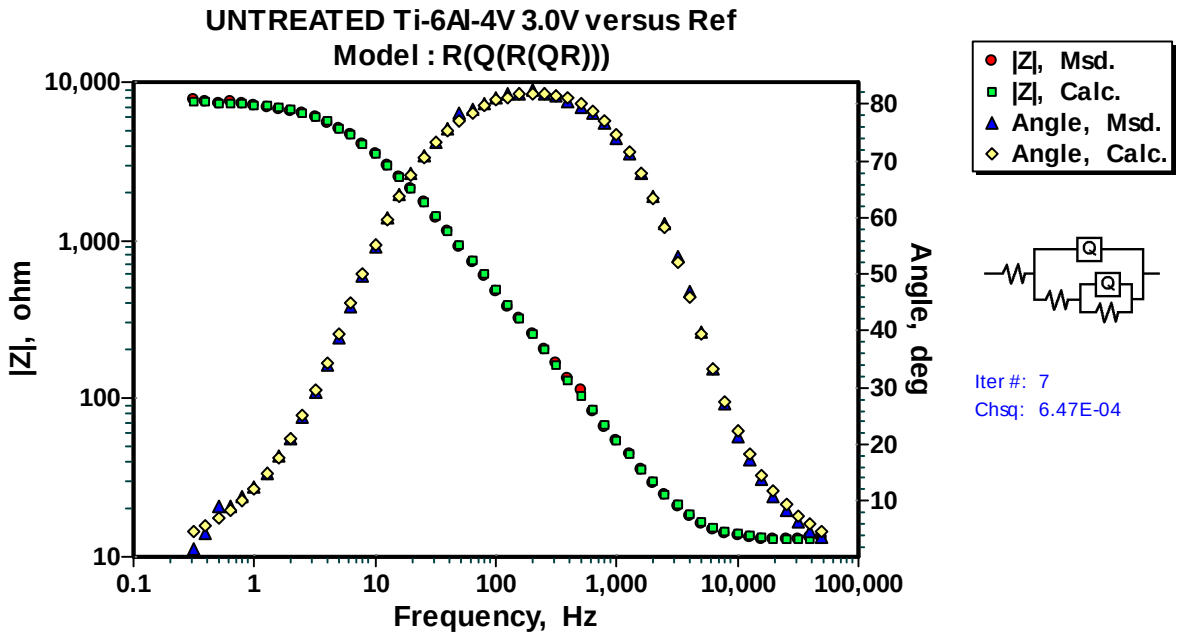

Figure 89: Bode Magnitude and Bode Phase plots for untreated Ti-6Al-4V at 3.0V_{SCE}.

16.2 TOTi-6Al-4V Potential Variation Impedance Plots

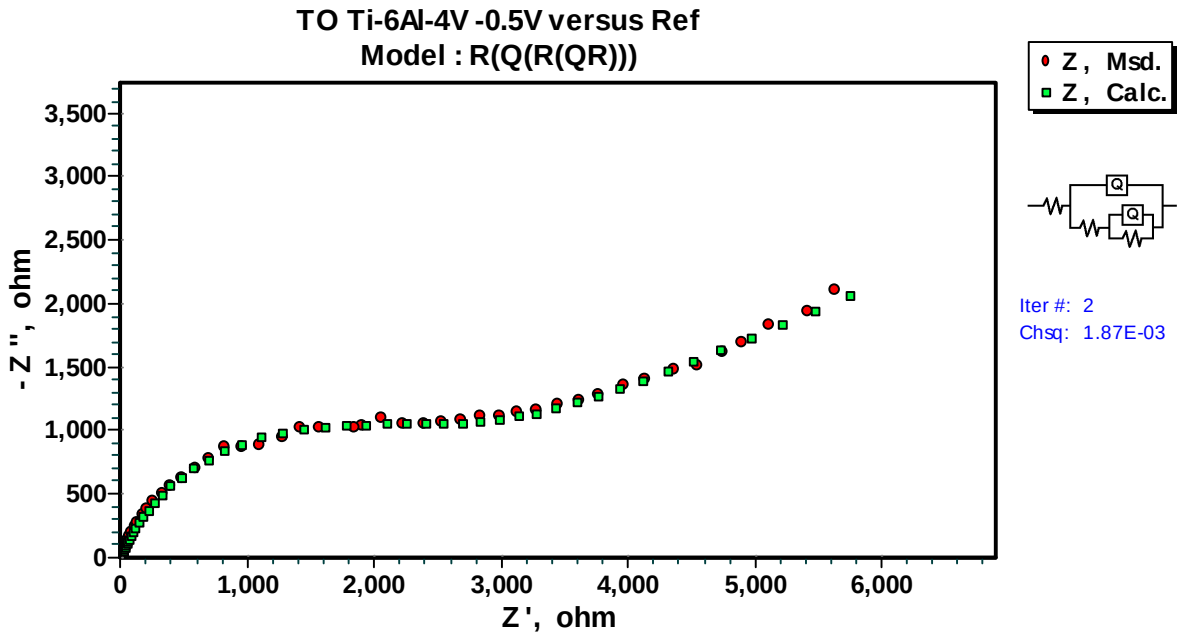

Figure 90: Nquist plot for TO Ti-6Al-4V at -0.5V_{SCE}.

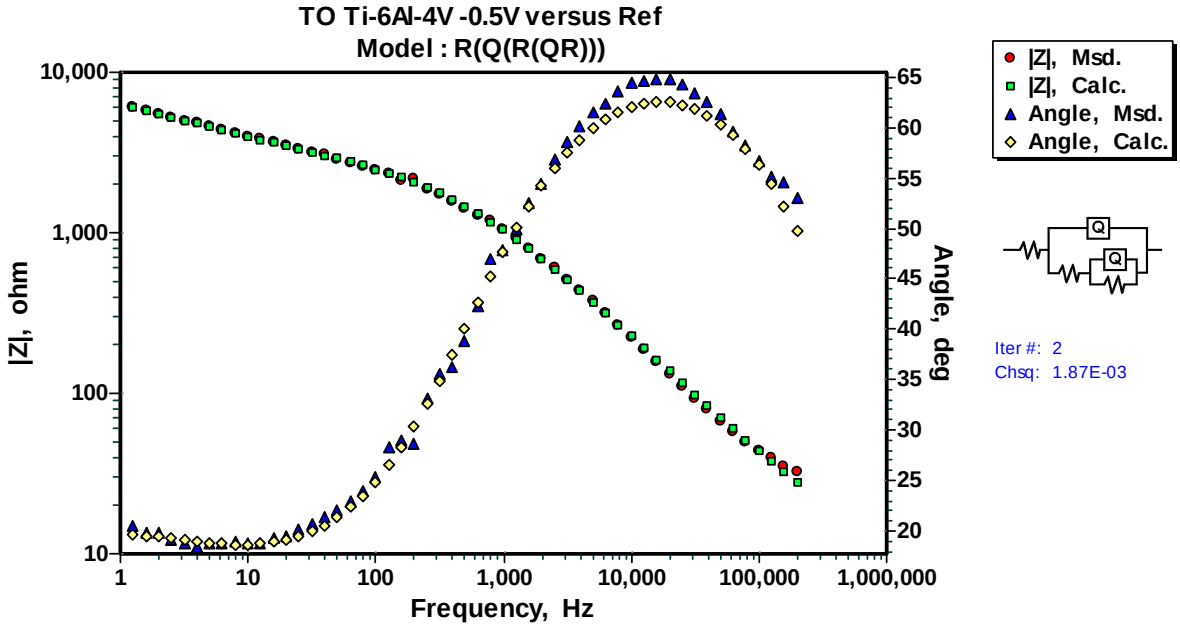

Figure 91: Bode Magnitude and Bode Phase plots for TO Ti-6Al-4V at -0.5V_{SCE}.

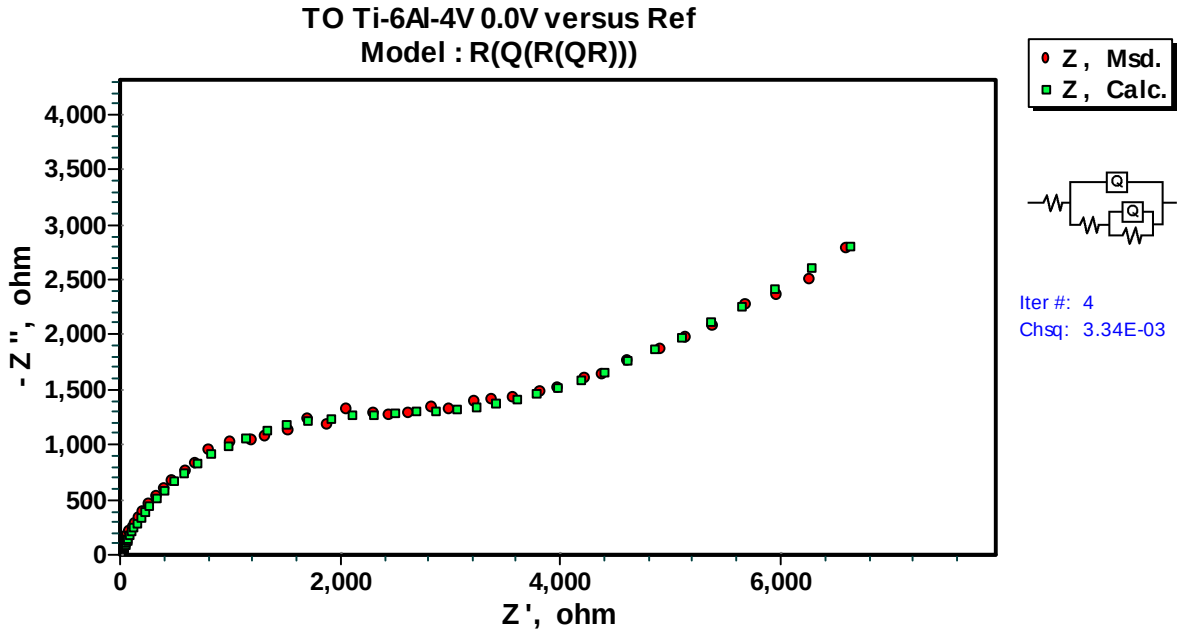

Figure 92: Nquist plot for TO Ti-6Al-4V at 0.0V_{SCE}.

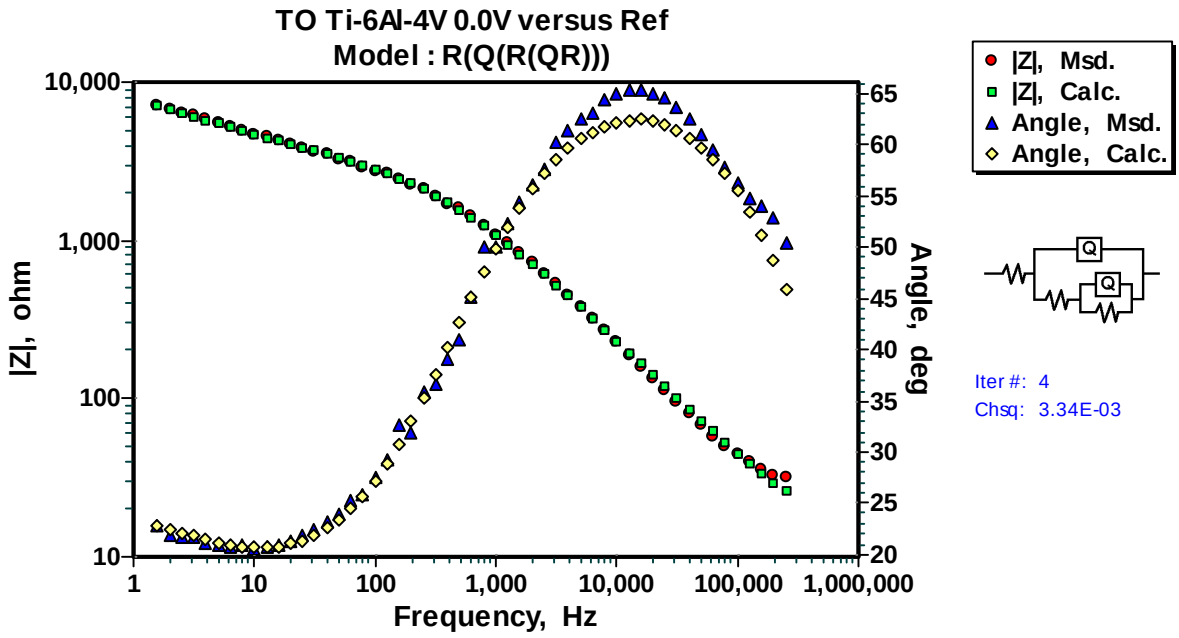

Figure 93: Bode Magnitude and Bode Phase plots for TO Ti-6Al-4V at 0.0V_{SCE}.

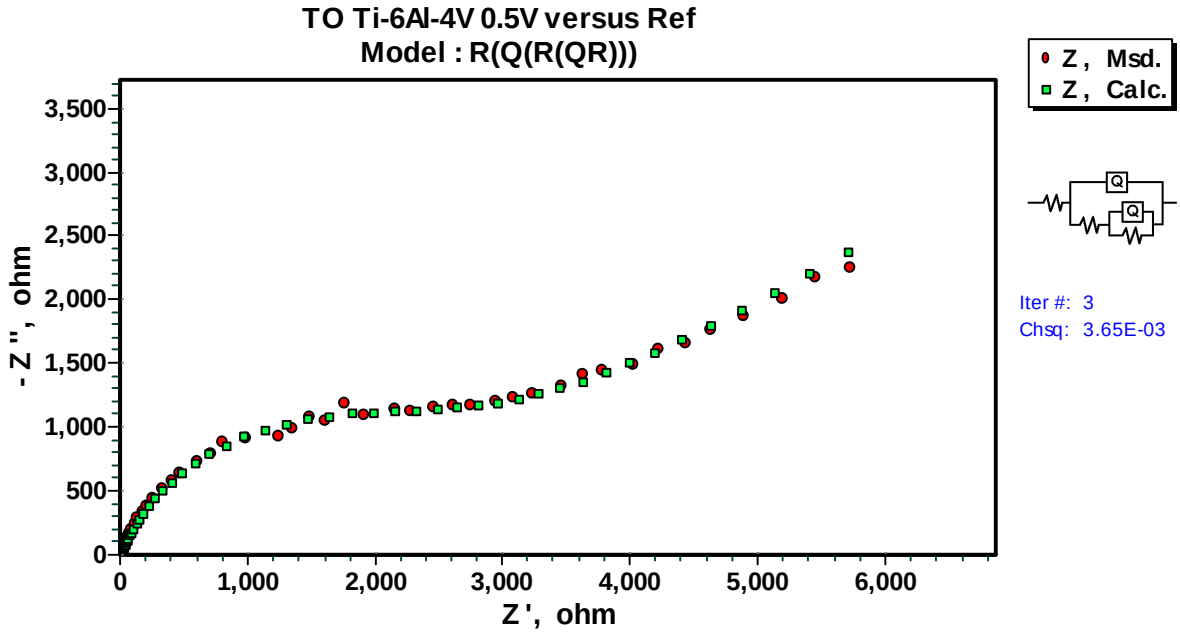

Figure 94: Nquist plot for TO Ti-6Al-4V at 0.5V_{SCE}.

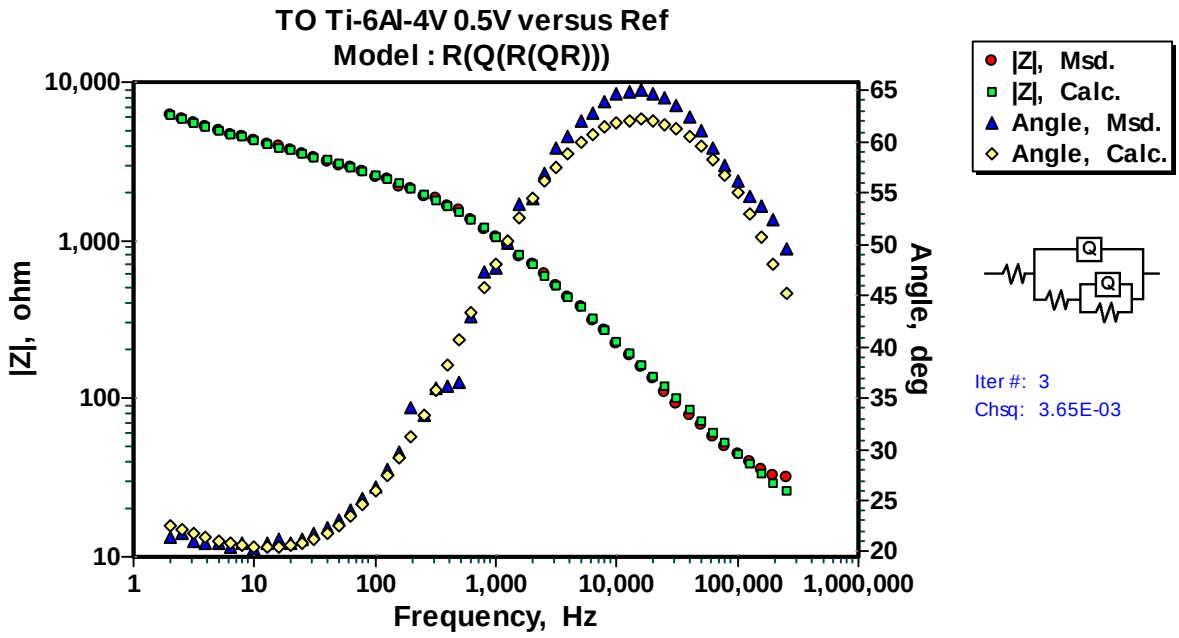

Figure 95: Bode Magnitude and Bode Phase plots for TO Ti-6Al-4V at 0.5V_{SCE}.

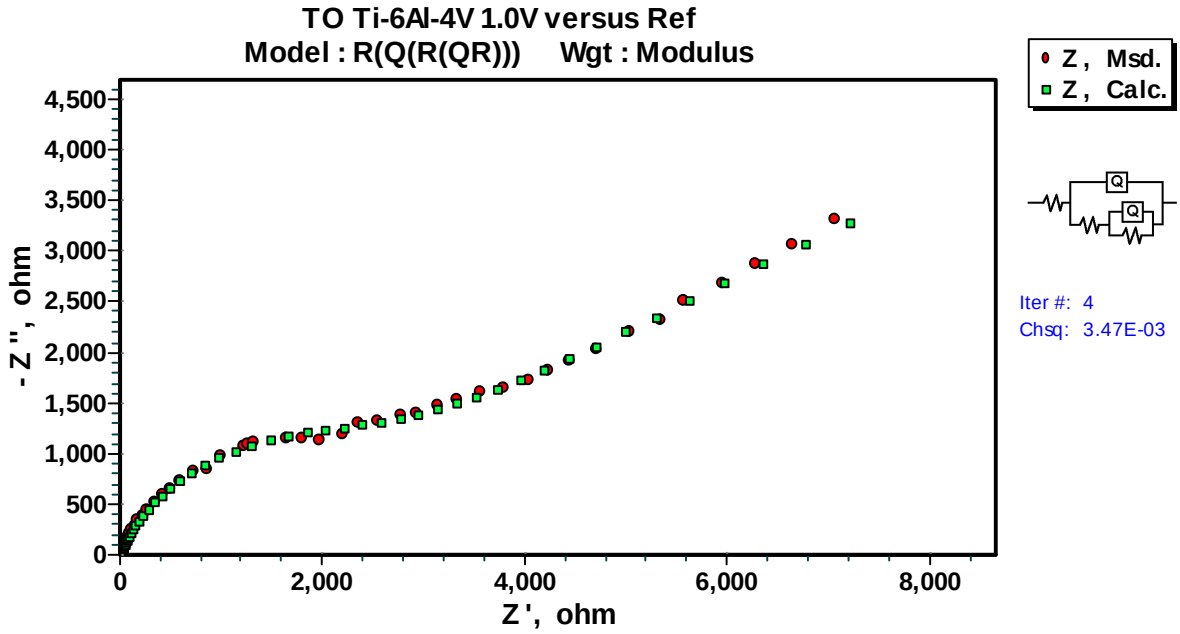

Figure 96: Nquist plot for TO Ti-6Al-4V at 1.0V_{SCE}.

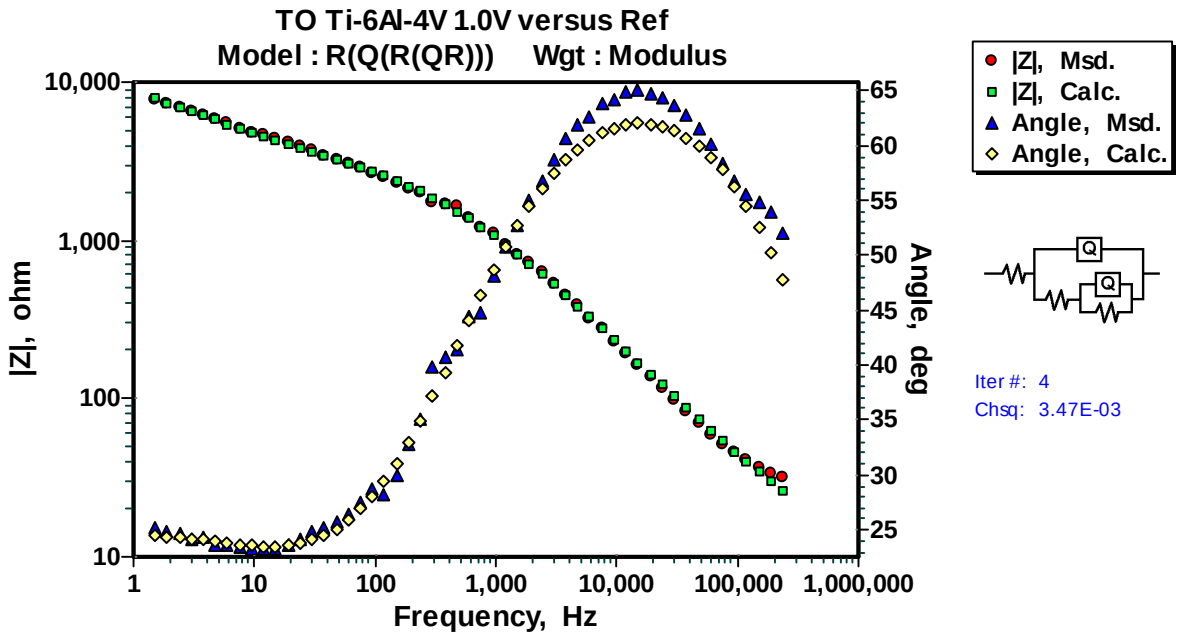

Figure 97: Bode Magnitude and Bode Phase plots for TO Ti-6Al-4V at 1.0V_{SCE}.

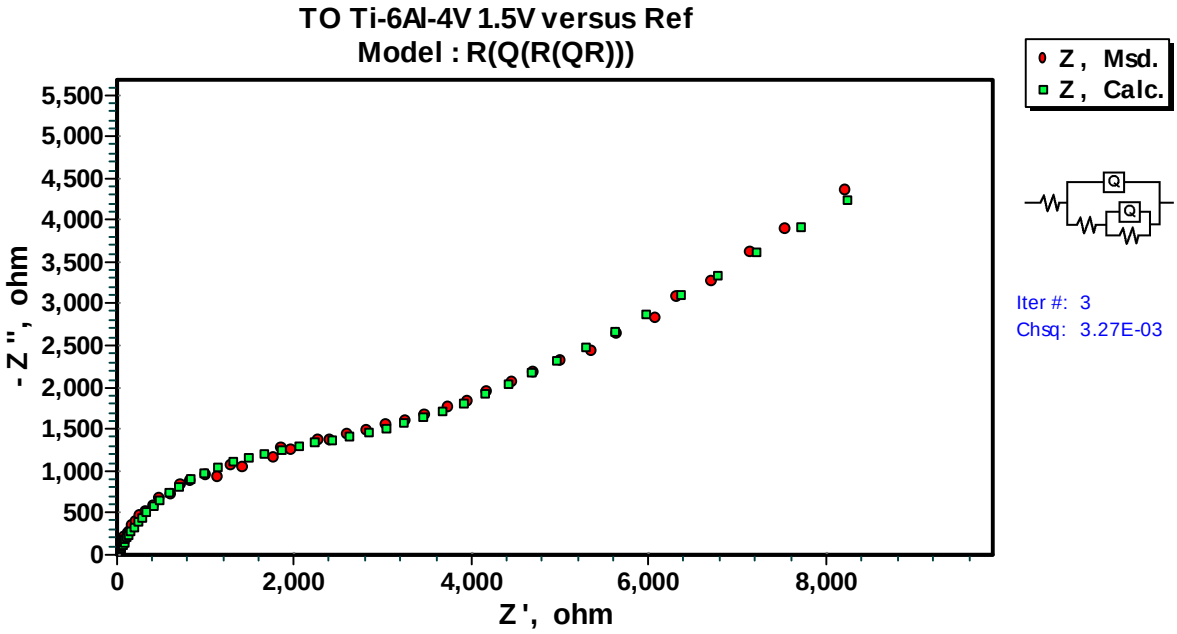

Figure 98: Nquist plot for TO Ti-6Al-4V at 1.5V_{SCE}.

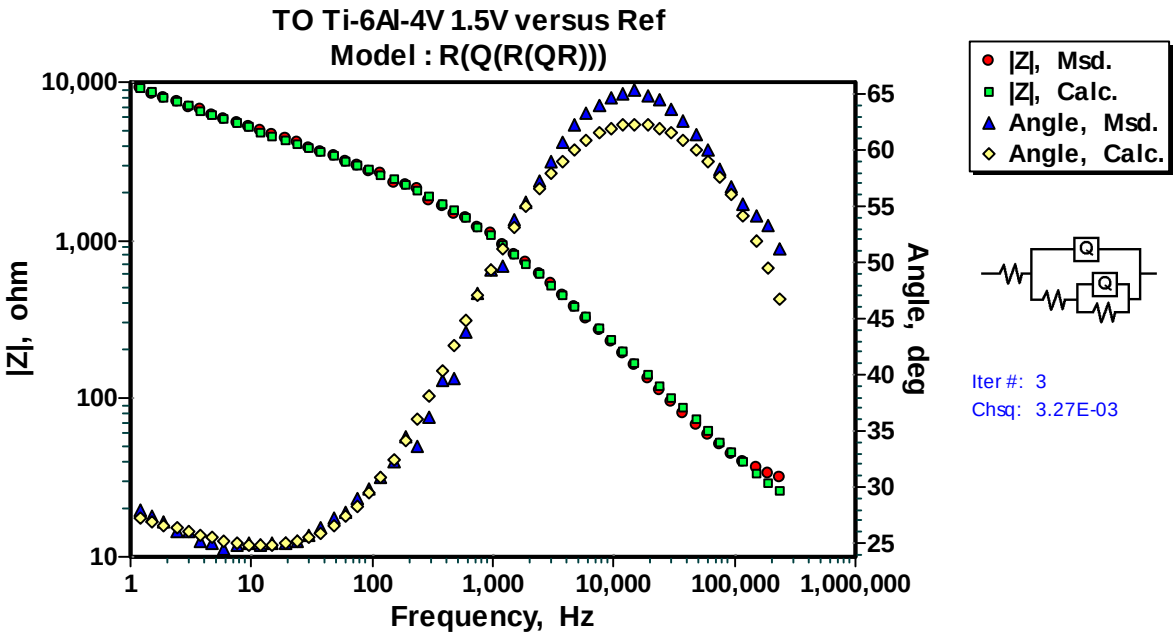

Figure 99: Bode Magnitude and Bode Phase plots for TO Ti-6Al-4V at 1.5V_{SCE}.

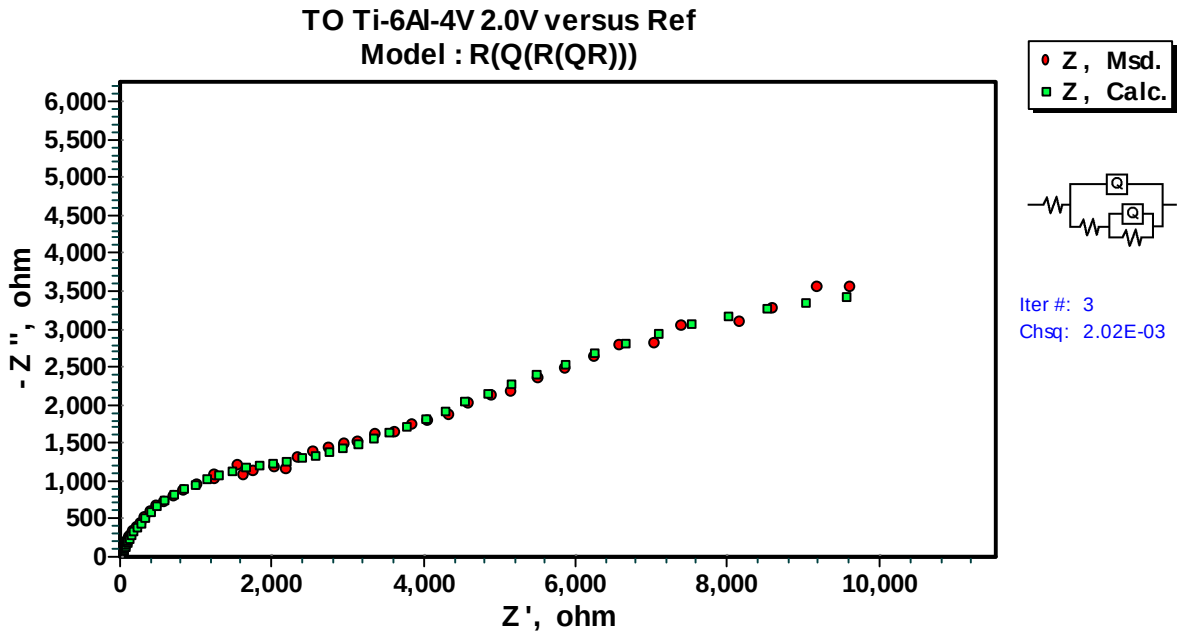

Figure 100: Nquist plot for TO Ti-6Al-4V at 2.0V_{SCE}.

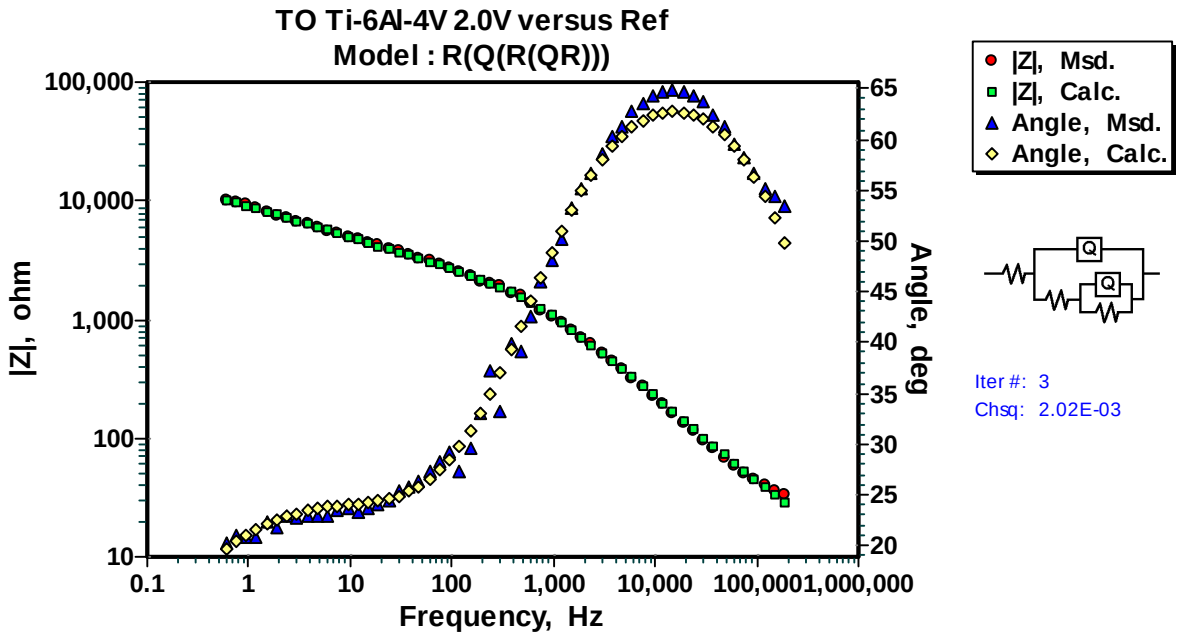

Figure 101: Bode Magnitude and Bode Phase plots for TO Ti-6Al-4V at 2.0V_{SCE}.

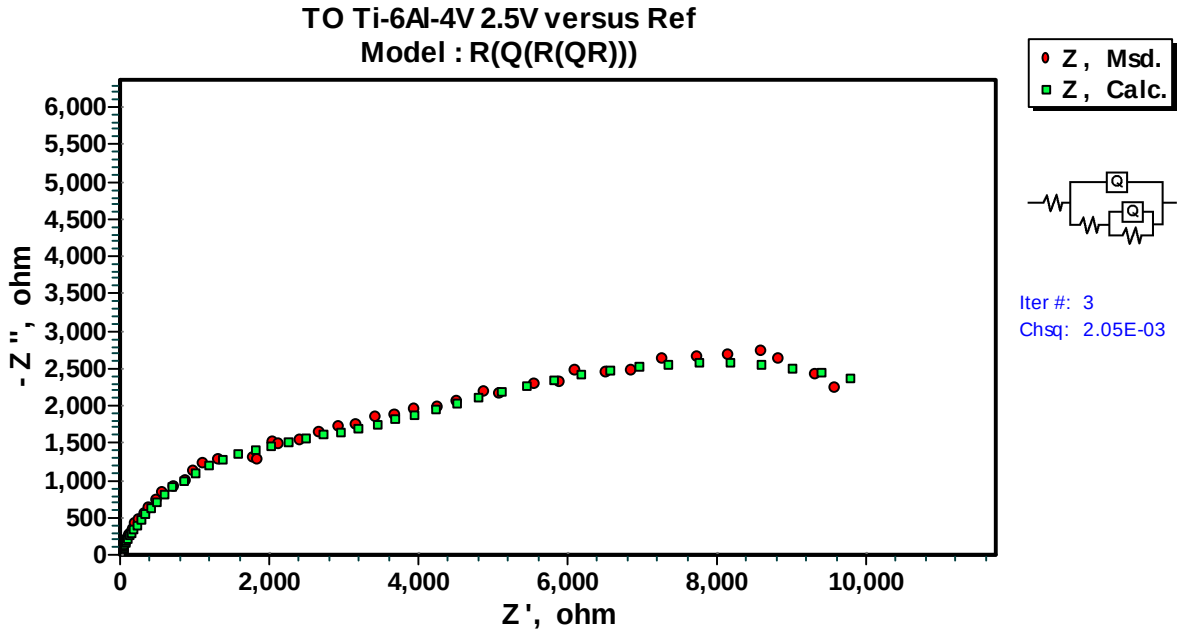

Figure 102: Nquist plot for TO Ti-6Al-4V at 2.5V_{SCE}.

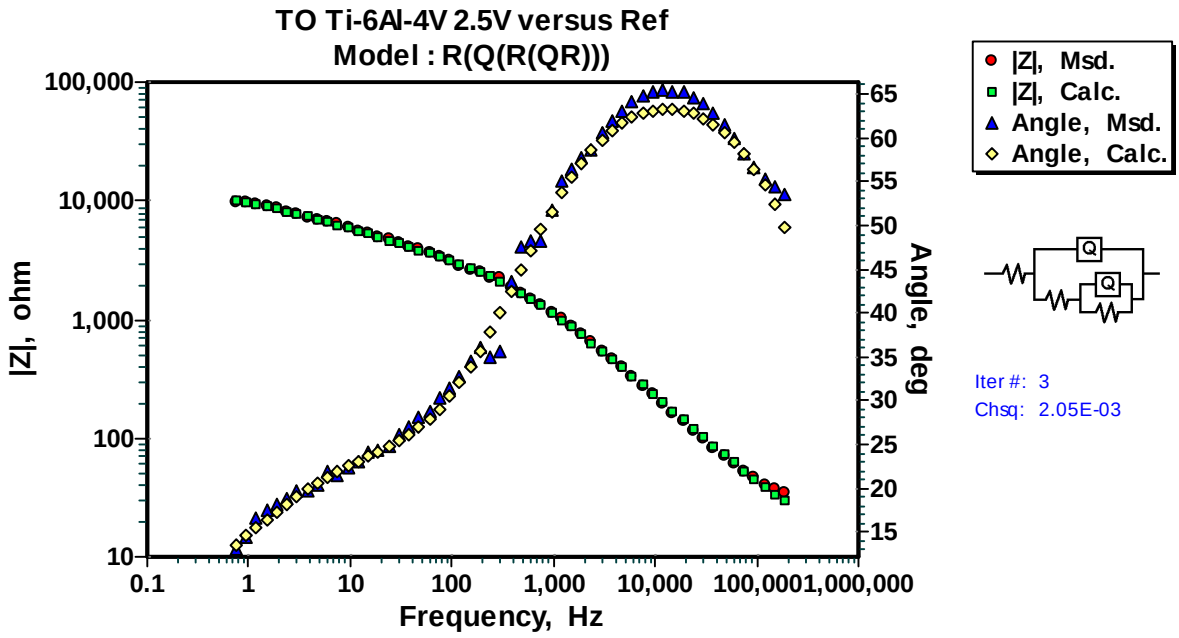

Figure 103: Bode Magnitude and Bode Phase plots for TO Ti-6Al-4V at 2.5V_{SCE}.

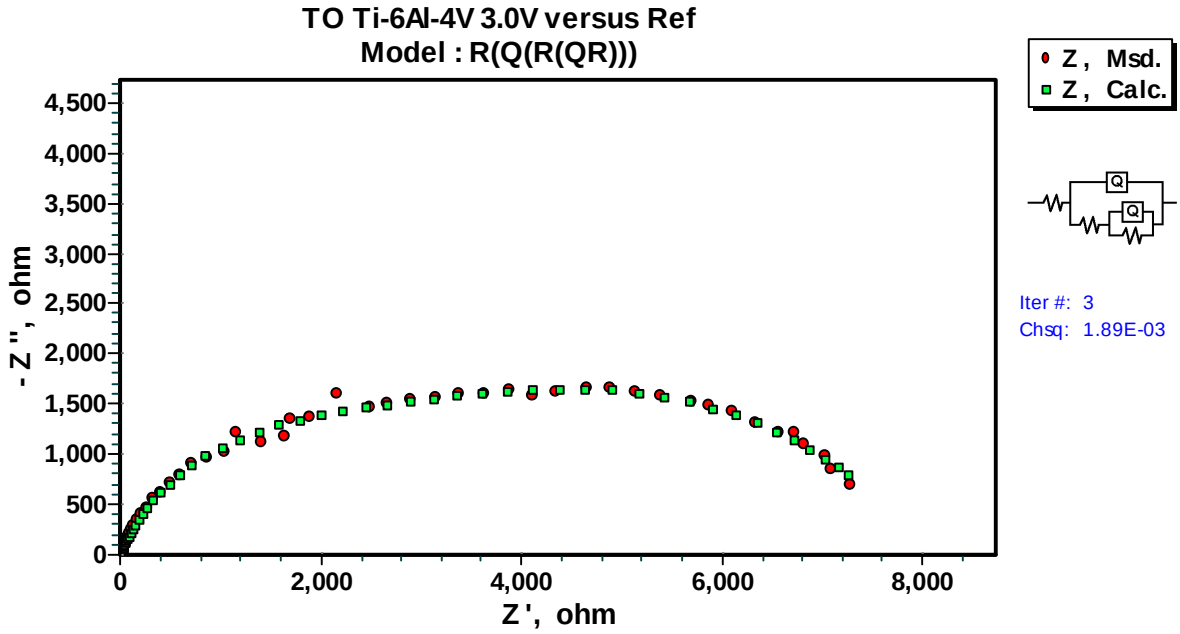

Figure 104: Nquist plot for TO Ti-6Al-4V at 3.0V$_{SCE}$.

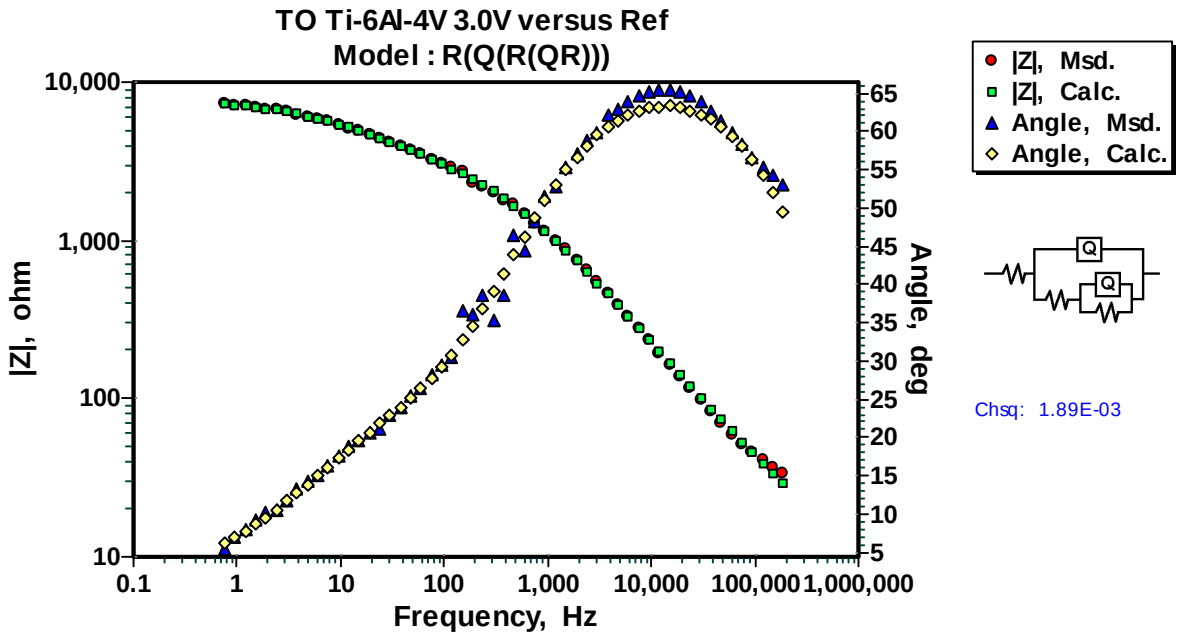

Figure 105: Bode Magnitude and Bode Phase plots for TO Ti-6Al-4V at 3.0V$_{SCE}$.

16.3 OBDH Ti-6Al-4V Potential Variation Impedance Plots

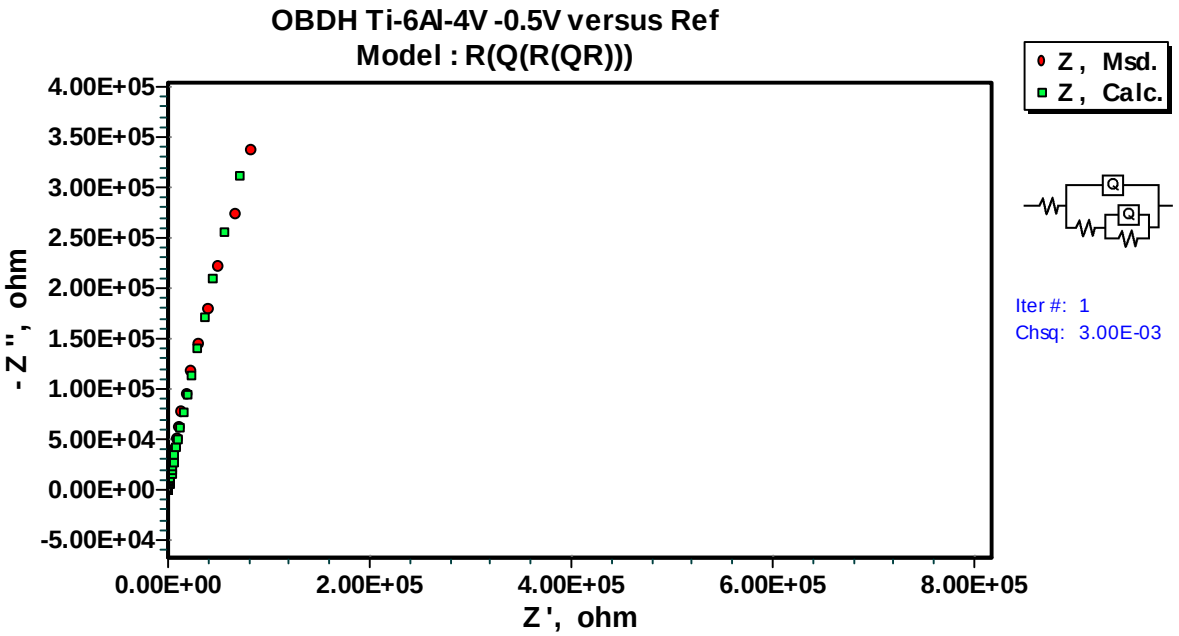

Figure 106: Nquist plot for OBDH Ti-6Al-4V at -0.5V_{SCE}.

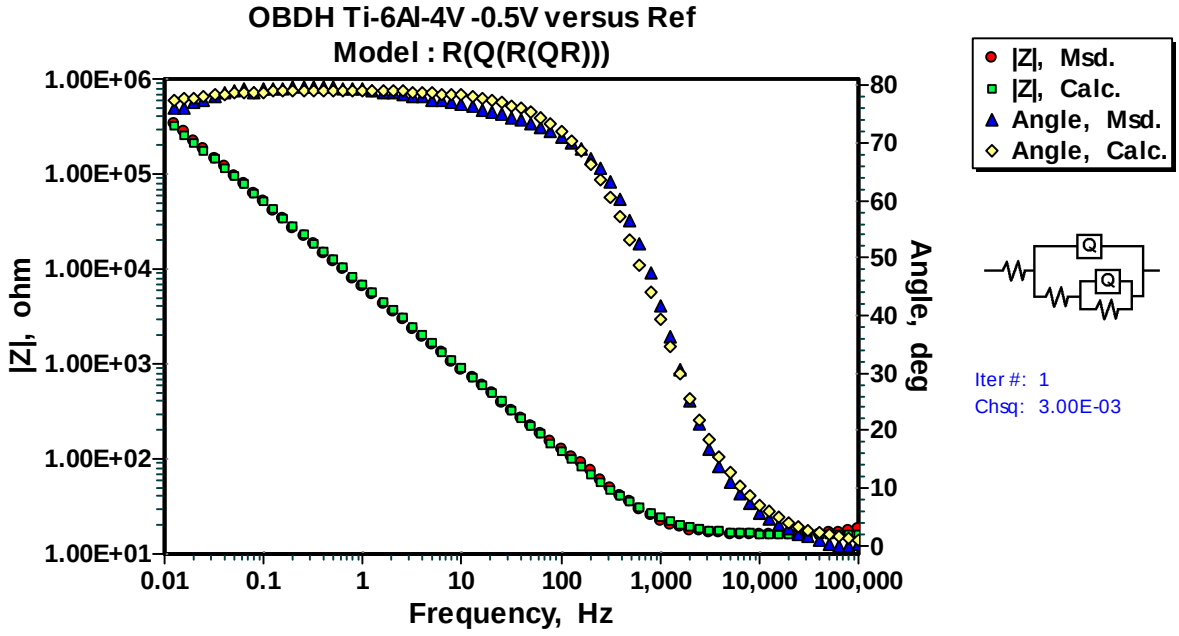

Figure 107: Bode Magnitude and Bode Phase plots for OBDH Ti-6Al-4V at -0.5V_{SCE}.

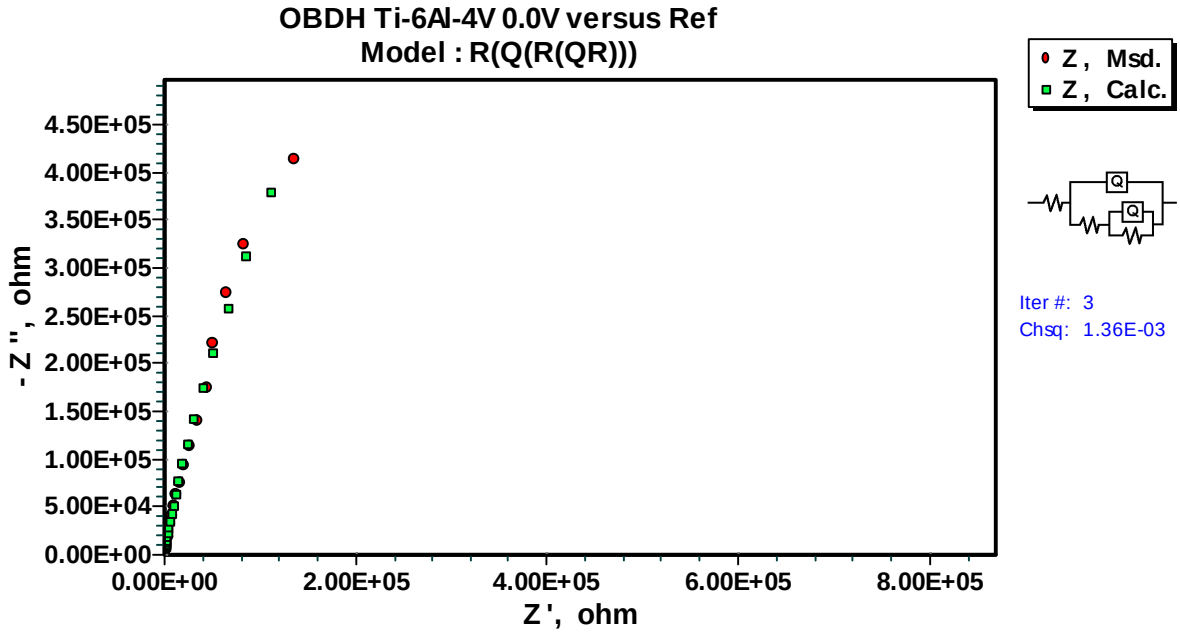

Figure 108: Nquist plot for OBDH Ti-6Al-4V at 0.0V_{SCE}.

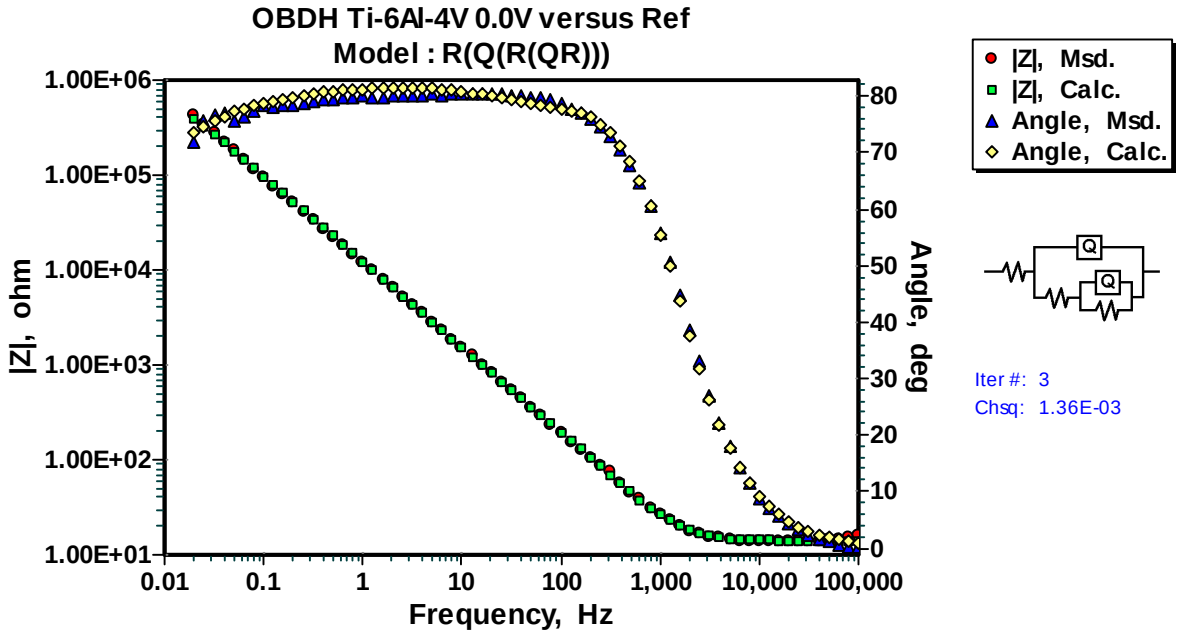

Figure 109: Bode Magnitude and Bode Phase plots for OBDH Ti-6Al-4V at 0.0V_{SCE}.

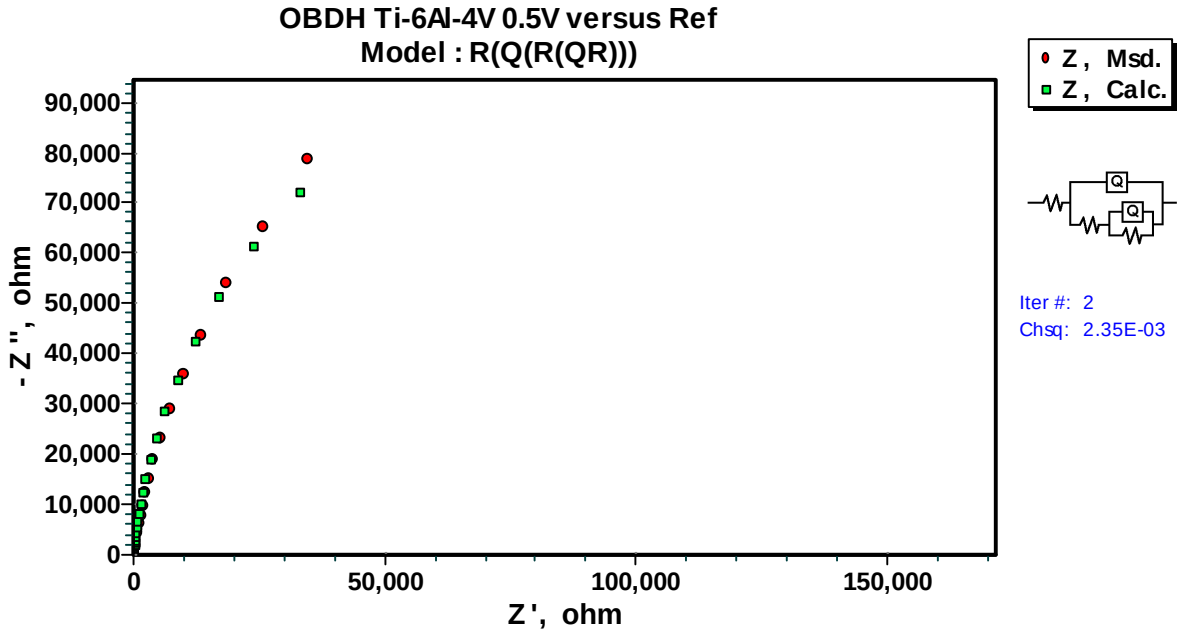

Figure 110: Nquist plot for OBDH Ti-6Al-4V at $0.5V_{SCE}$.

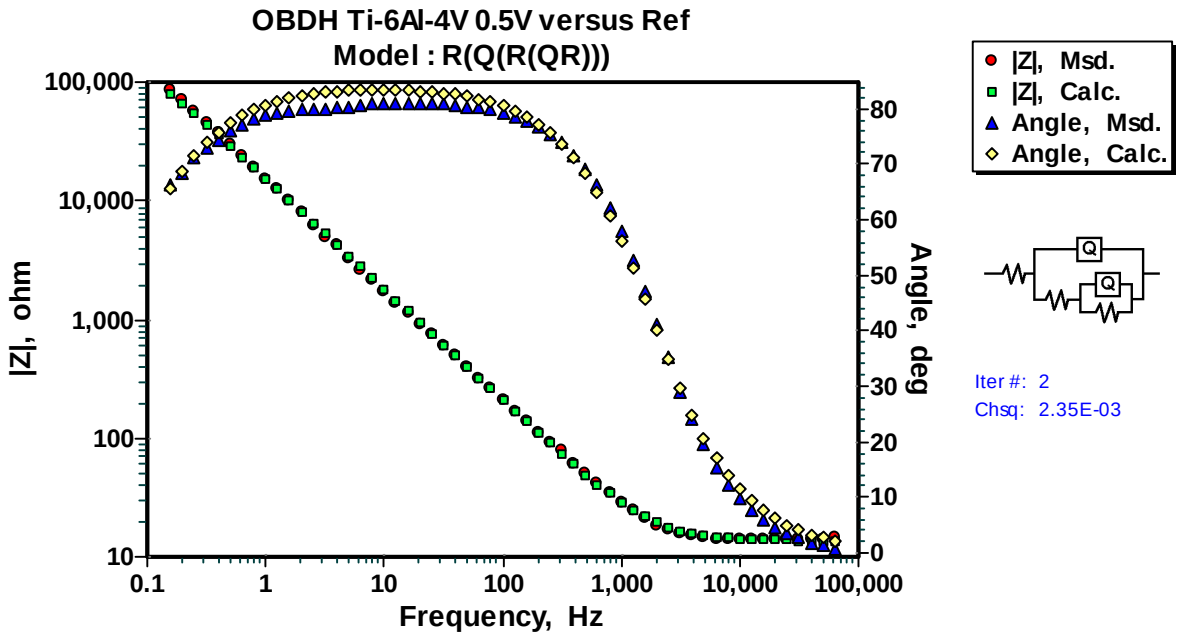

Figure 111: Bode Magnitude and Bode Phase plots for OBDH Ti-6Al-4V at $0.5V_{SCE}$.

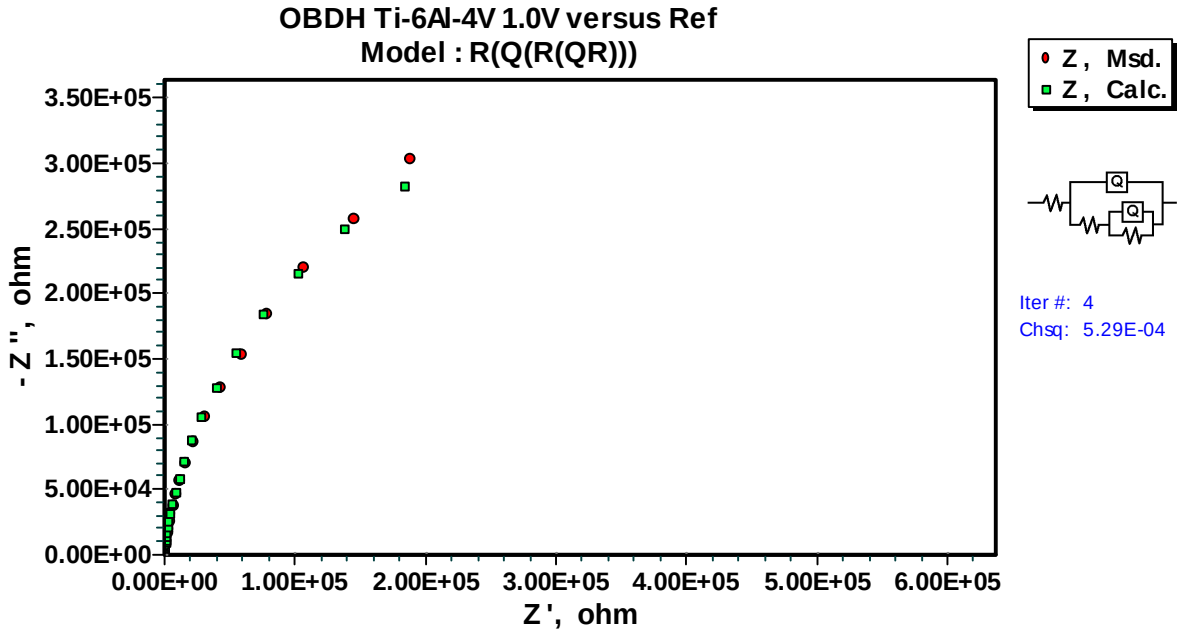

Figure 112: Nquist plot for OBDH Ti-6Al-4V at $1.0V_{SCE}$.

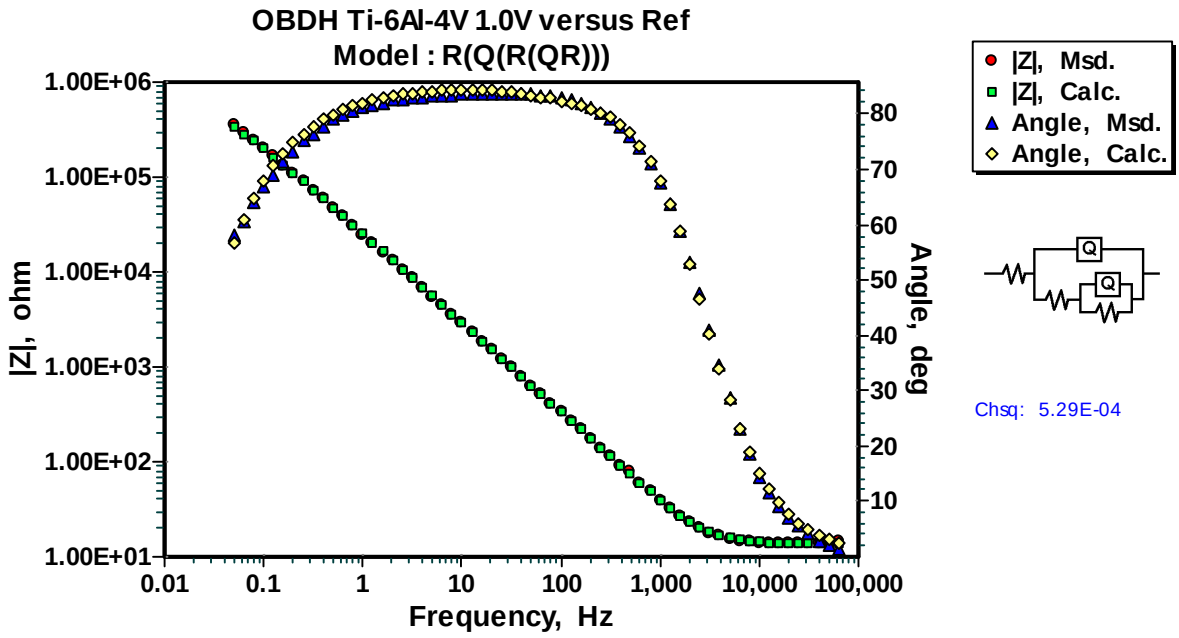

Figure 113: Bode Magnitude and Bode Phase plots for OBDH Ti-6Al-4V at $1.0V_{SCE}$.

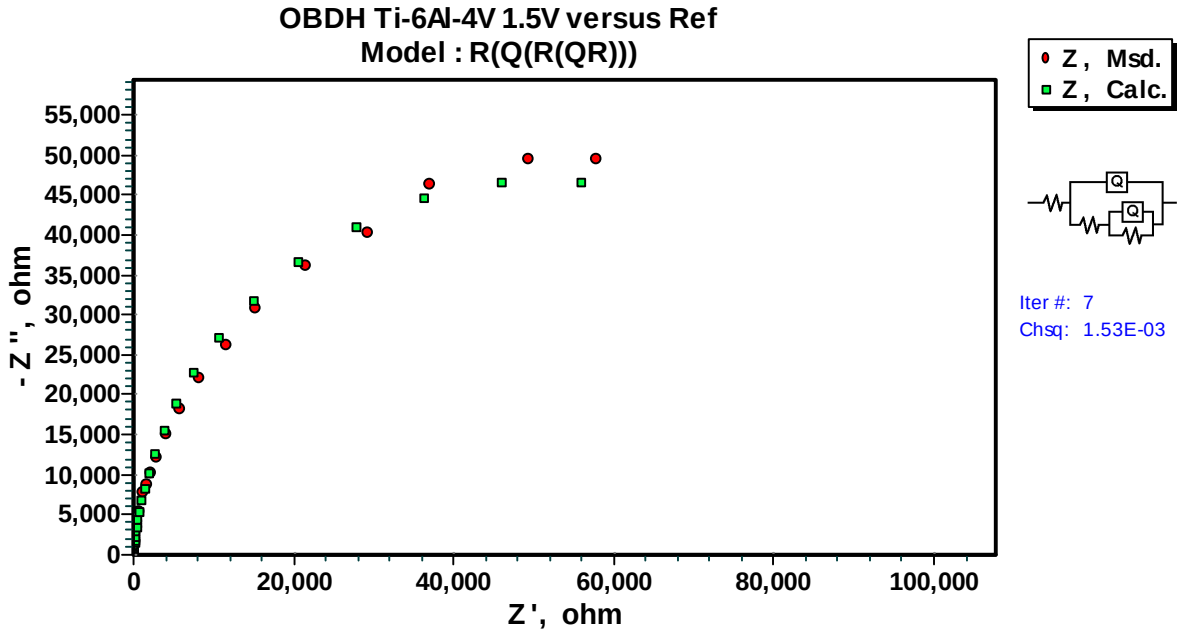

Figure 114: Nquist plot for OBDH Ti-6Al-4V at 1.5V_{SCE}.

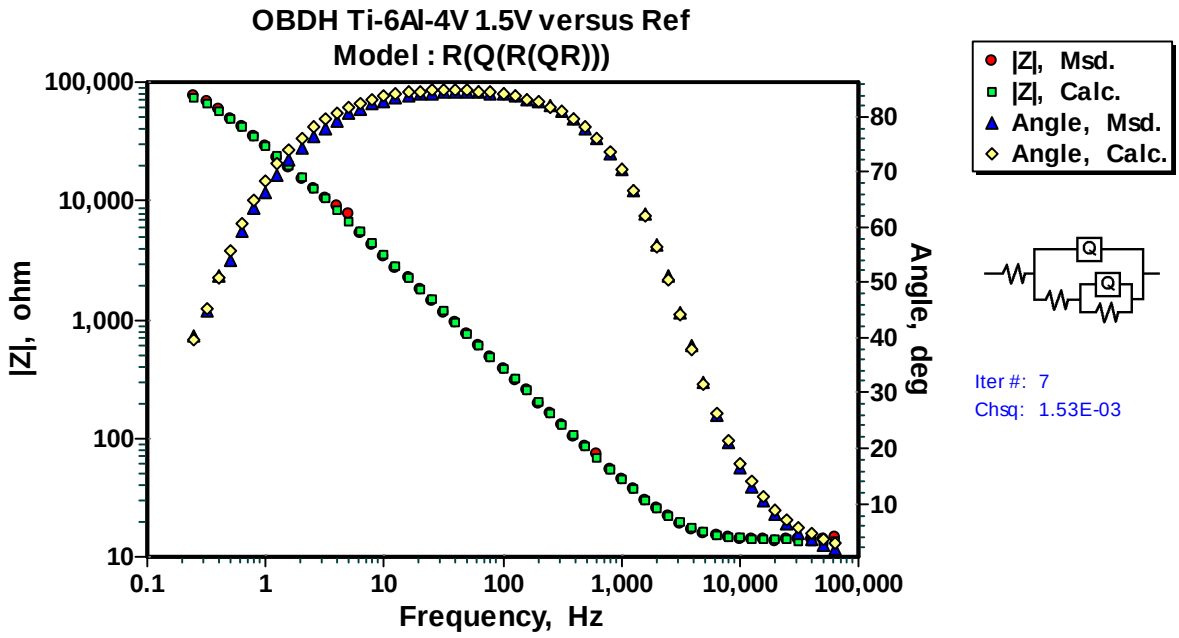

Figure 115: Bode Magnitude and Bode Phase plots for OBDH Ti-6Al-4V at 1.5V_{SCE}.

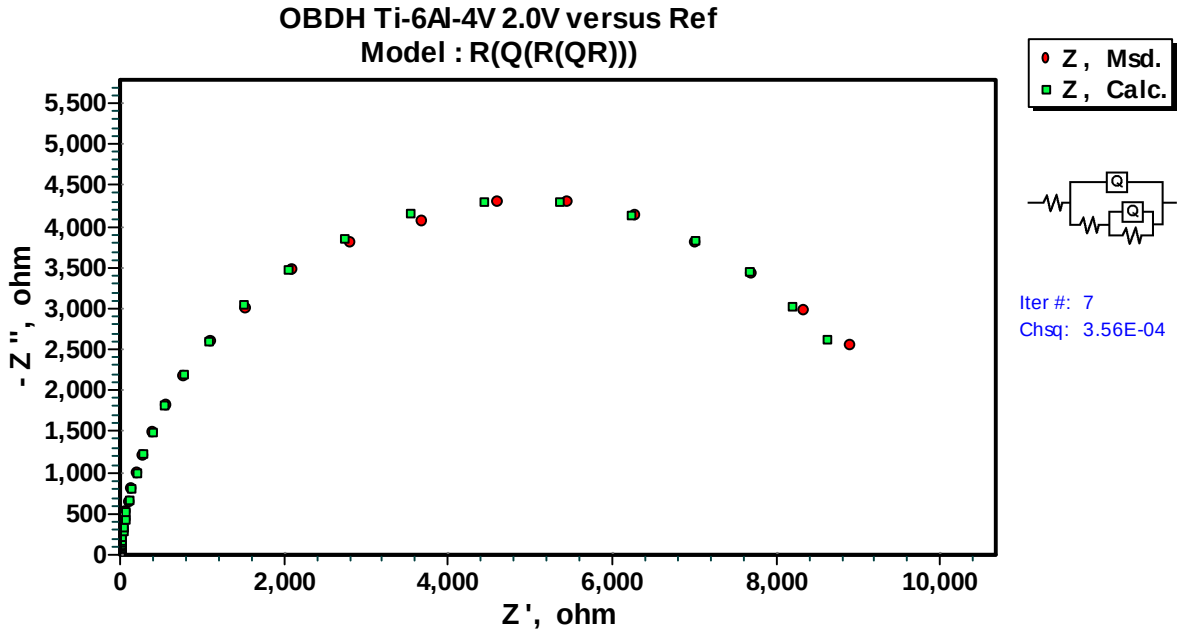

Figure 116: Nquist plot for OBDH Ti-6Al-4V at 2.0V_{SCE}.

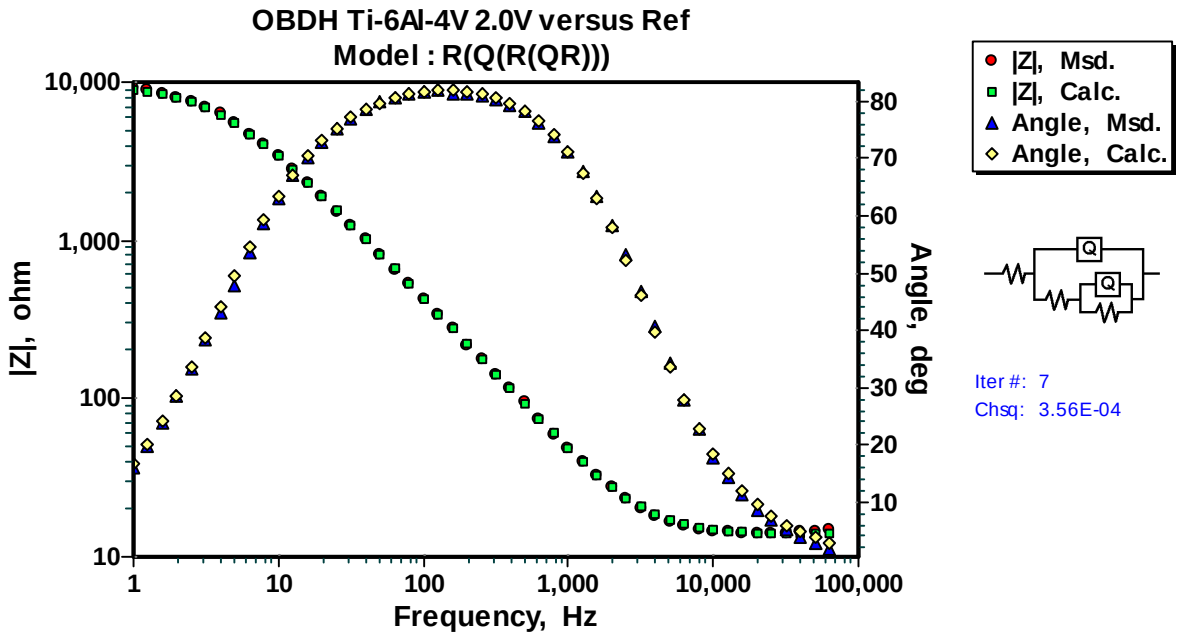

Figure 117: Bode Magnitude and Bode Phase plots for OBDH Ti-6Al-4V at 2.0V_{SCE}.

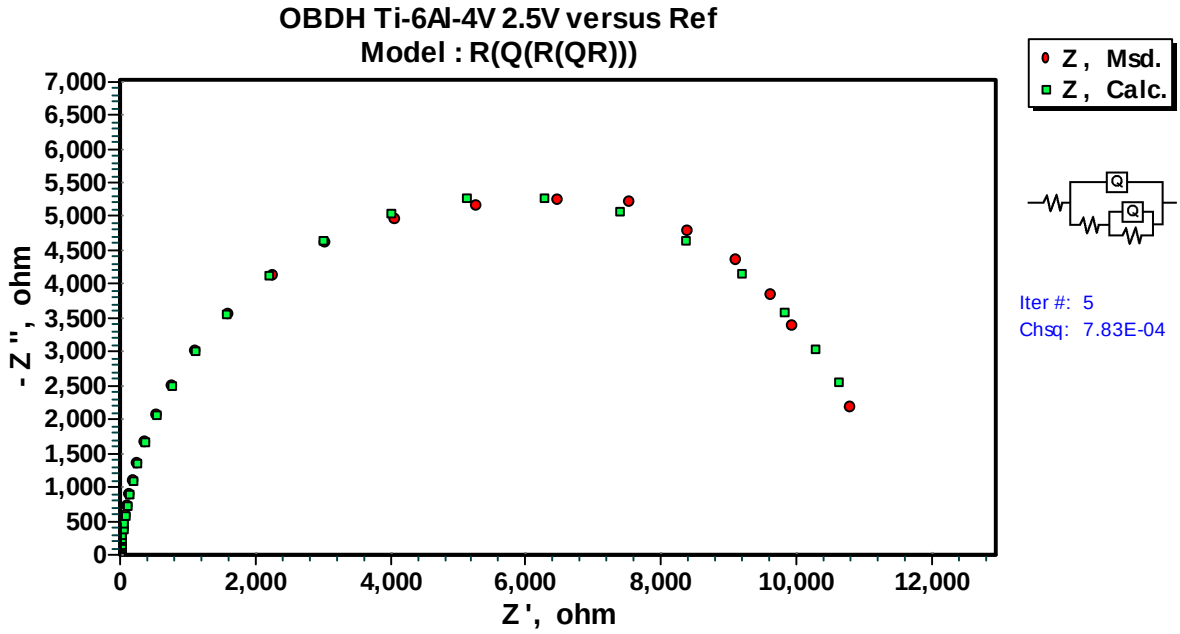

Figure 118: Nquist plot for OBDH Ti-6Al-4V at $2.5V_{SCE}$.

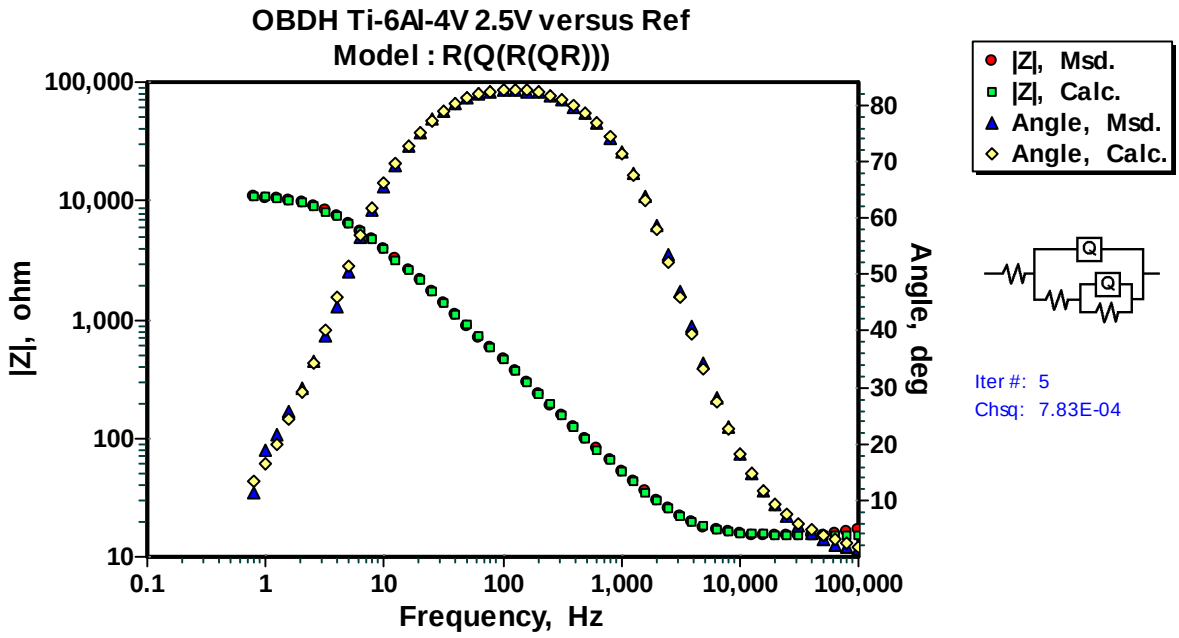

Figure 119: Bode Magnitude and Bode Phase plots for OBDH Ti-6Al-4V at $2.5V_{SCE}$.

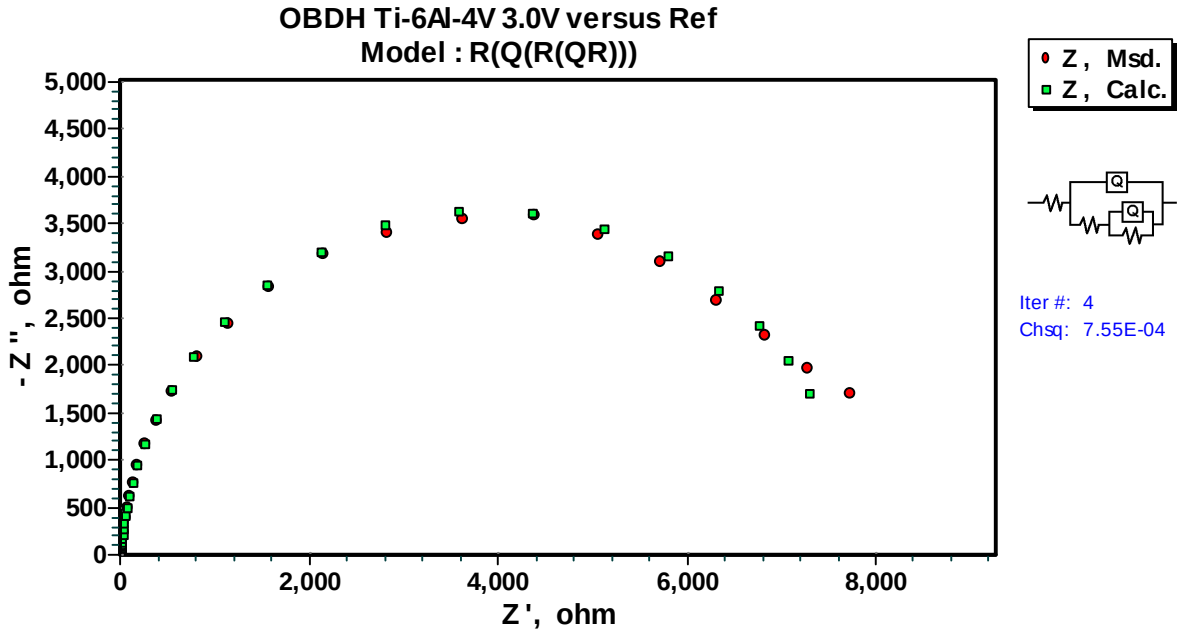

Figure 120: Nquist plot for OBDH Ti-6Al-4V at 3.0V_{SCE}.

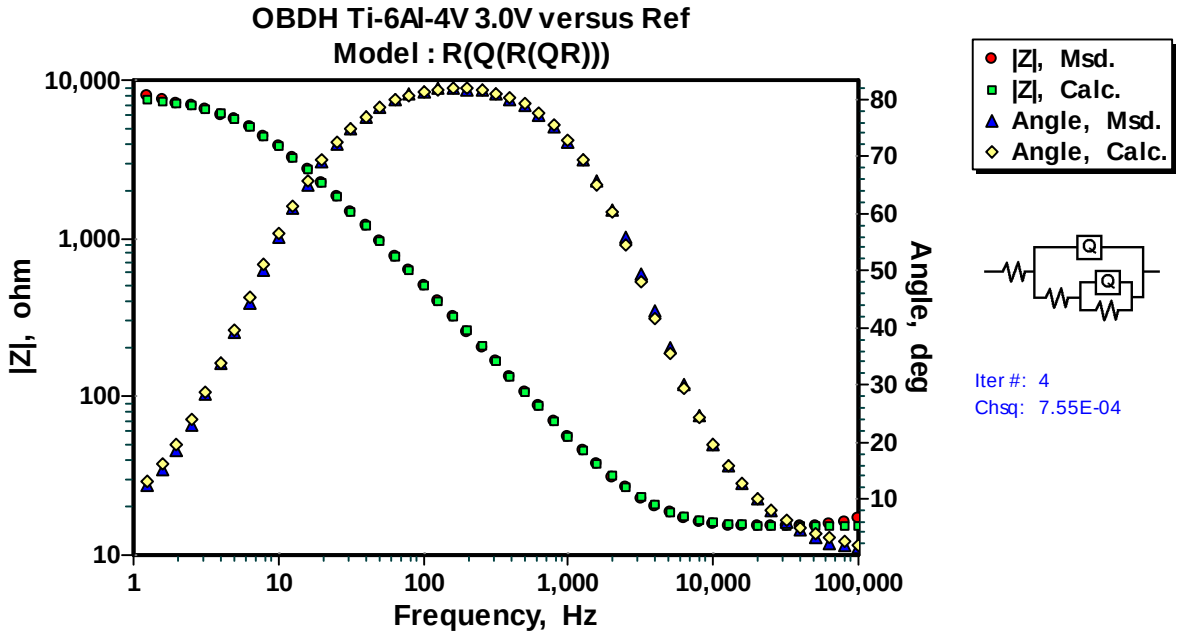

Figure 121: Bode Magnitude and Bode Phase plots for OBDH Ti-6Al-4V at 3.0V_{SCE}.